Analysis and practical considerations of linear and nonlinear piezoelectric energy conversion and harvesting techniques

Yi-Chieh Wu

To cite this version:

Yi-Chieh Wu. Analysis and practical considerations of linear and nonlinear piezoelectric energy conversion and harvesting techniques. Electronics. INSA de Lyon, 2013. English. NNT : 2013ISAL0085 . tel-01015934

HAL Id: tel-01015934
https://theses.hal.science/tel-01015934
Submitted on 27 Jun 2014

N° d'order 2013-ISAL-0085 Année 2013

THÈSE

présentée devant
L'INSTITUT NATIONAL DES SCIENCES APPLIQUÉES DE LYON

par
Yi-Chieh WU
Ingénieur INSA de Lyon

pour obtenir le grade de DOCTEUR

École doctorale : Mécanique, Energétique, Génie Civil et Acoustique de Lyon
Spécialité : Acoustique

Soutenue le 17 Sept 2013 devant la commission d'examen

Analyse et considérations pratiques de techniques de conversion et récupération d'énergie piézoélectrique linéaires et non-linéaires

-

Analysis and practical considerations of linear and nonlinear piezoelectric energy conversion and harvesting techniques

Membres du jury :

Ir.	Bertrand	DUBUS	Directeur de Recherche au CNRS	Examinateur
Pr.	Emmanuel	FOLTETE	Professeur à l'ENSMM de Besançon	Examinateur
Pr.	Daniel	GUYOMAR	Professeur à l'INSA de Lyon	Examinateur
Pr.	Einar	HALVORSEN	Professeur à Vestfold University College (Norvége)	Examinateur
Dr.	Mickaël	LALLART	Maître de conférence à l'INSA de Lyon	Co-directeur
Pr.	Elie	LEFEUVRE	Professeur à l'Universite Paris-Sud	Rapporteur
Pr.	Claude	RICHARD	Professeur à l'INSA de Lyon	Directeur
Pr.	Wen-Jong	WU	Professeur à National Taiwan University (Taïwan)	Rapporteur

Laboratoire de Génie Electrique et Ferroélectricité (LGEF) de l'INSA de Lyon

INSA Direction de la Recherche - Ecoles Doctorales – Quinquennal 2011-2015

SIGLE	ECOLE DOCTORALE	NOM ET COORDONNEES DU RESPONSABLE
CHIMIE	**CHIMIE DE LYON** **http://www.edchimie-lyon.fr** Insa : R. GOURDON	M. Jean Marc LANCELIN Université de Lyon – Collège Doctoral Bât ESCPE 43 bd du 11 novembre 1918 69622 VILLEURBANNE Cedex Tél : 04.72.43 13 95 directeur@edchimie-lyon.fr
E.E.A.	**ELECTRONIQUE, ELECTROTECHNIQUE, AUTOMATIQUE** **http://edeea.ec-lyon.fr** Secrétariat : M.C. HAVGOUDOUKIAN eea@ec-lyon.fr	M. Gérard SCORLETTI Ecole Centrale de Lyon 36 avenue Guy de Collongue 69134 ECULLY Tél : 04.72.18 60 97 Fax : 04 78 43 37 17 Gerard.scorletti@ec-lyon.fr
E2M2	**EVOLUTION, ECOSYSTEME, MICROBIOLOGIE, MODELISATION** **http://e2m2.universite-lyon.fr** Insa : H. CHARLES	Mme Gudrun BORNETTE CNRS UMR 5023 LEHNA Université Claude Bernard Lyon 1 Bât Forel 43 bd du 11 novembre 1918 69622 VILLEURBANNE Cédex Tél : 04.72.43.12.94 e2m2@biomserv.univ-lyon1.fr
EDISS	**INTERDISCIPLINAIRE SCIENCES-SANTE** **http://ww2.ibcp.fr/ediss** Sec : Safia AIT CHALAL Insa : M. LAGARDE	M. Didier REVEL Hôpital Louis Pradel Bâtiment Central 28 Avenue Doyen Lépine 69677 BRON Tél : 04.72.68 49 09 Fax : 04 72 35 49 16 Didier.revel@creatis.uni-lyon1.fr
INFOMATHS	**INFORMATIQUE ET MATHEMATIQUES** **http://infomaths.univ-lyon1.fr**	M. Johannes KELLENDONK Université Claude Bernard Lyon 1 LIRIS - INFOMATHS Bâtiment Nautibus 43 bd du 11 novembre 1918 69622 VILLEURBANNE Cedex Tél : 04.72. 43.19.05 Fax 04 72 43 13 10 infomaths@bat710.univ-lyon1.fr
Matériaux	**MATERIAUX DE LYON**	M. Jean-Yves BUFFIERE Secrétaire : Mériem LABOUNE INSA de Lyon École Doctorale Matériaux Mériem LABOUNE Bâtiment Antoine de Saint-Exupéry 25bis Avenue Jean Capelle 69621 VILLEURBANNE Tel : 04 72 43 71 70 Fax : 04 72 43 72 37 ed.materiaux@insa-lyon.fr
MEGA	**MECANIQUE, ENERGETIQUE, GENIE CIVIL, ACOUSTIQUE (ED n°162)**	M. Philippe BOISSE Secrétaire : Mériem LABOUNE Adresse : INSA de Lyon École Doctorale MEGA Mériem LABOUNE Bâtiment Antoine de Saint-Exupéry 25bis Avenue Jean Capelle 69621 VILLEURBANNE Tel : 04 72 43 71 70 Fax : 04 72 43 72 37 mega@insa-lyon.fr Site web : http://www.ed-mega.com
ScSo	**ScSo*** M. OBADIA Lionel Sec : Viviane POLSINELLI Insa : J.Y. TOUSSAINT	M. OBADIA Lionel Université Lyon 2 86 rue Pasteur 69365 LYON Cedex 07 Tél : 04.78.69.72.76 Fax : 04.37.28.04.48 Lionel.Obadia@univ-lyon2.fr

*ScSo : Histoire, Geographie, Aménagement, Urbanisme, Archéologie, Science politique, Sociologie, Anthropologie

Abstract

The battery replacement and disposal however become a big issue with the rapid development of electronic devices. Alternative power sources from our ambient environment therefore grasp people's interest in recent years. Among numbers of small-scale energy sources, using piezoelectric generators to convert vibrational energy into electrical energy received much attention as low-level mechanical vibrations are available in many environments and as piezoelectric transducers that allow the direct conversion of vibrations into electricity also permit easy maintenance and good integrability.

A nonlinear interface ("Synchronized Switching Harvesting on Inductor", SSHI), consisting in a switching device and an inductor, has been proved to improve the piezoelectric harvester performance especially for weakly-coupled harvesting system. This technique opens a new stage for piezoelectric energy harvesting system. However, existing works were usually done under the excitation with only one frequency information. A more practical excitation will contain more than one frequency information and usually broadband and random, for example the car motion, machine vibration, motor rotation, etc. In addition, the coupling effect due to the harvesting process is also an interesting issue to discuss. The modeling of piezoelectric harvester in the existing publications usually takes into account only the electromechanical coupling within the harvester during the harvesting process. Nevertheless, in practical applications of seismic or indirectly-coupled piezoelectric harvesters, the mechanical interaction between the host structure and the harvester is an essential issue. The purpose of this work is to analysis the seismic type piezoelectric harvester from a practical perspective and to provide an optimal design of the harvester. In this work, the broadband modeling based on the concepts of self-sampling and self-aliasing is described under broadband and/or random excitations for the nonlinear interface called "Periodic Switching Harvesting on Inductor" (PSHI). For PSHI technique, the switching device is considered to be turned on at a specific switching frequency, which can be any ratio of the harvester resonant frequency. Then this thesis work extends to the stochastic modeling in order to have mathematical expressions that can directly describe broadband performances of the harvester with the power spectral density (PSD) function of signals. As the switch is turned on at a given frequency, the modeling can be derived using cyclostationary theory. The effectiveness of stochastic modeling is also validated with experimental measurements and time-domain iterative calculations, and the harvester performance under a band-limited noise excitation is been discussed under noises with a bell-curved spectra. An optimal switching frequency slightly less than twice the harvester resonant frequency is proved to have the optimal power output under the optimal resistive load. This switching frequency is however dependent on the electromechanical coupling factor of the harvester; the smaller the electromechanical coupling factor, the closer the optimal switching frequency will be to twice the harvester resonant frequency.

The other part of this thesis work is to discuss the interaction (mechanical to mechanical coupling effect) between the host structure and the seismic harvester. The analysis is conducted with a Two-Degree-of-Freedom (TDOF) model consisting in a host structure and a harvester. An energy conversion loop is therefore formed between the host structure and the harvester, within the harvester and between the harvester and the resistive load. The TDOF model is verified with the Finite Element Method (FEM) model and the experimental work. An optimal mass ratio of harvester dynamic mass to host structure dynamic mass, which is about few percent, is proved to have the optimal power output at the optimal resistive load. The modeling is further applied to a practical self-powered Structural Health Monitoring (SHM) system providing the best design of the harvester. A practical consideration with the broadband excitation is also introduced with the stochastic showing the effect of frequency detuning between the host structure and the harvester. The analysis is conducted in two design criteria providing different energy harvesting processes, constant force factor and constant electromechanical coupling factor. With a constant electromechanical coupling factor, the harvester performance is surprisingly with very little change due to the mismatching of harvester and host structure resonant frequencies providing a larger tolerance in frequency detuning.

Keywords: Energy harvesting; scavenging; broadband modeling; piezoelectric; stochastic modeling; nonlinear processing; frequency detuning; backward coupling effect.

Résumé

La décroissance de la consommation électrique des dispositifs électroniques (tels que des réseaux de capteurs autonomes) leur a permis une croissance sans précédent. Néanmoins, les éléments de stockage d'énergie (piles et batteries), bien qu'ayant initialement promus ce développement, sont devenus un frein à la prolifération des microsystèmes électroniques. Cette limitation s'explique par la durée de vie relativement limitée de ces éléments (l'auto-décharge drainant quelquefois plus d'énergie que celle consommée par le système) nécessitant une maintenance non négligeable et prohibitive lorsque les dispositifs sont nombreux et/ou inaccessibles, ainsi que par des considérations environnementales ; le processus de recyclage des batteries étant complexe et coûteux.

Pour palier à ce problème, la possibilité d'exploiter l'énergie de l'environnement immédiat du dispositif a été proposée et a fait l'objet de nombreuses recherches au cours des dernières années. En particulier, la récupération d'énergie mécanique exploitant l'effet piézoélectrique est l'une des pistes les plus étudiées actuellement pour la conception de microgénérateurs autonomes capables d'alimenter les dispositifs électroniques. Par ailleurs, dans ce domaine, il a été démontré que l'utilisation d'interfaces électroniques effectuant un traitement non-linéaire de la tension de sortie de l'élément actif permet d'améliorer grandement les capacités de conversion (et donc de récupération) de l'énergie vibratoire. L'une de ces approches, nommée "Synchronized Switch Harvesting on Inductor" (récupération par commutation synchronisée sur inductance) s'est montrée particulièrement efficace, pouvant augmenter la quantité d'énergie récupérée par un facteur supérieur à 10 par rapport aux techniques linéaires. Cette technique consiste à connecter l'élément piézoélectrique sur une inductance pendant un bref instant. L'élément piézoélectrique ayant un comportement diélectrique, ceci forme ainsi un circuit résonant qui conduit à une oscillation de la tension. Si le temps de connexion est choisi comme étant égal à une demi-période du circuit résonant ainsi formé, il se produit une inversion de tension. Cette dernière conduit à un processus cumulatif qui augmente artificiellement la tension de sortie de l'élément piézoélectrique ainsi qu'à une réduction du déphasage entre tension et vitesse de déplacement ; ces deux effets conduisant à l'augmentation importante des capacités de conversion.

Néanmoins, l'étude des microgénérateurs d'énergie est quasiment toujours faite en considérant une excitation sinusoïdale, ce qui correspond rarement à la réalité. Peu de travaux expérimentaux, et encore moins théoriques, ont été menés en considérant une excitation large bande (impulsion, bruit...) ; ceci étant d'autant plus vrai pour les dispositifs incluant un élément non-linéaire. Ainsi l'objectif de cette thèse est d'étudier le comportement des récupérateurs d'énergie piézoélectriques interfacés de manière non-linéaire. Pour ce faire, différentes approches seront prises, en considérant le processus de commutation comme un "auto-échantillonnage" du signal, ou en appliquant des théories d'analyse stochastique pour quantifier les performances du dispositif. Ainsi, plusieurs formes d'excitation appliquée au système pourront être analysées, permettant d'étudier la réponse du système sous des conditions plus réalistes.

Toujours dans l'optique d'une implémentation réaliste, un autre objectif de cette thèse consistera à évaluer l'impact de la récupération d'énergie par couplage sismique sur la structure hôte, démontrant la nécessité d'envisager le système dans sa globalité afin de disposer de systèmes performants capables de convertir efficacement l'énergie vibratoire sous forme électrique pour un usage ultérieur.

Mots-clés: Matériaux piézoélectriques; transfert d'énergie; large bande; modélisation stochatique; désaccord de fréquence; effet de couplage; récupérateur sismique.

Acknowledgement

First and foremost, I would like to express my deeply gratitude to everyone who helped me during my doctoral study and be with me during these years. I have been fortunate having the financial funding from French Adminstration for accomplishing my PhD study in the lab Laboratoire de Gènie Electrique et Ferroèlectricitè (LGEF) at the Institut National des Sciences Appliquées de Lyon (INSA de Lyon).

I would like to express my heartfelt gratitude to Prof. Dr. Claude Richard and Dr. Mickaël Lallart for their motivation, guidance and indefatigable support without which this work would have remained only as a dream instead of indiscernible reality. Prof. Richard has been a great advisor and mentor who has always provided profound idea and detailed discussions no matter on technical or non-technique questions. Dr. Lallart has given me the opportunity to work on several research problems and he has provided me a lot of useful advices on academic and research. Also, I would like to express my special thanks to Prof. Dr. Daniel Guyomar for his support during my research work. He provides a full equipped experimental environment, where we can realize the concepts. I would like to thank Prof. Wen-Jong Wu from National Taiwan University for his assistance in the work of broadband modeling and my master work in NTU. I would like to extend my deepest gratitude to Prof. Einar Halvorsen for his great help on stochastic modeling. We had a very joyful and fruitful cooperation. I can always learn something from the discussion with him. Thanks to Lab LGEF for giving me the chances working with these professors, who I take as role-models.

I would like to thank Prof. Emmanuel Foltete, Prof. Daniel Guyomar, Prof. Einar Halverson, Prof. Wen-Jong Wu and Prof. Elie Lefeuvre for serving on my PhD committee.

My thanks are also due to my lovely colleagues, Masae, Dan, Bin, Yang, Kaixiang, Fouad, Hongying, Liuqing and Meng for their companies and help. With some of them, we had shared the same office for years and I truly enjoyed it. We always had exciting discussion on research and fun chat together. I will never forget the nights I walked home and shared sorrows with Masae and Dan after a long day work. Thanks to my friends, Ging-e, Wei-Wen, Ya-Shan and all my dearest Taiwanese friends, without your companionship, my life would not be balanced. I would like to appreciate the help from Mrs. Evelyne Dorieux for the administrative work. I would also like to thanks Mr. Frédéric Defromerie for his help in technical work and the accomplishment for everyday's lunch time. I really want to wish him a very happy future and I am sure he will definitely find someone who wants to share the life with him. Thanks to PHC Orchid program with NTU, Taiwan, I had passed a very pleasant summer in Taiwan with Mickaël, Jean-Fabien and his wife, Anaïs, a very warm friend who I like very much.

Lastly, I would like to express my great appreciation to my family, my dad, my mom and my brother. They accompany me no matter when I feel sad or happy or even when I am busying on my own work. I would like to express my apology to them because I am always too busy to talk to them and far from them.

Without the assistance I have received from my professors, my friends and my family, my individual inquiry would have been much more difficult, and the experience much less rewarding.

Thank you very much again, this work is dedicated to you.

— WU Yi-Chieh

Contents

Notations and abbreviations

Notations

Symbol	Signification
	Alphabetic character
$\mathbf{A}$	piezoelectric force factor vector
A	cross-sectional area of piezoelectric element
$\mathbf{B}$	input matrix
C	structural damping coefficient
$\mathbf{C}$	damping matrix
C_0	internal capacitance of piezoelectric element
$[c^E]$	elastic stiffness matrix determined at constant electric field
c	elastic rigidity
D	electric displacement
$[d]$	nodal degree of freedom
d_{31}	piezoelectric constant in 3-1 mode
E	electrical field
$E_{dissipated}$	total energy dissipation
E_s	extracted energy from source
$E\bar{I}$	flexural rigidity
s^E	compliance of piezoelectric material
e	piezoelectric stress matrix
$\mathbf{F}$	force vector
F	exerted-force
F_M	force magnitude
F_p	restoring force due to the stiffness of piezoelectric element
f	frequency
f_s	switching frequency

f_0	resonant frequency
$\mathrm{H}(t)$	Heaviside step function or Unit step function
H	transfer function
h_{AB}	impulse response of A to the input B
$\mathbf{I}_n$	identity matrix of size n
I	current
I_0	initial current
J	second moment of inertia
j	imaginary unit
K	stiffness
$\mathbf{K}$	stiffness matrix
K_{pE}	stiffness of piezoelectric element in short-circuit
K_s	structural stiffness
k^2	electromechanical coupling factor
L	inductance
l	beam length
$\mathbf{M}$	mass matrix
M	bending moment
M	mass
m_X	mean of signal X
$\bar{m}$	mass per unit length
$\mathbf{N}$	shape function
$\mathbb{N}$	natural numbers
P	harvested power
P_s	extracted power from source
Q	electric charge
Q_i	electrical quality factor
Q_M	mechanical quality factor
$q(x_1,t)$	external force applied at position x_1
q_i	modal displacement of i^{th} mode
R_L	resistance
R_{AB}	cross-correlation function between random signals A and B
R_{AB}^n	cyclic cross-correlation function between random signals A and B
S	material strain

S_{AB}	power spectral density between signals A and B
S^n_{AB}	spectral cross-correlation density (SCD) between random signals A and B
$[\epsilon^S]$	permittivity matrix evaluated at constant strain
$\mathbf{T}$	transfer matrix
T	material stress
T_{LCR}	oscillation period of LCR oscillator
T_s	switching period
t	time
t_0	time delay
t_a or $t_a^{'}$	switch closing time for step 1
t_b or $t_b^{'}$	switch closing time for step 2
t_i	inversion time
t_n	switching instant
t_p	thickness between two electrodes of piezoelectric element
$\tilde{U}$	Fourier transform of displacement
U_1	displacement magnitude of host structure
U_2	displacement magnitude of harvester
$\mathbf{u}$	displacement matrix
u	displacement or deflection
u_M	maximum displacement amplitude
V	voltage
$\tilde{V}$	voltage in frequency domain
$\tilde{V}_0$	piecewise function of voltage
V_M	voltage before inversion
V_m	voltage after inversion
w	beam width
$\mathbf{x}$	state vector
x_c	neutral axis
y	external excitation displacement
Z	electrical impedance
$\mathbb{Z}$	integers

Greek character

Symbol	signification

α	Force factor
χ	Multiplication factor for defining the damping matrix
β	Multiplication factor for defining the damping matrix
γ	Inversion factor
ρ	Density
ω	Angular frequency
ω_0	Natural angular frequency
ω_s	Angular switching frequency
ζ	Structural damping ratio
Φ	Magnetic flux
ϕ_i	Phase shift reference to the force excitation for i variable
η	Efficiency factor
λ	Ratio between open-circuit voltage and displacement
ψ	Young's modulus
υ	Poisson's ratio
θ	Deflection slope
δ	Dirac delta function
ν	Poisson's ratio

Subscripts

Symbol	signification
E	open circuit
D	short circuit
H	host structure
p	piezoelectric element
b	beam
h	harvester
s	switching
sup	supporter
$+$	just after the inversion
$-$	just before the inversion

Abbreviations

Symbol	signification
AC	Alternating Current
DC	Direct Current
FEM	Finite Element Method
FFT	Fast Fourier transform
I/O	Input/Output
LCR	Inductance-Capacitance-Resistance
MEMS	MicroElectroMechanical Systems
MOSFET	Metal-Oxide-Semiconductor Field-Effect-Transistor
MsM	Magnetostrictive materials
PSD	Power spectral density
PSHI	Periodic switching harvesting on inductor
PVDF	Poly(vinylidene Fluoride)
PZT	Lead-Zirconate Titanate
RFID	Radio Frequency Identification
RMS	Root Mean Square
SCD	Spectral cross-correlation density
SDOF	Single Degree Of Freedom
SHM	Structure Health Monitoring
SSD	Synchronized Switch Damping
SSDS	Synchronized Switch Damping on Short circuit
SSDI	Synchronized Switch Damping on Inductor
SSH	Synchronized Switch Harvesting
SSHS	Synchronized Switch Harvesting on Short circuit
SSHI	Synchronized Switch Harvesting on Inductor
SW	Switch
TDOF	Two Degree Of Freedom
TMD	Tuned Mass Damper
WSNs	Wireless Sensor Networks

1 Generalities on Energy Harvesting

This chapter aims at presenting the main physical phenomena and applications of energy harvesting with a direct link of the topics covered in this thesis. It gives a general introduction of energy harvesting in order to present the motivations that lead to the development of renewable energy, the potential energy source and then focuses on energy harvesting from vibration motion with piezoelectric materials. The other objective of this chapter is to summarize current scientific literatures related to this thesis work. A description of the state of the art in terms of energy harvesting, piezoelectric energy harvester and broadband modeling is thus also exposed.

1.1 Motivation

The mobile wireless applications has a rapid growth thanks to the decrease in consumption of electronic components and has brought the development in energy harvesting. Primary batteries, which initially promoted the development of portable electronic devices, have paradoxically became a brake on this growth, particularly because of associated maintenance issues (charging, replacement). Compared to the computational demands predicted by Moore's law, the battery capacity has improved very slowly (Figure 1.1), showing the need of micropower generators. For a Structural Health Monitoring (SHM) system, it is typically impractical and costly to change batteries periodically over the lifetime of the structure. Another energy system which is capable of being adapted to the infrastructure with a longer lifespan, for example, ambient energy in surrounding medium or infrastructure itself, is therefore required. Given these reasons, alternative power sources from our ambient environment has been paid much attention. Figure 1.2 shows a good example of an autonomous Wireless Sensor Network (WSN) nodes with energy supplied by a renewable energy harvesting system. Sensors and electronics powered up by energy harvesters could be placed on the structure with

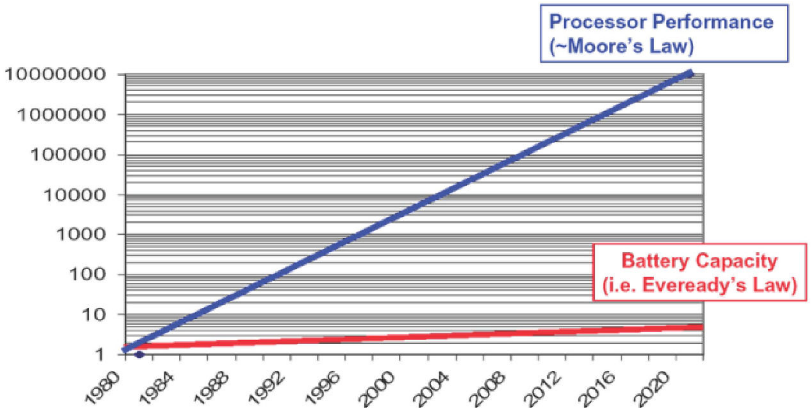

Figure 1.1: Battery capacity versus processor performance [1].

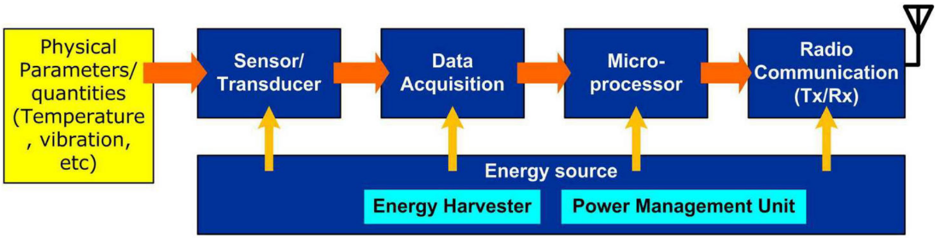

Figure 1.2: Block diagram of energy renewable Wireless Sensor Networks system [2]

limited accessibility, such as bridges, airplanes, ships and manufacturing plants, providing an unlimited power supply for the lifespan of electronic devices and make them completely self-sustaining. However, the dimension constrain is a tricky problem and optimal designs for energy harvesters being able to efficiently convert ambient energy into electrical energy and provide enough power to the electronics is still an open issue. The analytical work with practical considerations on real applications, for example, the heat losses induced by the environment for thermoelectric generators and broadband and/or random excitation for vibrational microgenerators, is still a subject less explored.

Table 1.1 provides the list of power requirement of various household electronic devices. Some of these equipments require only a small power level from 1 μW to 100 mW. Aside from applying on systems such as WSN and SHM, energy harvesters which are capable of continuously harvesting energy from ambient sources could be another option for supplying household electronics energy.

Table 1.1: Average power consumption of common household electronic devices

Product	*Average power consumption*
LCD screen (21-inch)	30-80 W
Laptop computer (fully on, charged)	30 W
Fluorescent light bulb	14 W
DVD player (playing)	10 W
ipad (wifi and video mode)	2.5 W
iphone 5 (talk/stand-by)	680 mW/24 mW
HTC One S smart phone (talk/stand-by)	630 mW/170 mW
Kindle touch Ereader (reading mode)	210 mW
TV remote	100 mW
Small portable FM radio	30 mW
Quartz wristwatch	1 μW

1.2 Potential Energy Conversion Mechanisms

Energy harvesting is the process that converts any kind of energy from the ambient environment to usable electrical energy. Ambient energy sources could be mechanical vibration, electromagnetic sources, light, airflow, heat, sun power, and temperature variations, as shown in Table 1.2. Several excellent literatures reviewed possible energy sources for energy harvesting and gave a comparison between them [3–6]. Priya has shown a broad survey of potential energy sources, which are listed in Figure 1.3 [5], for wireless sensor networks. This survey expands from natural energy, mechanical energy, thermal energy, radiation wave energy and battery capacities. Under direct sunlight, solar cell offers excellent power density about 15000 μW/cm^3, which is about 2 orders of magnitudes higher than other sources. The solar energy is definitely a very promising source for powering electronic devices, but the variation of light intensity could however lead to a significant drop in the power density. Also it is not possible to have an efficient solar power conversion inside buildings or under the cover, compromising their application in many cases. Otherwise, power scavenged from thermal gradients and from kinetic energy are the other most attractive sources, comprising of mechanical vibrations, air flow and human power. Roundy *et al* [3] concluded that for a device with a lifetime in the range of 1 year or less, the battery is the easiest and the most versatile solution (as shown in Figure 1.4), but mechanical vibrations profit more for a longer lifetime requirement.

This section provides an up-to-date assessment of available energy harvesting meth-

Table 1.2: Sources of energy available in the surrounding which are/can be tapped for generating electricity [5]

Human Body	*Vehicles*	*Structures*	*Industrial*	*Environment*
Breathing, blood pressure, exhalation, body heat	Aircraft, UAV, helicopter, automobiles, trains	Bridges, roads, tunnels, farm house structures	Motors, compressors, chillers, pumps, fans	Wind, solar, temperature gradient, daily temperature
Walking, arm motion, finger motion, jogging, swimming, eating, talking	Tires, tracks, peddles, brakes, shock absorbers, turbines	Control-switch, HVAC systems, ducts, cleaners, etc.	Conveyors, cutting and dicing, vibrating machine	Ocean currents, acoustic waves, EM waves, RF signal

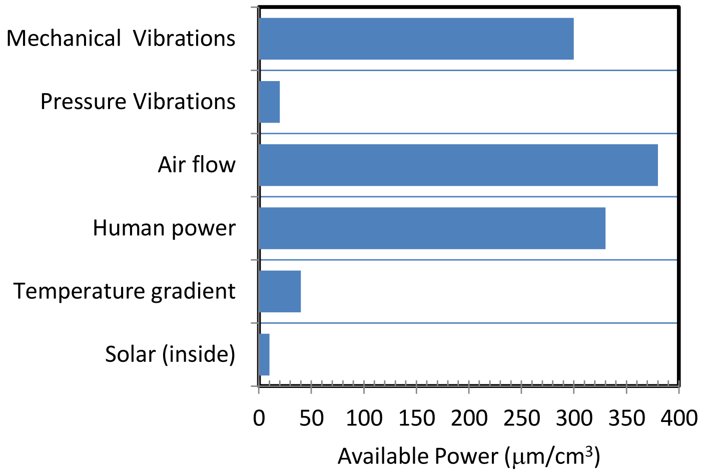

Figure 1.3: Comparison of various potential power sources for the sensor networks [5]

ods in the micro to mili-watt scale, which is suitable for low-power electronics. As the area of available energy sources is very broad, we can generalize these common renewable energy sources roughly into three main categories: 1. thermal conversion, 2. ambient-radiation sources and 3. vibration conversion.

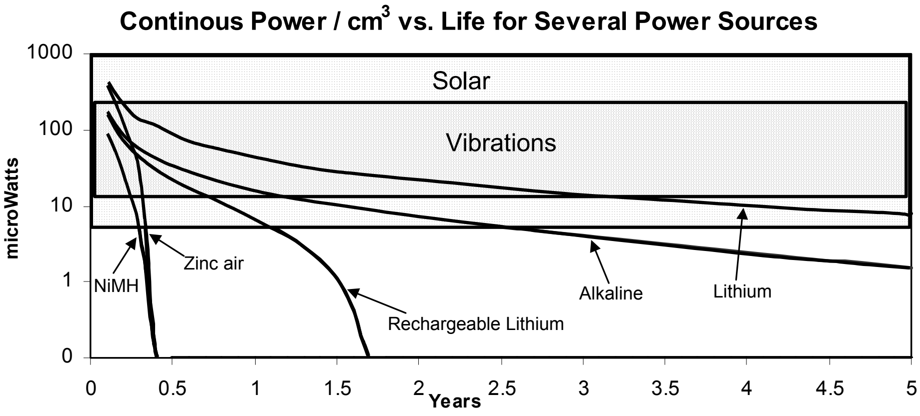

Figure 1.4: Comparison of power from vibrations, solar, and various battery chemistries [3]

1.2.1 Thermal Energy

The thermal energy exists ubiquitously in our daily life, such as heaters and heat induced by the friction motion. It commonly presents in two forms, 1. temperature gradient and 2. temperature time variation. The first form is also called Seebeck effect or thermoelectric effect, and the second form is the pyroelectric effect.

1.2.1.1 Seebeck (Thermoelectric) Effect

The temperature gradient in the environment could be directly converted to electric voltage through the Seebeck (thermoelectric) effect, discovered by Thomas Johann Seebeck. The Seebeck effect is illustrated in Figure 1.5, where the induced voltage is

$$V = \int_{T_1}^{T_2} (S_B(T) - S_A(T))dT, \tag{1.1}$$

S_A and S_B are the Seebeck coefficients of the metals A and B as a function of temperature, and T_1 and T_2 are the temperatures of the two junctions.

A traditional thermoelectric (TE) power generator consists in number of doped semiconductor elements arranged electrically in series but thermally in parallel. A practical example is the thermogenerator by the Micropelt GmbH, which is shown in Figure 1.6(a). TE leg pairs or thermocouples are composed of n- and p-type semiconductor materials which are separately produced and optimized on two silicon wafers. When heat is flowing through two silicon wafers (hot side and cold side), a voltage will be produced. TE legs are optimized with the doping Bi_2Te_3, which could have maximum 18% Carnot efficiency when the temperature difference is about 350K. The kit of termogenerator is capable of delivering few miliwatts under ten to thirty degree difference.

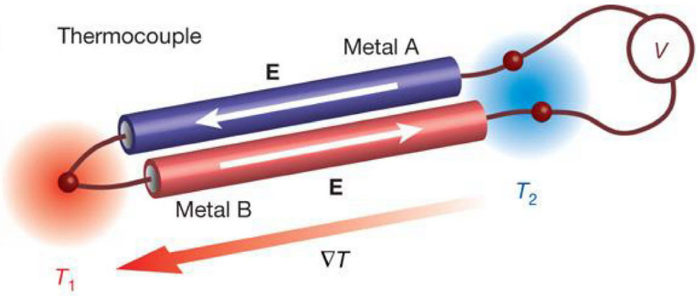

Figure 1.5: Illustration of a thermocouple. A thermocouple consists of two conductors (metals A and B) connected to each other. They have different Seebeck coefficients and, thus, the voltage V between the output terminals is proportional to the temperature difference T_1 - T_2 between the ends of the couple [7]

Thermoelectric generators are reliable and have the advantage of limited noise emission compared to vibration-based harvesters, but their performance is however still in low efficiency if there is only a small temperature gradient available. Chen *et al* [8] also mentioned that although the Seebeck effect of temperature gradient resulting in electric field is important, the heat loss caused by Joule and Peltier effect with electric current flowing in thermoelectric medium is also important. The development of materials raises the thermal heat flow and improve the figure of merit; it however also makes the maintenance of temperature gradient difficult caused by better conductivity and high heat exchange [9]. In addition, the costly fabrication, scarce and toxic material content and limited operational temperature make the usage of thermoelectric generators restrictive.

The use of hybrid thermoelectric system provides another choice for evaluating the efficiency of thermogenerator. Omer *et al* [10] proposed a two stage solar concentrator for combining heat and thermoelectric power generation. The thermal efficiency could be obtained more than 30 % when the collector tilt angle is from 0 to 20 degree at atmospheric pressure.

1.2.1.2 Pyroelectric Energy Harvesting

Instead of Seebeck effect, the thermal energy could be also with the form of temperature time-variation, which is also the pyroelectric effect. Certain materials which are able to generate an electrical charge because of a polarization change when they are under a time varying temperature are called pyroelectric materials. Not like the traditional thermoelectric power generator, the pyroelectric energy conversion does not need the

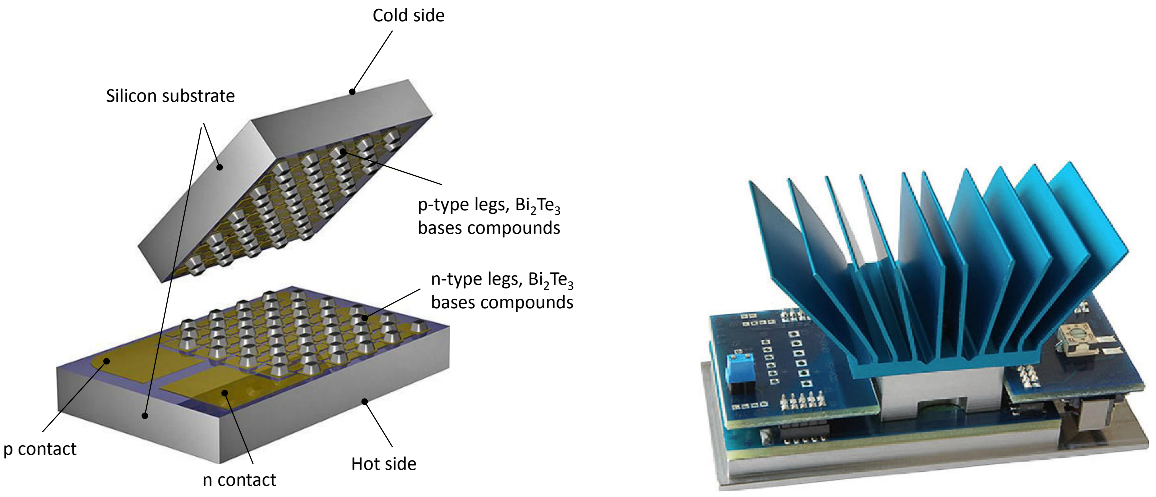

(a) (b)

Figure 1.6: Micropelt Thermogenerator: (a) Thermogenerator; (b) TE-Power PLUS (source: www.micropelt.com)

high temperature source. The performance of a pyroelectric material is described by its figure of merit of electric displacement, the breakdown voltage and the coupling between the time-variation of temperature and electric induction (as the pyroelectric equation is similar to the piezoelectric equation). A strong temperature dependent electric displacement could maximize the electrical charge extracted from a pyroelectric material when it is heated and cooled. The breakdown voltage decides the moment when the pyroelectric material suffers a destruction of charge storing capability. In 1983 Oslen's group proposed the first pyroelectric conversion cycle, 'Olsen cycle' or 'Ericsson cycle' [11]. For each cycle, a copolymer P(VDF-TrFE) was able to generate 30 mJ/cm^3 between 23 to 67 °C by applying maximum electric field of 55 kV/mm [12]. Zhu *et al* [13] examined the energy generated with electric-field-induced phase transitions through rhombohedral, orthorhombic and tetragonal phases during the Ericsson cycle with a 1.1 mm thick [110]-oriented PZN-4.5PT single crystals. The electric field is applied with varying frequency from 0.01 Hz to 1 Hz, and a 101.8 mJ/cm^3 energy is generated over the whole Ericsson cycle between 100 and 130 °C and electric field E_L =0 MV/m and E_H =2 MV/m. Although it is more difficult to obtain high temperature time-variation than temperature gradient, in the work of Sebald *et al* [9], a better power output had been shown for pyroelectric energy harvesting than thermoelectric energy harvesting at low frequency (10^{-4} Hz) and low heat exchange coefficient.

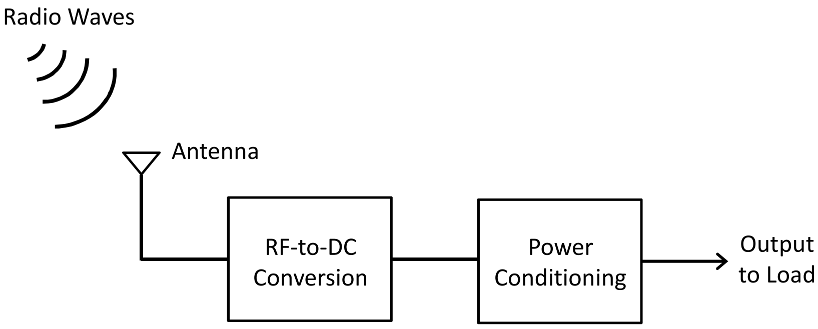

Figure 1.7: Overview of a RF energy harvesting system [21].

1.2.2 Ambient-Radiation Sources

The energy can be also converted from ubiquitous radio transmitters, but the energy harvesting from this kind of source has to be either with very large area for collecting radiation energy or very close to the radiation source to get useful energy level. The common example is to deliberately broadcast RF or electromagnetic wave energy [14] to power remote devices. A general RF energy harvesting is composed of receiving radio waves with an antenna, converting the signal, and then conditioning the output power, as shown in Figure 1.7. This is now commonplace in passive Radio Frequency Identification (RFID) systems. However, energy conversion systems of ambient RF energy are very limited in power, usually in the range of few μW. Yeatman [15] recalled that an electric field of 1 V/m recovers no more than 0.26 $\mu W/m^2$ while the maximum field near a source is within a few volts per meter. To improve the RF energy conversion efficiency and to maximize the output power, current research efforts on designing efficient antenna and rectennas (rectifying antenna) [16–19]. An array of rectennas has demonstrated that the voltage, current and power requirements for microwave power transmission can be satisfied by configuring the dipole rectenna elements in serial and parallel connections [20].

Another form of radiation energy is the light radiation. A nantenna (nanoantenna) is a solar collection device based on rectifying antennas. The idea of using antennas to collect solar energy was first proposed by Robert in 1972 [22]. A nantenna is an electromagnetic collector designed to absorb specific wavelengths that are proportional to the size of the nantenna. Idaho National Laboratories has designed a nantenna to absorb wavelengths in the range of 3-15 μm [23], which is shown in Figure 1.8. These wavelengths correspond to photon energies of 0.08-0.4 eV. Both modeling and experimental measurements demonstrate that the individual nantennas can absorb

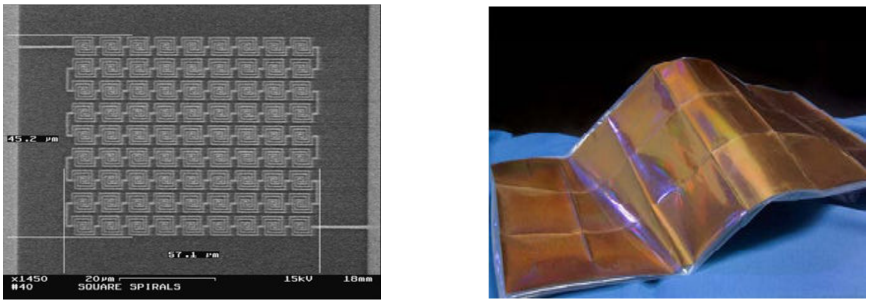

(a) (b)

Figure 1.8: Nantenna by Idaho National Laboratories: (a) An array of nantennas, printed in gold and imaged with a scanning electron microscope; (b) Nantenna sheet, stitched together from 18 coupons

close to 90 percent of the available in-band energy. A photovoltaic (PV) cell also has the capability of converting light energy into electrical energy using semiconducting material silicon to convert the energy from photons of light to electricity. Commercially available PV cells could provide 15 % conversion efficiency and the minimum average electrical power over a 24h period in a temperate location is around 2 $W\cdot m^{-2}$. In order to increase the conversion efficiency, engineers at Stanford University have figured out how to simultaneously use the light and heat of solar energy to generate more than twice as efficient as existing methods by coating a piece of semiconducting material with a thin layer of the metal cesium [24]. Overall, photovoltaic energy conversion could offer higher power output levels compared with other energy harvesting mechanisms, but its power output is nevertheless dependent on environmental conditions.

1.2.3 Vibration Conversion

Mechanical vibrations are common in many environments. They range from small vibrations of the walls and floor, rotating machinery to very high loads of mechanical parts in contact with an aircraft engine. It varies widely in frequency and amplitude as described in Table 1.3. It has the benefit of low restriction from exterior environmental factors. It simply uses the idea of converting vibration kinetic energy to electrical energy. The power density of vibration-based energy harvesting devices is comparable to some other power sources such as thin- and thick-film lithium and lithium-ion battery and thermoelectric energy (Figure 1.9).

Table 1.3: Acceleration magnitude and frequency of potential sources vibration among common commercial devices [25]

Vibration Source	*Acceleration* (m s^{-2})	*Frequency*$_{peak}$ (Hz)
Car engine compartment	12	200
Base of 3-axis machine tool	10	70
Blender casing	6.4	121
Clothes dryer	3.5	121
Person tapping their heel	3	1
Car instrument panel	3	13
Door frame just after door closes	3	125
Small microwave oven	2.5	121
HVAC vents in office building	0.2-1.5	60
Windows next to a busy road	0.7	100
CD on notebook computer	0.6	75
Second story floor of busy office	0.2	100

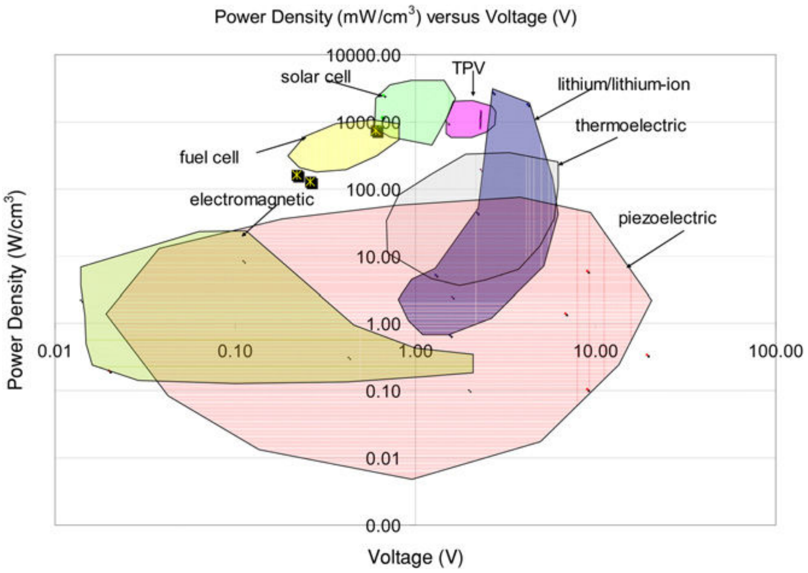

Figure 1.9: Power density versus voltage for common regenerative and lithium/lithium-ion power supply strategies [25]

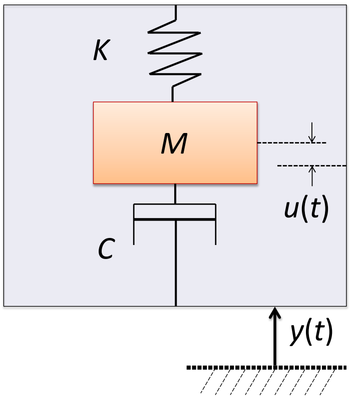

Figure 1.10: Schematic for a typical vibration-based energy harvester

The vibration conversion system is usually designed by exploiting the oscillation of a proof mass with a resonant second-order spring K and mass M system with a linear damper C (Figure 1.10). The differential equation that describes the movement of the seismic mass, $u(t)$, with the external excitation $y(t)$ is expressed as

$$M\ddot{u}(t) + C\dot{u}(t) + Ku(t) = -M\ddot{y}(t). \tag{1.2}$$

The first known device utilizing this type of energy is the watch made by Abraham-Louis Perrelet in 1770. The mechanism of this watch is automatically winded during movements of the wearer. The operation of the ambient vibration energy is an excellent way to replace the use of batteries which have limited lifetime. To this end, several types of micro-generators have been developed to convert mechanical energy into electrical energy. The vibration-based energy could be converted either via magnetic field (electromagnetic), or via variable capacitance (electrostatic), or via the electric field variation on electrostrictive polymers, or via the strain in a piezoelectric material. In this section, electromagnetic conversion, electrostatic conversion and electrostrictive polymers used for mechanical energy conversion will be introduced and the power harvesting based on piezoelectric materials will be discussed in detail separately in the next section.

General vibration-based energy harvesting systems are summarized in Figure 1.11. This figure gives a quick idea of vibration energy conversion mechanisms. The first row indicates the energy harvesting mechanism; the second row shows the actual implementation and tools employed to convert mechanical energy; the third row exposes energy harvesting techniques for each harvester mechanisms.

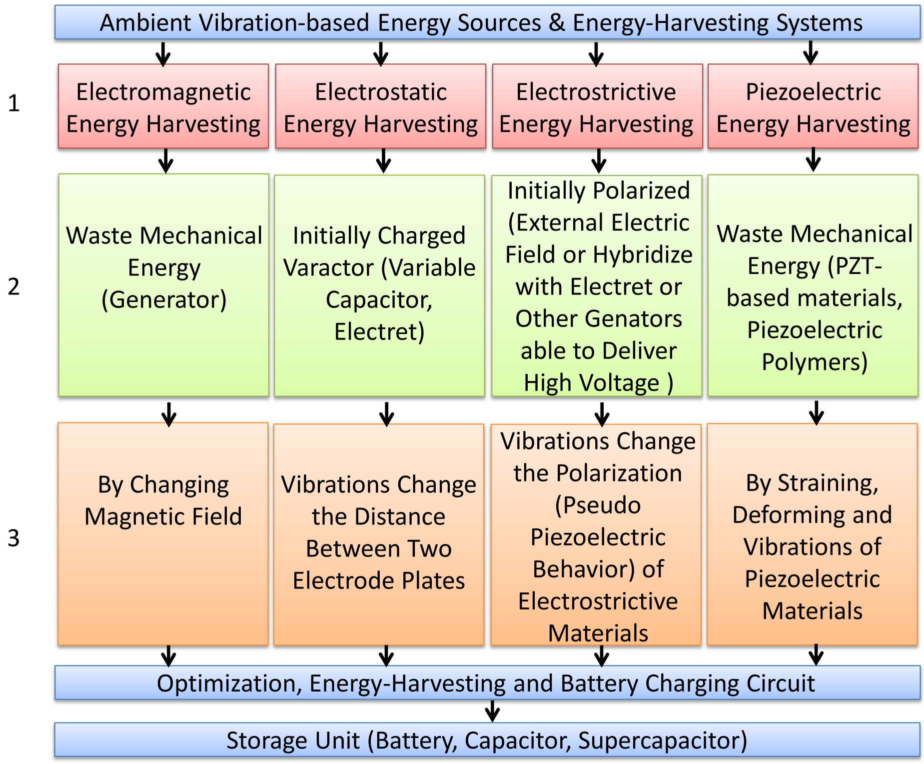

Figure 1.11: Vibration-based energy harvesting systems (partially references [6])

1.2.3.1 Electromagnetic Conversion

This section focuses on the use of electromagnetic transducers for harvesting the vibrational energy. Electromagnetic transducers were the first being used as a vibration power converter. The movement changes the magnetic flux Φ and induces a voltage V across the coil proportional to the time rate of change of magnetic flux linkage of the coil and the number of coil turns N (Eq. (1.3)), where the magnetic flux Φ through a surface A_i is defined by an surface integral of magnetic field B (Eq. (1.4)).

$$V = -\frac{d\Phi}{dt} = -N\frac{d\Phi}{dt} \tag{1.3}$$

$$\Phi = \int\int_{A_i} B \cdot dA \tag{1.4}$$

The electromagnetic power conversion is used in numerous applications from the large-scale power harvesting to smaller scale applications in microscale. Electromagnet microgenerators can harvest micro- to milli-watt levels of power using both rotational and linear devices. One of the simplest applications is the flashlight shown in Figure 1.12. When the flashlight is shaken, a magnet moves inside the coil. The electrical

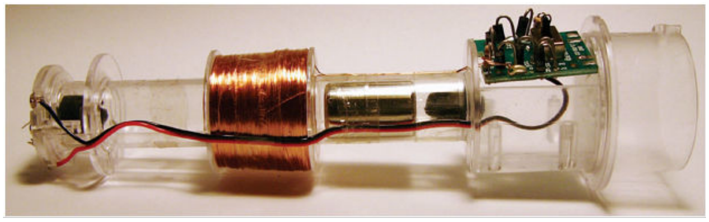

Figure 1.12: Flashlight by electromagnetic generator [4]

charge is created and then stored in a capacitor which allows the lighting of a diode. The power generated by this device is approximately 200 mW at a steady shake rate 200 cycle/min.

Many studies have been done on this subject. Some achievements corresponding to the MEMS (micro-electromechanical system) scale can generate powers between 1 μW and 100 μW. Other embodiments with larger structures could reach powers of a few hundred of μW. The device developed by Li *el al* [26] can supply an infrared transmitter. It occupies an area of about 1 cm^3 and provides a power of 70 μW. The basic mechanical schematic is shown in Figure 1.13. This work was continued by Lee *el al* [27] who carried out a micro-generator integrated in the size of a AA battery and used for a 914.8 MHz FM wireless temperature sensing system, as shown in Figure 1.14. Systems providing higher powers in the mW range have also been made, as the device of El-Hami *el al* [28], which can generate a little more than 1 mW for a volume of 240 mm^3 or that of James *el al* [29] whose power output reached 3 mW. Perpetuum LTd. proposed their cm^3 scale commercial products of vibration-based electromagnetic generators used in industrial or rail monitoring systems with an output up to 20 mW under a 10 g RMS vibration. From the studies introduced here, it is shown the electromagnetic converters perform well in macroscale. However, there is still some difficulties to fabricate and optimize them with MEMS scale systems due to the poor properties of planar magnets and the number of turns that can be achieved with limited planar coils.

Another energy conversion mechanism which could be categorized in this section is the magnetostrictive energy harvesting. Magnetostrictive materials (MsM) are a class of materials that change their shape under an applied magnetic field, or change magnetization under an applied mechanical stress (Villari effect). Since such devices can be controlled by magnetic field, they can be operated in a non-contact mode. Staley and Flatau [31] produced a Terfenol-D based magnetostrictive harvester with maximum DC voltage less than 0.35 V. The hybrid harvester combining PZT and Terfenol-D

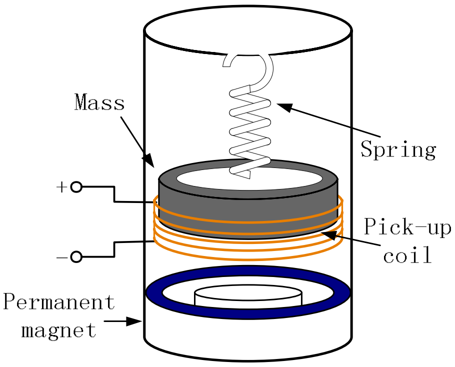

Figure 1.13: General mechanical schematic of electromagnetic generator [30]

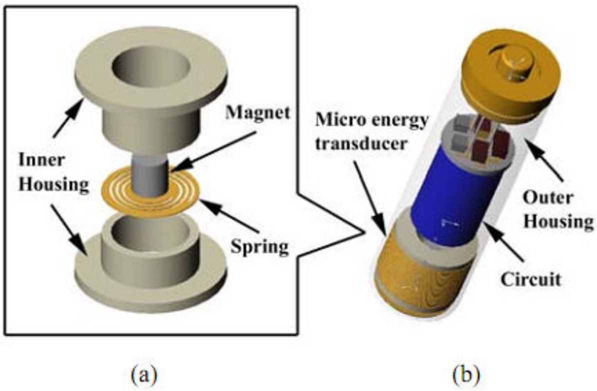

Figure 1.14: Illustrations of: (a) Inner structure of the micro power generator; (b) the AA size micro power generator which is integrated with a power-management circuit [27]

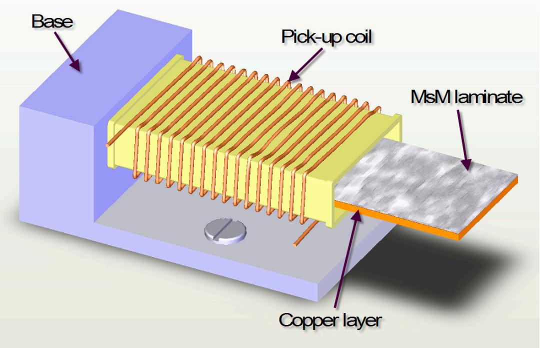

Figure 1.15: Prototype of MsM energy harvesting device [34]

[32, 33] would have better performance, but it is still not applicable. Instead of using Ferromagnetic materials, Wang and Yuan proposed a magnetostrictive harvester with the alloy (Metglas 2605SC) to promote the power output with a maximum output power and power density of 200 μW and 900 $\mu\mathrm{W/cm}^3$, respectively, at a low frequency [34].

1.2.3.2 Electrostatic Conversion

Electrostatic generators are constituted by a charged capacitor with one or two moveable electrodes. They have a better capability to be integrated with MEMS scale devices via the use of silicon micro-machining fabrication techniques. Unlike electromagnetic systems, electrostatic generators need to be preloaded before generating power. Meninger *el al* recalled the principle of operating these devices in [35]. The general idea is to put a certain amount of charge on the micro-generator, which acts as a capacitor plate, and extract the energy from it by changing the spacing between the electrodes when the plate is under motion. Electrostatic generators generally can be categorized into: 1. Electret-free electrostatic generators and 2. Electret-based electrostatic generators. There are two possible modes for electret-free electrostatic generator (Figure 1.16), either constraining the charge on the capacitor while the the capacitance decreases and voltage increases, or constraining the voltage across the capacitor while the capacitance decreases and the charge moves out from the capacitor. For the voltage-constrained conversion mode, the capacitance decreases as plates move and causes charges moving from the capacitor back into the reservoir. For the charge-constrained mode, as the capacity decreases, the voltage must increase to satisfy the constant charge condition, and thus the net energy is gained (the net area under the

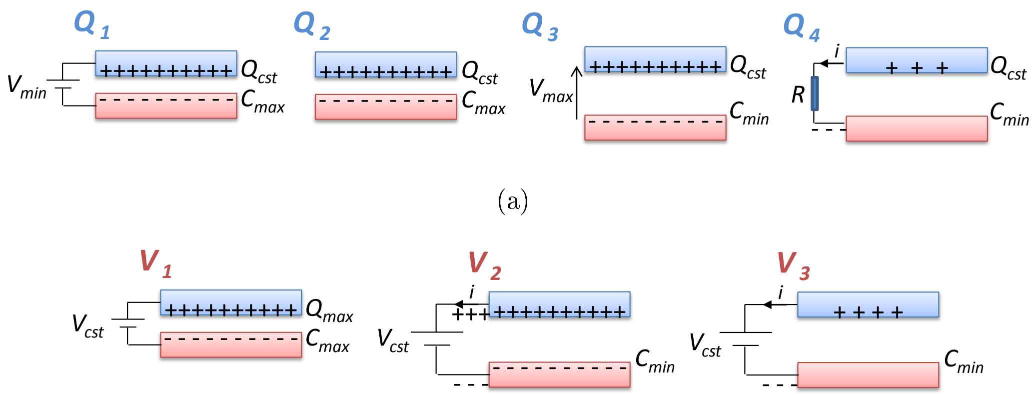

(a)

(b)

Figure 1.16: Principle of operation of the electrostatic transducer [36]: (a) Charge constrained cycle; (b) Voltage constrained cycle

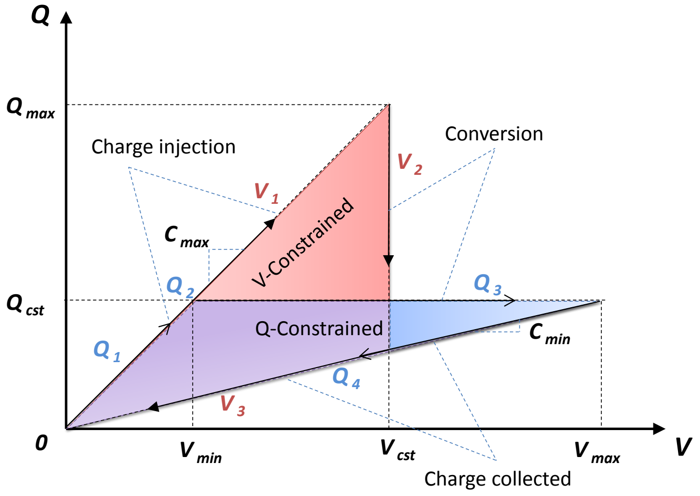

Figure 1.17: Standard energy conversion cycles for electret-free electrostatic devices [36]

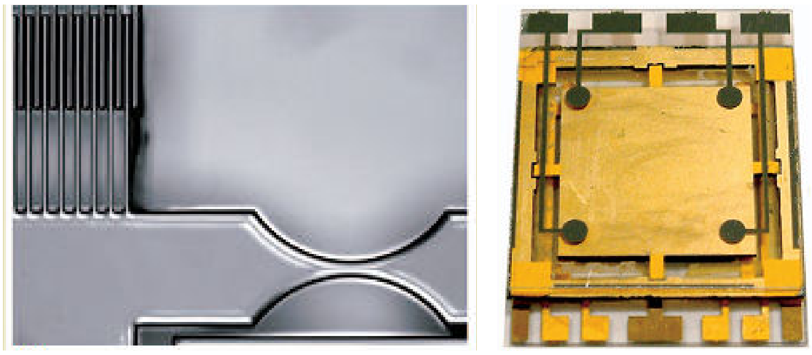
(a) (b)

Figure 1.18: Two electrostatic microgenerators: (a) a portion of a constant-gap variable capacitor fabricated at MIT for a 1 cm^2 device; (b) a 2 cm^2 compressible-plate capacitor fabricated at Imperial College [4]

$Q-V$ plot in Figure 1.17). For the same condition of C_{max} and C_{min} and assuming the same voltage level for the maximal voltage in charge constrained cycle and the external voltage applied in voltage-constrained cycle ($V_{cst} = V_{max}$), the voltage-constrained cycle could convert more energy than what is possible with the charge-constrained cycle. Instead of considering a classical implementation of electrostatic energy harvesting featuring a constant permittivity, Lallart *et al* have proposed the enhanced configuration with an added dielectric layer which has high permittivity and hence abruptly changes the equivalent permittivity. The comparison of the associated energy cycle with this enhanced electrostatic generator has proved the better harvester performance when it is under a constant charge constrained cycle in [37]. MIT and Imperial College both developed electret-free micro-electrostatic generators (Figure 1.18) using silicon micro-machining process. However, with this type of electrostatic generator, an active electronic circuit is required for applying the charge cycle and an external supply source (battery, charged capacitor) is needed to polarize the capacitor at the beginning of cycle or at least at the first cycle. Whether it is operated in charge-constrained or voltage-constrained cycles, electrostatic converters are based on a variable capacitive structure, and they generally can be classified into:

1. In-plane gap closing converter.

2. In-plane overlap converter.

3. Out-of-plane gap closing converter.

(a) in-plane gap closing converter

(b) in-plane overlap converter

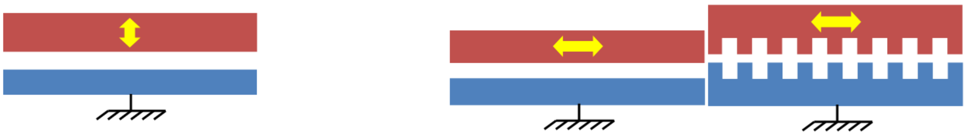

(c) out-of-plane gap closing converter

(d) in-plane converter with variable surface (full-plate and patterned version)

Figure 1.19: Basic configurations for electrostatic converters [36]

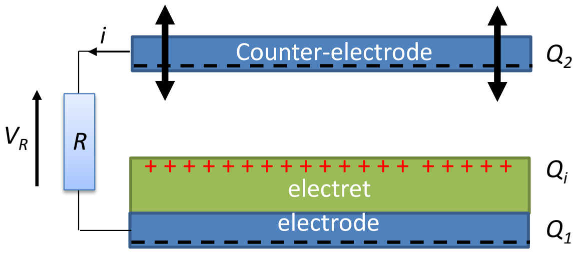

Figure 1.20: Electrostatic converter using an electret [38]

4. In-plane converter with variable surface.

These are illustrated in Figure 1.19.

One solution to avoid the requirement of charge or voltage input is to use electrets, the electrically charged dielectrics that is capable of polarizing electrostatic energy harvesters; in this case, the use of electrets is similar to the use of permanent magnets in the electromagnetic energy harvesting system. The use of electret-based electrostatic generator is similar to electret-free one. The main difference relies on that the electret layers are added to plates of the variable capacitor to polarize it as shown in Figure 1.20. Halvorsen *et al* [39] designed and fabricated a MEMS electrostatic energy harvester with an electret bias. This device works in out-of-plane motion and features a high voltage output in a continuous mode with about 1 μW power output at a 0.03 g^2/Hz acceleration power spectral density. Naruse *et al* have developed an electrostatic micro

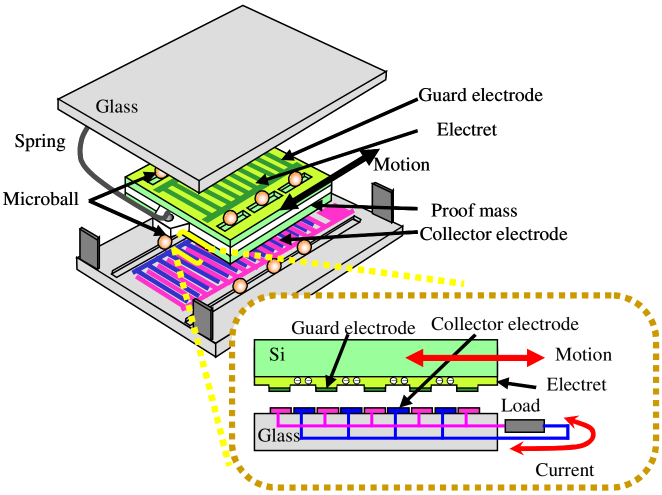

Figure 1.21: New structure of a electrostatic micro power generator supported on microball bearings [41]

power generator consisted in an electret structure for low-frequency energy harvesting applications. This generator shows a power output of 40 μW at very low frequency vibration (2 Hz, 0.4 g) with parallel sliding force on the support of microball bearings. Boisseau *et al* [40] modelled an in-plane multibump electret-based energy harvester with FEM software and compared simulation results with Boland's formula to show that the size of bumps (electrode width) and electrode spaces should be optimized to maximize the output power of the energy harvester.

An electrostatic is definitely a promising option for powering electronic devices because of their high mechanical-to-electrical coupling, low-cost and high integrability with MEMS systems. However, drawbacks of difficult capacitor gap control and the need of voltage or charge input or the stability of electret make the implementation of electrostatic generator difficult.

1.2.3.3 Electrostrictive Polymer

Lallart *et al* compared energy harvesting using electrostrictive polymers with piezoelectric and magnetostrictive materials in Figure 1.22, and showed that electrostrictive polymers have high deformation abilities, high elasticity and low operating frequency which is suitable for biomedical application such as human muscle.

Electrostriction is generally defined as quadratic coupling between strain S_{ij} and the electric flux density D_m under the assumption of linear relationship between the

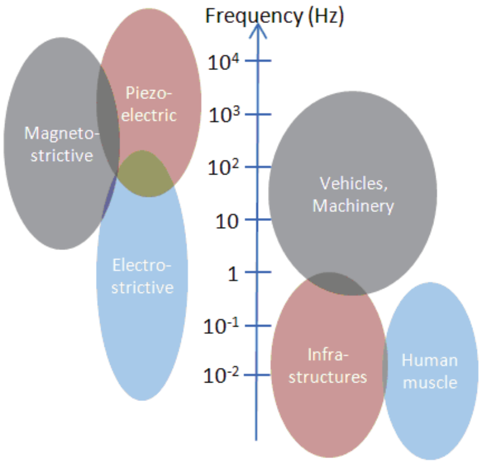

(a) Frequency contents

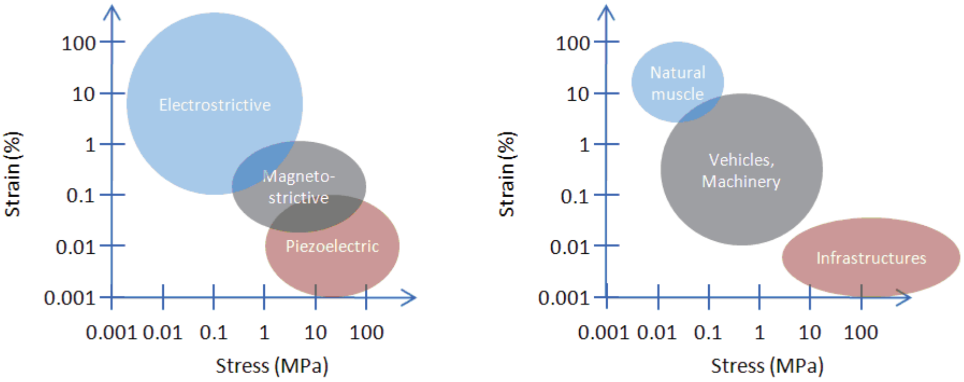

(b) Stress-strain curves

Figure 1.22: Comparison of (a) frequency contents and (b) stress-strain curves of electromechanical systems and typical applications [42]

polarization and the electric field [43, 44]:

$$\begin{cases} S_{ij} = M_{mnij} \cdot E_n \cdot E_m + s^E_{ijkl} \cdot T_{ij} \\ D_m = \varepsilon^T_{mn} \cdot E_n + 2 \cdot M_{mnij} \cdot E_n \cdot T_{ij}, \end{cases} \tag{1.5}$$

where s^E_{ijkl} is the elastic compliance, M_{mnij} is the electric-field-related electrostriction coefficient, ε^T_{mn} is the linear dielectric permittivity, T_{ij} is the stress and E_m, E_n the electric field.

The conversion between mechanical-to-electrical energy is based on electric field-induced molecule motion, dipolar movement or phase transition for electrostrictive polymers. There are generally two methods for harvesting energy using an electrostrictive polymer: 1. electrostrictive cycles and 2. pseudo-piezoelectric cycles. The cycle analysis is under the assumption that the dimensional change of material on the electrical boundary condition is negligible. The mechanical-to-electrical energy harvesting in electrostrictive materials could be illustrated by the mechanical stress/strain and electric field-intensity/flux-density loops. In order to maximize the harvesting energy density (J/m^3), the area inclosed in the loop should be as large as possible within the limitation of the polymer materials. There are many cycles being described to control electrical boundary conditions to optimize the inclosed area in the loop. In the following, electrostrictive cycles proposed by Liu *et al* [45] will be introduced:

a) Constant electric field stretching and open-circuit release (Figure 1.23):

   1. Stretching under a given electric field E_0.
   2. Releasing in open circuit (constant charge).
   3. Decreasing the electric flux density to the original position.

b) Constant electric field stretching and release (Figure 1.24):

   1. Stretching under a constant electric field E_0.
   2. Increasing electric field to E_1.
   3. Releasing the applied stress.
   4. Decreasing electric field to E_0.

c) Open-circuit stretching and release (Figure 1.25):

   1. Stretching in open circuit (constant electric flux density) with an initial electric field E_0.
   2. Increasing electric field to E_1.
   3. Releasing in open circuit (constant electric flux density).
   4. Decreasing electric field to E_0.

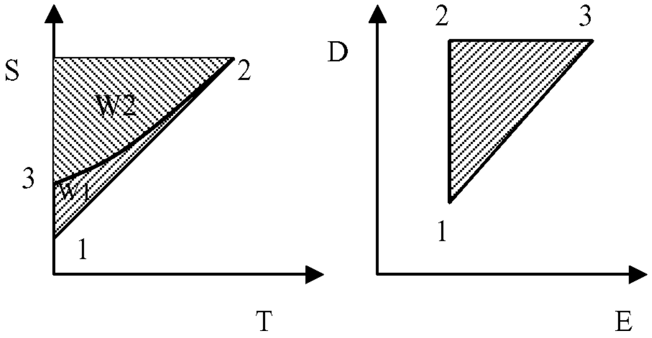

Figure 1.23: Energy harvesting cycle under constant field (1-2) and open circuit (2-3) electrical boundary conditions [45]

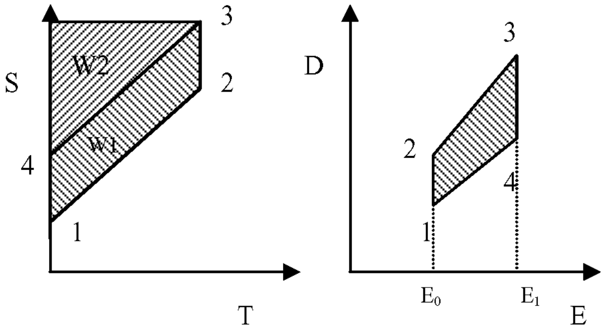

Figure 1.24: Energy harvesting cycle under constant electrical field conditions as the material is stressed and unstressed [45]

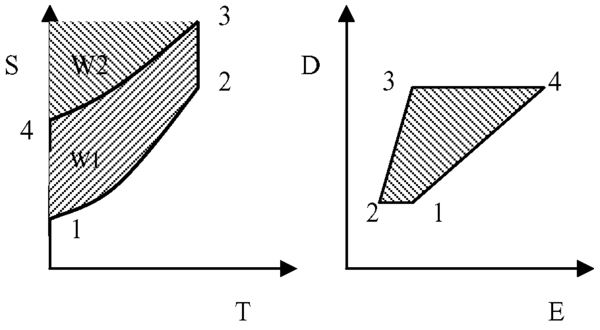

Figure 1.25: Energy harvesting cycle under open-circuit conditions as stress is applied and removed [45]

Table 1.4: Energy Balance Considering Electrostrictive Harvesting Techniques [42]

	Constant Electric Field Stretching and Open-Circuit Release	**Constant Electric Field Stretching and Release**	**Open-Circuit Stretching and Release**
Provided electrical energy density	$2MT_0E_0^2$	$MT_0\left(E_0^2+E_1^2\right)+\frac{1}{2}\varepsilon\left(E_1^2-E_0^2\right)$	$\frac{1}{2}\left(\varepsilon+2MT_0\right)E_1^2-\frac{1}{2}\frac{\varepsilon^2}{\varepsilon+2MT_0}E_0^2$
Extracted electrical energy density	$2MT_0\left(1+\frac{MT_0}{\varepsilon}\right)E_0^2$	$2MT_0E_1^2+\frac{1}{2}\varepsilon\left(E_1^2-E_0^2\right)$	$\frac{1}{2}\left[\frac{\left(\varepsilon+2MT_0\right)^2}{\varepsilon}E_1^2-\varepsilon E_0^2\right]$
Harvested energy density	$2\frac{M^2}{\varepsilon}T_0^2E_0^2$	$MT_0\left(E_1^2-E_0^2\right)$	$\left(\frac{\varepsilon+2MT_0}{\varepsilon}\right)MT_0E_1^2-\left(\frac{\varepsilon}{\varepsilon+2MT_0}\right)MT_0E_0^2$

Lallart *et al* [42] summarized the associated energy balance for each cycle in Table 1.4. Pure electrostrictive cycles require nonzero electrical initial conditions (leading to nonzero initial strain as well), and therefore some energy waste might occur due to the losses in the material. In addition, these cycles require driving the electrical conditions of the materials for a long time period, hence making them quite complex to implement in an autonomous, self-powered system.

Another family for harvesting energy from electrostrictive is subjecting a DC-biased electric field to the sample [46, 47], allowing the polymer to operate in a pseudo piezoelectric behavior. The dynamic behavior of an electrostrictive element in a pseudo piezoelectric cycle could be expressed with the linearized electrostrictive equations by assuming that the generated electric field E_{AC} is negligible compared to the bias electric field E_{DC}, and the stress magnitude remains small enough so that $\varepsilon \gg 2MT$:

$$\begin{cases} \dot{S} = s\dot{T} + 2M(E_{DC}+E_{AC})^2 \\ \dot{D} = (\varepsilon + 2MT)\,\dot{E}_{AC} + 2M\,(E_{DC}+E_{AC})\,\dot{T}, \end{cases} \tag{1.6}$$

which are similar to those obtained when using piezoelectric elements, with an equivalent piezoelectric coefficient $d = 2ME_{DC}$. The maximum energy density is then given in Lallart's work [48] as:

$$W_{\max} \approx 2\pi\frac{M^2}{\varepsilon}E_{_{DC}}^2T_{_0}^2. \tag{1.7}$$

The performance of energy harvesting with electrostricive polymers are obviously dependent on material properties themselves (e.g. permittivity, electrostrictive coefficient and elasticity). A better performance in energy harvesting can be particularly obtained by increasing the dielectric constant of the electrostrictive polymers [47, 48]. Although the energy harvested using electrostrictive polymers is still very small for supplying an electronic device, these materials are relatively new and there are still great improvements to be accomplish with regard to the design process. However, the mechanical characteristics of the polymers may still make them a good candidates for energy harvesting, especially suitable for human motion.

1.3 Energy Harvesting using Piezoelectric Materials

Piezoelectric materials have been commonly used for many years to convert mechanical energy into electrical energy. Piezoelectric generators can potentially power electronic devices ranging from a few μW to several hundred mW. Compared to other two main mechanisms of vibration energy harvesting systems, electrostatic harvester and electromagnetic harvester, piezoelectric energy harvesters have benefits in their high integrability with small-scale systems, easy maintenance, easy implementation, robustiness, high energy density and appropriate voltage output (Table 1.5 and Figure 1.26). According, piezoelectric energy harvesting systems have received much attention in recent decades. In this thesis work, the focus will be put on piezoelectric energy harvesting systems. The basic knowledge of piezoelectric materials and piezoelectric harvesting systems, how to optimize piezoelectric energy harvester mechanically and electrically will be introduced in an organized order in this section.

1.3.1 Brief Introduction of Piezoelectric Harvester

Piezoelectric materials have property of directly transforming the mechanical strain to electricity current. When the crystal is mechanically strained, or when the element is deformed by the application of an external stress, electric charges appear on certain of the element surfaces; and when the direction of the strain reverses, the polarity of the electric charge is reversed. This is called direct piezoelectric effect, which is shown in Figure 1.27. According to IEEE standards, piezoelectric equations may be written

Table 1.5: Comparison of vibration Energy-Harvesting Techniques

	Electrostatic	*Electromagnetic*	*Piezoelectric*
Compatibility with MEMS *systems*	Very good	Difficult	Good
Energy density	Low	High	High
Current size	Micro	Macro	Macro/micro
Problems	Need of adding charge source or electret; very low current output	Very low output voltages; bulky	Moderate output voltages; limited mechanical strain
Advantages	High output voltage; easier to integrate in microsystems	Long lifetime; Robustness; no voltage source needed	No need control any gap; no voltage source needed

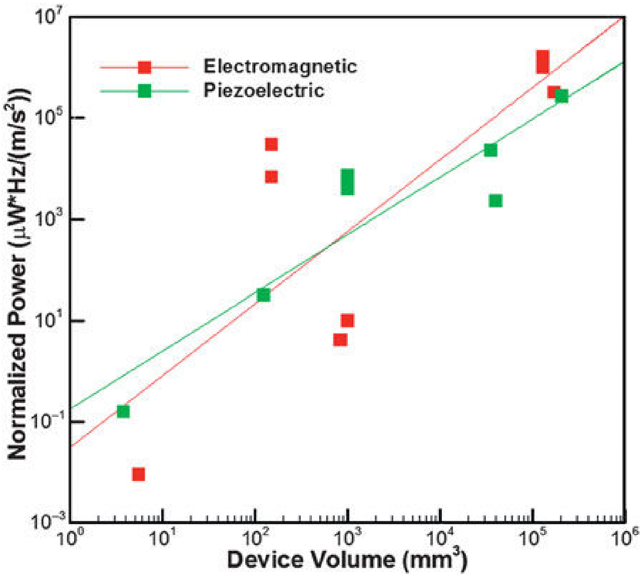

Figure 1.26: Output power as a function of effective material volume for piezoelectric and electromagnetic vibration energy harvesting mechanisms [49]

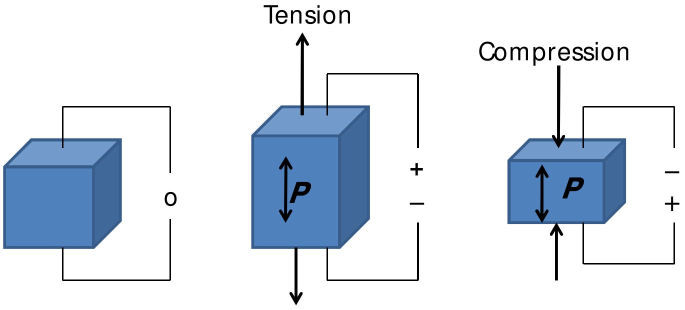

Figure 1.27: The direct piezoelectric effect. source: http://bostonpiezooptics.com/?D=6

as Eq. (1.8), where $\{T\}$, $\{S\}$, $\{E\}$ and $\{D\}$ are respectively the stress, the strain, the electric field and the electrical induction tensors. Piezoelectric material physical properties are the elastic stiffness matrix determined at constant electric field, $[c^E]$, the transpose piezoelectric stress matrix $[e^t]$ and the permittivity matrix evaluated at constant strain, $[\varepsilon^S]$. In the case of a piezoelectric disk poled along its symmetry axis and uniformly stressed on both sides in the polarization axis direction, the constitutive equations can rewrite as Eq. (1.9) linking the thickness variation of the disk (or displacement) u, the force F_p applied on the disk, the voltage V across the disk electrodes and the outgoing electric charge Q. Equation (1.10) denotes the clamped capacitance C_0, the force factor α, and the stiffness in short-circuit K_{pE} of the piezo-disk. A and t_p are respectively the area of the electroded surface and thickness between the two electrodes.

$$\begin{Bmatrix} T \\ D \end{Bmatrix} = \begin{bmatrix} c^E & -e^t \\ e & \varepsilon^S \end{bmatrix} \begin{Bmatrix} S \\ E \end{Bmatrix} \tag{1.8}$$

$$\begin{cases} F_p = K_{pE} u + \alpha V \\ Q = \alpha u - C_0 V \end{cases} \tag{1.9}$$

$$C_0 = \frac{\varepsilon_{33}^S A}{t_p}, \quad \alpha = \frac{e_{33} A}{t_p}, \quad K_{pE} = \frac{c_{33}^E A}{t_p} \tag{1.10}$$

Figure 1.28 illustrates two practical coupling modes in which piezoelectric material may be used, the 31 mode and 33 mode, where the 3 direction is also the poling direction. In the 31 mode, the stress is applied in the direction perpendicular to the poling direction so that the induced voltage is in the 3 direction and strained is in 1 direction. The 31 modes leads to the use of thin bending element and induce a large

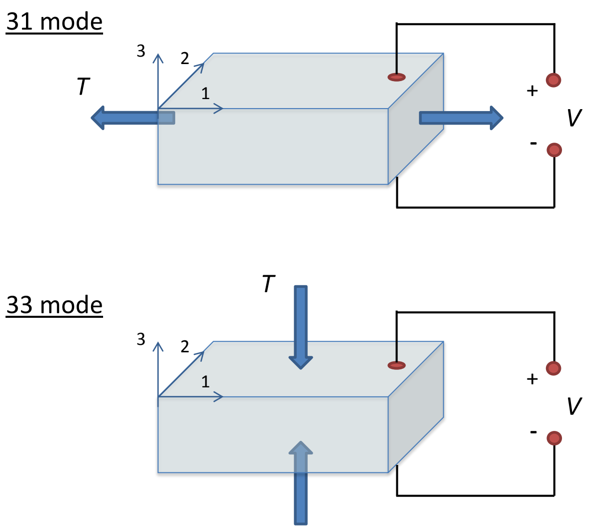

Figure 1.28: Illustration of 31 mode and 33 mode operation for piezoelectric material

strain in the 1 direction. The most common type of 31 mode is a bimorph. In the 33 mode, the stress is applied in the same direction than the poling direction, such as the compression of a piezoelectric block that is poled on its top and bottom surface. In 33 mode, the voltage and stress are in the same direction. In practice, the 31 mode has been most commonly used coupling mode. Baker *el al* [50] showed that, for different types of piezoelectric materials, the 31 mode has a lower electromechanical coupling factor, k^2. However, under the equal volumes, it is observed that the cantilever with 31 mode produces two orders more of power magnitude when subjected to the same force as a larger strains can be produced. Roundy *el al* [3] also presented that the resonant frequency for the 31 mode is much lower. Then it is concluded that in a small force, low vibration level environment, the 31 mode is more efficient as larger strains can be produced with smaller input forces.

Except the effect of different modes, the type of applied input would also lead different energy conversion performances. Generally, power harvesting by piezoelectric materials could be classified into two categories, 1. direct mechanical-to-electrical coupling, 2. indirect mechanical-to-electrical coupling (Figure 1.29). For directly-coupled piezoelectric harvesters, the stress is applied directly or via a mechanism to constrain a piezoelectric material, and a conversion between mechanical and electrical is considered as directly driven i.e.without intermediate storage of energy in mechanical form (intermediate storage could be, for example, a mass movement or a vibrating structure). In practice, the power recovered by this kind of device is very low as the piezoelectric

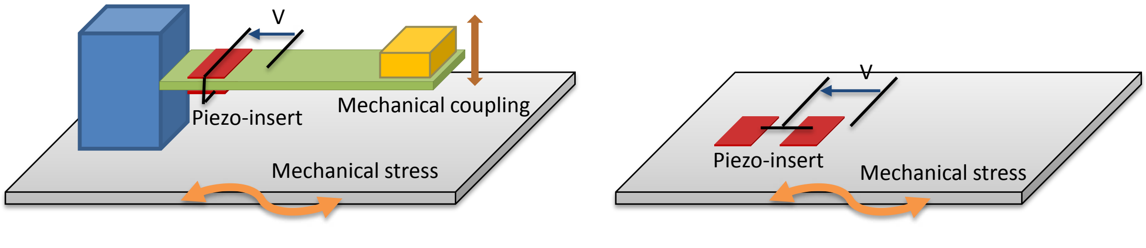

(a) (b)

Figure 1.29: General types of piezoelectric conversion [52]: (a) indirect mechanical-to-electrical coupling; (b) direct mechanical-to-electrical coupling

element releases energy when the stress is removed and the released energy is considered as lost or unusable. As the deformation of piezoelectric materials is difficult to implement, how to apply the piezoelectric element in such a converting system is important. The piezoelectric shoe developed by MIT is a famous example, the converted power is relatively low (8 mW) compared to the available mechanical energy and the efficiency is only of the order of 1 % or less [51]. This is mainly due to the difficulty of applying stress on the piezoelectric elements from the movement of the foot. This example illustrates the fact that the overall performance of micro-generators with direct conversion is generally limited by the losses of mechanical device. However, it is easier to implement directly-coupled piezoelectric harvesters under a broadband excitation as there is no need in frequency tuning.

The indirectly-coupled piezoelectric harvester (or seismic piezoelectric harvester) allows the independent design of host structure persuading the easier micro-generator maintenance and optimization of the system response. The easiest implementation of this type is shown in Figure 1.30. It is a cantilever beam on which piezoelectric elements are bonded. The cantilever beam system provides a supplementary energy conversion stage, which is effective for single mode excitation. The cantilever beam configuration is the most common type of piezoelectric harvester and is the focus in this work. However, factors that will change the resonant frequency have to be considered when designing this type of harvester. Also, a seismic piezoelectric harvester suffers defects of narrow frequency band and frequency tuning issue. A cantilever beam configured (or indirectly-coupled or seismic) piezoelectric harvester is usually modeled as a lumped mass-spring-damper-piezo single-degree-of-freedom (SDOF) system as shown in Figure 1.31 with the frequency response a narrow band. The effective mass M is bounded on a structural stiffness K_s, a damper C, and a piezoelectric element characterized by

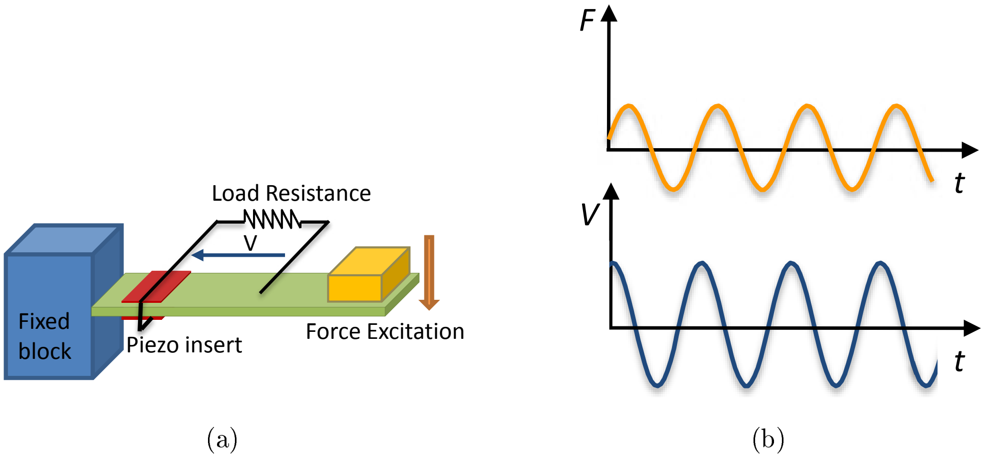

Figure 1.30: Classic system for indirect conversion: (a) system schematic; (b) sinusoidal input and response

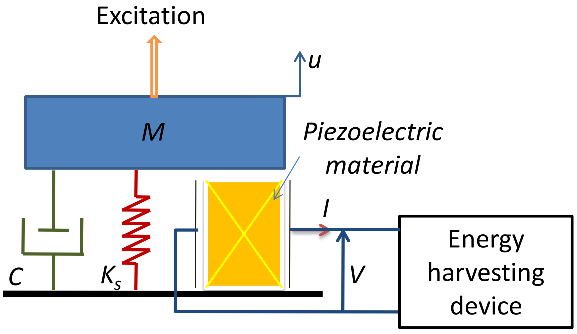

Figure 1.31: Model of vibrating structure including a piezoelectric element

the force factor α and the internal capacitance C_0. An external excitation is applied on the effective mass M. The governing equations of the piezoelectric harvester with simplified lump system can be described by [53–55]:

$$M\ddot{u} + C\dot{u} + K_s u = F - F_p, \tag{1.11}$$

$$\text{where} \quad F_p = K_{pE}u + \alpha V,$$

$$I = \alpha\dot{u} - C_0\dot{V}. \tag{1.12}$$

F_p is the restoring force due to the stiffness of piezoelectric element K_{pE} and the electrical force αV and F is the excitation force.

Williams and Yates [56] first proposed an analysis of a micro-electric generator for microsystems with a very simple model considering a constant damping coefficient and they concluded that the power harvesting is proportional to the cubic vibration frequency. However, there exists a damping effect induced by the energy conversion process yielding the decrease in vibration [57,58], especially for highly-coupled harvester systems, causing an overestimation in power harvesting when the vibration magnitude is assumed to be constant [59]. Lu *el al* [60] studied the power and performance based on piezoelectric cantilever beam with the load resistance. The work shows that the load resistance would modify the performance of harvester itself and there is an optimal resistance value for which the harvested power and performance simultaneously reach a maximum value. Richards *el al* [61] discussed the efficiency of a piezoelectric energy conversion device when it is excited at its resonance by a harmonic force with constant amplitude. This work confirms the existence of a resistance value that maximizes performance and the efficiency strongly depends on the product of the mechanical quality factor Q_M and electromechanical coupling factor k^2. This efficiency expression is given in Eq. (1.13), where electromechanical coupling coefficient, k^2, defines the conversion efficiency of a piezoelectric element, and the mechanical quality factor, Q_M, characterizes the the ratio of capable energy storage and the dissipated energy by structural internal damping. Lefeuvre *et al* [62], Shu and Lien [55] however have shown that the same maximum power will appear for two resistance values for medium to highly-coupled systems ($k^2 Q_M > \pi$). From the efficiency expression proposed by Richards *et al* (Eq. (1.13)), we can see that performance increases logically with the coupling factor and mechanical quality and finally reaches a saturated power limit.

$$\eta = \frac{1}{1 + \frac{2}{k^2 Q_M}} \tag{1.13}$$

1.3.2 Performance Optimization

Roundy *et al* [63] did a detailed analysis with different proof masses, coupling coefficients and working frequencies on a two-layer bimorph cantilever-configured piezoelectric harvester with simply a resistive load. The analysis was performed with a standard beam equation, the constitutive piezoelectric equations and circuit equations, leading the output power expressed as a function of vibration amplitude and frequency. The analysis shows that the power output is maximized when the driving frequency ω is equal to the natural frequency of the harvester ω_n, and it drops off dramatically as ω_n deviates from ω (Figure 1.32(a)). The power output depends on the harvester proof mass in a proportional trend (Figure 1.32(b)); the thickness is changing with the proof mass to fix the natural frequency by modifying the volume of piezoelectric materials. In

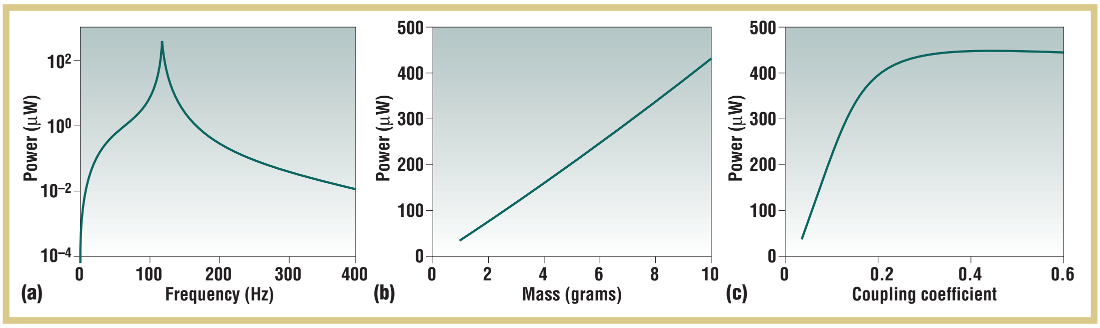

Figure 1.32: Simulations for a 1 cm^3 piezoelectric scavenger driven by vibrations of 2.5 $\mathrm{m/s}^2$: (a) Power output versus driving frequency. The design resonance frequency is 120 Hz, and its proof mass is 9 g; (b) Power output versus proof mass. All parameters are constant except piezoelectric-beam thickness; maximum deflection is approximately 90 μm; (c) Power output versus coupling coefficient. The proof mass is 9 g, and the maximum deflection is approximately 90 μm [63]

this work, the tradeoff between the host structure vibration and harvester performance during the mechanical energy converting process is not taken into account with varying harvester mass. With increasing coupling k^2, the power output increases quickly up to a point and then the increase becomes quite modest, reaching a saturation value. The optimization of the performance of piezoelectric harvesters can be either done through the mechanical configuration or the electrical circuit. A detailed discussion of how to improve piezoelectric harvesters through either piezoelectric configurations or circuitry and power storage can be found in the review work of Anton and Sodano [64].

1.3.2.1 Mechanical Structure Optimization

Typically, a seismic piezoelectric harvester needs to be tuned to have a resonant frequency as close as possible than the excitation frequency to maximize the harvested power. In addition, the increase in induced strain is also a key parameter for maximizing the power output. Therefore, piezoelectric harvester optimization in mechanical structure design can be split into two parts with frequency tuning consideration and mechanical strain optimization. With respect to frequency tuning mechanism, the work reviewed in this paragraph concentrates on single frequency excitations, which means the harvester is capable of frequency tracking but not with widen-band; broadband excitation issue will be discussed in the next section.

Given to the frequency tuning issue, Roundy and Yang [65] proposed an analysis based on Williams's model [56] for actively altering either the effective stiffness or mass

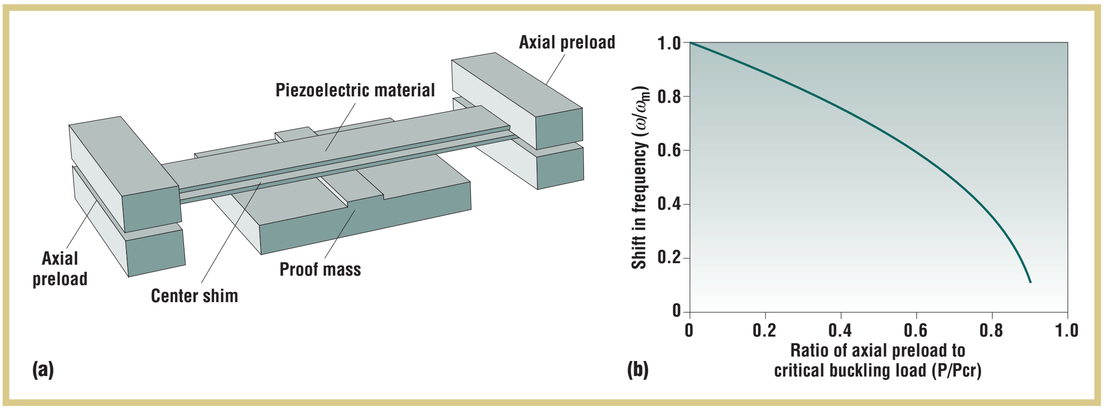

Figure 1.33: Applying axial loads to alter beam stiffness. (a) Schematic of a simply supported piezoelectric beam scavenger with an axial preload (with the top half of proof mass removed for the sake of simplicity); (b) Ratio of tuned resonance frequency to original resonance frequency as a function of the axial preload [63]

to tune the natural frequency of the harvester. However, it is found that altering the effective stiffness or the mass using an active actuator will never result in a net increase in power output as required energy is larger than the harvested energy. Extending this analysis, altering the damping ratio with active tuning actuators was proposed, which is also proved to be not benefit in harvested power as the power required by the actuator always exceeds the increase in power output. Instead of tuning the harvester in an active way, Roundy *et al* [63] introduced another method to alter the stiffness of the beam by applying axial loads. The beam is modeled as a simply supported beam with a proof mass in the middle as shown in Figure 1.33. The preload can be achieved by screwing or other devices that push on the clamps at either end of the beam. The resonance frequency of the beam can be reduced by approximately 40 % by using a preload equal to half of the critical buckling load (Figure 1.33(b)). Lallart *et al* [66] have proposed a low-cost semi-active self-tuning technique consisting in a nonlinear stiffness tuning scheme described by Guyomar *et al* in [67]. When the piezoelectric element is switching on and is connected to the circuit, a voltage source would apply a pre-stress on it and therefore allows the control of the stiffness ensuring a net positive energy output and a wider bandwidth. Challa *et al* [68] also proposed a piezoelectric harvester with tunable stiffness using bidirectional repulsive and attractive magnetic forces at the beam free end. This technique enforces the harvester resonance frequency tunable from 22 to 32 Hz and enables a 240 to 280 μW power output. Zhu *et al* have done a detailed review work in [69] covering both mechanical and electrical methods.

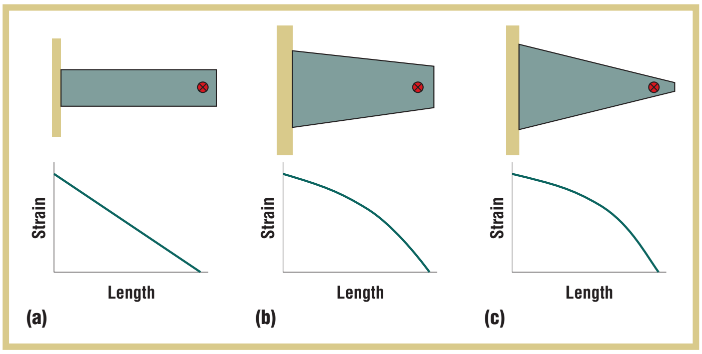

Figure 1.34: Relative bending energies and strain profiles for alternative beam geometries. (a) U = 1; (b) U = 1.54; and (c) U = 2.17. The red circles indicate the point at which load is applied [63]

To maximize the mechanical strain and concurrently avoiding the brittle fracture on some piezoelectric materials (for example, piezoelectric ceramics [1]), improving the geometry of the piezoelectric element is a major improvement area for piezoelectric harvester optimization. Roundy *et al* [63] summarized that with the same volume of piezoelectric material (Lead zirconate titanate (PZT) in this work), an increasingly triangular trapezoidal profile will lead to a more evenly distributed strain and would possess about twice the bending energy than a rectangular cantilever (Figure 1.34). The efficiency and maximum tolerable excitation amplitude of piezoelectric beam harvesters were examined with different beam shapes in the work of Goldschmidtboeing and Woias [70]. The design of beam shapes followed the limitation of piezoelectric material surface area and the criterion of maximizing the strain of the beam but preventing exceed the yielding stress. The work examined three beam shapes with different tip masses and their effect on the efficiency and the maximum tolerable excitation amplitude. A triangular shape beam was found to have the maximum tolerable excitation amplitude and a heavy tip mass (no more than beam mass) optimizes the harvester efficiency. Instead of changing the shape of piezoelectric materials, Patel *et al* [71] investigated the geometric parameter of piezoelectric coverage (piezoelectric layer length, piezoelectric layer thickness and piezoelectric layer position) on a rectangular cantilever energy harvester. The work reveals that an optimal piezoelectric layer length (and substrate thickness, to fix the natural frequency) exists to have maximum power, and the piezoelectric thickness (and tip mass inertia, to fix the natural frequency) is observed to

---

[1] In piezoelectric harvesters, piezoelectric ceramics is not the only choice, however, it is the common choice.

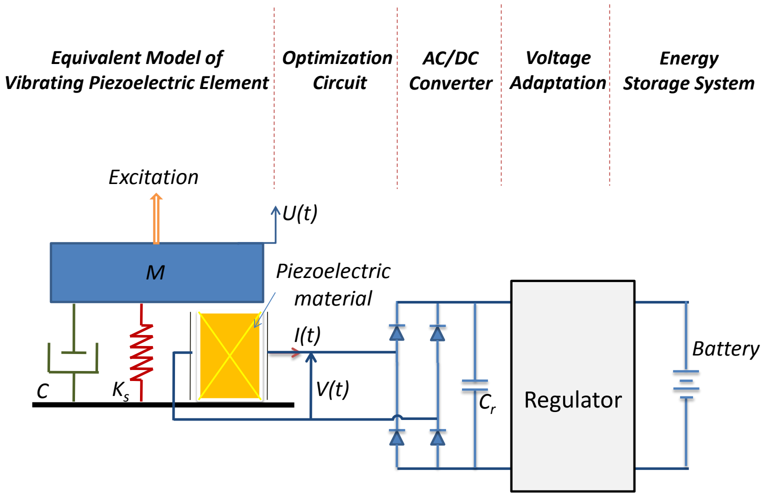

Figure 1.35: An equivalent model for a piezoelectric vibration energy harvesting system

have a significant influence on power output. Cao *et al* [72,73] investigated the optimal design for a PZT thin-film device with the optimized electromechanical coupling factor k^2 analytically and experimentally showing that the electromechanical coupling factor reaches an optimum value when the electrode coverage is around 42 % of membrane area. The best combination of substrate and piezoelectric thickness was also found to achieve the optimal k^2; in addition, the effect of substrate stiffness on electromechanical coupling factor was obtained. In their experimental work, for a 2μm thick substrate, an increase of factor 4 can be achieved in the coupling coefficient by increasing the piezoelectric thickness from 1μm to 3μm.

1.3.2.2 Electrical Circuitry Optimization

The improvement of piezoelectric harvester can also be achieved in optimizing the power circuitry. The complete system of piezoelectric harvester is shown in Figure 1.35 generally with three portions, the left portion of this figure is the equivalent model of vibrating piezoelectric element near one of the resonance frequency, and the right portion represents the energy storage system which is connected through a diode bridge rectifier with the vibrating part. The energy storage system is however out of scope in this thesis. Except the energy storage circuit system, optimization circuits and voltage adaption circuit can exist to optimize the energy conversion. The interface circuit will actively change the mechanical-electrical properties of vibrating piezoelectric element and accordingly, interface circuit design becomes very important. Generally, the interface between piezoelectric element and energy storage system can be usually separated

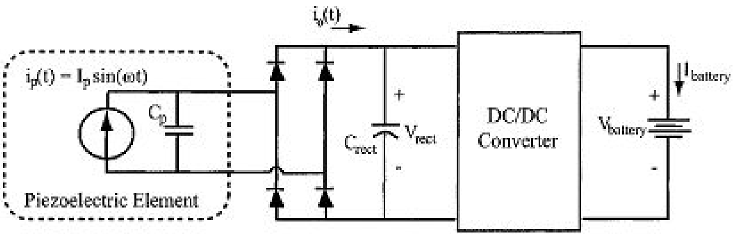

Figure 1.36: Adaptive energy harvesting circuit [75]

into 3 parts, 1. simply the conversion between AC and DC (for example, conversion AC / DC by a diode bridge) , 2. adaptive energy harvesting circuit (DC-DC converter), 3. optimization of energy extraction [74].

A bridge rectifier generally is followed by a filter capacitor to convert the AC voltage delivered by piezoelectric inserts to DC voltage. Shu and Lien [55] did a detailed analysis with different approaches for weakly-coupled, medium-coupled and highly-coupled AC-DC rectified piezo-harvesters. The simplest adaptive interface circuit could be a resistance load, a capacitive load, or an inductive load. However, compared to the resistance load, both capacitive and inductive load will strongly affect the vibrating piezoelectric element performance, for example, a higher capacitance will result a lower electromechanical coupling coefficient k^2. Lu's work [60] shows that there is an optimal load resistance for which the power delivered by the piezoelectric inserts is maximum. To obtain the applicable voltage level for the rechargeable battery or a supercapacitor and the optimized power, a DC-DC converter was proposed by Ottman *et al* [75] (Figure 1.36). They have first proposed a step-down, adaptive DC-DC converter used to maximize the power harvested from the piezoelectric device [76]. For a step-down converter operating in a discontinuous current conduction mode, an optimal duty cycle has to be determined where power flow from the piezoelectric device is maximized, which depends strongly on the excitation frequency. The use of the converter is shown to increase the power to the energy storage element, an electrochemical battery, by 4 times compared to when the battery was directly charged with a piezoelectric and a AC-DC rectifier. Extended the work of Ottman, Lefeuvre [62] *et al* developed a piezoelectric harvester system with a buck-boost converter (or a flyback switching mode DC-DC converter). The buck-boost DC-DC converter acts as a constant input average resistance which achieves the optimization criteria of seismic piezoelectric harvester, so there is no need an extra load resistance to optimize the harvesting power, and it can work effectively whether the rectified voltage of piezoelectric harvester (or the input voltage of DC-DC converter) is higher or lower than the applicable voltage level of battery, with 88% efficiency considering the control circuit consumption. Instead of having a switching frequency decided by the duty cycle of a buck-boost converter, the converter or a switch device is turned at each extremum of the mechanical displacement synchronizing the electric charge process with the system vibration. This interface is called 'Synchronous Electric Charge Extraction (SECE)' technique (Figure 1.37(c)) proposed in [77]. As SECE technique shares the same concept with the buck-boost converter, it also has the independency in resistive load and could improve the power harvesting with a factor 4 compared to the interface consisting in simply a resistive load (standard technique).

A self-adaptive power harvesting circuit has been developed by Guyomar *el al* [54] from an idea addressing the vibration damping problem on mechanical structure, 'Synchronized Switch Damping' (SSD) [78] [79] to optimize the extracted energy from the piezoelectric element. The main principle of this nonlinear interface 'Synchronized Switch Harvesting (SSH)' consists in synchronizing the piezoelectric open-circuit voltage with the system vibration to improve the efficiency of the energy conversion process. Several works have been addressed in this technique [54, 80–82]. Compared with standard technique (simply connected with a resistive load), this nonlinear technique makes the electrical harvested power increase above 900% under a proper design. Nonlinear technique implements a switch in series with an inductor and connected with the piezoelectric element in parallel (Parallel-SSHI, Figure 1.37(e)) or in series (Series-SSHI, Figure 1.37(g)); the switch is closed when extreme displacement occurs for harmonic excitation. Few works reviewed and compared these nonlinear electronic interfaces [81, 83–86] as shown in Figure 1.37 and Table 1.6. If the quantity of used piezoelectric material is roughly proportional to the figure of merit k^2Q_M, SSH techniques permits a dramatic reduction of the quantity of piezoelectric material compared to the standard technique. SECE seems to work well for low-coupled harvester systems; its performance however decreases after reaching the optimal power output at $k^2Q_M = \pi/4$. With respect to the load adaption, Parallel SSHI technique works at a higher resistive load to achieve a higher power while Series SSHI technique requires a lower resistive load compared to standard technique. The benefit of SECE technique is that it does not need load adaption for optimizing energy conversion, which also makes it well adapted to multimodal or broadband excitation. Shu *et al* also mentioned that

Table 1.6: Comparison of nonlinear interfaces for piezoelectric harvester

	Maximum Power Expression	**Suitable Harvester System**	**Resistive Load Adaption**
Standard DC Interface	$k^2Q_M \leq \pi$, $P_{\max} = \frac{\pi}{2}\frac{k^2Q_M}{(\pi+k^2Q_M)^2}\frac{{F_M}^2}{C}$ $k^2Q_M \geq \pi$, $P_{\max} = \frac{{F_M}^2}{8C}$	Highly-coupled	$k^2Q_M \leq \pi$, $R_{opt} = \frac{\pi}{2C_0\omega}$ $k^2Q_M \geq \pi$, $R_{opt} = \frac{2\alpha^2-\pi C_0C\omega\pm 2\alpha\sqrt{\alpha^2-\pi C_0C\omega}}{2C(C_0\omega)^2}$
SECE DC Interface	$P = \frac{2}{\pi}\frac{k^2Q_M}{\left(1+\frac{4}{\pi}k^2Q_M\right)^2}\frac{{F_M}^2}{C}$	Low-coupled	No need load adaption
Parallel SSHI DC Interface	$P_{\max} \approx$ $\frac{k^2Q_M}{\pi(1-\gamma)+8k^2Q_M}\frac{{F_M}^2}{C}$	Very low and medium-coupled	Higher than R_{opt} of standard interface, $R_{opt} = \frac{\pi}{C_0\omega(1-\gamma)}\frac{1}{1+\frac{8k^2Q_M}{\pi(1-\gamma)}}$
Series SSHI DC Interface	$P_{\max} \approx \frac{k^2Q_M}{2\pi\frac{1-\gamma}{1+\gamma}+8k^2Q_M}\frac{{F_M}^2}{C}$	Very low and medium-coupled	Lower than R_{opt} of standard interface, $R_{opt} = \frac{\pi}{2C_0\omega}\left(\frac{1-\gamma}{1+\gamma}+\frac{4}{\pi}k^2Q_M\right)$

both Series and Parallel SSHI techniques significantly improve the energy harvester bandwidth [66, 80, 87]. The comparison between standard interface, SECE interface, Parallel SSHI interface and Series SSHI interface can be found in Table 1.6.

Except the nonlinear interfaces mentioned above, transformations of these nonlinear interfaces are also very interesting in terms of different consideration and requirement. The SSHI MR (Magnetic Rectifier) technique proposed by Garbuio *et al* [88] ultimately reduces the losses due to the threshold voltage of the diodes. The 'Double Synchronized Switch Harvesting' (DSSH) circuit proposed by Lallart *et al* [89] improves the power output for a very weakly-coupled harvester system. This technique associates the Series SSHI circuit and the SECE circuit and an intermediate energy storage capacitor is included allowing decoupling extraction and storage stage and controlling the trade-off between energy extraction and damping effect. In addition, the use of SECE circuit makes the independency to the load adaption.

The using nonlinear treatments for energy harvester allows a significant increase of

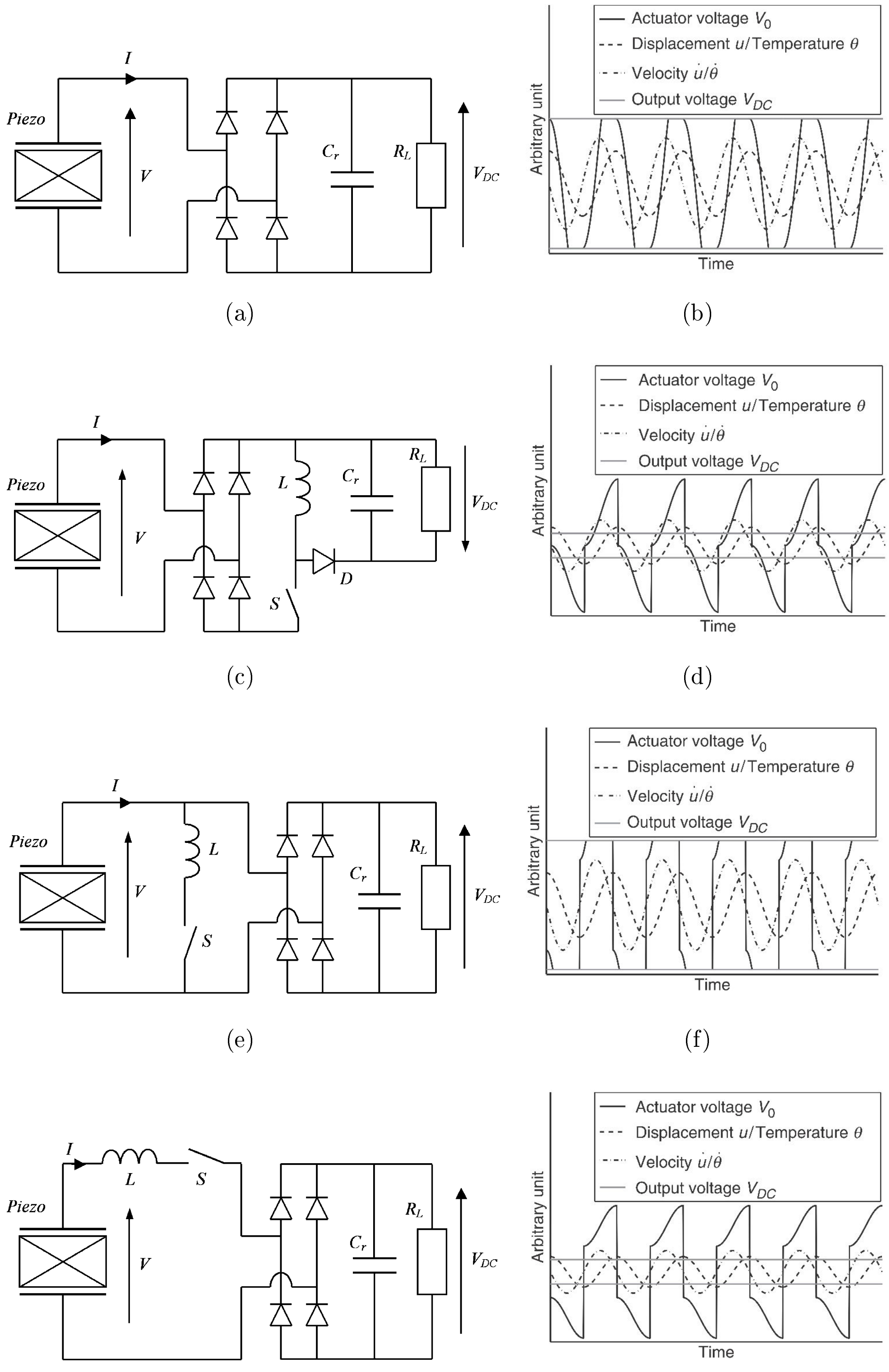

(a) (b)

(c) (d)

(e) (f)

(g) (h)

Figure 1.37: Nonlinear interfaces for piezoelectric harvester [81, 86]: (a) Standard interface; (b) Standard interface DC waveforms; (c) SECE DC interface; (d) SECE DC interface waveforms; (e) Parallel SSHI DC interface; (f) Parallel SSHI DC interface waveforms; (g) Series SSHI DC interface; (h) Series SSHI DC interface waveforms

the performance of vibration-based microgenerator. However, the nonlinear process may seem to be delicate in a realistic implementation. The group of LGEF, INSA de Lyon [90, 91], have proposed an easy and energy-efficient way in implementing the nonlinear technique based on the detection of maximum values using delayed version of the voltage (the maximum value is reached when the delayed signal becomes grater than the original piezo-voltage), generating a pulsed voltage that drives a transistor acting as the digital switching. Hence, such a process can be made truly self-powered (it usually consumes very little energy, typically 3 % of the electrostatic energy available on the piezoelectric element) using widely available components and may be easily integrated.

1.4 Energy Harvesting under Broadband Vibrations

In the previous section, different piezoelectric harvester mechanisms and optimization interfaces are described. However, most studies were devoted to the single frequency vibration and analyzed the harvester performance under simpler sinusoidal excitations, which is not robust to variations in the excitation frequency. In practical, vibrations surrounding us usually contains band-limited or wideband frequency information (for example, engine vibration, airplane wing vibration, etc.), which makes a dramatic efficiency decrease in a seismic (or cantilever) piezoelectric harvester. A piezoelectric harvester with a wider bandwidth might increase the efficiency as real excitations usually variate in frequency spectrum. So, in this section, methods for widening the bandwidth of piezoelectric harvester will be first introduced. Another issue concerning to the broadband excitation is that the more realistic signal would induce a more complex and ambiguous response, especially when connected with nonlinear interface circuits. In the SSD and SSH nonlinear techniques, the switching algorithm in the shunting circuit, due to its nonlinearities, is critical to the system performance. Accordingly, the analysis of this switching algorithm for multi-modal or broadband input system has to be discussed elaborately. The proposed methods and studies could be roughly divided into two categories: 1. Simulation and experimental work and 2. stochastic analysis. The analysis of piezoelectric harvester under a broadband/random excitation will be introduced in the second part of this section.

1.4.1 Piezoelectric Harvesters with Wide Bandwidth

A common drawback of piezoelectric harvester is their poor performance when out of resonance. To widen their operational bandwidth and increase practical bandwidth where energy can be harvested, several approaches can be implemented, such as an array of structures each with different natural frequencies, an amplitude limiter, coupled oscillators, nonlinear springs and bi-stable structures [69, 92, 93].

The use of several piezoelectric beam harvesters with different resonance frequencies in parallel has been proposed in [94] and [95] shown as in Figure 1.38. Lien and Shu have proposed an analysis of piezoelectric harvester array connected with different interfaces (Figure 1.39) based on the idea of equivalent impedance (transforming the mechanical model as an equivalent circuit model). It is found that the power output increases more when the deviations in system parameters are small (system parameters for each beam in the array), and if the deviations are relatively large, the harvester connected with the Parallel-SSHI interface turns into a wideband mode. However, this result was acquired under PSpice environment and there is no experimental work validating the modeling. In addition, the optimal resistance value for optimal power when system parameters are identical is surprisingly higher for Series-SSHI interface and lower for Parallel-SSHI interface, which contradicts what was presented in the previous work [81]. The piezoelectric beam array harvester obviously increases the bandwidth of the generator and also shortens the charging time of the storage capacitor to a given voltage level but also decreases the available power per weight as only the in-resonance generator contributes to the output power while the off-resonance beams do not produce significant power, which can easily be observed from Lien's and Shu's work [96] that shows that the output power decreases when each beams has different natural frequencies.

A wide bandwidth piezoelectric harvester can also be achieved with mechanical stoppers (amplitude limiter) [97–99]. Liu *et al* [99] evaluated a piezoelectric MEMS energy harvester system with top- and bottom-stoppers leading to a wider operation range of the harvester from 30Hz to 48Hz. Blystad *et al* [97] have investigated numerically a piezoelectric MEMS energy harvesting system with mechanical stoppers considering four different interface circuits (standard AC, standard DC, SSHI and SECE) in SPICE environment. The harvester connected with standard AC and SECE interfaces is found to have a proportional relation between the harvested power and acceleration spectral density until stopper impacts become important. Later on, an experimental

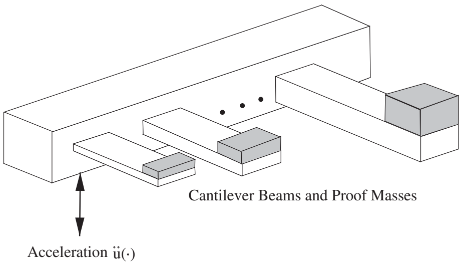

Figure 1.38: An ensemble of cantilever beams with proof masses at their tips. When dimensions of the beams and masses of the proof masses are chosen appropriately, this ensemble can function as a band-pass filter [94]

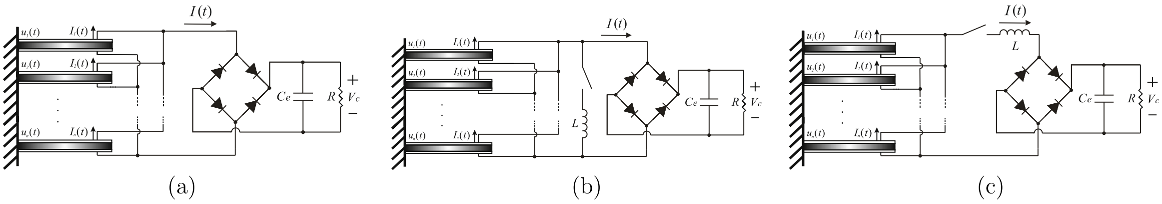

Figure 1.39: An array of piezoelectric energy harvesters connected in parallel. It is connected to (a) standard interface; (b) parallel-SSHI interface; (c) series-SSHI interface [96]

work was proposed in [100] to verify the previous simulation work in which the mechanical stopper is well modeled using a parallel spring-dashpot system. A lossless rigid end stop was found to be benefit in maximizing the bandwidth of harvester under a high acceleration levels, where nonlinearities due to mechanical end stop impacts are significant. A coupled oscillator consists of N spring-mass-damper systems has also been proposed by researchers as a method to widen the harvester bandwidth [63, 101, 102]. Aladwani *et al* [103] proposed a dynamic magnifier connected to a cantilevered piezoelectric harvester to increase the power output and widen the bandwidth around a single resonance using an additional mass with spring between the harvester beam and the vibration base. Zhou *et al* [104] further proposed a new type of harvester with a multiple mode dynamic magnifier which is able to enhance the power and widen the operation bandwidth over virtually all natural frequencies. Erturk *et al* [105] transformed the conventional rectangle shape beam into a L-shaped cantilever beam which enables the second frequency peak of original beam to be closer to the first frequency peak and enhances the bandwidth of the harvester. Harvesters with nonlinear stiffness might be another solution for widening the bandwidth of the piezoelectric harvester [106, 107]. The nonlinear bistable harvester can be realized with a magnetic spring (Figure 1.40). A piezoelectric harvester coupled to permanent magnets as a bistable system was ex-

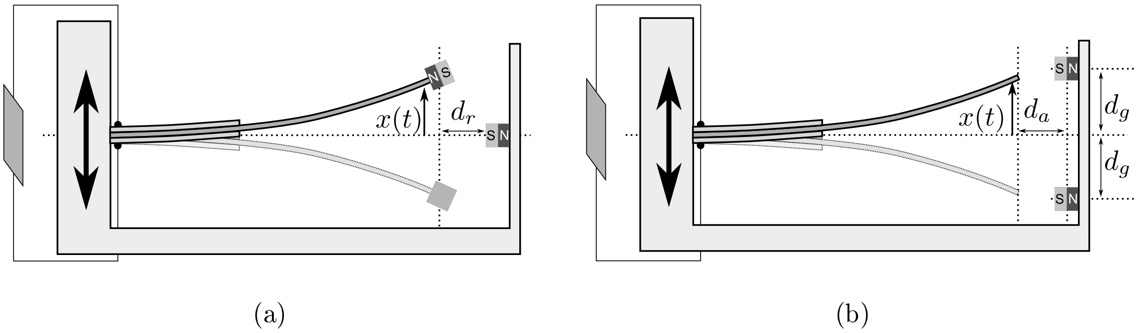

Figure 1.40: Piezoelectric energy harvesters with nonlinear stiffness: (a) Bistable magnetic repulsion harvester; (b) Magnetic attraction harvester [106]

ploited by Ferrari *et al* in [108]. Analysis and simulations show that a nonlinear bistable harvester gives better performances under a band-pass-filtered white-noise excitation with respect to a linear harvester (the analysis and simulation were done with a mass-spring model). Sebald *et al* [109, 110] have discussed in both experimental and simulation works for a piezoelectric harvester consisting in a Duffing resonator with the hardening effect to broaden the working bandwidth for energy harvesting. The nonlinear piezoelectric harvester with Duffing resonator has shown a 7.75 % bandwidth than a 1.4 % bandwidth of a linear harvester under a harmonic excitation of amplitude 1 ms^{-1}. Although in terms of maximum power output, a nonlinear harvester could only have 0.92 mW and a linear harvester could have 2.2 mW, the nonlinear harvester is suitable for harvesting energy from harmonic excitations when the excitation frequency is subject to changes (for example, due to temperature variations, aging or fatigue). Wickenheiser and Garcia further discussed the effect of magnet strength and the spacing between each magnets for a multistable harvester system in [111]. The multistable harvester with softening effect under a harmonic excitation shows that the magnet has an increasing effect when the base excitation frequency decreases to zero as at very low frequencies, the relative tip deflection is negligible, disturbances due to magnetic force are relatively large. A broadband, stochastic excitation was then applied on this nonlinear harvester and it was shown that the linear harvester is much more sensitive to the driving frequency than the nonlinear harvester and the nonlinear harvester can harvest 4 times more than the linear harvester under a broadband excitation. A bistable harvester is applicable for stochastic excitation and can further improve the performance by proper periodic change of potential barrier (stochastic resonance) [112]. However, such methods require external energy input and are more difficult to implement.

A piezoelectric harvester with wide bandwidth has the potential to cope with the mismatch between the resonant frequency and the vibration frequency. To widen the bandwidth of the harvester, a drawback is that there is a trade-off between the system bandwidth and the Q_M factor. A possible way to have a wider bandwidth without decreasing in Q_M factor is to have an array of small harvesters. However, the assembled harvester must be carefully designed so that each of small harvester does not affect the others, which makes the design and fabrication complicated. Therefore, this approach is not volume efficient. The use of mechanical stoppers might limit the vibration amplitude and so the output power, and might induce a fatigue failure in the cantilever beam. A coupled harvester would have a flat response in the frequency domain; it might however, have a significant decrease in the maximum output power than the harvester with only one mass. A nonlinear or bistable harvester can improve the performance of the harvester at higher or lower frequency bands relative to its natural frequency. However, the complicated mathematical modeling might increase the complexity in design and implementation; in addition, there is hysteresis in nonlinear harvester that performance during a down-sweep (or an up-sweep) can be worse than that during an up-sweep for hard nonlinearity (or a down-sweep for soft nonlinearity) or worse than the linear harvester depending on the sweep direction.

1.4.2 Analysis of Piezoelectric Energy Harvesters under a Broadband Excitation

In many applications, the vibration is random and rich in frequency information. However, except different designs for widening the harvester bandwidth, there are still very few analytical works describing the response of a piezoelectric harvester when it is excited by a random or/and broadband vibration. The performance of piezoelectric harvester under a broadband excitation can be either performed based on the simulation result, experimental measurement with probability and statistic strategies or analyzed by stochastic modeling.

1.4.2.1 Simulation and Experimental Work of Piezoelectric Harvester Driven by Broadband Vibrations

Miller *et al* [113] studied the MEMS energy harvesting from ambient vibrations with Finite-Element simulations and experimental verification. The finite-element model can work under arbitrary acceleration input and corresponds well with the measurement in predicting frequency peaks; a maximum 82 % discrepancy is however between the model and experiment in power output. The group of Vestfold University College, Norway, utilized SPICE, a numerical circuit simulator, to simulate the harvested energy in response to random vibrations [97,114,115]. Zhao and Erturk presented two numerical modelings using Fourier series-based Runge-Kutta method and Euler-Maruyama solution to describe the cantilevered piezoelectric harvester performance under broadband random vibrations [116]. Numerical simulations were compared with analytical solution and experimental results showing a very good agreement for a range of resistive load conditions and input PSD levels. Lefeuvre *et al* first considered the broadband vibration in the context of energy harvesting with nonlinear interface circuit [117]. In their work, the harvester cantilever beam is subjected to a random force in the 10 Hz to 2 kHz band, and the corresponding displacement spectrum reveals the mechanical filtering of cantilever beam, which is mainly composed of three bending modes. From the experimental results, it is shown that the average powers with the standard technique and SECE (Synchronous Electric Charge Extraction) technique under different frequency bands. Under the right switch triggering time, the SECE technique roughly increases the harvested power by a factor 2 in the random operation, whereas the in harmonic operation, the factor is 3.

Statistic strategies for nonlinear circuit control in vibration control might be interesting in energy harvester. Concerning the use of nonlinear interface circuits under a random vibration, Guyomar *et al* stated the importance of proper switching instant when using a nonlinear techniques for semi-passive vibration control (SSD) [118], and developed the alternative strategy, based on the statistical analysis of the voltage or displacement, in order to optimize the vibration control (which can be also applied in energy harvesting). In the case of broadband excitation, it induces more complexity as the system has not only an unique extreme displacement but different local maxima, which makes difficult to choose the switching instant. With the alternative strategy, instead of each extremum, the switch is allowed to turn on when the piezoelectric voltage reaches a significant value (v_m). Moreover, the voltage will be inverted on the global maximum, for which the energy stored on the piezoelectric element is maximum. The effect of the alternative strategy shows in Figure 1.41. There therefore exists a tradeoff between the number of switch and the instant of switch. With more numbers of switches, the energy extraction happens more often, however, it could not provide

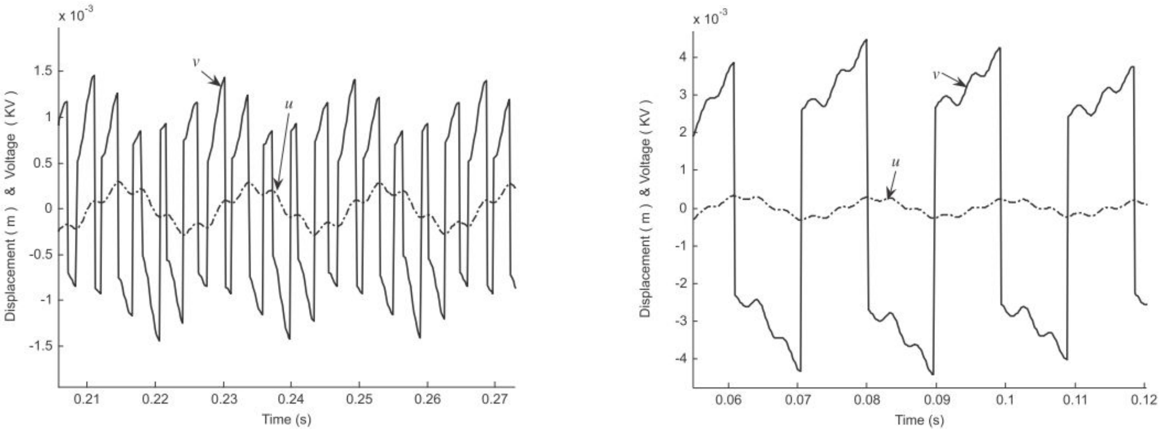

(a) (b)

Figure 1.41: Illustration of two different strategies for SSDI control : (a) original strategy with switching on each extremum. (b) alternative strategy consisting of selecting specific maximum (sloid line is the piezoelement voltage; dashed line is the structure strain of deflection).

enough time for voltage increasing to a sufficient value. With respect to the principles mentioned above, Guyomar *et al* [118] discussed the various control strategies: 1. Control Probability Law (CPL) [119], 2. Statistics methods and 3. Root mean square method. The simulation results for the three methods lead to better results than simple SSDI, which consequently induce a better energy extraction. However, these control strategies require the knowledge of the signal and preliminary works to decide proper parameters, which is different from each force input cases. To facilitate a self-powered switching circuit which has ability in choosing the switching instants at the global extrema instead of every extrema, Lallart *et al* [91] have proposed a new self-powered adaptive SSDI circuit consisting in envelope detectors with different time constants and enforcing a threshold voltage for switch.

1.4.2.2 Stochastic Modeling of Piezoelectric Harvester under Broadband Vibrations

Real-world signals with multimodal or broadband character has been paid attention recently either by simulation [115] or by experimental work [117,120]. Nevertheless, because of the complexity and variety of broadband signal, the theoretical investigation of energy harvester properties, such as displacement of the mass and the outgoing voltage from embedded piezoelectric, are difficult to be shown as a closed-form. Halvorsen [121] characterized the excitation with its power spectral density (PSD) to make the linear system problem equivalent to the propagation of a random signal through a linear filter which allows the analysis result to be in closed-form. A support structure with a random time-dependant acceleration, which is characterized by its PSD, S_a, has been modeled in this work. When the harvester structure with standard interface circuit is subject to a white noise excitation, the average power delivered into the load resistance would be

$$P = \frac{mS_a}{2}\left(\frac{r_P}{r_P + r_S + r_L}\right)^2 \frac{r_L k^2 Q_M}{1 + (\frac{1}{Q_M} + k^2 Q_M)r + r^2}, \tag{1.14}$$

$$r = \frac{r_P(r_S + r_L)}{r_P + r_S + r_L}, \tag{1.15}$$

where $k^2 Q_M$ is the product of mechanical quality factor and the electromechanical coupling factor, r is the dimensionless resistance contributed by the dimensionless load resistance r_L, the dimensionless stray series resistance r_S and the dimensionless shunt resistance r_P. The average power P increases with this quantity.

The nonlinear effect either through mechanical form or electrical form makes the analytical solution of a piezoelectric harvester under a random and broadband excitation more complex. To obtain random response quantities for the system with nonlinear effects, it is necessary to solve the random process problem, which means to solve the coupled stochastic differential equations. Fokker-Planck equation is one of the most common formula for the random process analysis. It solves the probability density p of the state variables. A Fokker-Planck equation was used to describe the Brownian motion of particles [122]. From solving Fokker-Planck equation under specific conditions, closed-form expressions for p would be obtained [123]. In Halvorsen's work [121], the Fokker-Planck equation governing the probability density function of the harvested power for a cantilever beam system was derived and was proved to agree with the stochastic modeling (Eq. (1.14)). However, the calculation is long and difficult.

Adhikari *et al* [124] also derived the harvested power by the theory of stationary random vibrations for a linear piezoelectric harvester. It considered a direct-coupled type harvester, which has a polarization along the d_{33} direction, vibrating due to stationary Gaussian white noise base excitation. The two dimensional stochastic differential equations are solved by the theory of linear random vibrations. The normalized mean power of a harvester was analyzed under different adaptive inductance and resistance values. Closed-form expressions presented in this work is useful in quantifying the harvested power of a direct-coupled piezoelectric harvester under random vibration. However, the approach described in this work can be extended to filtered white noise and non-Gaussian excitation which are more realistic excitation spectra.

Zhao and Erturk [116] have derived the analytical expression of expected power output for a linear piezoelectric harvester with the resistive load considering the entire spectrum of excitation and all vibration modes of the harvester by stochastic modeling. The single mode derivation is compared with given expressions of Halvorsen [121] and Adhikari [124]. The analytical solution is validated with numerical solutions in deterministic approach (Fourier series-based Runge Kutta solution) and in stochastic approach (Euler-Maruyama) and experimental results under a Gaussian white noise-type random excitation.

The exact closed-form expressions of the harvested power for linear harvesters have been derived under a Gaussian white noise excitation in the last paragraphs. Nevertheless, due to its unpredictable properties, nonlinear systems until now have not been well discussed and have a general and well-constructed expression for describing harvester performance. In addition, an analytical model considering a more realistic excitation, for example filtered white noise or non-Gaussian excitation needs to be further investigated.

2 Broadband Modeling of Nonlinear Techniques for Energy Harvesting

In the previous section, several aspects for optimization of energy harvesting using vibrating piezoelectric element has been expressed. Particularly, "Synchronized Switch Harvesting" (SSH) techniques have been shown to be an efficient way for artificially increasing the conversion potential between the mechanical energy stored in piezoelectric element and the electrical energy, and thus magnifying the harvesting abilities. The nonlinear technique (SSHI: Synchronized Switch Harvesting on Inductor), proposed by Guyomar et al*, shows a significant increase in harvested power over 900%. It assumes the switch is turned on for a very short period and reverse the voltage of piezoelectric transducer at all extrema of displacement response. This switching algorithm is effective in single frequency excitation, however, it will leads to a tradeoff between the number of switching events and the voltage amplitude that can be accumulated under a broadband excitation. In this chapter, a brief introduction of SSH techniques would be presented first and then the newly-constructed broadband modeling with a periodical switching strategy for these nonlinear techniques would be described in detail based on the theory of self-sampling and self-aliasing in the frequency domain.*

The aim of this chapter is to provide a first step for the analysis of nonlinearly interfaced piezoelectric harvesters with a broadband and/or random excitation. The modeling is derived from fundamental formula in order to have a general form describing the harvester's performance. It is then applied to several well-known cases to show its effectiveness. In this work,

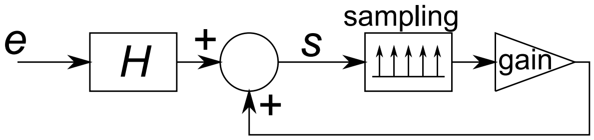

Figure 2.1: Principles of the self-sampling process

> *the "self-sampling" process is defined as modification of a continuous signal s by its own sampled signal, as depicted in Figure 2.1, where e is the input and H a transfer function. In addition, if the sampling frequency is chosen to be less than twice the maximal frequency of signal s, aliasing occurs and is fed back to s, leading to the concept of "self-aliasing". The harvester's overall response can be seen as self-samplings of the response at system resonant frequency due to the periodic switching process, which we call it as "Periodic Switch Harvesting on Inductor" (PSHI). With a proper switching frequency, a self-aliasing phenomenon will occur between samplings inducing a constructive response if the phase is chosen properly.*

2.1 Introduction of Nonlinear Techniques

The considered energy harvesting devices consist of a vibrating mechanical structure with bonded piezoelectric elements. The structure with piezoelectric elements is modeled as a {spring+mass+piezo+damper} system such as the one shown in Figure 2.2. It could be considered as being composed of a rigid mass M, a spring K_s representing the stiffness of the host structure and a viscous damper C for the mechanical losses. The external force F (or Ma expressed by the input acceleration a for a seismic type vibration assuming the correction factor to be 1 [105]) results from the mechanical excitation applied on the rigid mass M. Under this excitation the proof mass moves with a displacement u and induces a voltage V across the piezoelectric transducer and an outgoing current I.

According to Newton's second law of motion, the sum of the force on the rigid mass then generates the governing equation (2.1) of the {spring+mass+piezo+damper} system

$$M\ddot{u} = F - K_\mathrm{E}u - \alpha V - C\dot{u}, \tag{2.1}$$

where K_E is the global stiffness for short circuited condition defined as a sum of the stiffness of piezoelectric element K_{pE} and the structural stiffness K_s, and α is the force

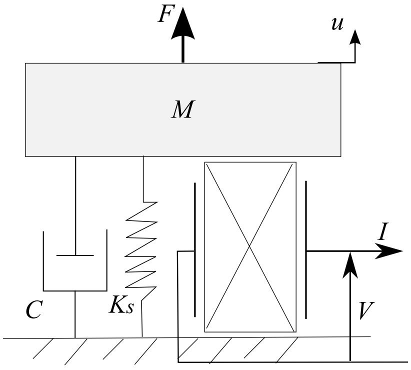

Figure 2.2: Equivalent mechanical model for piezoelectric structure

factor for a given structure, relating the piezoelectric converse effect. The energetic analysis is obtained by integration of the equation of motion (2.1) and the velocity over the time variable:

$$\int F\dot{u}\,dt = \frac{1}{2}M\dot{u}^2 + \frac{1}{2}K_{\mathrm{E}}u^2 + \int C\dot{u}^2\,dt + \int \alpha V\dot{u}\,dt. \tag{2.2}$$

The expression (2.2) is considered as the energy balance of the input energy provided by the external driving force F and the sum of the kinetic energy, potential elastic energy, mechanical losses and the converted energy. From the piezoelectric equation (2.3), it can be shown that the converted energy (Eq. (2.4)) is the sum of electrostatic energy stored on the piezoelectric element and the energy delivered to the connected electrical device, where C_0 is the internal capacitance of the piezoelectric element.

$$I = \alpha\dot{u} - C_0\dot{V} \tag{2.3}$$

$$\int \alpha V\dot{u}\,dt = \frac{1}{2}C_0 V^2 + \int VI\,dt \tag{2.4}$$

In order to increase the converted energy, the phase between the piezoelectric voltage V and the mechanical velocity $\dot{u}$ has to be reduced and the voltage amplitude has to be improved. The basic principle of nonlinear techniques used on vibration control SSD and on energy harvesting SSH is to reduce the phase shift between V and $\dot{u}$, and, coincidentally, to increase the voltage amplitude and further increase the energy conversion.

The extension of SSD technique in the field of energy harvesting is called 'Synchronized Switch Harvesting on Inductor' (SSHI), which is simply the SSDI interface in parallel or series with a load. They share the same technique switching on when the displacement reaches its extrema, but in SSHI, the converted energy is harvested

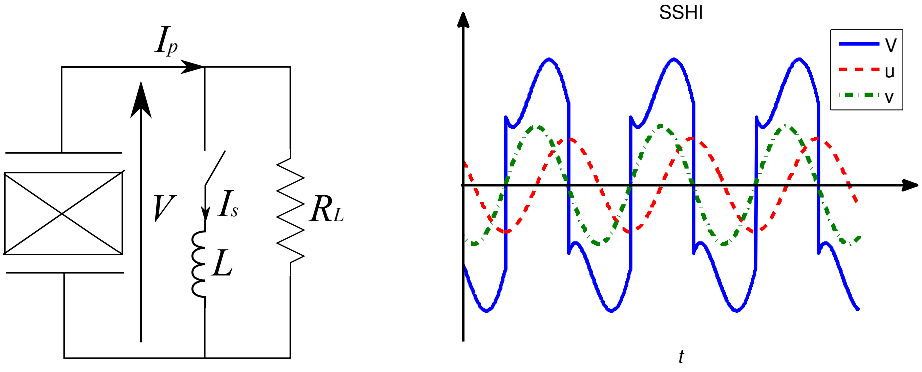

(a) (b)

Figure 2.3: SSHI technique: (a) SSHI circuit interface; (b) waveforms under sinusoidal excitation

through the resistive load. The interface and the piezoelectric voltage waveform for SSHI technique are shown in Figure 2.3. The switching event leads to a piezoelectric voltage V in-phase with the vibrating velocity v and induces a piecewise constant function, which increases the voltage amplitude. Connecting an inductor with the switching device enforces a $L - C_0 - R$ oscillator with an oscillation period $T_o = 2\pi\sqrt{LC_0}$; after the inversion time $t_i = \pi\sqrt{LC_0}$, the voltage would start from a non-zero value with the opposite sign and so the voltage amplitude can be improved. However, as the switching network is not perfect, there is loss during the voltage inversion, which is defined by an electrical quality factor Q_i or the inversion factor $\gamma = e^{\frac{-\pi}{2Q_i}}$ which is generally ranging from $0.6 \sim 0.9$. The relation between voltages before and after switching is expressed by this factor as in Eq. (2.5):

$$V(t_n^+) = -\gamma V(t_n^-). \tag{2.5}$$

Applying the Kirchhoff's current law, the sum of the currents flowing through the electrical components is equal to the current flowing out from the piezoelement. The sum of currents flowing through the resistive load $\frac{V(t)}{R_L}$, to the internal piezoelement capacitance $C_0\dot{V}(t)$ and to the switch is equal to the current from the current source $\alpha\dot{u}(t)$. The current only flows through the switching circuit when the switching device is closed, stating that it is null during all the vibration period except at the switching instant $t = t_n$. As the switch is turned on with a frequency much higher than the vibrating frequency, the switching process could be defined by a δ function as an impulse response. Accordingly, the current flows through the switching device could be expressed by a series of Dirac function $\sum\limits_{n=-\infty}^{\infty} \delta\left(t - t_n\right)$ and the piezoelectric voltage of SSHI technique would be expressed as Eq. (2.6), which is nonlinear for each switching time instants, t_n.

$$\frac{V(t)}{R_L} = \alpha\dot{u}(t) - C_0\dot{V}(t) - (1+\gamma)\,C_0 \sum_{n=-\infty}^{\infty} V(t)\delta\,(t-t_n), \tag{2.6}$$

In realistic excitation, which would be barely monochromatic but more likely random, there would be a tradeoff between the number of switching events and the value of the voltage at the switching instants. The energy delivered to the connected electrical devices, $E_{\text{extracted}}$, is proportional to the summation of voltage at every switching instant t_n:

$$E_{\text{extracted}} \propto C_0 \sum_n {V_n}^2. \tag{2.7}$$

V_n denotes the voltage value at the n^{th} switching instants. This equation shows that the higher extraction energy is achieved by increasing the number of switching and the value of cumulative voltage. However, the voltage amplitude at each switching instant might decrease with increasing number of switching processes as part of $E_{\text{extracted}}$ will be dissipated by the switching device. Hence, a careful control of switching algorithm is critical for the performance. Guyomar *et al* [118, 119] developed alternative strategies based on the statistical or probabilistic analysis of the voltage or displacement in order to optimize the vibration control. However, to have a detailed broadband excitation analysis, a theoretical broadband modeling is required. To understand more about the effect of switching algorithm on random vibration and to have the broadband response directly without tedious statistic calculation or recursive time-domain computation, a well-constructed modeling would be introduced in the following section. The switching process could be seen as a self-sampling sequence of the voltage. Furthermore, it will be shown that with a proper chosen switching frequency, a self-aliasing effect would bring a constructive interference, denoting the conversion magnification.

2.2 Broadband Modeling

In this section, an introduction of the new approach for broadband modeling of Periodic Switching Harvesting on Inductor (PSHI) technique will be presented. It consists in a switching device periodically closed for a very short time period and inducing a voltage inversion on the piezoelectric transducer at a specific switching frequency f_s or switching period T. It is slightly different from SSHI technique as in this approach, the switching process is periodic and with all possibilities of switching frequency. However, for a resonant structure, if the response is analyzed in small time-windows, periodic switching process shares the same principle with SSHI technique as the switching instant is easily synchronized with optimal displacements for a windowed signal. Although with PSHI technique, the harvesting efficiency is less than using SSHI technique under some excitation cases as the nonlinear interface is not switched on the displacement extrema, the periodic switching process can seen as a time-invariant process and the analysis can be simplified in order to get a closed-form expression. Due to the switching procedure, the output voltage $V(t)$ in time domain has to be recalculated for each switching steps. Instead of this tedious calculation sequence, the analysis in frequency domain, which is more common in signal analysis, would be discussed. Although most of the electronic components are powered with DC sources, this AC to DC process would induce another nonlinear effect, and in order to simplify the problem, we consider only the AC source in the work. In addition, with the AC process, more harmonics can be taken into account in the analysis. With the DC process, only the first harmonic is considered in the analysis.

The broadband modeling will be implemented with the concept of self-sampling and self-aliasing of the open-circuit voltage signal. The concept of self-sampling and self-aliasing can be explained with a simple sinusoidal function as depicted in Figure 2.4. When a sine signal is under a self-sampling process (expressed as a Dirac comb function) at a sampling frequency which equals to twice the frequency of the sinusoidal signal (Figure 2.4(a)), the original frequency components have the same frequency as the added sampled signal, and the sampled response (represented in dashed line) adds up to the original response. Hence, with a proper phase choice, there will be a self-aliasing effect (Figure 2.4(b)) which introduces a constructive response as Figure 2.4(c) shows.

2.2.1 Periodic Switching Process

The most simplest nonlinear switching interface is to connect a switching device in a short circuit (Figure 2.5(a)). With this interface, after the switching process, the initial condition on voltage would change to zero at each switching period. If the switch is connected in series with an inductor (Figure 2.5(b)), after the inversion, the initial condition of voltage would no longer be zero but with a factor $-\gamma$. The switching constant in this case would not be independent to the voltage on previous periods, so a

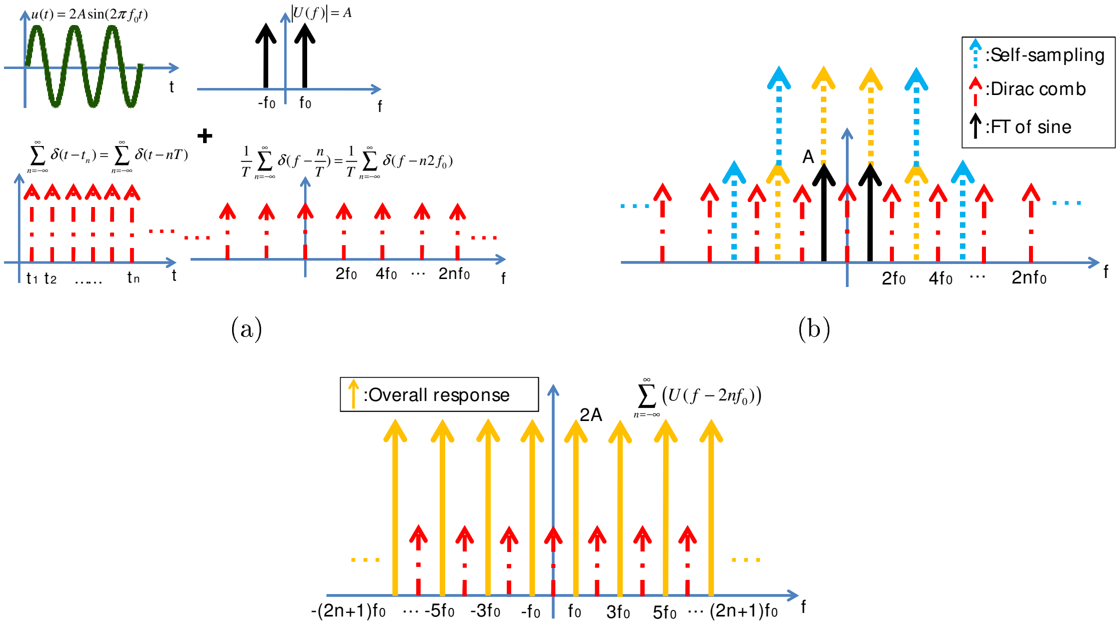

(a) (b)

(c)

Figure 2.4: Concept of self-sampling and self-aliasing for a sine signal: (a) A sine signal plus a Dirac comb function; (b) A sine signal under a self-sampling process; (c) The overall response after the sampling process

cumulative effect is introduced on the switching constant. In the following paragraphs, these two cases would be discussed in detail separately.

2.2.1.1 Periodic Switching Process on Short Circuit

Since the initial condition of voltage would be changed after the switching process, the voltages before and after the switch instant have to be formulated separately. Here we consider the two switching instants t_{n-1} and t_n as shown in Figure 2.6, which presents an example of how the switching process works on short circuit. In this model, the piezoelectric element is in open-circuit and has no resistive load and so the integration of Eq. (2.3) yields:

$$V(t) = \frac{\alpha}{C_0}u(t) + \kappa(t), \tag{2.8}$$

where $\kappa(t)$ is a piecewise constant function. The switch turns on at the time instant t_{n-1} and at this time instant the voltage reaches $V(t_{n-1})$; during the switching process, the voltage would be canceled due to a piecewise constant voltage. As the voltage is expressed as a composition of a scaled displacement ($\frac{\alpha}{C_0}u(t)$) representing the open-circuit voltage and a piecewise constant voltage due to the switching effect

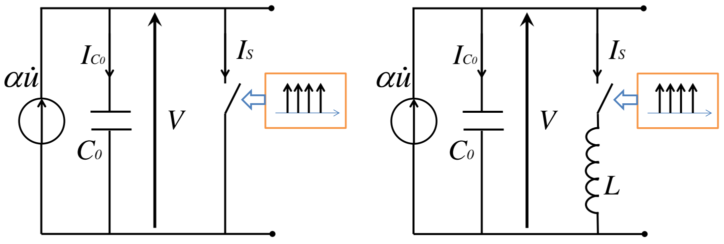

(a) (b)

Figure 2.5: Periodic switching interface with a current source: (a) switching on short circuit; (b) switching on an inductor

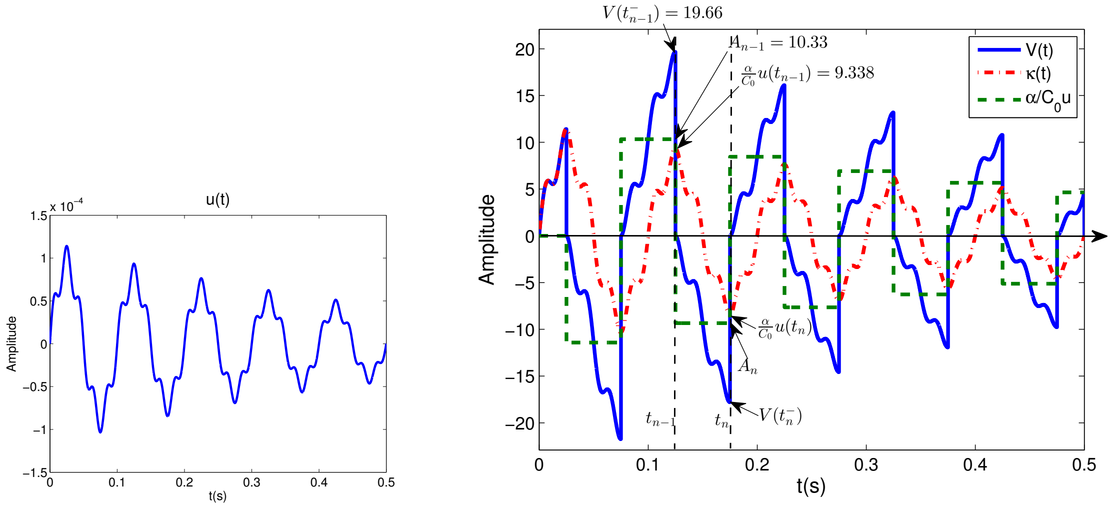

(a) (b)

Figure 2.6: An example shows the relationship of u and V at switching instant for periodic switching process on short circuit technique: (a) excitation displacement; (b) corresponding waveforms

$\kappa(t)$ representing the coupling from the circuit to the electromechanical system as in Eq. (2.8), the voltage at the switching instant t_{n-1} could be expressed by Eq. (2.9); A_{n-1} denotes the amplitude of piecewise constant function at $t = t_{n-1}$ or the integration constant; $A_n = \kappa(t_n^+) = \kappa(t_{n+1}^-)$. The switch is turned off after the switching time t_i considered to be very short. Then the switch is kept open until the next switching instant t_n and the voltage increases with the scaled displacement under the base of the existed piecewise constant A_{n-1}. Therefore the voltage just before the next switching instant $V(t_n)$ is expressed as Eq. (2.10). At the instant t_n^-, the switch turns on again and the same process as previous applies. The inverted voltage at t_n^+ would be again 0 and it could be formulated as Eq. (2.11):

$$0 = \frac{\alpha}{C_0}u(t_{n-1}) + A_{n-1}, \tag{2.9}$$

$$V(t_n^-) = \frac{\alpha}{C_0}u(t_n) + A_{n-1}, \tag{2.10}$$

$$0 = \frac{\alpha}{C_0}u(t_n) + A_n. \tag{2.11}$$

The switching constant A_n at $t = t_n^+$ for each switching step could be therefore acquired from voltage magnitudes at switching instants t_{n-1} and t_n:

$$A_n = -\frac{\alpha}{C_0}\left[u(t_n) - u(t_{n-1})\right] + A_{n-1}. \tag{2.12}$$

The difference between A_n and A_{n-1} is the output voltage change due to the switching event at time t_n and displacement difference, and A_n is given by the cumulative effects of all prior switching events which leads to:

$$A_N = -\frac{\alpha}{C_0}\sum_{n=-\infty}^{N}\left[u(t_n) - u(t_{n-1})\right], \tag{2.13}$$

which depends only on the displacement as voltage cancels. In Eq. (2.13), the summation term denotes the cumulative process and this cumulative process depends on every previous process. Accordingly, the piecewise constant function $\kappa(t)$ can be expressed through the unit step function $\mathrm{H}(t - t_n)$ and is given by

$$\kappa(t) = -\frac{\alpha}{C_0}\sum_{n=-\infty}^{\infty}\left[u(t_n) - u(t_{n-1})\right]\mathrm{H}(t - t_n). \tag{2.14}$$

The output voltage $V(t)$ could be then completely specified from Eqs. (2.8) and (2.14) as

$$V(t) = \frac{\alpha}{C_0}u(t) - \frac{\alpha}{C_0}\sum_{n=-\infty}^{\infty}\left[u(t_n) - u(t_{n-1})\right]\mathrm{H}(t - t_n). \tag{2.15}$$

With regard to Figure 2.5(a), the derivative of Eq. (2.15) gives the current that flows out of the source, decomposed into the current flowing into the piezoelectric internal capacitance and into the switching device as

$$\alpha \dot{u}(t) = C_0 \dot{V}(t) + \alpha \sum_{n=-\infty}^{\infty} \left[u(t) - u(t - (t_n - t_{n-1}))\right] \delta(t - t_n). \tag{2.16}$$

The current flowing into the switching device is expressed with the Dirac comb function at sampling instant t_n as the time duration of switching process is much less than the vibrational period. The Dirac comb function also introduces the concept of sampling. If the switch is considered to be turned on periodically (T_s as the switching period), the voltage response can be seen as self-sampled after the switching process. The switching instant t_n could be replaced with $nT_s - t_0$, where t_0 is the effect of a switching delay which could arise from imperfections of the electrical switching circuitry or be deliberately introduced for synchronization as the switching process in PSHI technique is independent on the time-domain displacement. The derivation of the voltage is then expressed with the Dirac comb function $\sum\limits_{n=-\infty}^{\infty} \delta(t - nT_s - t_0)$ as:

$$\dot{V}(t) = \frac{\alpha}{C_0} \dot{u}(t) - \frac{\alpha}{C_0} \sum_{n=-\infty}^{\infty} \left[u(t) - u(t - T_s)\right] \delta(t - nT_s - t_0). \tag{2.17}$$

The Fourier transform of a Dirac comb function is still a Dirac comb function:

$$\sum_{n=-\infty}^{\infty} \delta(t - nT_s) \underset{F^{-1}}{\overset{F}{\rightleftharpoons}} \frac{2\pi}{T_s} \sum_{n=-\infty}^{\infty} \delta(\omega - n\frac{2\pi}{T_s}). \tag{2.18}$$

However, the period of the transferred comb function in the frequency domain is in an inverted proportion of the original time period of the comb function and the amplitude of the transferred function is scaled by the inverse of the time-period. According to the convolution theorem and Fourier transform, the output voltage in frequency domain is described as

$$V(\omega) = \frac{\alpha}{C_0} U(\omega) - \frac{1}{j\omega} \frac{a}{C_0} \frac{1}{T_s} \sum_{n=-\infty}^{\infty} \left[U(\omega - n\frac{2\pi}{T_s}) \left(1 - e^{-j\left(\omega - n\frac{2\pi}{T_s}\right)T_s}\right) e^{-jn\frac{2\pi}{T_s}t_0} \right]. \tag{2.19}$$

The derivation of the piecewise constant function $\kappa(t)$ in the frequency domain is considered to be a convolution between the switching constant K_N and the Dirac comb function. A signal convoluted with the Dirac comb function is considered to be sampled at constant intervals of retardation, which is expressed by a series of repetitive impulse function. In accordance with the sampling theorem, the self-sampling process of the voltage response introduced by the switching process is again clearly shown from the expression of voltage frequency response.

2.2.1.2 Periodic Switching Process on an Inductor

To make the nonlinear technique more efficient, an inductor is connected in series with the switch so that when the switch is closed, a $L - C_0$ oscillator is formed and the inverted voltage is increased to $-\gamma V(t_n^-)$ and also brings an cumulative effect in the output voltage. In this case, the inversion coefficient γ is not zero but with a value generally between 0.6 to 0.9. Accordingly, the voltage at the switching instants t_{n-1} and t_n would be Eq. (2.20) and Eq. (2.22) and the voltage before the inversion $V(t_n)$ would be Eq. (2.21) expressed as the open-circuit voltage plus a constant switching voltage A_n coming from the switching process:

$$-\gamma V(t_{n-1}^-) = \frac{\alpha}{C_0} u(t_{n-1}) + A_{n-1}, \tag{2.20}$$

$$V(t_n^-) = \frac{\alpha}{C_0} u(t_n) + A_{n-1}, \tag{2.21}$$

$$-\gamma V(t_n^-) = \frac{\alpha}{C_0} u(t_n) + A_n. \tag{2.22}$$

The switching constant A_n could be considered as the sum of the difference between two open-circuit voltage ($\frac{\alpha}{C_0}u(t_n)$ and $\frac{\alpha}{C_0}u(t_{n-1})$), the difference between initial voltages after switching ($\gamma V(t_n)$ and $\gamma V(t_{n-1})$) and the effect from the previous switching process A_{n-1}. To be noted that in this case, connecting the switching device with an inductor, the switching constant A_n depends on the voltage from the previous switching period $V(t_{n-1})$, which denotes the cumulative effect.

$$A_n = -\frac{\alpha}{C_0} \left[u(t_n) - u(t_{n-1})\right] - \gamma \left[V(t_n) - V(t_{n-1})\right] + A_{n-1}. \tag{2.23}$$

After substituting the voltage expressed as a function of displacement, the difference between two switching constant would be shown as

$$\begin{aligned} A_n - A_{n-1} &= -\frac{\alpha}{C_0} \left[u(t_n) - u(t_{n-1})\right] - \gamma \left[\left(\frac{\alpha}{C_0} u(t_n) + A_{n-1}\right) - \left(\frac{\alpha}{C_0} u(t_{n-1}) + A_{n-2}\right)\right] \\ &= -\frac{\alpha}{C_0} (1+\gamma) \left[u(t_n) - u(t_{n-1})\right] - \gamma \left[(A_{n-1}) - (A_{n-2})\right]. \end{aligned} \tag{2.24}$$

From Eq. (2.24), it is shown that every switching constant contains not only the effect from previous switching period but also the switching constant from the previous two periods. To simplify the equation, R_n is used to replace $A_n - A_{n-1}$, so that the equation becomes:

$$R_n = -\frac{\alpha}{C_0} (1+\gamma) \left[u(t_n) - u(t_{n-1})\right] - \gamma R_{n-1}, \tag{2.25}$$

which has the generalized form

$$R_n = -\frac{\alpha}{C_0}(1+\gamma)\sum_{k=-\infty}^{n}(-\gamma)^{n-k}\left[u(t_k)-u(t_{k-1})\right]. \tag{2.26}$$

Therefore, the switching constant A_N can be expressed as a double summation of the scaled displacement difference

$$\begin{aligned} A_n &= -\frac{\alpha}{C_0}(1+\gamma)\sum_{k=-\infty}^{n}(-\gamma)^{n-k}\left[u(t_k)-u(t_{k-1})\right]+A_{n-1},\\ A_N &= -\frac{\alpha}{C_0}(1+\gamma)\sum_{n=-\infty}^{N}\left(\sum_{k=-\infty}^{n}(-\gamma)^{n-k}\left[u(t_k)-u(t_{k-1})\right]\right) \end{aligned} \tag{2.27}$$

The switching constant at $t = t_n$ for the technique switching on an inductor can not be discussed only in one switching period (from t_{n-1} to t_n) like in the switching on short circuit technique; effects from previous periods due to the cumulative effect have to be considered. The piecewise constant function $\kappa(t)$ is then shown with a unit step function $\mathrm{H}(t-t_n)$ as

$$\kappa(t) = -\frac{\alpha}{C_0}(1+\gamma)\sum_{n=-\infty}^{\infty}\left[\left(\sum_{k=-\infty}^{n}(-\gamma)^{n-k}\left[u(t_k)-u(t_{k-1})\right]\right)\mathrm{H}(t-t_n)\right] \tag{2.28}$$

With the expression of $\kappa(t)$, the output voltage could be thus expressed as

$$V(t) = \frac{\alpha}{C_0}u(t) - \frac{\alpha}{C_0}(1+\gamma)\sum_{n=-\infty}^{\infty}\left[\left(\sum_{k=-\infty}^{n}(-\gamma)^{n-k}\left[u(t_k)-u(t_{k-1})\right]\right)\mathrm{H}(t-t_n)\right], \tag{2.29}$$

and the derivation of the voltage will introduce the Dirac comb function as

$$\begin{aligned} \dot{V}(t) &= \frac{\alpha}{C_0}\dot{u}(t)\\ &-\frac{\alpha}{C_0}(1+\gamma)\sum_{n=-\infty}^{\infty}\left[\left(\sum_{k=-\infty}^{n}(-\gamma)^{n-k}\left[u(t-(t_n-t_k))-u(t-(t_n-t_{k-1}))\right]\right)\delta(t-t_n)\right]. \end{aligned} \tag{2.30}$$

The voltage is sampled at a sampling time t_n with the expression of Dirac comb function. If $\gamma = 0$, only $n = k$ could lead non zero in the summation term and the derivation of voltage would share the same equation as previous case, periodic switching on a short circuit Eq. (2.17).

The rearrangement of this equation as Eq. (2.31) presents clearly that the current flowing out from the piezoelectric element $\alpha\dot{u}(t)$ is decomposed into the current flowing to the piezoelectric internal capacitance $C_0\dot{V}(t)$ and to the switch:

$$\begin{aligned}\alpha\dot{u}(t) &= C_0\dot{V}(t)\\ &+ (1+\gamma)\sum_{n=-\infty}^{\infty}\left[\left(\sum_{k=-\infty}^{n}(-\gamma)^{n-k}\left[\alpha u(t-(t_n-t_k)) - \alpha u(t-(t_n-t_{k-1}))\right]\right)\delta(t-t_n)\right].\end{aligned} \tag{2.31}$$

If the switch is assumed to be turned on periodically, it leads to a self-sampled voltage response and the switching instants t_n could be replaced by nT_s, where T_s is the switching period. The derivation of voltage with time would be:

$$\begin{aligned}\dot{V}(t) &= \frac{\alpha}{C_0}\dot{u}(t)\\ &- \frac{\alpha}{C_0}(1+\gamma)\sum_{n=-\infty}^{\infty}\left[\left(\sum_{k=-\infty}^{n}(-\gamma)^{n-k}\left[u(t-(n-k)T_s) - u(t-(n-k+1)T_s)\right]\right)\delta(t-nT_s)\right]\\ &= \frac{\alpha}{C_0}\dot{u}(t) - \frac{\alpha}{C_0}(1+\gamma)\sum_{n=-\infty}^{\infty}\left[\left(\sum_{k'=0}^{\infty}(-\gamma)^{k'}\left[u(t-k'T_s) - u(t-(k'+1)T_s)\right]\right)\delta(t-nT_s)\right].\end{aligned} \tag{2.32}$$

From the Fourier transform and considering a switching delay t_0, the voltage expression in frequency domain would be:

$$V(\omega) = \frac{\alpha}{C_0}U(\omega) - \frac{\alpha}{C_0}(1+\gamma)\frac{1}{j\omega}\frac{1}{T_s}\sum_{n=-\infty}^{\infty}\left(U(\omega - n\frac{2\pi}{T_s})\left(1-e^{-jT_s\omega}\right)e^{-jn\frac{2\pi}{T_s}t_0}\sum_{k=0}^{\infty}(-\gamma)^k e^{-jkT_s\omega}\right). \tag{2.33}$$

The internal summation $\sum\limits_{k=0}^{\infty} a^k$ could be considered as a summation of geometric series; for $-1 < a < 1$, the sum converges as $\frac{1}{1-a}$:

$$\sum_{k=0}^{\infty}(-\gamma)^k e^{-kT_sj\omega} = \frac{1}{(1+\gamma e^{-T_sj\omega})}, \tag{2.34}$$

and the voltage in the frequency domain could be simplified as:

$$V(\omega) = \frac{\alpha}{C_0}U(\omega) - \frac{\alpha}{C_0}(1+\gamma)\frac{1}{j\omega}\frac{1}{T_s}\left(\frac{1}{1+\gamma e^{-jT_s\omega}}\right)\left(1-e^{-jT_s\omega}\right)\sum_{n=-\infty}^{\infty}\left(U(\omega - n\frac{2\pi}{T_s})e^{-jn\frac{2\pi}{T_s}t_0}\right). \tag{2.35}$$

When $\gamma = 0$, it corresponds to the switching on short circuit case as Eq. (2.19) shows.

2.2.2 Periodic Switch Harvesting (PSH) Techniques

In this subsection, a resistive load is connected in parallel with the piezoelectric transducer and the switching interfaces shown in Figure 2.3(a) to harvest the extracted en-

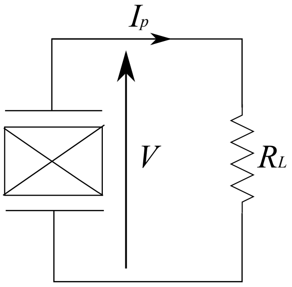

Figure 2.7: Standard piezoelectric harvester interface

ergy from the structure. For synchronized switch harvesting techniques, the broadband modeling is not so instinct as the previous cases. We could start with the standard (or classic) interface having no switching circuit to explain the basic concept of harvesting systems. Then the simplest nonlinear harvesting technique, periodic switch harvesting on short circuit (PSHS) will be presented and the interface with an inductor connected in series with the switching device (PSHI) would be introduced after.

The standard (or classic) energy harvesting technique simply consists of connecting a resistive load with the piezoelectric transducer (Figure 2.7). For standard technique, the piezoelectric equation could be written as a linear nonhomogeneous ordinary differential equation (ODE), which is the rearrangement of the piezoelectric equation (2.3):

$$I(t) = \alpha\dot{u}(t) - C_0\dot{V}(t) \tag{2.36}$$

$$\dot{V}(t) + \frac{1}{R_L C_0}V(t) = \frac{\alpha}{C_0}\dot{u}(t). \tag{2.37}$$

This ODE could be solved by Laplace transform with initial conditions $V(0) = 0$ and $u(0) = 0$ as Eq. (2.38).

$$V(s) = \frac{\alpha}{C_0}sU(s)\left[\left(\frac{1}{s+\frac{1}{R_L C_0}}\right)\right] \tag{2.38}$$

In the time domain, the solution is simply a homogeneous solution $h(t)$ convoluted with the nonhomogeneous term as Eq. (2.39):

$$\begin{aligned} V(t) &= \frac{\alpha}{C_0}\dot{u}(t) * e^{\frac{-t}{R_L C_0}}\mathrm{H}(t) \\ &= \dot{u}(t) * h(t), \end{aligned} \tag{2.39}$$

"*" denotes the convolution sign. Therefore the voltage response is seen as the system output with the system input $u(t)$ and the impulse response $h(t)$. The impulse response

$h(t)$ is a combination of a unit step function $\mathrm{H}(t)$ enforcing causality and an exponential decay in a factor $1/R_L C_0$ due to the resistive load.

$$h(t) = \frac{\alpha}{C_0} e^{-\frac{t}{R_L C_0}} \mathrm{H}(t) \tag{2.40}$$

2.2.2.1 Periodic Switch Harvesting on Short Circuit (PSHS) Technique

Connecting a switching device in parallel with the standard interface would induce a pulsed current I_s flowing to the switching branch when the switch is closed and the sum of the current in the network is expressed as:

$$I(t) = \alpha \dot{u}(t) - C_0 \dot{V}(t) - I_s(t). \tag{2.41}$$

The rearrangement of this equation leads the nonhomogeneous ODE as :

$$\dot{V}(t) + \frac{V(t)}{R_L C_0} = \frac{\alpha}{C_0} \dot{u}(t) - \frac{I_s(t)}{C_0}. \tag{2.42}$$

Taking the same procedure as for standard technique, the voltage expression for PSHS techniques would be:

$$V(t) = \dot{u}(t) * h(t) - \frac{I_s(t)}{C_0} * \frac{C_0}{\alpha} h(t), \tag{2.43}$$

which could be seen as a combination of the scaled source current and the scaled switching current convoluted with the effect of resistive load.

The derivation of the voltage response is acquired based on the differentiation property of the convolution $((f * g)' = f' * g = g' * f)$ as:

$$\dot{V}(t) = \dot{u}(t) * \dot{h}(t) - \frac{I_s(t)}{C_0} * \frac{C_0}{\alpha} \dot{h}(t). \tag{2.44}$$

The second term in Eq. (2.44) resulting from the switching event can be expressed as the self sampling of open-circuit voltage as shown in Section Section 2.2.1.1. However, the open-circuit voltage would be changed as a convolution with the magnitude of the impulse response $h(t)$ when connecting a resistive load. In addition, for energy harvesting interface, the function imposed by switching process $\kappa(t)$ describing the step response would no longer be a piecewise constant function but itself times an exponential decay caused by the resistive load. With reference to Eq. (2.17) in Section 2.2.1.1, the normalized current on the switch device $\tilde{I}_s$ is derived as:

$$\begin{aligned}\tilde{I}_s(t) &= \frac{I_s(t)}{C_0} \\ &= \left[\sum_{n=-\infty}^{\infty}\left([\dot{u}*h]_t - [\dot{u}*h]_{t-T_s} e^{-\frac{T_s}{R_L C_0}}\right)\delta\left(t-nT_s\right)\right] * \frac{C_0}{\alpha}\dot{h},\end{aligned} \tag{2.45}$$

and the general form of voltage derivation for PSHS technique would be denoted as:

$$\dot{V}(t) = \left[\dot{u}*\dot{h}\right]_t - \left[\sum_{n=-\infty}^{\infty}\left([\dot{u}*h]_t - [\dot{u}*h]_{t-T_s} e^{-\frac{T_s}{R_L C_0}}\right)\delta\left(t-nT_s\right)\right] * \frac{C_0}{\alpha}\dot{h}. \tag{2.46}$$

The equation stated above can be explained by Figure 2.8 as an good example. For energy harvesting case, the function $k(t)$ induced by the switching process is no longer a piecewise constant function but a piecewise exponentially decayed function. The switching constant at the switching instant t_n could still be considered as the difference between two open-circuit voltages (one at the switching instant t_n and another at the previous switching instant t_{n-1}). Nevertheless, for the energy harvesting technique, the switching constant is no longer a constant value after turning off the switch but with an exponential decay with a factor $e^{-\frac{T_s}{R_L C_0}}$. Here, because the switch is on a short circuit (the initial condition of voltage turns to be zero), the switching constant depends on the resistive effect only within one switching period T_s. In the frequency domain and considering the switching delay t_0, the voltage expression would be:

$$\begin{aligned}V(\omega) &= [j\omega U(\omega)h(\omega)] \\ &\quad - \frac{C_0}{\alpha}\left[h(\omega)\frac{1}{T_s}\sum_{n=-\infty}^{\infty}\left[\left([j\omega U(\omega)h(\omega)]\left(1-e^{-j\omega T_s}e^{-\frac{T_s}{RC_0}}\right)\right) * \delta\left(\omega-\frac{n2\pi}{T_s}\right)e^{-jn\frac{2\pi}{T_s}t_0}\right]\right]\end{aligned} \tag{2.47}$$

$$\begin{aligned}&= j\omega U(\omega)h(\omega) - j\frac{C_0}{\alpha}h(\omega)\frac{1}{T_s} \\ &\quad \times \sum_{n=-\infty}^{\infty}\left[\left(\omega-\frac{n2\pi}{T_s}\right)U(\omega-\frac{n2\pi}{T_s})h(\omega-\frac{n2\pi}{T_s})\left(1-e^{-j\left(\omega-\frac{n2\pi}{T_s}\right)T_s}e^{-\frac{T_s}{R_L C_0}}\right)e^{-jn\frac{2\pi}{T_s}t_0}\right].\end{aligned} \tag{2.48}$$

2.2.2.2 Periodic Switch Harvesting on Inductor (PSHI) Technique

With an inductor connected with the switch device, when the switch is closed, a $L-C_0$ oscillator forms. During the switching time t_i, the current flows from the piezo-internal capacitance C_0 to the inductor L. The voltage across the capacitance C_0 consequently

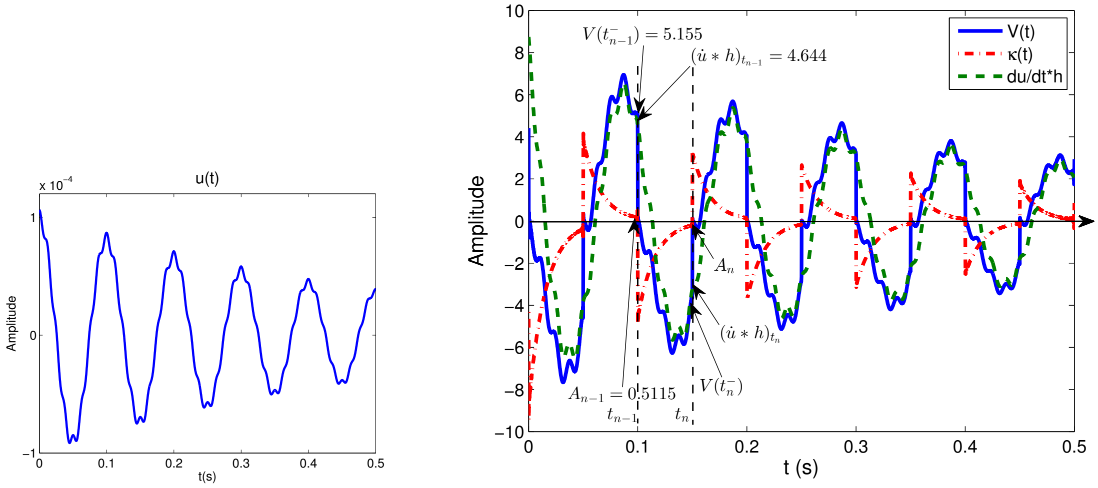

(a) (b)

Figure 2.8: An example shows the relationship of u, V and K_n at switching instant for periodic switch harvesting on short circuit technique: (a) excitation displacement; (b) corresponding waveforms

changes to $-\gamma V$. Before the next half pseudo-period starts, the switch was turned off in order to hold the voltage value as a start point for next switching period. Every switching period starts from the inverted voltage of previous switching period and this inverted voltage depends on its previous switching period; for example, the n^{th} switching period starts from $-\gamma V(t_{n-1})$, however, $V(t_{n-1})$ changes with $V(t_{n-2})$ etc.. Accordingly, the voltage at the switching instant t_n depends not only on the voltage at previous switching instant t_{n-1} but also on the voltage before the previous switching as a cumulative response, which shares the same feature as the periodic switching on inductor case Eq. (2.31). Taking the same procedure as for PSHS technique and with the reference to Eq. (2.32), the scaled current on the switch branch is derived as:

$$\tilde{I}_s = -(1+\gamma) \sum_{n=-\infty}^{\infty} \left[\sum_{k'=0}^{\infty} (-\gamma)^{k'} \left([(\dot{u} * h)]_{t-k'T_s} e^{-\frac{k'T_s}{R_L C_0}} - [(\dot{u} * h)]_{t-(k'+1)T_s} e^{-\frac{(k'+1)T_s}{R_L C_0}} \right) \delta(t - nT_s) \right]. \tag{2.49}$$

When $\gamma = 0$, it shares the same equation as PSHS technique Eq. (2.45). It can also be seen as a cumulative response as the starting voltage value of each switching event depending on the inverted voltage of the previous switching event. However, for the energy harvesting interface, the starting voltage value of each switching is a convolution with $h(t)$. In addition, as the system is connected to a resistive load, the function induced by the switching process is no longer a step response but an exponential decay. Inserting Eq. (2.49) into Eq. (2.43) and taking the Fourier transform of the voltage time-domain derivative, the general expression for the voltage response in the frequency domain considering the switching delay t_0 can be obtained as:

$$\begin{aligned} V(\omega) &= j\omega U(\omega)h(\omega) \\ &-j(1+\gamma)\frac{C_0}{\alpha}\frac{1}{T_s}\frac{\left(1-e^{-T_s j\omega}e^{-\frac{T_s}{R_L C_0}}\right)}{\left(1+\gamma e^{-T_s j\omega}e^{-\frac{T_s}{R_L C_0}}\right)}h(\omega)\left[\sum_{n=-\infty}^{\infty}\left[\left(\omega-\frac{n2\pi}{T_s}\right)U(\omega-\frac{n2\pi}{T_s})h(\omega-\frac{n2\pi}{T_s})\right]e^{-jn\frac{2\pi}{T_s}t_0}\right], \end{aligned} \tag{2.50}$$

which directly gives the voltage as a function of given displacement with harvesting process. The self-aliasing effect is clearly shown in the summation term.

2.3 Broadband Modeling under Force or Acceleration Excitations

In the previous section, the piezoelectric device is modeled as a current source in parallel with its internal capacitance C_0 and the current source is assumed to be independent with the external load impedance. However, the piezoelectric constitutive equation Eq. (2.3) shows a close relationship between the current source or voltage and the displacement. If the electromechanical system is excited near one of its resonance frequency, the displacement depends not only on the mechanical damping but also the electrical damping. The nonlinear interface and energy harvesting process would induce a backward coupling to the vibration system and thus modify the displacement magnitude [80]. In other words, from the mechanical point of view, the electrical energy extracted and harvested from the electromechanical system leads to a reduction of the mechanical energy and so of the vibration magnitude for a system excited with an imposed force or acceleration, especially for highly coupled, lightly damped structures with high product $k^2 Q_M$ of mechanical quality factor Q_M and coupling coefficient k [89]. Therefore, in order to have a more practical modeling, the case of force input instead of imposed displacement will be precisely introduced in this section. The force can be expressed with the acceleration a and the lumped mass of the system M as $F = Ma$.

2.3.1 Periodic Switch Harvesting on Inductor (PSHI) Technique

In frequency domain, the equation of motion between the input force F and the reacted forces could be described as:

$$\left(-M\omega^2 + jC\omega + K_E\right) U(\omega) = F(\omega) - \alpha V(\omega). \tag{2.51}$$

By substituting the voltage expression obtaineds from Section 2.2.2.2 (Eq. (2.50)) into the Fourier transform of the equation of motion Eq. (2.51), we get

$$\lambda(\omega)^{-1}U(\omega) - F(\omega) = \eta\left(\omega\right)\sum_{n=-\infty}^{\infty}\left(\omega - n\frac{2\pi}{T_s}\right)U\left(\omega - n\frac{2\pi}{T_s}\right)h\left(\omega - n\frac{2\pi}{T_s}\right)e^{j\left(\omega - n\frac{2\pi}{T_s}\right)t_0}, \tag{2.52}$$

where

$$\eta(\omega) = j\frac{(1+\gamma)\left(1 - e^{-T_s j\omega}e^{-\frac{T_s}{RC_0}}\right)}{\left(1 + \gamma e^{-T_s j\omega}e^{-\frac{T_s}{RC_0}}\right)}\frac{e^{-j\omega t_0}C_0}{T_s}h(\omega) \tag{2.53}$$

and

$$\lambda\left(\omega\right) = \frac{1}{-M\omega^2 + jC\omega + K_E + j\omega\alpha h(\omega)}. \tag{2.54}$$

It can be observed that the self-aliasing term, i.e. the summation in Eq. (2.52), is invariant under shifts by the angular switching frequency $\omega_s = 2\pi/T_s$. This is seen by evaluating the sum at $\omega - k\omega_s$ followed by a subsequent shift of summation variable $n \to n' = n + k$:

$$\begin{aligned}&\frac{U(\omega - k\frac{2\pi}{T_s})}{\lambda\left(\omega - k\frac{2\pi}{T_s}\right)} - F(\omega - k\frac{2\pi}{T_s})\\&= \eta(\omega - k\frac{2\pi}{T_s})\sum_{n'=-\infty}^{\infty}\left[\left(\omega - n'\frac{2\pi}{T_s}\right)U(\omega - n'\frac{2\pi}{T_s})h(\omega - n'\frac{2\pi}{T_s})e^{j\left(\omega - n'\frac{2\pi}{T_s}\right)t_0}\right].\end{aligned} \tag{2.55}$$

Taking Eq. (2.52) and the corresponding equation for $\omega \to \omega - k\omega_s$, it is possible to eliminate the self-aliasing term to obtain the frequency-shifted displacement $U(\omega - k\omega_s)$ given by

$$U(\omega - k\frac{2\pi}{T_s}) = \lambda\left(\omega - k\frac{2\pi}{T_s}\right)F\left(\omega - k\frac{2\pi}{T_s}\right) + \frac{\left[\lambda(\omega)^{-1}U(\omega) - F\left(\omega\right)\right]e^{j\omega t_0}}{h(\omega)}\beta\left(\omega - k\frac{2\pi}{T_s}\right), \tag{2.56}$$

where

$$\beta\left(\omega\right) = h\left(\omega\right)e^{-j\omega t_0}\lambda\left(\omega\right). \tag{2.57}$$

By substituting Eq. (2.56) back into the self-aliasing term, the summation term can be expressed as:

$$\begin{aligned}\sum_{k=-\infty}^{\infty}&\left[\left(\omega-k\frac{2\pi}{T_s}\right)U\left(\omega-k\frac{2\pi}{T_s}\right)h\left(\omega-k\frac{2\pi}{T_s}\right)e^{j\left(\omega-k\frac{2\pi}{T_s}\right)t_0}\right]\\ &=S_F(\omega)+\left[\lambda(\omega)^{-1}U(\omega)-F(\omega)\right]S_h(\omega),\end{aligned}\tag{2.58}$$

where

$$S_F\left(\omega\right)=\sum_{n=-\infty}^{\infty}\left[\left(\omega-n\frac{2\pi}{T_s}\right)\lambda\left(\omega-n\frac{2\pi}{T_s}\right)F\left(\omega-n\frac{2\pi}{T_s}\right)h\left(\omega-n\frac{2\pi}{T_s}\right)e^{j\left(\omega-n\frac{2\pi}{T_s}\right)t_0}\right],\tag{2.59}$$

$$S_h\left(\omega\right)=\frac{e^{j\omega t_0}}{h(\omega)}\sum_{n=-\infty}^{\infty}\left[\left(\omega-n\frac{2\pi}{T_s}\right)\beta\left(\omega-n\frac{2\pi}{T_s}\right)h\left(\omega-n\frac{2\pi}{T_s}\right)e^{j\left(\omega-n\frac{2\pi}{T_s}\right)t_0}\right],\tag{2.60}$$

and the displacement response in frequency domain $U(\omega)$ can be expressed completely in terms of known quantities as

$$\begin{aligned}U(\omega)&=\lambda(\omega)F(\omega)+\frac{\eta(\omega)\lambda(\omega)S_F(\omega)}{1-\eta(\omega)S_h(\omega)}\\ &=U_1(\omega)+U_2(\omega).\end{aligned}\tag{2.61}$$

The displacement of a piezoelectric harvester with periodic-switching interface under an arbitrary force excitation is thus splitted into two parts. The first part (U_1) shows the effect of constant driving force magnitude with a classical energy harvesting interface (simply connecting a piezoelectric transducer to the resistive load) [81]. The second part (U_2) represents the effect of the switching process with the self-sampling and self-aliasing effects.

The average harvested power P can be expressed as the harvested energy over a vibration period T_v by Parseval's theorem with the output voltage $V(\omega)$ expressed in frequency domain and its complex conjugate $V^*(\omega)$ over the resistive load R_L, where the voltage response is a function of the displacement response $U(\omega)$:

$$P=\frac{1}{T_v}\frac{1}{2\pi}\int_{-\infty}^{\infty}\frac{V(\omega)V^*(\omega)}{R_L}d\omega\tag{2.62}$$

with:

$$V(\omega) = j\omega U(\omega)h(\omega) - \frac{\eta(\omega)}{\alpha}\sum_{n=-\infty}^{\infty}\left[\left(\omega - n\frac{2\pi}{T_s}\right)U\left(\omega - n\frac{2\pi}{T_s}\right)h\left(\omega - n\frac{2\pi}{T_s}\right)e^{j\left(\omega - n\frac{2\pi}{T_s}\right)t_0}\right], \tag{2.63}$$

where

$$\eta(\omega) = j\frac{(1+\gamma)\left(1 - e^{-T_s j\omega}e^{-\frac{T_s}{RC_0}}\right)}{\left(1 + \gamma e^{-T_s j\omega}e^{-\frac{T_s}{RC_0}}\right)}\frac{e^{-j\omega t_0}C_0}{T_s}h(\omega). \tag{2.64}$$

2.4 Case Study

In the previous section, the broadband modeling has been derived step by step in the frequency domain. In this section, the broadband modeling will be applied under several well-known excitation signals including both broadband and narrowband types to validate the approach. The electromechanical structure with a constant magnitude monochromatic vibration without considering the backward coupling from the harvesting process will be presented first as an introductory work. Then the constant magnitude cosine force input and impulse response considering no backward coupling effect will been discussed for periodic switching energy harvesting techniques. In order to harvest energy, a resistive load is connected with the nonlinear technique and the switch is turned on at an angular frequency ω_s depending on the input and the structural response in order to have a constructive interference effect. The broadband modeling is simplified for each excitation cases and we call this simplified model as the theoretical analysis. In the final subsection, a random force input case will be examined. In order to present the effectiveness of the broadband modeling, the system response (displacement and voltage), obtained in frequency domain through iterative computation using (Eq. (2.50) when no damping effect is considered and (Eqs. (2.50) and (2.61)) for force or acceleration excitations, will be compared with results calculated in time-domain with recursive numerical method based on Euler algorithm. For both time-domain and frequency-domain analysis, Matlab software with home-made scripts were used.

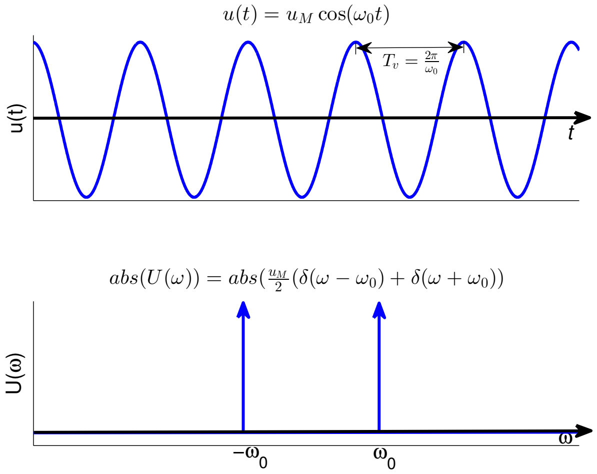

Figure 2.9: Waveform of cosine excitation in time and frequency domain

2.4.1 Case 1: Monochromatic Displacement Excitation Considering no Backward Coupling Effect

A sine or cosine response is usually used as the simplest case to describe an excitation when analyzing vibration problems although in practical, most of waves contain more than a single frequency.

The two-sided Fourier transform of a cosine signal vibrating at an angular frequency ω_0 would be a combination of two Dirac delta functions at the positive and negative angular frequencies $\pm\omega_0$. A cosine displacement excitation with an angular frequency ω_0 and the amplitude u_M shown in Eq. (2.65) would have the double-sided frequency response described as:

$$u(t) = u_M \cos(\omega_0 t) \tag{2.65}$$

$$U(\omega) = \frac{u_M}{2}\left[\delta(\omega-\omega_0)+\delta(\omega+\omega_0)\right], \tag{2.66}$$

and the waveform of cosine excitation in the time and frequency domains are shown in Figure 2.9.

According to the sampling theorem, the switching process in nonlinear interfaces could be considered as a self-sampling process on response itself with the sampling period T_s (or equivalently a sampling frequency ω_s). Therefore, to have an optimal voltage response, the switching frequency is chosen to be twice the excitation frequency ω_0 considering the aliasing effect in this case, which leads a constructive interference under a proper switching delay. The self-aliased voltage response is described in Figure

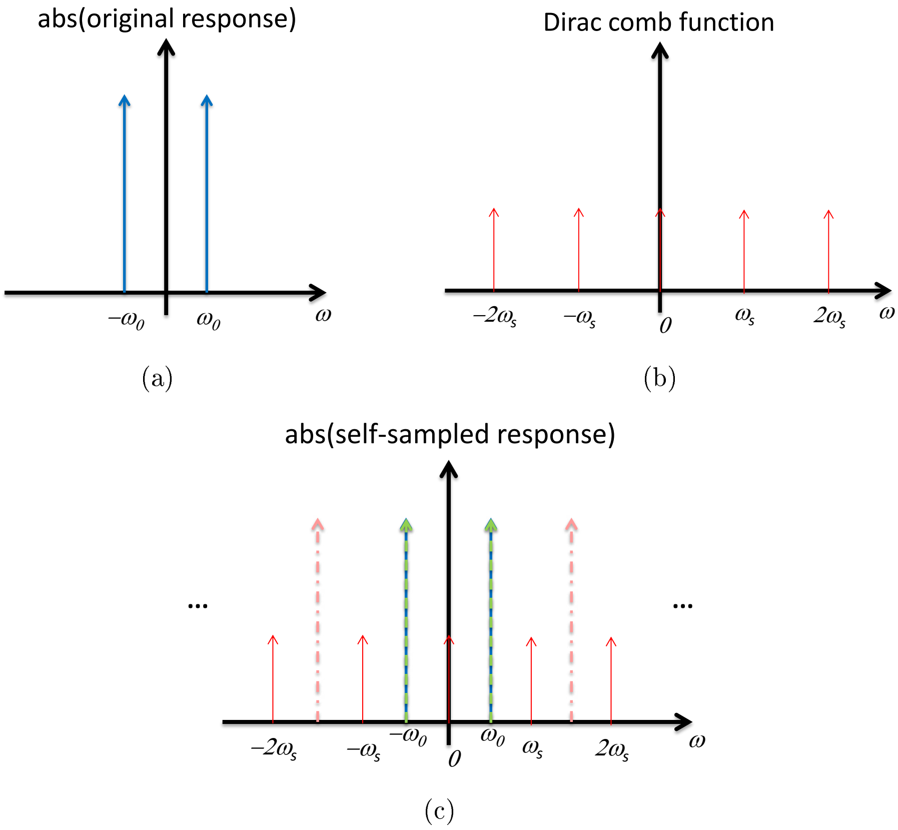

Figure 2.10: Description of self-sampling procedure under constant magnitude cosine displacement input: (a) spectrum of original function; (b) spectrum of the sampling function; (c) spectrum of the sampled function with sampling frequency $\omega_s = 2\omega_0$; dashed lines represent sampled responses

2.10. Under the self-sampling process (or switching process), the frequency response of cosine function would be doubled thanks to the aliasing effect (the repeated copies are totally overlapped with each other) as the switching frequency is chosen to be twice the excitation frequency ω_0 and with a proper phase.

The voltage response for PSHI technique could be referenced from Section 2.2.2.2 as:

$$\begin{aligned} &V(\omega) = j\omega U(\omega)h(\omega) \\ &-j(1+\gamma)\frac{C_0}{\alpha}\frac{1}{T_s}\frac{\left(1-e^{-T_s j\omega}e^{-\frac{T_s}{R_L C_0}}\right)}{\left(1+\gamma e^{-T_s j\omega}e^{-\frac{T_s}{R_L C_0}}\right)}\left[h(\omega)\sum_{n=-\infty}^{\infty}\left[\left(\omega-\frac{n2\pi}{T_s}\right)U(\omega-\frac{n2\pi}{T_s})h(\omega-\frac{n2\pi}{T_s})\right]e^{-jn\frac{2\pi}{T_s}t_0}\right]. \end{aligned} \tag{2.67}$$

As the switching frequency is chosen to be $\omega_s = 2\omega_0$ to have a self-aliasing effect, the equivalent switching period $T_s = 2\pi/2\omega_0$ and the voltage at $\omega = \omega_0$ is therefore with the maximum amplitude and is expressed as:

$$\begin{aligned}V(\omega_0) = [j\omega_0 U(\omega_0)h(\omega_0)] - j(1+\gamma)\frac{C_0}{\alpha}\frac{\omega_0}{\pi}\frac{\left(1+e^{-\frac{\pi}{R\omega_0 C_0}}\right)}{\left(1-\gamma e^{-\frac{\pi}{R\omega_0 C_0}}\right)}h(\omega_0)\\ \times \sum_{n=-\infty}^{\infty}\left[(\omega_0-2n\omega_0)\,U(\omega_0-2n\omega_0)h(\omega_0-2n\omega_0)\right]e^{-jn2\omega_0 t_0}.\end{aligned} \tag{2.68}$$

The first term of Eq. (2.68) states that the non-switching voltage which is proportional to the displacement with a phase shift induced by the resistive load as using standard technique. The summation term could be taken as the effect of switching algorithm (self-sampling) on non-switching voltage. As the non-switching voltage is proportional to the displacement, it has nonzero value only at $\pm\omega_0$, which implies the summation terms are non zero only for $n=0$ and $n=1$. Accordingly, the response of voltage at ω_0 could be simplified as:

$$\begin{aligned}V(\omega_0) =& \frac{u_M}{2}j\omega_0 h(\omega_0)\\ &- j(1+\gamma)\frac{C_0}{\alpha}\frac{{\omega_0}^2}{\pi}\frac{\left(1+e^{-\frac{\pi}{R\omega_0 C_0}}\right)}{\left(1-\gamma e^{-\frac{\pi}{R\omega_0 C_0}}\right)}h(\omega_0)\frac{u_M}{2}\left[h(\omega_0)-h(-\omega_0)e^{-j2\omega_0 t_0}\right].\end{aligned} \tag{2.69}$$

Voltages at other frequencies can be obtained from the same procedure that the self-sampled voltage has nonzero response only at $\omega=(2k+1)\omega_0$ (k is real constant) or $\omega = m\omega_0$ as the original response (response that before switching process) has nonzero value only at $\pm\omega_0$, and the amplitude of self-sampled response decreases with the increase of frequency. Therefore, the overall voltage response could be seen as a combination of a series of the self-sampled response multiplied with a weighting function. In addition, as cosine is a real function in time-domain, only the positive frequency component is considered for the theoretical analysis, and the negative frequency component is the complex conjugate of the positive part. The voltage response at $m\omega_0$ for $m\neq\pm1$ is obtained by setting $n=(m-1)/2$ and $n=(m+1)/2$ to get the non-zero summation term:

$$\begin{aligned}V(m\omega_0) = -j(1+\gamma)\frac{C_0}{\alpha}\frac{{\omega_0}^2}{\pi}\frac{\left(1+e^{-\frac{\pi}{R\omega_0 C_0}}\right)}{\left(1-\gamma e^{-\frac{\pi}{R\omega_0 C_0}}\right)}h(m\omega_0)e^{-jm\omega_0 t_0}\\ \times\frac{u_M}{2}\left(h(\omega_0)e^{j\omega_0 t_0}-h(-\omega_0)e^{-j\omega_0 t_0}\right).\end{aligned} \tag{2.70}$$

The voltage expression for PSHI technique with a constant magnitude cosine vibration considering no backward coupling for weakly-coupled structure could be therefore

Table 2.1: Model parameters for the harvester with very low coupling coefficient

C_0	20 nF
α	0.0001 N/V
K_E	3000 Nm^{-1}
M	200 g
C	0.4 $Nm^{-1}s^{-1}$
Q_I	5.6
f_0	19.49 Hz
k^2	0.0164%
Q_M	61.24
k^2Q_M	0.0102

summarized as below:

$$V(\omega_0) = \frac{u_M}{2} j\omega_0 h(\omega_0) - j(1+\gamma)\frac{C_0}{\alpha}\frac{{\omega_0}^2}{\pi}\frac{\left(1+e^{-\frac{\pi}{R\omega_0 C_0}}\right)}{\left(1-\gamma e^{-\frac{\pi}{R\omega_0 C_0}}\right)} h(\omega_0)\frac{u_M}{2}\left[h(\omega_0) - h(-\omega_0)e^{-j2\omega_0 t_0}\right], \tag{2.71}$$

and when $m \neq \pm 1$:

$$V(m\omega_0) = -j(1+\gamma)\frac{u_M}{2}\frac{C_0}{\alpha}\frac{{\omega_0}^2}{\pi}\frac{\left(1+e^{-\frac{\pi}{R\omega_0 C_0}}\right)e^{-jm\omega_0 t_0}}{\left(1-\gamma e^{-\frac{\pi}{R\omega_0 C_0}}\right)} h(m\omega_0)\left(h(\omega_0)e^{j\omega_0 t_0} - h(-\omega_0)e^{-j\omega_0 t_0}\right),$$

otherwise, $V(\omega) = 0$. (2.72)

The numerical simulation based on the theoretical analysis (simplified model) and the general broadband modeling will be compared with the iterative numerical calculation based on the Euler algorithm in time-domain, which is called time-resolution. The harvester is modeled using a set of model parameters given in Table 2.1 under a constant magnitude cosine displacement excitation with the amplitude $u_M = 0.4$ mm. The parameters are taken from the literature [54] and with a slight modification consisting in decreasing the mechanical quality factor (Q_M=61.24), the force factor ($\alpha = 10^{-4}$) and the short-circuit stiffness ($K_E = 3000$ N/m) to reflect a weakly-coupled harvester system. The vibration frequency is taken as the same as the resonant frequency of harvester[1]. The frequency domain response from theoretical analysis and time-domain resolution is first compared in Figure 2.11(a) considering a 20% vibration period switching delay. Then the time domain response is presented in Figure 2.11(b) with the inverse Fourier transform of theoretical analysis results. The comparison in Figure 2.11 exposes the effectiveness of theoretical analysis as the simulation results

---

[1] The resonant frequency is between open-circuit and short-circuit frequency because of the resistive load, but the two values are very close.

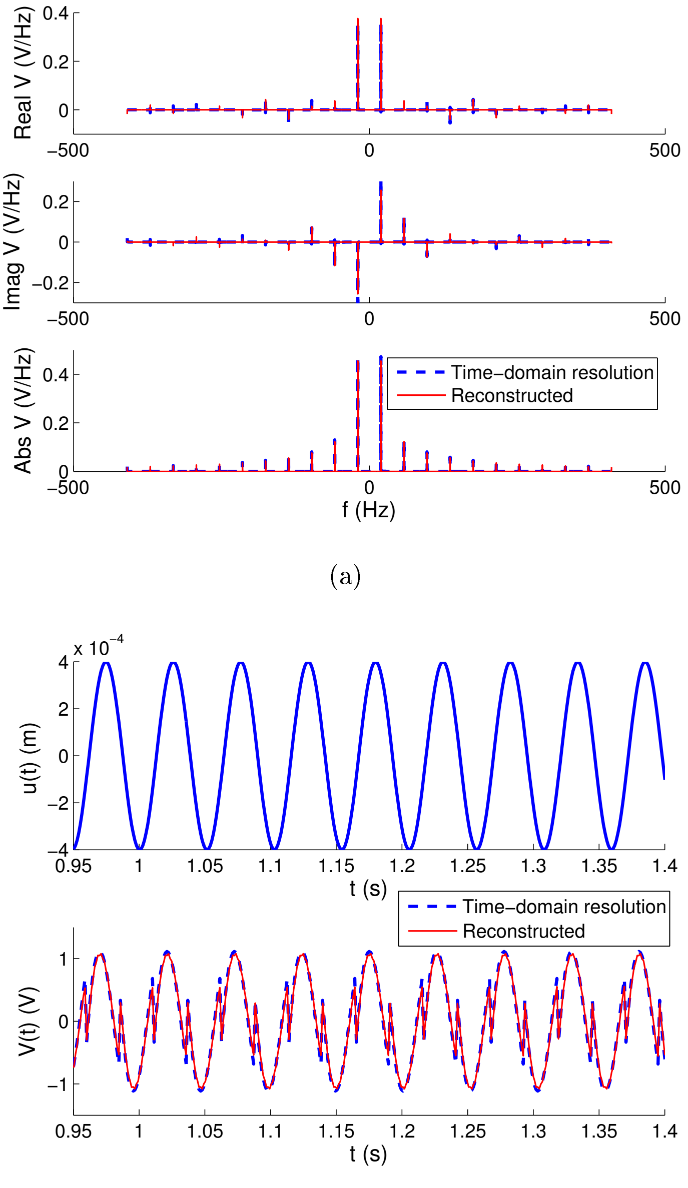

(a)

(b)

Figure 2.11: Simulation results for constant magnitude cosine displacement excitation based on theoretical analysis (in red plain line) and numerical time-domain resolution (in blue dashed line) with PSHI interface considering a 20% vibration period switching delay: (a) Frequency-domain comparison; (b) Time-domain comparison

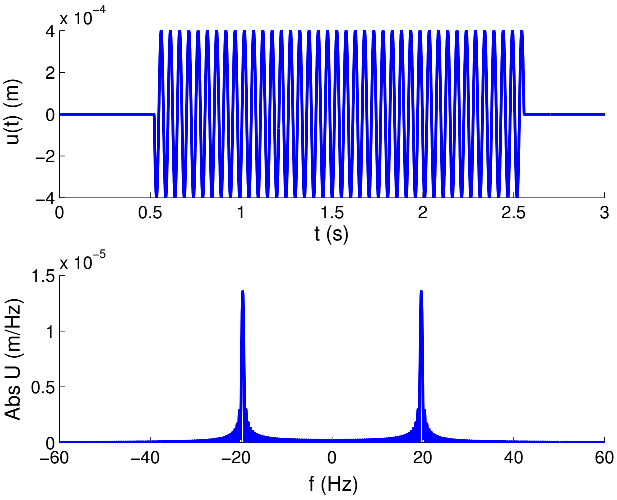

Figure 2.12: Input displacement with applied window function

match well with the time-domain resolution although only 10 harmonics ($k = 0 \sim 9$, the negative frequency components are the complex conjugate of the positive frequency components) are considered in this simulation.

The theoretical analysis presented above provides approximated results considering a limit number of frequency ranges. The numerical analysis based on the general broadband modeling offers another solution. The numerical calculation from general broadband modeling is also compared with the time-domain resolution in Figure 2.13. However, in this case, when doing the Inverse Discrete Fourier Transform (IDFT), an originally finite segment spreads in an infinite time range and so the waveform starts from minus infinity to infinity instead of its real starting point. In order to prevent this circumstance, a window function as shown in Figure 2.12 is applied with the excitation signal to prevent the artifacts in the spectrum (time-aliasing effect) and so that the displacement in frequency domain is a convolution of two Dirac delta functions with a Sinc function. The numerical calculation considers more harmonics, therefore, the inverse Fourier transform in time-domain would be smoother than it under the theoretical analysis but it takes a longer time to calculate. In addition, in both time-domain and frequency-domain, the simulation results from general broadband modeling match very well with the time-domain resolution, which proves the validity of broadband modeling. The average harvested power under different load resistances and different switching delays is obtained from theoretical analysis and shown in Figure 2.14. The average harvested power and the load resistance are normalized in relation to the critical optimized harvested power and optimal resistive load for the standard tech-

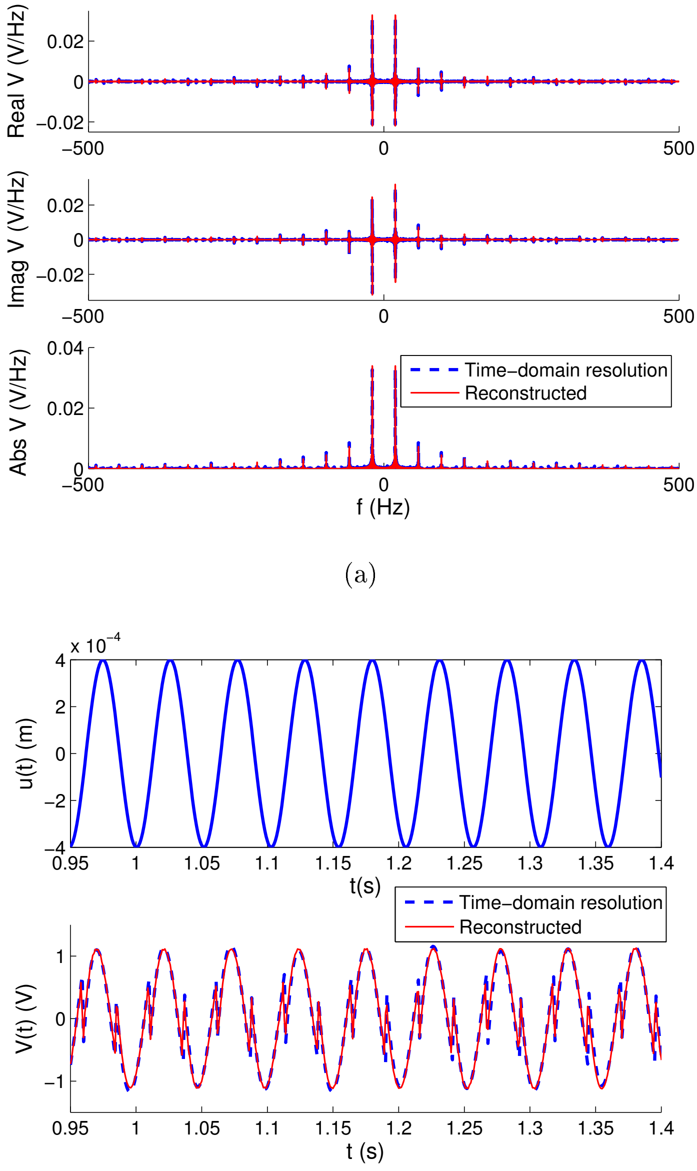

!h

(a)

(b)

Figure 2.13: Simulation results for constant magnitude cosine displacement excitation based on numerical broadband analysis (in red plain line) and numerical time-domain resolution (in blue dashed line) with PSHI interface considering a 20% vibration period switching delay: (a) frequency-domain comparison; (b) time-domain comparison

nique ($P_{max} = \frac{\alpha^2}{4C_0}\omega_0 u_M^2$, $R_{opt} = \frac{1}{\omega_0 C_0}$). It is shown that with the technique consisting in a periodic switching nonlinear circuit (or synchronized switching technique as here $\omega_s = 2\omega_0$) will improve the harvester performance 4.5 times more than using standard technique when there is no switching delay, which corresponds well with the work of Badel *et al* in [125] for a very weakly-coupled harvester with $k^2 \approx 10^{-4}$. From Figure 2.14(a), we could see that as the switching delay increases, the harvested power decreases as the phase between the vibration speed and voltage increases. In addition, when the switching delay increases, the optimized resistive load decreases, which is due to the voltage decrease with the increase of t_0; to have a higher harvested power, the resistance has to be smaller. For this case, a -5% to 5% switching delay would lead to a 20% decrease in harvested power, which states that within a specific range of switching delay, the decrease in harvested power is very small and could be neglected.

2.4.2 Case 2: Monochromatic Force Excitation with PSHI Interface

To take into account the backward damping effect introduced by the harvesting process, instead of having a constant magnitude displacement excitation, a constant magnitude force excitation is applied to the harvester. A constant magnitude (F_M) cosine force excitation $F(t) = F_M \cos(\omega_0(t - t_0))$ is common in the analysis of a piezoelectric harvester as it is very simple. The mass-spring-damper structure is tuned to have a resonance frequency at ω_0 to get the optimal vibration. For this excitation case, we choose the switching frequency as twice the vibration frequency, i.e. $\omega_s = 2\omega_0$ to have a self-aliasing effect that leads to a constructive response. The effect of a switching delay t_0 is also considered. With these assumptions, the force and its responses can be represented by complex Fourier series with ω_0 as the fundamental angular frequency. The force excitation has Fourier coefficients given by:

$$F(n\omega_0) = \frac{F_M}{2}\left[e^{-j\omega_0 t_0}\delta_{n,1} + e^{j\omega_0 t_0}\delta_{n,-1}\right], \tag{2.73}$$

where n denotes an integer.

Only the positive frequency component is considered for the theoretical analysis as here the signal is a real function of time and the negative frequency component is the complex conjugate of the positive part. The electromechanical system is seen to be filtered by a band-pass filter which is a narrow filter around the center frequency $f_c = f_0$ (or $\omega_c = \omega_0$) due to the natural characteristics of cantilever beam structures. Based on

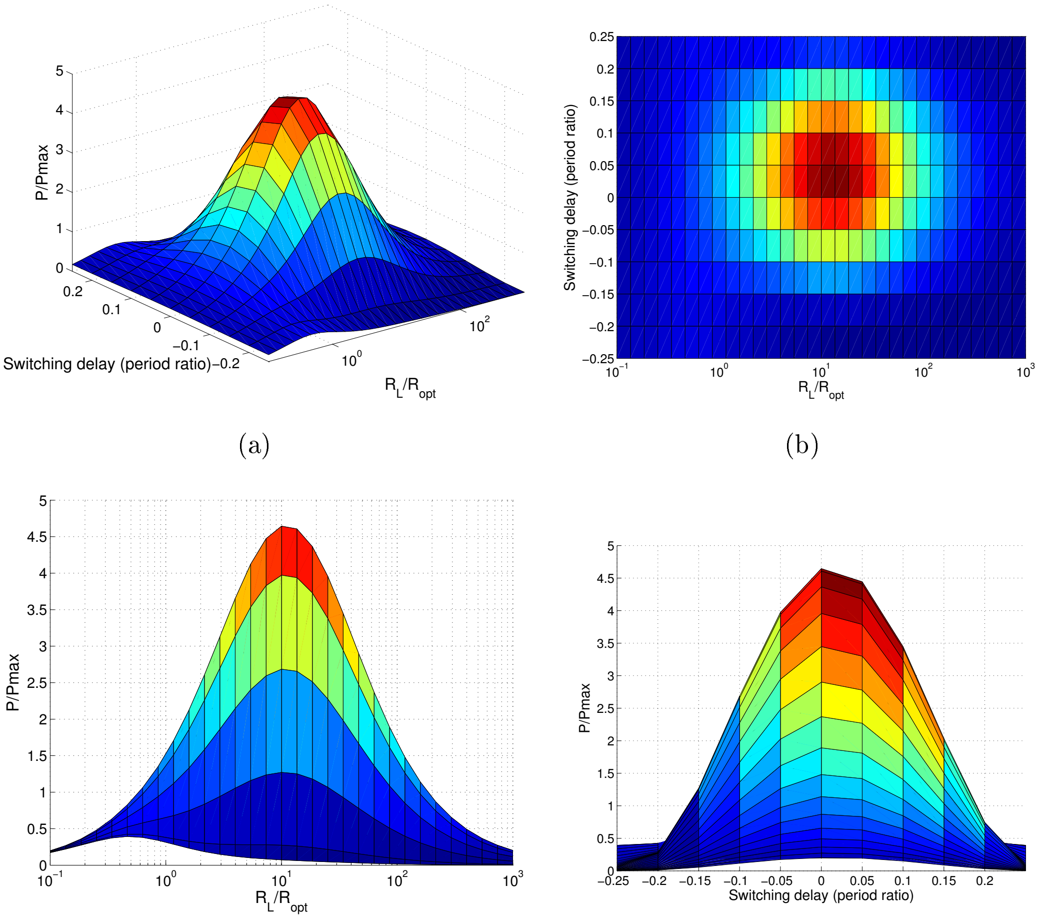

(a) (b)

(c) (d)

Figure 2.14: Normalized harvested power as a function of switching delay and resistance load under constant magnitude cosine displacement excitation with PSHI interface: (a) 3D view of normalized harvested power as a function of R/R_{opt} and switching delay (in the ratio of a period); (b) top view of normalized harvested power as a function of R_L/R_{opt} and switching delay (in the ratio of a period); (c) side view of normalized harvested power as a function of R_L/R_{opt}; (d) side view of normalized harvested power as a function of switching delay (in the ratio of a period)

the property of the cantilever beam structure and the cosine excitation function, the transfer function between host structure displacement and the excitation force could be approximated with the response at ω_0. From Eq. (2.61), the displacement response at $\omega = \omega_0$ when $m = 1$ is expressed as a function of the force $F(\omega_0) = F_M \exp(-j\omega_0 t_0)/2$ as

$$U(\omega_0) = \lambda(\omega_0)F(\omega_0) + \frac{\lambda(\omega_0)\eta(\omega_0)S_F(\omega_0)}{1-\eta(\omega_0)S_h(\omega_0)}. \tag{2.74}$$

To obtain a more accurate result, responses at other frequencies are considered as shown in the following paragraph. With a switching frequency equals to twice the vibration frequency, the response is self-sampled and self-aliased to have a constructive response for a properly chosen phase, and has nonzero components only at $\omega = (2k+1)\omega_0$, where k is an integer. The response of displacement at $\omega = (2k+1)\omega_0 = m\omega_0$ with $m \neq \pm 1$ is then given as

$$U(m\omega_0) = \frac{\lambda(m\omega_0)\eta(m\omega_0)S_F(m\omega_0)}{1-\eta(m\omega_0)S_h(m\omega_0)} \tag{2.75}$$

with

$$\eta\left(m\omega_0\right) = j\frac{(1+\gamma)}{\left(1-\gamma e^{-\frac{T_s}{RC_0}}\right)}\frac{C_0}{T_s}h(m\omega_0)e^{-jm\omega_0 t_0}\left(1+e^{-\frac{T_s}{RC_0}}\right), \tag{2.76}$$

$$S_F\left(m\omega_0\right) = \omega_0\lambda\left(\omega_0\right)F\left(\omega_0\right)h\left(\omega_0\right)e^{j\omega_0 t_0} - \omega_0\lambda\left(-\omega_0\right)F\left(-\omega_0\right)h\left(-\omega_0\right)e^{-j\omega_0 t_0}, \tag{2.77}$$

$$S_h\left(m\omega_0\right) \approx \frac{e^{jm\omega_0 t_0}}{h(m\omega_0)}\left[\omega_0\beta\left(\omega_0\right)h\left(\omega_0\right)e^{j\omega_0 t_0} - \omega_0\beta\left(-\omega_0\right)h\left(-\omega_0\right)e^{-j\omega_0 t_0}\right] \tag{2.78}$$

where S_F and S_h are simplified because $F(m\omega_0 - 2n\omega_0)$ has nonzero values only when $n = (m-1)/2$ and $n = (m+1)/2$. The voltage response at $\omega = (2k+1)\omega_0 = m\omega_0$ is then given as

$$V(m\omega_0) = jm\omega_0 U(m\omega_0)h(m\omega_0) - \frac{\eta(m\omega_0)}{\alpha}\left[\omega_0 U(\omega_0)h(\omega_0)e^{j\omega_0 t_0} - \omega_0 U(-\omega_0)h(-\omega_0)e^{-j\omega_0 t_0}\right]. \tag{2.79}$$

This expression of the voltage response in terms of its harmonics is new in the analysis of the switched power conversion techniques as all of the previous time-domain analysis consider only the first harmonic neglecting the effect from other ones.

Table 2.2: Model parameters for the harvester with moderate coupling coefficient

C_0	20 nF
α	0.001 N/V
K_E	3000 Nm^{-1}
M	200 g
C	0.2 $Nm^{-1}s^{-1}$
Q_I	5.6
f_0	19.49 Hz
k^2	1.64%
Q_M	122.475
k^2Q_M	2.009

When the switching frequency is approaching zero (switching period $T_s \to \infty$) and the switching delay takes the ideal value $t_0 = 0$, the voltage response at $\omega = \omega_0$ reduces to the expression for the standard interface [54]:

$$V(\omega_0) = j\omega_0 U(\omega_0) h(\omega_0) = j\omega_0 U(\omega_0) \frac{\alpha R_L}{1 + jR_L C_0 \omega_0}. \tag{2.80}$$

The simulation results under the theoretical analysis and the numerical calculation based on general broadband modeling will be compared with the numerical calculation of time-resolution. The set of model parameters listed in (Table 2.2) is used in the simulation. The parameters are taken from the literature [54] and with a slight modification consisting in decreasing the mechanical quality factor (Q_M=122.745) and the short-circuit stiffness (K_E = 3000 N/m) to reflect a more common case with a moderate coupling coefficient.

Frequency domain response from the simplified theoretical analysis and the numerical time-domain simulation are first compared in Figure 2.15(a) considering a 10% vibration period switching delay. Then the time domain response is presented in Figure 2.15(b) by the inverse Fourier transform of the theoretical analysis. In this case, 150 harmonics ($k = 0 \sim 149$) is taken to have a better time-domain resolution. The comparison in Figure 2.15 exposes the effectiveness of exposed approach as the simulation results match well with the numerical time-domain simulation, while being directly obtained (i.e. without iterative calculation). In addition, compared to previous works, in this work, the theoretical modeling consists in more frequency information than only the first harmonic. The numerical calculation from general broadband modeling is also compared with the numerical time-domain simulation in Figure 2.16. A window function is applied with the excitation signal to prevent the artifacts in the spectrum (time-aliasing effect). The numerical calculation in this case takes a very long time to calculate and the response is unstable, so that the inverse Fourier transform in

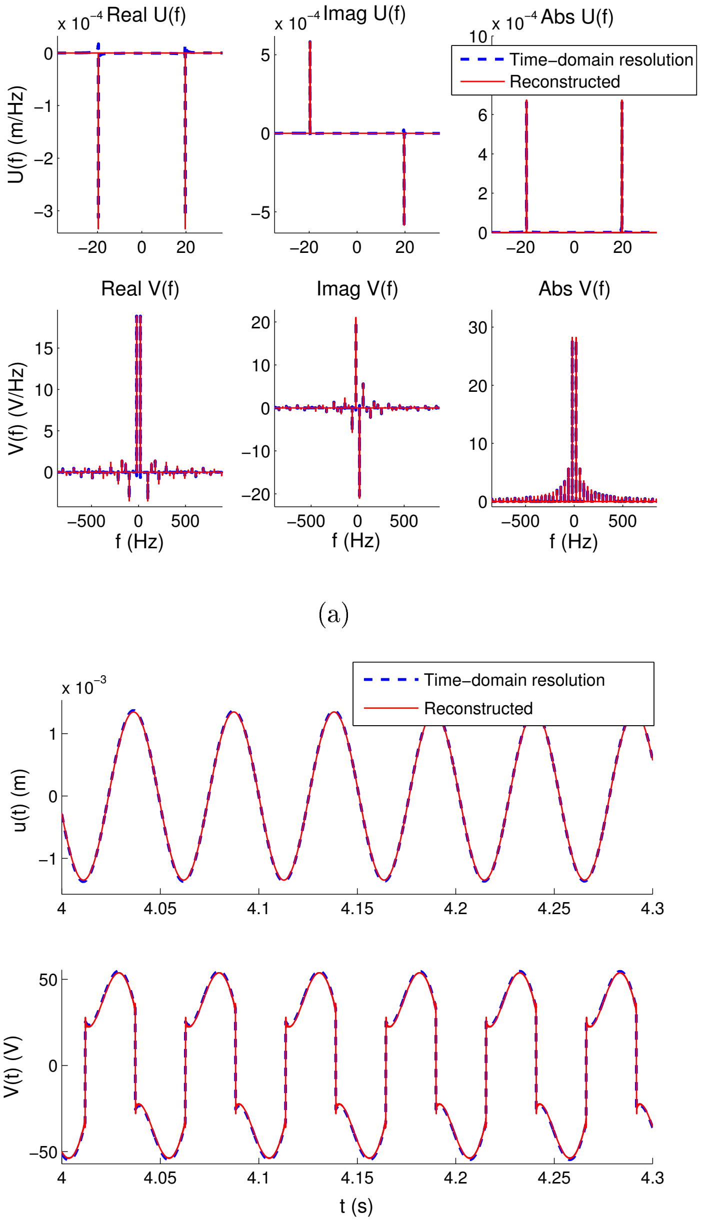

(a)

(b)

Figure 2.15: Simulation results for constant magnitude cosine force excitation based on theoretical analysis (in red plain line) and numerical time-domain resolution (in blue dashed line) with PSHI interface considering a 10% vibration period switching delay: (a) frequency-domain comparison; (b) time-domain comparison

time-domain is not perfectly matched with the time-domain resolution as there is a trade-off between frequency resolution and time resolution based on Heisenberg uncertainty principle. However, in both time and frequency domains, the simulation results from general broadband modeling are still proved to be effective as the waveforms match well with the time-resolution in a certain degree. The harvested power under different resistive load values and different switching delays is obtained from theoretical analysis and shown in Figure 2.17. The average harvested power and resistive load are normalized in relation to their critical value with standard interface [54]:

$$\begin{cases} R_{opt} = \frac{1}{\omega_0 C_0} \\ P_{limit} = \frac{F_M^2}{8C}. \end{cases} \tag{2.81}$$

The harvested power tends to the same power limit (Eq. (2.81)) no matter the connecting interfaces, and this power limit only depends on the mechanical losses in the structure. The harvested power can be optimized introducing a slight switching delay and the improvement, however, would not exceed a few percent. In fact, this result indicates that especially in the case of energy harvesting, a small switching delay is not harmful and may even slightly improved energy harvesting, as has already been shown in [126]. In addition, when the switching delay increases, the optimized resistive load decreases. Because when t_0 increases, the voltage decreases; to have a higher harvested power, the resistance tends to be smaller. With a proper switching instant, the harvested power approaches to the power limit as the electromechanical coupling coefficient $k^2 \approx 10^{-2}$. The harvested power as a function of resistive load (Figure 2.18) also corresponds well with previous works [54].

2.4.3 Case 3: Impulse Response Considering no Backward Damping Effect

In the previous two sections, the cosine excitation has been introduced with PSHI interface considering that the energy is constantly supplied to the electromechanical structure. Although a monochromatic excitation is simple and acts as a very good example for analyzing a piezoelectric harvester, it is not practical when a real application is considered. A more practical excitation would spread in more than one frequency. In this subsection, an impulse response with no backward coupling effect from the connected circuit for lightly damped and weakly coupled structure will be presented.

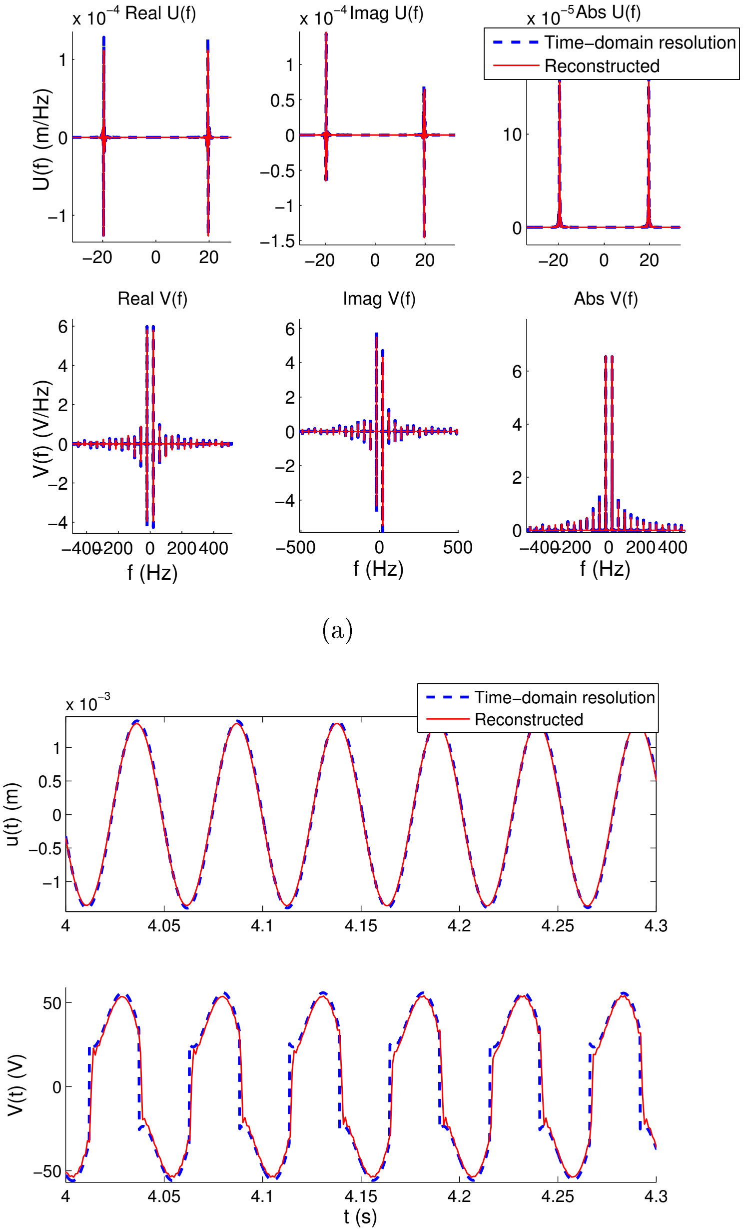

(a)

(b)

Figure 2.16: Simulation results for constant magnitude cosine force excitation based on numerical broadband analysis (in red plain line) and numerical time-domain resolution (in blue dashed line) with PSHI interface considering a 10% vibration period switching delay: (a) frequency-domain comparison; (b) time-domain comparison

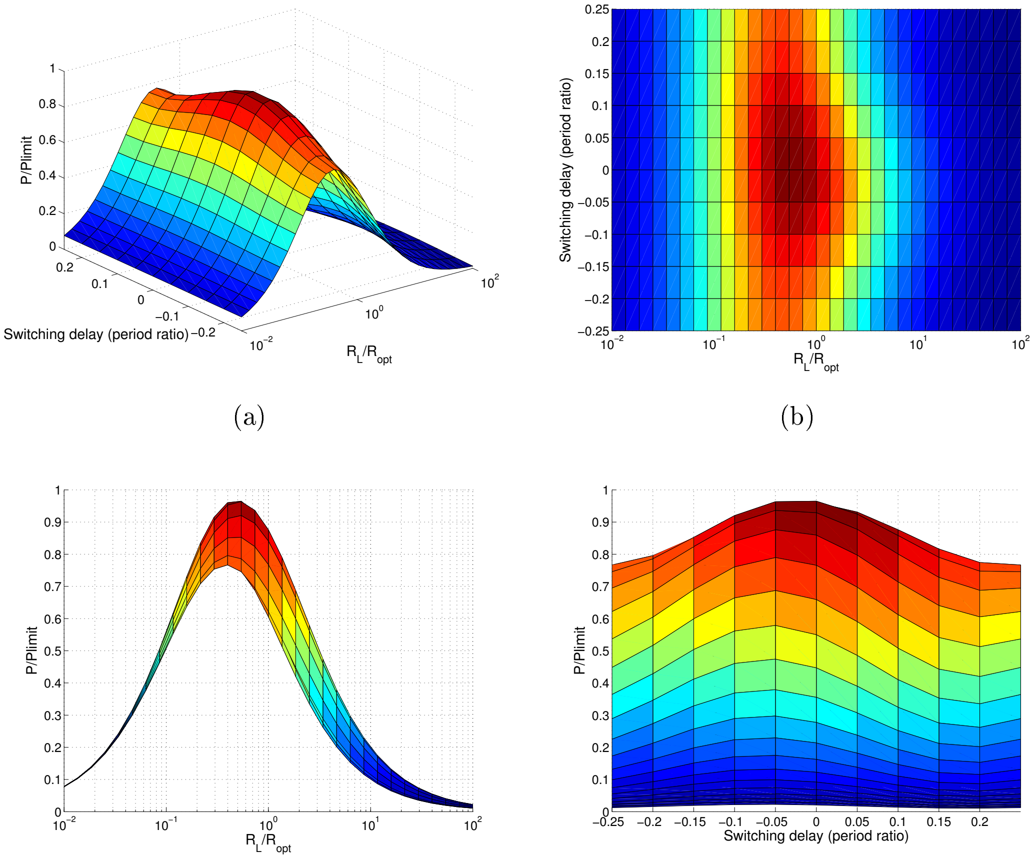

(a) (b)

(c) (d)

Figure 2.17: Normalized harvested power as a function of switching delay and resistance load under constant magnitude cosine force excitation with PSHI interface: (a) 3D view of normalized harvested power as a function of R/R_{opt} and switching delay (in the ratio of a period); (b) Top view of normalized harvested power as a function of R_L/R_{opt} and switching delay (in the ratio of a period); (c) Side view of normalized harvested power as a function of R_L/R_{opt}; (d) Side view of normalized harvested power as a function of switching delay (in the ratio of a period)

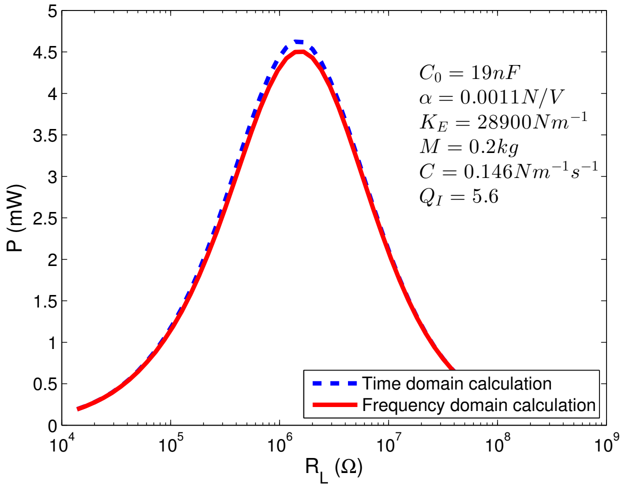

Figure 2.18: Harvested energy versus the resistive load using the experimental data

An imposed pulsed force with impulse F_M is applied to the host structure at $t = t_p$ (Eq. (2.82)). The pulsed force is approximated by a Dirac delta function as it is applied to the system for an extremely short period; in frequency domain, it spreads in a wider band,

$$\begin{cases} F(t) = F_M \delta(t - t_p) \\ F(\omega) = F_M e^{-j\omega t_p}. \end{cases} \tag{2.82}$$

For a weakly-coupled or highly damped structures, the backward coupling which induces a damping effect to the host structure could be neglected as it is very small compared to the structural damping. The self-sampled impulse response under different sampling frequencies for an impulsed response could be explained by Figure 2.19. Figure 2.19(c) and 2.19(d) shows the different results for two sampling frequency, one permits that $\omega_s > 2\omega_0$ and another one is when $\omega_s = 2\omega_0$. When the sampling frequency it taken as twice the frequency when having maximal response, ω_0, the self-sampled response would have self-aliasing effect and have a constructive response. The Fourier transform of a Dirac delta function would be everywhere unit amplitude in the frequency domain. However, due to the natural characteristic of host structure consisting of the structural resonant frequency ω_0, the electromechanical system is seen as being filtered by a band-pass filter with $\omega = \omega_0$. Accordingly, the switching frequency could be chosen to be twice the resonant frequency of host structure $\omega_s = 2\omega_0$. Under the switching process, the response is seen as self-sampled with a sampling frequency $2\omega_0$. From the response of forced damped vibration (Figure 2.20), we know that if the

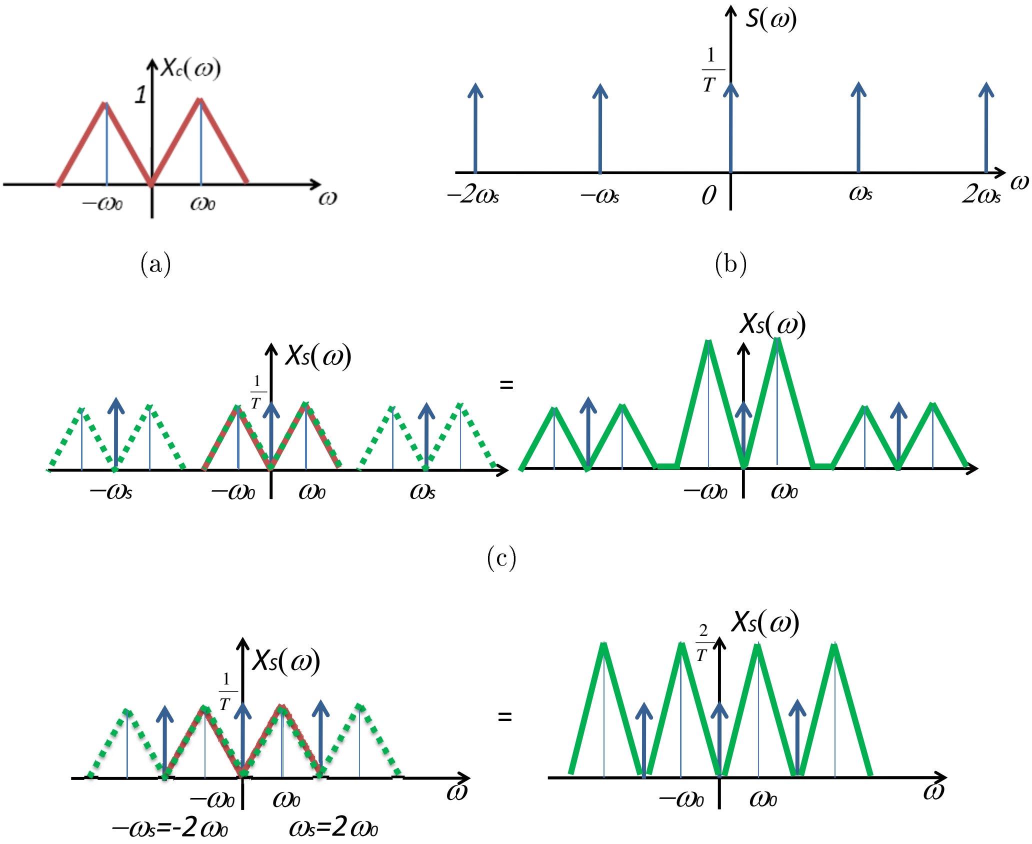

(a) (b)

(c)

(d)

Figure 2.19: Effect of different sampling frequency on the response: (a) spectrum of the original signal; (b) spectrum of the sampling function; (c) spectrum of the sampled signal with $\omega_s > 2\omega_0$; (d) spectrum of the sampled signal with $\omega_s = 2\omega_0$

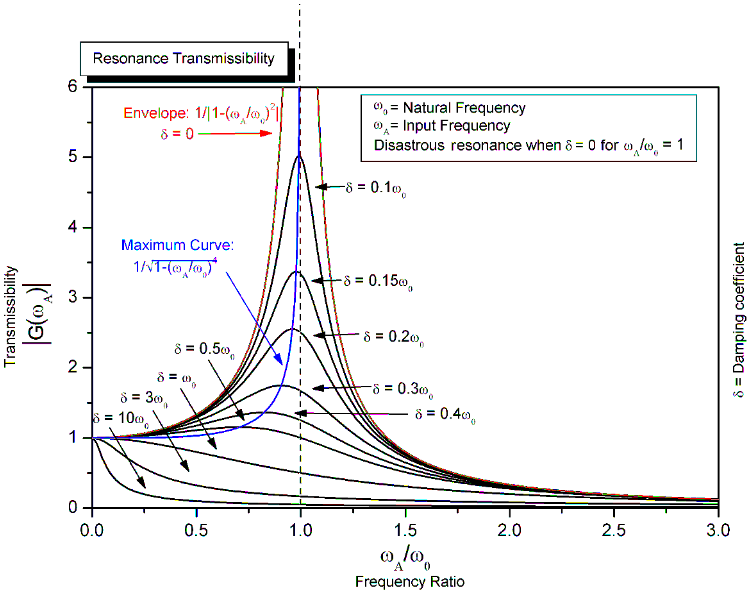

Figure 2.20: The amplitude of a damped single DOF system as a function of the frequency ratio (http://en.wikipedia.org/wiki/Damping)

structural damping is low enough, the response could be seen as symmetric with respect to its resonant frequency. In addition, as there is a 180 degree phase difference for negative and positive frequency component, the self-sampled impulse response is the minus conjugate. Figure 2.21 and Figure 2.22 expose self-sampled impulse responses for relatively highly damped ($C = 5$, $Q_M = 3.1831$) and lightly damped ($C = 0.4$, $Q_M = 39.7887$) electromechanical systems. For a relatively highly damped system, the response cannot be considered as symmetric with respect to zero frequency, so that the self-sampled response (the negative frequency part of original response) could not be approximated as the minus of the positive frequency part. However, for a relatively lightly damped system, self-sampled responses could be considered approximately equal to the minus of the original response. The structural damping factor C increases with decreasing mechanical quality factor Q_M and the general coupling factor $k^2 Q_M$ increases with increasing Q_M, so that only with a limited range of mechanical quality factor Q_M or a very small coupling factor k would have the symmetric response with respect to $\pm\omega_0$ and also a weakly coupled electromechanical system considering no coupling effect.

Due to the resonant nature of the electromechanical structure, the harvester would have a comparably large displacement response around $\omega = \pm\omega_0$. Since the displacement is a real function in time-domain, the analysis could be presented only with

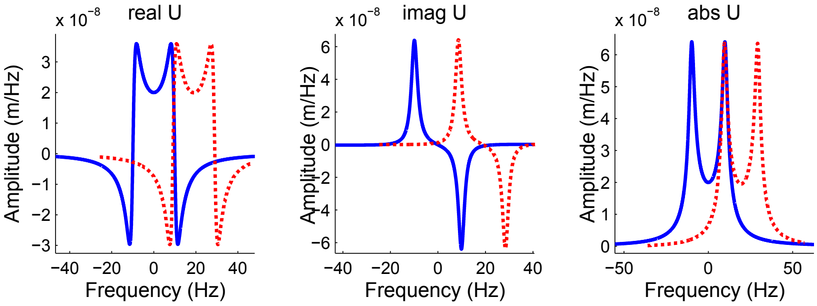

Figure 2.21: Self-sampled impulse response for highly damped system, – and ⋯ denote the original and sampled responses respectively

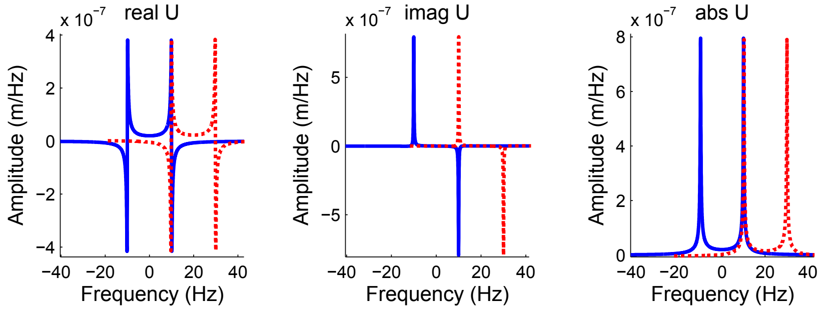

Figure 2.22: Self-sampled impulse response for lightly damped system, – and ⋯ denote the original and sampled responses respectively

positive frequency components. Within a specific range of Q_M or with a small coupling factor k, the electromechanical system is considered to have no backward coupling effect and the impulse displacement response in the frequency domain $U(\omega)$ could be obtained according to the equation of motion:

$$U(\omega) = \frac{F(\omega)}{-M\omega^2 + jC\omega + K_E} = \lambda_0(\omega)F(\omega). \tag{2.83}$$

Substituting Eq. (2.83) into the broadband voltage expression of PSHI interface, the impulse voltage response considering no backward coupling effect is denoted as:

$$\begin{aligned} V(\omega) &= j\omega U(\omega)h(\omega) \\ &- \frac{\eta(\omega)}{\alpha}\sum_{n=-\infty}^{\infty}\left[(\omega - 2n\omega_0)\frac{F(\omega - 2n\omega_0)}{\left(-M(\omega - 2n\omega_0)^2 + jC\left(\omega - 2n\omega_0\right) + K_E\right)}h\left(\omega - 2n\omega_0\right)e^{j(\omega - 2n\omega_0)t_0}\right], \end{aligned} \tag{2.84}$$

where

$$\eta(\omega) = j\frac{(1+\gamma)\left(1 - e^{-T_s j\omega}e^{-\frac{T_s}{RC_0}}\right)}{\left(1 + \gamma e^{-T_s j\omega}e^{-\frac{T_s}{RC_0}}\right)}\frac{e^{-j\omega t_0}C_0}{T_s}h(\omega). \tag{2.85}$$

As the switching event is described by Dirac comb function, the switching process could be seen as a self-sampling process, and the electromechanical system response is a combination of the original response and a weighted summation of shifted responses. For a weakly damped system, the response is narrow-banded around the system resonance and the conjugate, $U((2k+1)\omega_0) \cong 0$ with $k \neq -1, 0$. Considering a switching frequency $\omega_s = 2\omega_0$, in frequency domain, the voltage signal could be seen as a combination of band-responses ranging across each ω_s ranges ($0 < \omega < \omega_s$, $\omega_s < \omega < 2\omega_s$, and so on). The forced damped vibration response can be seen as as symmetric with respect to the resonance frequency ω_0 if the structural damping is low enough. In addition, as there is a 180 degree phase difference for negative and positive frequency component, the self-sampled impulse response is the minus conjugate. First, we considering the frequency range from 0 to $\omega_s = 2\omega_0$ as a very simple example, which implies $n = 0, 1$, the first self-sampled displacement $U(\omega - 2\omega_0)$ is:

$$U(\omega - 2\omega_0) = \frac{F(\omega - 2\omega_0)}{\left(-M(\omega - 2\omega_0)^2 + jC\left(\omega - 2\omega_0\right) + K_E\right)}. \tag{2.86}$$

With a pulsed input applied at $t = t_p$, the first self-sampled displacement could be approximated as the minus conjugate of the original response, because it is a real time-domain function and has symmetric responses in frequency domain:

$$\begin{aligned} U(\omega-2\omega_0) &= \frac{F(\omega-2\omega_0)}{\left(-M(\omega-2\omega_0)^2+jC\left(\omega-2\omega_0\right)+K_E\right)} \\ &\approx -U(\omega) = -\frac{F(\omega)}{\left(-M(\omega)^2+jC\left(\omega\right)+K_E\right)}. \end{aligned} \tag{2.87}$$

The voltage in the range $0 < \omega < 2\omega_0$ $(n = 0, 1)$ would therefore be:

$$\begin{aligned} V(\omega) = j\omega U(\omega)h(\omega) - &\left\{ \frac{\eta(\omega)}{\alpha} e^{j(\omega)t_0} \left(\frac{F\left(\omega\right)}{-M(\omega)^2+jC\left(\omega\right)+K_E} \right) \right. \\ &\left. \times \left[(\omega)\, h\left(\omega\right) - \left(\omega-2\omega_0\right) h\left(\omega-2\omega_0\right) e^{-j(2\omega_0)t_0} \right] \right\}, \quad 0 < \omega < 2\omega_0. \end{aligned} \tag{2.88}$$

For the following range, from $2\omega_0$ to $4\omega_0$ $(n = 1, 2)$, the voltage response could be obtained with the same method:

$$\begin{aligned} V(\omega) =& j\omega U(\omega)h(\omega) \\ &- \left\{ \frac{\eta(\omega)}{\alpha} \left(\frac{F\left(\omega-2\omega_0\right)}{-M(\omega-2\omega_0)^2+jC\left(\omega-2\omega_0\right)+K_E} \right) e^{j(\omega-2\omega_0)t_0} \right. \\ &\left. \times \left[\left(\omega-2\omega_0\right) h\left(\omega-2\omega_0\right) - \left(\omega-4\omega_0\right) h\left(\omega-4\omega_0\right) e^{-j(2\omega_0)t_0} \right] \right\}, \quad 2\omega_0 < \omega < 4\omega_0. \end{aligned} \tag{2.89}$$

Accordingly, for a weakly coupled and lightly damped system, in the frequency range from $2k\omega_0$ to $2(k+1)\omega_0$ $(n = k, k+1)$, the displacement is given as:

$$\begin{aligned} U(\omega-2\left(k+1\right)\omega_0) &= \lambda_0\left(\omega-2(k+1)\omega_0\right) F\left(\omega-2(k+1)\omega_0\right) \\ &\approx -U(\omega-2k\omega_0) = -\lambda_0(\omega-2k\omega_0)F(\omega-2k\omega_0), \end{aligned} \tag{2.90}$$

and the voltage response in the range $2k\omega_0 < \omega < 2(k+1)\omega_0$ is summarized as

$$\begin{aligned} V(\omega) =& j\omega U(\omega)h(\omega) \\ &- \left\{ \frac{\eta(\omega)}{\alpha} \lambda_0\left(\omega-2k\omega_0\right) F\left(\omega-2k\omega_0\right) e^{j(\omega-2k\omega_0)t_0} \right. \\ &\left. \times \left[\left(\omega-2k\omega_0\right) h\left(\omega-2k\omega_0\right) - \left(\omega-2\left(k+1\right)\omega_0\right) h\left(\omega-2\left(k+1\right)\omega_0\right) e^{-j(2\omega_0)t_0} \right] \right\}. \end{aligned} \tag{2.91}$$

The simulation based on this theoretical analysis is evaluated with parameters in Table 2.3 with very low damping constant and relatively low coupling coefficient from the experimental data [126]. A pulsed force with $F_M = 0.001$N, $t_p = 1$s is applied, and a 10% vibration period switching delay is considered. In Figure 2.23, the simulation results from theoretical analysis are compared with time-domain resolution in both time domain and frequency domain. The waveform comparison in time domain matches well although only 15 harmonics are considered as in this case, the figure of merit k^2Q_m is very low and the response fades out in high frequency region.

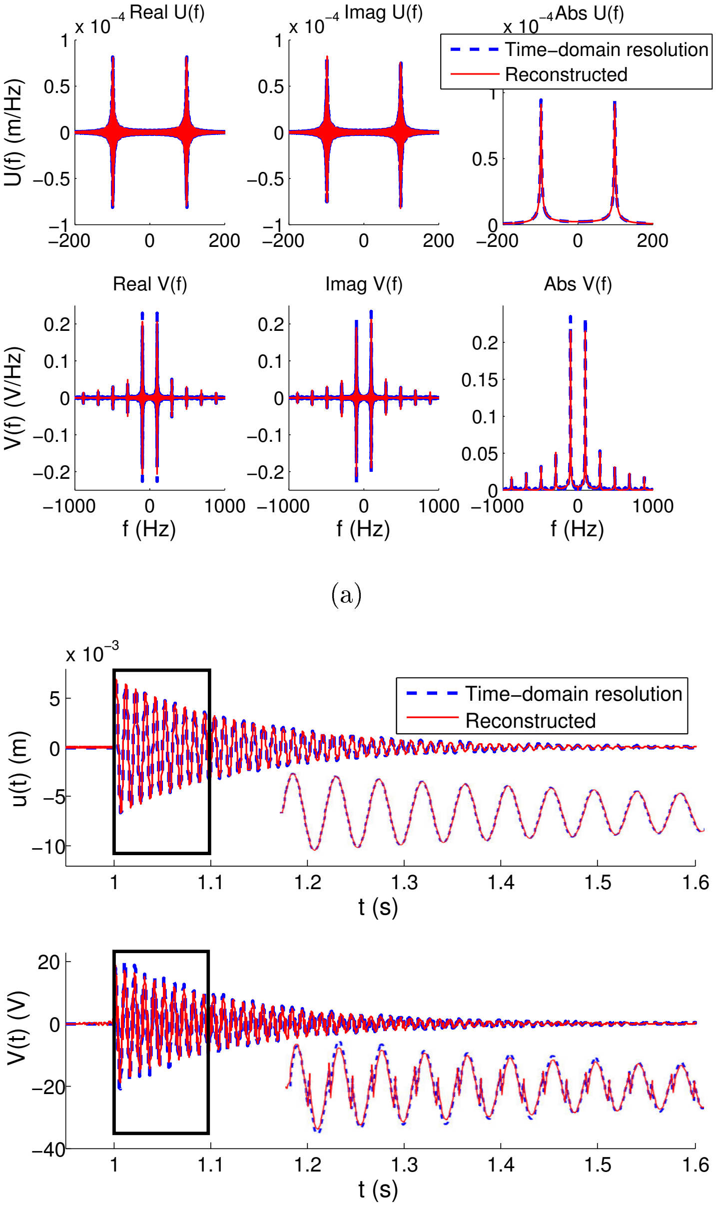

(a)

(b)

Figure 2.23: Simulation results for impulse response considering no damping effect based on theoretical analysis (in red plain line) and numerical time-domain resolution (in blue dashed line) with PSHI interface considering a 10% vibration period switching delay: (a) frequency-domain comparison; (b) time-domain comparison

Table 2.3: Model parameters for weakly coupled and lightly damped system.

C_0	14.7 nF
α	7.26×10^{-5} N/V
K_E	87.8 Nm^{-1}
M	0.23 g
C	0.0032 $Nm^{-1}s^{-1}$
γ	0.6
f_0	98.4 Hz
k^2	0.405%
Q_M	43.8
k^2Q_M	0.1774

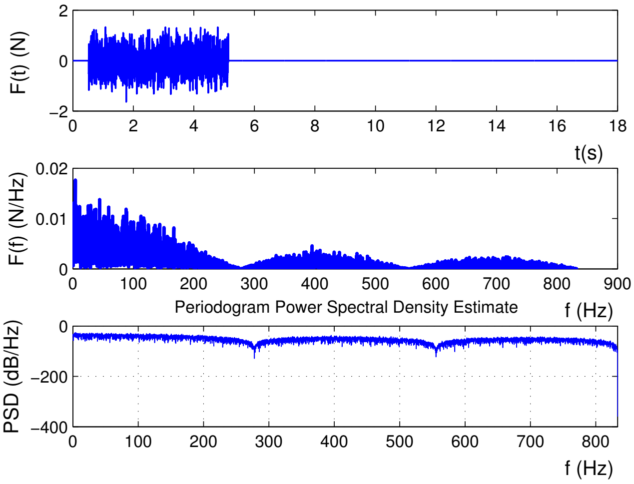

Figure 2.24: Random force in time domain and frequency domain and its power spectral density

2.4.4 Case 4: Random Force Excitation with PSHI Interface

To investigate a piezoelectric harvester with periodic switching frequency under a more practical situation, a random force is applied. The input is a moving average (in order to smoother the waveform) of a Gaussian distributed random force with null mean and unit standard deviation. Accordingly, in frequency domain, it is the convolution between the original Gaussian distributed random function and the rectangular time-window (Figure 2.24). The excitation is still considered as random. To prevent a time-domain aliasing effect caused by the inverse discrete Fourier transform (IDFT), a time window is applied to the excitation force from 0.5s to 5.15s. The simulation is conducted using model parameters of Table 2.2. The response of the harvester under this force excitation is calculated with the modeling developed in Section 4.2.

When the switching frequency is chosen as twice the first resonance of electromechanical structure and with a 10 % vibration period of switching delay, the harvester responses calculated with the broadband modeling Eqs. (2.61) and (2.64) in time and frequency domain are as shown in Figure 2.25. The simulation results from broadband modeling match well with time-domain simulation in both cases, which proves the effectiveness of the modeling.

Under a random force excitation, the strategy of switching process has to be discussed in more detail as there is a tradeoff between the number of switching processes and the limit of the voltage increase. The response of the piezoelectric harvester is analyzed with several switching frequencies from $0.1\omega_0$ to $8\omega_0$. The response is investigated carefully around $\omega_s = \omega_0$ and $\omega_s = 2\omega_0$ as the switch has more possibilities to be turned on at extremum or null displacement when the switching delay is assumed to be zero. To get a more representative value, the surface plot (Figure 2.26) of the harvested energy as a function of the resistive load (normalized value with respect to optimal resistive load of standard interface) and switching frequencies (in units of first mechanical resonance) is the average value of 20 simulations. In Figure 2.26, it is noted that when switching frequency is slightly less than $2\omega_0$, the harvester has a better performance than at other switching frequencies. When the switching frequency increases, the harvested energy will decrease as the loss caused by the switching process increases. It appears that there are notches in the response at certain switching frequencies, especially when the switching frequency is a is around $2\omega_0/p$, $p \in \mathbf{N}$.

2.5 Conclusion and Further Works

We have established a closed-form modeling for proof mass displacement and output voltage for a piezoelectric harvester with a switching interface that closes periodically at any chosen frequency. This modeling is based on the fundamental equations for a piezoelectric harvester and makes the complex behavior under a broadband excitation easier to analyze and understand. The modeling is constructed using the sampling theory and the concept of frequency aliasing (by modeling the switching process as a self-sampling of the voltage), allowing multiple frequency components in the theoretical analysis and giving the direct response of the harvester.

From the comparison with time-domain simulation for several excitation cases, the effectiveness of such a modeling was proved. Results also agree well with previous works under the same conditions and with the same model parameters. For a monochromatic force excitation case and with a properly chosen phase, the harvester has a constructive

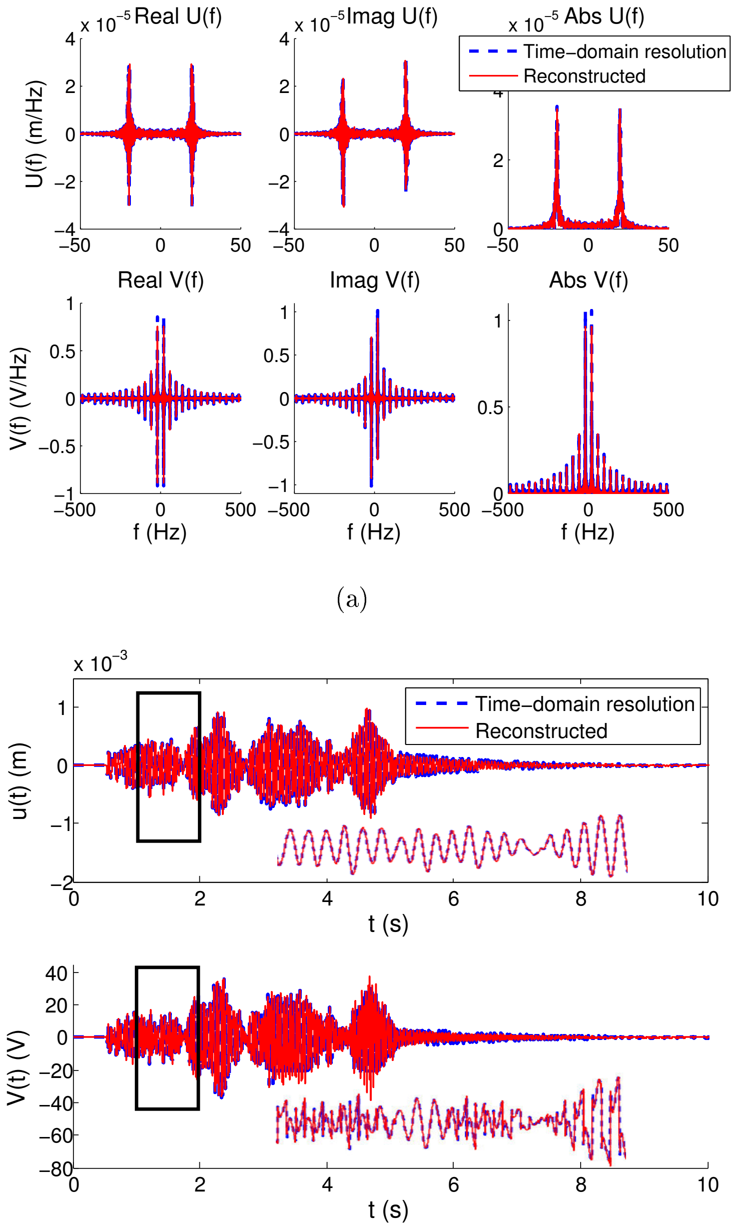

(a)

(b)

Figure 2.25: Simulation results under a random force excitation with PSHI technique based on numerical broadband modeling (in red line) and numerical time-domain resolution (in blue (dashed) line) when switching frequency is $2\omega_0$ and with a 10% switching delay: (a) frequency-domain comparison; (b) time-domain comparison

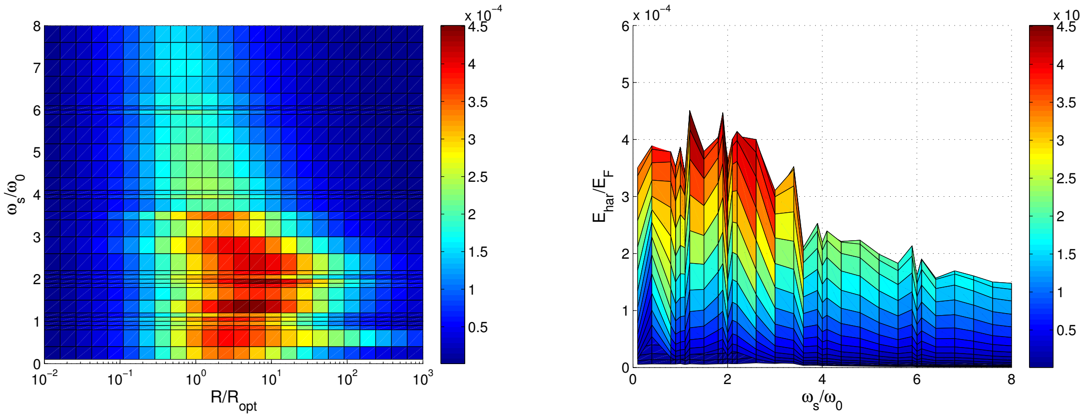

(a) (b)

Figure 2.26: Harvested energy (averaging with 10 simulations) as a function of resistive load (normalized with optimal load when using standard interface) and switching frequency (in a ratio of harvester natural frequency ω_0) under a random force excitation simulated with the broadband modeling: (a) top view of normalized harvested power as a function of R_L/R_{opt} and switching delay (in the ratio of a period); (b) side view of normalized harvested power as a function of switching delay (in the ratio of a period)

response when the switching frequency is set as twice the system resonance frequency to allow the self-aliasing effect. The effect of a switching delay is limited within a certain range of delays showing that there is some robustness towards deviations from ideal timing. For a random force input, the performance has to be analyzed statistically as the response is not unique and the phase effect is different. The result was averaged over 20 simulations to reduce variance. In this case, the harvester performs better when the switching frequency is slightly less than twice the first resonance of harvester. There appears to be notches in the response that deserves further investigation.

Statistical methods based on spectral densities or probability distributions have to be considered in future work to gain further insight into the random and broadband excitation case and the phase effect. In addition, it is also interesting to have a smart strategy consisting in applying the PSHI technique to a windowed response in order to approach SSHI operations. With this strategy, the choice of switching instant would be easier.

3 Stochastic Modeling in Frequency Domain for PSHI AC Technique

In the previous chapter, the piezoelectric harvester with nonlinear techniques which can artificially decrease the phase shift between the voltage and the proof-mass velocity and thereby increases the energy conversion has been introduced. Furthermore, to analyze the broadband performance of nonlinear interfaced piezoelectric harvesters under a random vibration, a nonlinear technique consisting in a periodically switched circuit, which is called "Periodic Switching Harvesting on Inductor" (PSHI), has been introduced and the harvester is modeled with the self-sampling and self-aliasing theories in frequency domain. The previous chapter serves as the first step in introducing the working principle of PSHI AC technique and the broadband performance of the piezoelectric harvester. In this chapter, the modeling work is extended based on the stochastic theory so that the harvester performance can be directly obtained with the excitation power spectral density (PSD) function.

3.1 Introduction

In the literature, the piezoelectric energy harvesting system is usually modeled as a Single-Degree-of-Freedom (SDOF) spring-mass-damper system, and the external excitation is usually simplified as a monochromatic force. In the case of inertial devices, the force is the fictitious force due to acceleration. Nevertheless, real excitations might have more than one characteristic frequency peak or a wide range of power spectral density shapes [3, 113, 127]. Such real-world signals make the analysis of piezoelectric harvester performance more complex and require a simulation work to assess it, especially with nonlinear interface. Halvorsen *et al* has demonstrated the simulation of a vibration energy harvester driven by broadband vibrations in SPICE simulator [115]. In experiments by Lefeuvre *et al*, a piezoelectric electrical generator with SECE (Synchronous Electric Charge Extraction) technique was investigated under an excitation with bandwidth from 20 Hz to 2 kHz [117]. There are also experimental works [118,119] in terms of probabilistic method carried out with switching damping techniques (from which the SSHI technique was proposed) under a random vibration. For a piezoelectric harvester with standard interface, there are also few theoretical works presented with stationary stochastic theory. Halvorsen derived the close-form equations describing the harvested power from a linear harvester when it is subjected to a white or band-limited noise with the power spectral density (PSD) of the noise itself [121]. Adhikari *et al* derived corresponding equations for a white-noise driven linear harvester featuring an inductor in series with the load resistance [124].

The complexity and the variety of broadband signals and the nonlinearity introduced by the SSHI AC technique, make theoretical modeling of piezoelectric harvesters with the SSHI AC technique difficult under a random vibration, and it is particularly hard to obtain closed-form solutions. In previous chapter, frequency-domain formulas were derived to describe the performance of a nonlinearly interfaced piezoelectric harvester driven by a given random vibration of finite duration based on the Fourier transform of the force or acceleration excitation. The nonlinear interface is assumed to operate at a fixed frequency ω_s in order to simplify the problem, and the modeling is conducted with the theory of self-sampling and self-aliasing. We refer to this technique as "Periodic Switching Harvesting on Inductor" (PSHI). The fixed frequency of switching and the assumption of short switching time allows the dynamics of the nonlinear switching circuit itself to be held outside the mathematical modelling of the electromechanical system. The system equations then become linear, but time variant. Chapter 2 provides the fundamental formula for analyzing and understanding the complex behavior when a switching-interfaced energy harvester is excited with a broadband signal. However, to gain further insight into the random and/or broadband excitation cases, modeling based on the stochastic theory is necessary for obtaining the harvester performance without the extra burden of doing statistical analysis on results from multiple time series. In addition, with the stochastic modeling, the phase effect can be directly taken into account and the harvester performance can be expressed with the power spectral density function of the signals, which is more realistic in analyzing broadband problems.

Extending the work from previous chapter (Lallart *et al* [126]), this chapter work aims at providing frequency-domain formula for analyzing the performance of nonlinearly interfaced piezoelectric harvesters driven by broadband and/or random excitation specified by a spectral density function. This is accomplished using cyclostationary stochastic theory [128] in combination with the self-sampling and self-aliasing theory developed previously in Chapter 2. Firstly, the background knowledge of cyclostationary stochastic process will be introduced. In Section 3.3, the stochastic modeling of nonlinear interfaced harvester will be introduced for the general case (with arbitrary coupling) and for the weakly coupled system. Then numerical results obtained with the model are investigated in Section 3.4 and experimentally validated in Section 3.5. Finally Section 3.7 concludes the broadband performance of PSHI interfaced piezoelectric harvester.

3.2 Probabilistic Approach and Cyclostationary Stochastic Process

Probabilistic analysis and stochastic modeling are tools which can be employed to quantify uncertainties, unpredictability and randomness due to the random or stochastic process. For a system has the response with random and unpredictable properties, the ensemble of all possible signals should be considered in the analysis and the modeling, which refers to the probabilistic approach and the stochastic modeling. The background of stochastic process can be referenced to [129–132]. The stochastic modeling is based on a set of probabilistic parameters, which are going to be introduced in the following paragraphs. The simplest way describing a random process $X(t)$ is through the *probability* “Pr" and the *distribution function* “$F_X(x;t)$" for an event $(X(t) \leq x)$ happening in $X(t)$

$$F_X(x;t) = \Pr\{X(t) \leq x\}, \qquad -\infty < x < \infty, \tag{3.1}$$

defining the distribution functions of the random process $X(t)$ as functions of the real number x for $X(t) \leq x$. The distribution function contains all the information available about a random process before its value is determined by experiment. If a random process is with associated continuously distributed random variables, $X(t)$,

$t \in \mathbb{Z}$, then the random process $X(t)$ is called continuous random process and its distribution function $F_X(x;t)$ is a continuous function of x. If there is a nonnegative function $f_X(x;t)$ defined for $-\infty < x < \infty$ such that

$$\Pr\{\mathrm{a} < X(t) \leq b\} = \int_a^b f_X(x;t)\,dx \qquad \text{for } -\infty < a < b < \infty, \tag{3.2}$$

then $f_X(x;t)$ is called the *probability density function* for the random variable X [129]. If $X(t)$ is a continuous random process with probability density function $f_X(x;t)$, then its m^{th} moment is given by

$$E[X(t)^m] = \int_{-\infty}^{\infty} x^m f_X(x;t)dx, \tag{3.3}$$

provided that this integral converges absolutely. The first moment ($m = 1$) is commonly called the *mean* of $X(t)$ and written as $m_X(t)$. The second central moment is called the variance of $X(t)$ and written as $\sigma_X^2(t)$ or $\mathrm{Var}[X(t)]$ with the equivalent formulas $\mathrm{Var}[X(t)] = E[(X(t) - m_X(t))^2] = E[X(t)^2] - m_X(t)^2$. The autocorrelation function of a random process $X(t)$, denoted by $R_{XX}(t_1, t_2)$ is defined as the joint moment of $X(t_1)$ and $X(t_2)$:

$$R_{XX}(t_1, t_2) = E[X(t_1)X(t_2)] = \langle X(t_1)X(t_2)\rangle. \tag{3.4}$$

In general, a broadband signal has a narrower-peaked autocorrelation function than a narrowband one. It is often useful to characterize the relationship between two random processes. The cross-correlation function of random processes $X(t)$ and $Y(t)$, denoted by $R_{XY}(t_1, t_2)$, is defined as the joint moment of $X(t_1)$ and $Y(t_2)$:

$$R_{XY}(t_1, t_2) = E[X(t_1)Y(t_2)] = \langle X(t_1)Y(t_2)\rangle. \tag{3.5}$$

The random process $X(t)$ is a stationary (S) process if and only if the distribution function $F_X(t)$ is independent of time parameter t, i.e. $F_X(x_1, \ldots, x_k; t_1, \ldots, t_k) = F_X(x_1, \ldots, x_k; t_1 + \Delta t, \ldots, t_k + \Delta t)$ for any arbitrary Δt, any k and sampling times $t_1, \ldots, t_k$. The mean of a stationary process does not depend on time, and its autocorrelation function depends only on the time difference of two samples [130], that is,

$$m_X(t) = m_X; R_X(t_1, t_2) \equiv R_X(t_2 - t_1). \tag{3.6}$$

Letting $\tau = t_2 - t_1$, we use the notation $R_X(\tau) \equiv E[X(t)X(t+\tau)]$. In practice, many processes which are non-stationary can show a stationary behavior in the mean value and the autocorrelation function, and then the process $X(t)$ is said to be *wide-sense stationary* (WSS) (or weakly stationary). With a real value wide-sense stationary random process $X(t)$, we have the following properties:

- The average power of $X(t)$ is given by $R_X(0) = E[X(t)^2] \geq 0$.
- $R_X(\tau) = E[X(t)X(t+\tau)] = E[X(t-\tau)X(t)] = R_X(-\tau)$, the autocorrelation is an even function of τ.
- $|R_X(\tau)|^2 \leq R_X(0)^2$, based on the Cauchy-Schwarz inequality.
- If $R_X(T) = R_X(0)$ for some T, then $R_X(\tau)$ is periodic with period T, i.e. $R_X(\tau + T) = R_X(\tau)$ for all τ, and $X(t)$ is a mean square periodic process, i.e. $E[(X(t+T) - X(t))^2] = 0$.
- If $R_X(\tau)$ is continuous at $\tau = 0$, it is continuous everywhere.

The cross-correlation function R_{XY} between two WSS processes $X(t)$ and $Y(t)$ satisfies:

- $R_{XY}(\tau) = R_{XY}$.
- By the Cauchy-Schwarz inequality, $R_{XY}(\tau)^2 \leq E[X(0)^2]E[Y(\tau)^2] = R_X(0)R_Y(0)$.
- $|R_{XY}(\tau)| = 1/2(R_X(0) + R_Y(0))$.

The power spectral density (PSD) function $S_{XX}(\omega)$ of a WSS process $X(t)$ is defined as the Fourier transform of its autocorrelation function $R_{XX}(\tau)$:

$$S_{XX}(\omega) = \int_{-\infty}^{\infty} R_{XX}(\tau)\, e^{-j\omega t} dt, \tag{3.7}$$

and therefore the autocorrelation function $R_{XX}(\tau)$ is defined as the inverse Fourier transform of the PSD function $S_{XX}(\omega)$:

$$R_{XX}(\tau) = \frac{1}{2\pi} \int_{-\infty}^{\infty} S_{XX}(\omega)\, e^{j\omega\tau} d\omega. \tag{3.8}$$

For two jointly wide-sense stationary processes $X(t)$ and $Y(t)$, the cross power spectral density is defined to be:

$$S_{XY}(\omega) = \int_{-\infty}^{\infty} R_{XY}(\tau)\, e^{-j\omega t} dt. \tag{3.9}$$

Given the properties of the autocorrelation function $R_{XX}(\tau)$, the following properties can be established for the power spectral density function [130]:

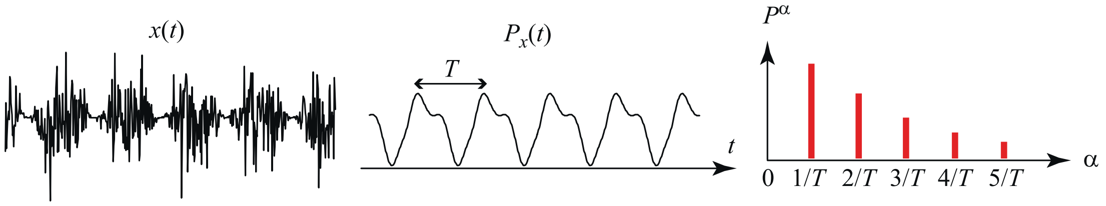

Figure 3.1: Example of a cyclostationary signal $x(t)$; $P_x(t)$ is referred to the mean instantaneous power of the signal; P^{α} is the cyclic powers of the signal [128]

- $S_{XX}(\omega)$ is real, even if the process $X(t)$ is complex.
- If $X(t)$ is real, then $S_{XX}(\omega)$ is an even function, since $R_{XX}(\tau)$ is an even function.
- $S_{XX}(\omega)$ is nonnegative.

The power spectral density has the interpretation of a density function for average power in the random process $X(t)$ per unit frequency.

Many processes encountered in nature arise from periodic phenomena. The process that give rise to random data whose statistical characteristics vary periodically with time is called *cyclostationary* process [133]. The background knowledge of cyclostationary process can be found in references [128, 133, 134]. An example of a cyclostationary signal can be seen from Figure 3.1.

A stochastic process $X(t)$ is said to be cyclostationary if the joint probability density (or mass) function $f_X(x;t)$ is invariant when the time origin is shifted by a period T. That is, for any k and sampling times $t_1, \ldots, t_k$, we have

$$f_X(x_1, \ldots, x_k; t_1, \ldots, t_k) = f_X(x_1, \ldots, x_k; t_1 + T, \ldots, t_k + T). \tag{3.10}$$

Although the cyclostationary process is not a periodic function of time, the periodicity of the process could come from modulation, sampling (which is the case in this chapter work), multiplexing and coding operations [134]. A wide-sense cyclostationary stochastic process would have the mean and the autocorrelation function varying periodically in time with some period T,

$$m_X(t+T) = m_X(t); \quad R_{XX}(t,\tau) = R_{XX}(t+T,\tau), \tag{3.11}$$

for all $\tau \in (-T, T)$. For a cyclostationary process, its autocorrelation function can therefore be expanded in a Fourier series whose coefficients referred to as *cyclic autocorrelation function*, depending on the lag parameter (the cyclic frequencies α):

$$R_{XX}(t,\tau) = \sum_{a} R_{XX}^{\alpha}(\tau)\, e^{j2\pi\alpha t}, \quad \alpha = \frac{n}{T}, n \in \mathbb{Z}; \tag{3.12}$$

the cyclic autocorrelation function is expressed as the coefficient of the Fourier series by

$$R_{XX}^{\alpha}(\tau) = \frac{1}{T}\int_{0}^{T} R_{XX}(t,\tau)\, e^{-j2\pi\alpha t} dt. \tag{3.13}$$

Cyclostationary processes are characterized in the frequency domain by a *spectral correlation density function* (SCD), which is the Fourier transforms of the cyclic autocorrelation function R_{xx}^{α}:

$$S_{XX}^{\alpha}(\omega) = \int_{-\infty}^{\infty} R_{xx}^{\alpha}(\tau)\, e^{-j\omega\tau} d\tau; \tag{3.14}$$

with the non-unitary inverse Fourier transform, the cyclic autocorrelation function can also be expressed as:

$$R_{xx}^{\alpha}(\tau) = \frac{1}{2\pi}\int_{-\infty}^{\infty} S_{xx}^{\alpha}(\omega)\, e^{j\omega\tau} d\omega. \tag{3.15}$$

For $\alpha = 0$, $R_{xx}^{0}(\tau)$ reduces to the conventional autocorrelation function and $S_{XX}^{0}(\omega)$ is the conventional power spectral density (PSD) function. Compared to a non-cyclostationary signal, the cyclostationary signal is sensitive in sensing the time delay or phase of the signal [133].

Considering a stationary signal $x(t)$ which is transformed by a linear filter with the transfer function $h(t)$, the output signal $z(t)$ is then expressed as $z(t) = h(t) * x(t)$ in time domain, where "$*$" denotes the convolution operation, and $Z(f) = H(f)X(f)$ in frequency domain. As a result, the PSD function is scaled by the squared magnitude of $H(f)$ as

$$S_z(f) = |H(f)|^2 S_x(f). \tag{3.16}$$

On the other hand, the SCD function of a cyclostationary signal $x(t)$ after filtering is given by

$$S_z^{\alpha}(f) = H(f+\frac{\alpha}{2}) S_x^{\alpha}(f) H^*(f-\frac{\alpha}{2}), \tag{3.17}$$

where * denotes the complex conjugate. Considering a filter that is simply a time delay t_0 with respect to the input signal, then $h(t) = \delta(t - t_0)$, where δ is the Dirac delta function, and $H(f) = e^{-j2\pi f t_0}$. Therefore, the input-output SCD functions relation is

$$S_z^{\alpha}(f) = S_x^{\alpha}(f) e^{-j2\pi\alpha t_0}, \tag{3.18}$$

indicating that the SCD of cyclostationary signal is sensitive to the time or phase delay of the signal.

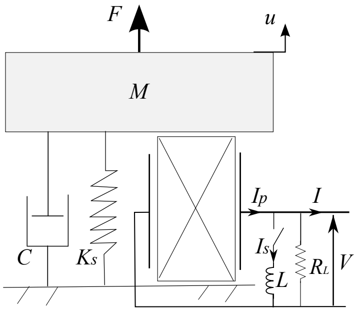

Figure 3.2: Equivalent model for piezoelectric harvester (proof mass M, structure stiffness K_s, damper C, inductor L and resistive load R_L)

3.3 Stochastic Modeling

In this section, a modeling of Periodic Switching Harvesting on Inductor (PSHI) AC technique will be proposed based on the stochastic modeling. The harvester system is shown as a single degree of freedom spring-mass-damper model in Figure 3.2. From piezoelectric constitutive equations, the piezoelectric element is modeled as a current source (proportional to the proof mass velocity $\dot{u}$ with a force factor α) with an internal capacitance C_0; so the current I_p flowing out from the piezoelectric element is

$$I_p(t) = \alpha\dot{u}(t) - C_0\dot{V}(t). \tag{3.19}$$

The equation of motion of a linear energy harvester is expressed in terms of the proof mass position u, its velocity $\dot{u}$ and the voltage V across the transducer:

$$M\ddot{u}(t) = F(t) - K_{\mathrm{E}}u(t) - \alpha V(t) - C\dot{u}(t). \tag{3.20}$$

The global stiffness K_E is the sum of K_{pE} (the stiffness of piezoelectric element with short-circuited electrical port) and K_{s} (the structure stiffness); the damping coefficient is expressed with the damping ratio ζ or the mechanical quality factor Q_M as $C = 2M\omega_{0E}\zeta = M\omega_{0E}/Q_M$ and ω_{0E} defines the short-circuit resonant angular frequency ($\omega_{0E} = \sqrt{K_E/M}$) of the harvester. The external force excitation could be also expressed through the base acceleration a as $F = Ma$ for an inertially driven system.

From Kirchhoff's current law, the current V/R_L flowing through the resistive load equals to the current I_p flowing out the piezoelectric element minus the current I_s that flows through the switch device. Accordingly, the voltage V across the resistive load can be expressed as the impulse response h convoluted with the proof mass velocity $\dot{u}$ and the scaled switching current $\tilde{I}_s C_0/\alpha$. Therefore, the derivative of piezoelectric voltage $\dot{V}$ can be expressed as the consequence of proof mass motion and the backward coupling from the switching device, $\tilde{I}_s$ (the scaled switching current):

$$\dot{V}(t) = \dot{u}(t) * \dot{h}(t) + \tilde{I}_s(t) * \frac{C_0}{\alpha}\dot{h}(t), \tag{3.21}$$

where h is the impulse response combining an unit step function $\mathrm{H}(t)$ enforcing causality and an exponential decay with time constant τ_{e} representing the power consumption of the resistive load R_L:

$$\begin{aligned} h(t) &= \frac{\alpha}{C_0} e^{-\frac{t}{\tau_{\mathrm{e}}}} \mathrm{H}(t) \\ \tau_{\mathrm{e}} &= R_L C_0. \end{aligned} \tag{3.22}$$

Integrating Eq. (3.21), the voltage can also be expressed as

$$V(t) = \int_{-\infty}^{\infty} h(t-t_1) v(t_1) dt_1 + \frac{C_0}{\alpha} \int_{-\infty}^{\infty} h(t-t_2) \tilde{I}_s(t_2) dt_2, \tag{3.23}$$

where $\tilde{I}_s(t)$ is given in terms of a current impulse-response h_s and the velocity (referenced to Section 2.2.2.2) as

$$\tilde{I}_s(t) = \int_{-\infty}^{\infty} h_s(t, t_1) v(t_1) dt_1, \tag{3.24}$$

and as demonstrated in the previous chapter:

$$\begin{aligned} h_s(t,t_1) = -(1+\gamma) \sum_{n=-\infty}^{\infty} \Bigg[\sum_{k'=0}^{\infty} (-\gamma)^{k'} \Bigg(& h\left(t - k'T - t_1\right) e^{-\frac{k'T}{\tau_{\mathrm{e}}}} \\ & - h\left(t - \left(k'+1\right)T - t_1\right) e^{-\frac{(k'+1)T}{\tau_{\mathrm{e}}}} \Bigg) \delta\left(t - nT\right) \Bigg]. \end{aligned} \tag{3.25}$$

Note that the impulse response h_s is dependent on two time instants, and not only a time difference, because the periodic switching breaks the time-invariance.

3.3.1 General Case

We will now consider the cross-correlation functions $K_{AB}(t,t') = \mathrm{E}\left[A(t)B(t')\right] = \langle A(t)B(t')\rangle$ for signals A and B, where A and B denote either the state variables u, v and V or the input force F. E[ ] denotes statistical expectation. Instead of using the notation R_{AB} everywhere as the cross-correlation function, here we use K_{AB} to indicate the cross-correlation function depending on two time instants t_1 and t_2, and R_{AB} for time instant t and time difference τ. Equations of motion for the correlation functions are conveniently derived from the state-space form of (Eq. (3.20)):

$$\dot{u}(t) = v(t) \tag{3.26}$$

$$\dot{v}(t) = -{\omega_{0E}}^2 u(t) - \frac{\omega_{0E}}{Q_M} v(t) - \frac{\alpha}{M} V(t) + \frac{1}{M} F(t). \tag{3.27}$$

Furthermore, a voltage impulse-response h_{Vv} to a velocity input is defined such that the voltage across the piezoelectric element is

$$V(t) = \int_{-\infty}^{\infty} h_{Vv}(t, t_1) v(t_1) dt_1. \tag{3.28}$$

From Eqs. (3.23) and (3.24), the impulse response h_{Vv} is

$$h_{Vv}(t, t_1) = h(t - t_1) + \frac{C_0}{\alpha} \int_{-\infty}^{\infty} h(t - t_2) h_s(t_2, t_1) dt_2. \tag{3.29}$$

Equations for the cross-correlations now follow from time differentiation and application of Eqs. (3.26) and (3.27), or from direct application of Eq. (3.28). The smallest required set of coupled equations to be solved is

$$\langle \dot{u}(t) v(t') \rangle = \frac{\partial}{\partial t} K_{uv}(t, t') = K_{vv}(t, t') \tag{3.30}$$

$$\begin{aligned}\langle \dot{v}(t) v(t') \rangle = \frac{\partial}{\partial t} K_{vv}(t, t') &= -{\omega_{0E}}^2 K_{uv}(t, t') - \frac{\omega_{0E}}{Q_M} K_{vv}(t, t') \\ &\quad - \frac{\alpha}{M} K_{Vv}(t, t') + \frac{1}{M} K_{Fv}(t, t')\end{aligned} \tag{3.31}$$

$$\langle V(t) v(t') \rangle = K_{Vv}(t, t') = \int_{-\infty}^{\infty} h_{Vv}(t, t_1) K_{vv}(t_1, t') dt_1 \tag{3.32}$$

$$\langle F(t) \dot{u}(t') \rangle = \frac{\partial}{\partial t'} K_{Fu}(t, t') = K_{Fv}(t, t') \tag{3.33}$$

$$\begin{aligned}\langle F(t) \dot{v}(t') \rangle = \frac{\partial}{\partial t'} K_{Fv}(t, t') &= -{\omega_{0E}}^2 K_{Fu}(t, t') - \frac{\omega_{0E}}{Q_M} K_{Fv}(t, t') \\ &\quad - \frac{\alpha}{M} K_{FV}(t, t') + \frac{1}{M} K_{FF}(t, t')\end{aligned} \tag{3.34}$$

$$\langle F(t) V(t') \rangle = K_{FV}(t, t') = \int_{-\infty}^{\infty} h_{Vv}(t', t_1) K_{Fv}(t, t_1) dt_1. \tag{3.35}$$

Note that the set Eqs. (3.33) to (3.35) is closed if K_{FF}, which characterizes the force excitation, is given. Likewise Eqs. (3.30) to (3.32) is closed if K_{Fv}, which can be obtained from Eqs. (3.33) to (3.35), is given.

Due to the periodic switching events, the system state can be seen as a wide-sense cyclostationary process if the force F is a wide-sense stationary process (or a wide sense cyclostationary process with the same period as the switching). In order to solve Eqs. (3.30)-(3.35), it is convenient to introduce the cross-correlation $R_{AB}(t,\tau) \equiv K_{AB}(t_2,t_1)$ which depends on the central time $t = (t_1+t_2)/2$ and the time lag $\tau = t_2 - t_1$ instead of two time instants t_2 and t_1 associated with A and B respectively. For a cyclostationary process, $R_{AB}(t,\tau)$ is periodic in time domain t with the cyclostationary period T_s and has a corresponding cyclostationary angular frequency ω_s [128]. In our case, these are respectively the switching period and frequency. We therefore have the Fourier series representation

$$\begin{aligned} R_{AB}(t,\tau) &= \sum_n R^n_{AB}(\tau) e^{j\omega_s n t}; \\ R^n_{AB}(\tau) &= \frac{1}{T_s}\int_0^{T_s} R_{AB}(t,\tau) e^{-j\omega_s n t} dt; \end{aligned} \tag{3.36}$$

for integer n. The spectral cross-correlation density (SCD) is defined as the Fourier transform of cyclic cross-correlation function R^n_{AB} [135]:

$$\begin{aligned} S^n_{AB}(\omega) &= \int_{-\infty}^{\infty} R^n_{AB}(\tau) e^{-j\omega\tau} d\tau \\ R^n_{AB}(\tau) &= \frac{1}{2\pi}\int_{-\infty}^{\infty} S^n_{AB}(\omega) e^{j\omega\tau} d\omega. \end{aligned} \tag{3.37}$$

Applying the change of variables $\tau = t_2 - t_1$ and $t = (t_1 + t_2)/2$, the cross-correlation function between signals A and B at time instants t_2 and t_1 is represented in terms of the spectral correlation density function ${S^n}_{AB}$:

$$K_{AB}(t_2,t_1) = \frac{1}{2\pi}\int_{-\infty}^{\infty} \sum_n S^n_{AB}(\omega) e^{j\left(\omega+\frac{1}{2}\omega_s n\right)t_2 - j\left(\omega-\frac{1}{2}\omega_s n\right)t_1} d\omega. \tag{3.38}$$

The system of linear equations (3.30), (3.31), (3.33), (3.34) then becomes

$$j\left(\omega+\frac{1}{2}\omega_s n\right)S^n_{uv}(\omega)=S^n_{vv}(\omega) \tag{3.39}$$

$$j\left(\omega+\frac{1}{2}\omega_s n\right)S^n_{vv}(\omega)=-{\omega_{0E}}^2S^n_{uv}(\omega)-\frac{\omega_{0E}}{Q_M}S^n_{vv}(\omega)-\frac{\alpha}{M}S^n_{Vv}(\omega)+\frac{1}{M}S^n_{Fv}(\omega) \tag{3.40}$$

$$-j\left(\omega-\frac{1}{2}\omega_s n\right)S^n_{Fu}(\omega)=S^n_{Fv}(\omega) \tag{3.41}$$

$$-j\left(\omega-\frac{1}{2}\omega_s n\right)S^n_{Fv}(\omega)=-{\omega_{0E}}^2S^n_{Fu}(\omega)-\frac{\omega_{0E}}{Q_M}S^n_{Fv}(\omega)-\frac{\alpha}{M}S^n_{FV}(\omega)+\frac{1}{M}S^n_{FF}(\omega), \tag{3.42}$$

which can be reduced to

$$\frac{L\left(\omega+\frac{1}{2}\omega_s n\right)}{j\left(\omega+\frac{1}{2}\omega_s n\right)}S^n_{vv}(\omega)=-\frac{\alpha}{M}S^n_{Vv}(\omega)+\frac{1}{M}S^n_{Fv}(\omega) \tag{3.43}$$

$$\frac{L^*\left(\omega-\frac{1}{2}\omega_s n\right)}{-j\left(\omega-\frac{1}{2}\omega_s n\right)}S^n_{Fv}(\omega)=-\frac{\alpha}{M}S^n_{FV}(\omega)+\frac{1}{M}S^n_{FF}(\omega), \tag{3.44}$$

where

$$L(\omega)=-\omega^2+{\omega_{0E}}^2+2j\omega\zeta\omega_{0E}; \tag{3.45}$$

$L^*(\omega)$ is the complex conjugate of $L(\omega)$ and $\zeta=\frac{1}{2Q_M}$ the damping ratio. Note that $S^n_{FF}=0$ for $n\neq 0$ if F is a wide sense stationary process. In that case S^0_{FF} is the power spectral density of the excitation force F.

As the cross-correlation function can also be expressed with the central time t and the time lag τ ($R_{AB}(t,\tau)\equiv K_{AB}(t_2,t_1)$), Eq. (3.35) can be further expressed as

$$R_{FV}(t,\tau)=K_{FV}(t+\frac{1}{2}\tau,t-\frac{1}{2}\tau)=\int_{-\infty}^{\infty}h_{Vv}(t-\frac{1}{2}\tau,t_1)K_{Fv}(t+\frac{1}{2}\tau,t_1)dt_1. \tag{3.46}$$

With the representation of the cross correlation function (Eq. (3.38)), the cross-correlation defined in Eq. (3.35) gives R_{FV} in terms of S^n_{Fv}:

$$R_{FV}(t,\tau)=\frac{1}{2\pi}\int\limits_{-\infty}^{\infty}d\omega\sum_n S^n_{Fv}(\omega)e^{j\left(\omega+\frac{1}{2}\omega_s n\right)\left(t+\frac{1}{2}\tau\right)}$$
$$\times\left[\int\limits_{-\infty}^{\infty}h_{Vv}(t-\frac{1}{2}\tau,t_1)e^{-j\left(\omega-\frac{1}{2}\omega_s n\right)t_1}dt_1\right]. \tag{3.47}$$

The cyclostationary property of h_{Vv} makes it possible to write the integral in the brackets as a phase factor times a t-periodic function $y = y(t, \omega)$ which can be expressed in terms of its Fourier coefficients y_k, that is

$$\int\limits_{-\infty}^{\infty} h_{Vv}(t, t_1) e^{-j\omega t_1} dt_1 = e^{-j\omega t} y(t, \omega) = \sum_k y_k(\omega) e^{j(-\omega + k\omega_s)t}, \tag{3.48}$$

or

$$e^{j\omega t} \int_{-\infty}^{\infty} h_{Vv}(t, t_1) e^{-j\omega t_1} dt_1 = \sum_k y_k(\omega) e^{jk\omega_s t}. \tag{3.49}$$

The Fourier coefficients are found directly from the Fourier integral of (Eq. (3.29)) and are given by

$$\begin{aligned} y_k(\omega) &= \frac{1}{T_s} \int_0^{T_s} \left(e^{j\omega t} \int_{-\infty}^{\infty} h_{Vv}(t, t_1) e^{-j\omega t_1} dt_1 \right) e^{-j\omega_s k t} dt \\ &= \frac{1}{T_s} \int_0^{T_s} \left(\hat{h}^*(\omega) - (1+\gamma) \frac{\hat{h}^*(\omega) e^{\left(j\omega - \frac{1}{\tau}\right)t}}{1 + \gamma e^{\left(j\omega - \frac{1}{\tau}\right)T_s}} \right) e^{-j\omega_s k t} dt \\ &= \hat{h}^*(\omega) \times \left(\delta_{k,0} - \frac{1}{T_s} \cdot \frac{1+\gamma}{-j\omega + \frac{1}{\tau} + j\omega_s k} \cdot \frac{1 - e^{\left(j\omega - \frac{1}{\tau}\right)T_s}}{1 + \gamma e^{\left(j\omega - \frac{1}{\tau}\right)T_s}} \right) \end{aligned} \tag{3.50}$$

where $\hat{h}^*(\omega)$ denotes the complex conjugate of $\hat{h}(\omega)$. The cross-correlation function R_{FV} is then expressed with the $t-$periodic function $y(t, \omega)$:

$$\begin{aligned} R_{FV}(t, \tau) &= \int_{-\infty}^{\infty} \frac{1}{2\pi} \sum_i {S_{Fv}}^i(\omega) \left[\sum_k y_k(\omega - \frac{1}{2}\omega_s i) e^{j\left(-\omega + \frac{1}{2}\omega_s i + \omega_s k\right)\left(t - \frac{1}{2}\tau\right)} \right] e^{j\left(\omega + \frac{1}{2}\omega_s i\right)\left(t + \frac{1}{2}\tau\right)} d\omega \\ &= \int_{-\infty}^{\infty} \frac{1}{2\pi} \sum_i {S_{Fv}}^i(\omega) \left[\sum_k y_k(\omega - \frac{1}{2}\omega_s i) e^{j(\omega_s i + \omega_s k)t} e^{j(2\omega - \omega_s k)\frac{\tau}{2}} \right] d\omega. \end{aligned} \tag{3.51}$$

The cyclic cross-correlation function R_{FV}^n is obtained by applying Eq. (3.51) into Eq. (3.36) and integrating:

$$\begin{aligned} R_{FV}^n(\tau) &= \frac{1}{T_s} \int_0^{T_s} R_{FV}(t, \tau) e^{-j\omega_s n t} dt \\ &= \left(\int_{-\infty}^{\infty} \frac{1}{2\pi} \sum_i S_{Fv}^i(\omega) \left[\sum_k y_k(\omega - \frac{1}{2}\omega_s i) e^{j(2\omega - \omega_s k)\frac{\tau}{2}} \right] d\omega \right) \frac{1}{T_s} \int_0^{T_s} e^{j(i+k-n)\omega_s t} dt \\ &= \left(\int_{-\infty}^{\infty} \frac{1}{2\pi} \sum_i S_{Fv}^i(\omega) \left[\sum_k y_k(\omega - \frac{1}{2}\omega_s i) e^{j(2\omega - \omega_s k)\frac{\tau}{2}} \right] d\omega \right) (\delta_{n,i+k}) \\ &= \frac{1}{2\pi} \int_{-\infty}^{\infty} \sum_i S_{Fv}^i(\omega) y_{n-i}(\omega - \frac{1}{2}\omega_s i) e^{j\left(\omega - \frac{1}{2}\omega_s (n-i)\right)\tau} d\omega \end{aligned} \tag{3.52}$$

In order to discriminate the integer number n in the summation term and the number of cycles in R^n_{FV}, here we replace the index n in the summation term with i. The SCD S^n_{FV} of F and V is the Fourier transform of the cyclic cross-correlation function:

$$\begin{aligned} S^n_{FV}(\omega) &= \int_{-\infty}^{\infty} R^n_{FV}(\tau) e^{-j\omega\tau} d\tau \\ &= \int_{-\infty}^{\infty} \left(\frac{1}{2\pi} \int_{-\infty}^{\infty} \sum_i S^i_{Fv}(\omega') y_{n-i}(\omega' - \frac{1}{2}\omega_s i) e^{j\left(\omega' - \frac{1}{2}\omega_s (n-i)\right)\tau} d\omega' \right) e^{-j\omega\tau} d\tau; \quad (3.53) \end{aligned}$$

the integration of the exponential term can be expressed with the Dirac delta function as:

$$\left(\int_{-\infty}^{\infty} e^{j\left(\omega' - \frac{1}{2}\omega_s (n-i) - \omega\right)\tau} d\tau \right) = 2\pi\delta(\omega' - \frac{1}{2}\omega_s (n-i) - \omega), \quad (3.54)$$

so finally S^n_{FV} can be expressed as the summation of SCD (S^i_{Fv}) function between F and v times the $t-$periodic term $y_{n-i}(\omega)$:

$$S^n_{FV}(\omega) = \sum_i S^i_{Fv}(\omega + \frac{1}{2}\omega_s (n-i)) y_{n-i}(\omega - \omega_s i + \frac{1}{2}\omega_s n). \quad (3.55)$$

The same procedure applied to the SCD of voltage and velocity gives

$$S^n_{Vv}(\omega) = \sum_i S^i_{vv}(\omega - \frac{1}{2}\omega_s (n-i)) y^*_{n-i}(\omega + \omega_s i - \frac{1}{2}\omega_s n). \quad (3.56)$$

Hence, the SCD S^n_{Fv} between force F and velocity v and the SCD S^n_{vv} of velocity itself can be found by inserting expressions of S^n_{FV} (Eq. (3.13)) and S^n_{Vv} (3.14) into Eqs. (3.43) and (3.44) respectively.

The average harvested power over one switching period has the general expression as:

$$P = \frac{1}{T_s} \int_0^{T_s} \frac{1}{R_L} \left\langle V^2(t) \right\rangle dt. \quad (3.57)$$

The mean square voltage across the piezoelement is then given by the voltage impulse response h_{Vv} and the shifted SCD ($\tilde{S}^n_{vv}(\omega) = S^n_{vv}(\omega + \omega_s n/2)$) as:

$$\begin{aligned} P &= \frac{1}{T_s} \frac{1}{R_L} \int_0^{T_s} \int_{-\infty}^{\infty} \int_{-\infty}^{\infty} h_{Vv}(t, t_1) h_{Vv}(t, t_2) K_{vv}(t_1, t_2) dt_1 dt_2 dt \\ &= \frac{1}{R_L} \frac{1}{2\pi} \int_{-\infty}^{\infty} d\omega \sum_n \tilde{S}^n_{vv}(\omega) \Bigg(\hat{h}^*(\omega) \hat{h}(\omega + \omega_s n) \\ &\qquad \times \left(\delta_{n,0} + (1+\gamma) \frac{1}{T_s} J_n(\omega) \right) \Bigg), \quad (3.58) \end{aligned}$$

where

$$
\begin{aligned}
J_n(\omega) = {} & \frac{1}{\left(-j\omega - \frac{1}{\tau_{\mathrm{e}}}\right)} \frac{1 - e^{\left(-j\omega - \frac{1}{\tau_{\mathrm{e}}}\right)T_s}}{1 + \gamma e^{\left(-j\omega - \frac{1}{\tau_{\mathrm{e}}}\right)T_s}} + \frac{1}{\left(j\left(\omega + \omega_s n\right) - \frac{1}{\tau_{\mathrm{e}}}\right)} \frac{1 - e^{\left(j\omega - \frac{1}{\tau_{\mathrm{e}}}\right)T_s}}{1 + \gamma e^{\left(j\omega - \frac{1}{\tau_{\mathrm{e}}}\right)T_s}} \\
& + \frac{\tau_{\mathrm{e}}}{2} \frac{(1+\gamma)\left(1 - e^{-\frac{2T_s}{\tau_{\mathrm{e}}}}\right)}{\left(1 + \gamma e^{\left(j\omega - \frac{1}{\tau_{\mathrm{e}}}\right)T_s}\right)\left(1 + \gamma e^{\left(-j\omega - \frac{1}{\tau_{\mathrm{e}}}\right)T_s}\right)}.
\end{aligned}
$$

3.3.2 Weak Coupling Case

In this subsection, a simplified model for weak coupling harvester system will be developed. For a weak coupling system, the equation of motion of the proof mass reduces to

$$M\ddot{u} \cong F - K_{\mathrm{E}}u - C\dot{u}. \tag{3.59}$$

With the force excitation as a wide-sense stationary process and u and v independent of the switching process according to Eq. (3.59), u and v are also wide sense stationary processes, therefore

$$K_{vv}^{0}(t_1, t_2) \equiv K_{vv}^{0}(t_1 - t_2, 0) = R_{vv}^{0}(\tau). \tag{3.60}$$

The power spectral density (PSD) of a wide-sense stationary signal is the Fourier transform of its corresponding autocorrelation function:

$$
\begin{aligned}
S_{vv}^{0}(\omega) &= \textstyle\int_{-\infty}^{\infty} R_{vv}^{0}(\tau) e^{-j\omega\tau} d\tau \\
R_{vv}^{0}(\tau) &= \textstyle\int_{-\infty}^{\infty} \frac{1}{2\pi} S_{vv}^{0}(\omega) e^{j\omega\tau} d\omega.
\end{aligned}
\tag{3.61}
$$

The power spectral density function of the proof mass velocity v can be written in terms of the PSD of the excitation force F:

$$S_{vv}^{0}\left(\omega\right) = \left|\hat{h}_{vF}\left(\omega\right)\right|^2 S_{FF}^{0}\left(\omega\right) \ . \tag{3.62}$$

The impulse response function between v and F is found from the reduced equation of motion (Eq. (3.59)) and its corresponding frequency response is

$$\hat{h}_{vF}(\omega) = j\omega \hat{h}_{uF}(\omega) = j\omega \frac{1}{M}\left(\frac{1}{-\omega^2 + 2\xi j\omega\omega_{0E} + {\omega_{0E}}^2}\right). \tag{3.63}$$

The average harvested power over a switching period (3.17) is reduced to an expression in terms of S_{vv}^{0} only as the electromechanical coupling due to the harvesting process can be neglected. From (3.62), we can obtain

$$P = \frac{1}{R_L}\frac{1}{2\pi}\int_{-\infty}^{\infty}\left|\hat{h}_{vF}(\omega)\right|^2\left|\hat{h}(\omega)\right|^2\left[1+\frac{1+\gamma}{T_s}J_0(\omega)\right]S_{FF}^0(\omega)d\omega \tag{3.64}$$

where $\hat{h}_{vF}$ can be found from the simplified equation (3.63) and

$$\begin{aligned} J_0(\omega) = {} & \frac{1}{\left(-j\omega-\frac{1}{\tau_e}\right)}\frac{1-e^{\left(-j\omega-\frac{1}{\tau_e}\right)T_s}}{1+\gamma e^{\left(-j\omega-\frac{1}{\tau_e}\right)T_s}}+\frac{1}{\left(j\omega-\frac{1}{\tau_e}\right)}\frac{1-e^{\left(j\omega-\frac{1}{\tau_e}\right)T_s}}{1+\gamma e^{\left(j\omega-\frac{1}{\tau_e}\right)T_s}} \\ & +\frac{\tau_e}{2}\frac{(1+\gamma)\left(1-e^{-\frac{2T_s}{\tau_e}}\right)}{\left(1+\gamma e^{\left(j\omega-\frac{1}{\tau_e}\right)T_s}\right)\left(1+\gamma e^{\left(-j\omega-\frac{1}{\tau_e}\right)T_s}\right)}. \end{aligned}$$

3.3.3 Standard Case

Considering a piezoelectric transducer connected with the classical standard technique, which is only with an adaptive resistance load, the switching frequency is zero (the switching period is infinity) and the inversion factor $\gamma = 0$. Furthermore, the current balance equation is reduced to

$$I_p = I = \frac{V}{R_L} = \alpha\dot{u}(t) - C_0\dot{V}(t), \tag{3.65}$$

and the impulse response h_{Vv} between V and v is reduced to the impulse response h in Eq. (3.22) as the switching current I_s is null. The power spectral density function of the voltage V can be expressed with the PSD of velocity v with the impulse response h_{Vv} as

$$S_{VV}^0 = \left|\hat{h}_{Vv}(\omega)\right|^2 S_{vv}^0 = \left|\hat{h}(\omega)\right|^2 S_{vv}^0. \tag{3.66}$$

With a wide-sense stationary force excitation and considering no switching processes, the harvester response is also a wide-sense stationary process, and therefore, the average harvested power is reduced to an expression with S_{VV}^0 only. From Eq. (3.17) and Eq. (3.66), we can obtain

$$\begin{aligned} P &= \frac{1}{R_L}\frac{1}{2\pi}\int_{-\infty}^{\infty}\left|\hat{h}(\omega)\right|^2 S_{vv}^0 d\omega \\ &= \frac{1}{R_L}\frac{1}{2\pi}\int_{-\infty}^{\infty} S_{VV}^0 d\omega, \end{aligned} \tag{3.67}$$

where $\hat{h}$ can be found from Eq. (3.22). With a simple resistive load adaption, the current I passed through the resistor is the ratio between the voltage V and the resistance R_L, and the PSD function of the current I can be expressed with the PSD function of V as

$$I(\omega) = \frac{V(\omega)}{R_L} \tag{3.68}$$

$$S_{II}^{0}(\omega) = \frac{S_{VV}^{0}(\omega)}{{R_L}^2}. \tag{3.69}$$

The average harvested power then can be expressed as

$$P = R_L \frac{1}{2\pi} \int_{-\infty}^{\infty} S_{II}^{0}(\omega) d\omega. \tag{3.70}$$

As Eq. (3.70) shares the same expression as in Halvorsen's work [121], the average power can be further expressed with the PSD of the force excitation F by using his work. The average power in Eq. (3.70) can be reduced to an expression in terms of S_{FF}^{0}, which can be also expressed with the PSD function of the acceleration excitation a over the squared mass ($S_{FF}^{0} = S_{aa}^{0}/M^2$), and an impulse response h_{Ia} between the current I and the acceleration excitation a:

$$\begin{aligned} P &= R_L \frac{1}{2\pi} \int_{-\infty}^{\infty} S_{II}^{0}(\omega) d\omega \\ &= R_L \frac{1}{2\pi} \int_{-\infty}^{\infty} \left| \hat{h}_{Ia}(\omega) \right|^2 S_{aa}^{0}(\omega) d\omega \\ &= R_L \frac{1}{2\pi} \int_{-\infty}^{\infty} \left| \hat{h}_{Ia}(\omega) \right|^2 \frac{S_{FF}^{0}(\omega)}{M^2} d\omega, \end{aligned} \tag{3.71}$$

where $\hat{h}_{Ia}$ can be obtained from the work of Halvorsen [121] as

$$\hat{h}_{Ia}(\omega) = \frac{j\omega k \sqrt{K_{\mathrm{D}} C_0}}{\left(1-k^2\right) {\omega_{0D}}^2 - \left(1 + \frac{R_L C_0 \omega_{0D}}{Q_{MD}}\right) \omega^2 + j\omega\omega_{0D} \left(\frac{1}{Q_{MD}} + R_L C_0 \omega_{0D} \left(1 - \frac{\omega^2}{{\omega_{0D}}^2}\right)\right)}. \tag{3.72}$$

$\omega_{0D} = \sqrt{K_{\mathrm{D}}/M}$ denotes the open-circuit resonant angular frequency; the open-circuit stiffness $K_{\mathrm{D}} = K_{\mathrm{E}} + \alpha^2/C_0$ and Q_{MD} denotes the mechanical quality factor at open-circuit resonant frequency, $Q_{MD} = M\omega_{0D}/C$. When the excitation is a white noise process, S_{FF}^{0} is independent from the frequency and can be taken out of the integral in Eq. (3.71) and the average harvested power under a white noise force excitation with the standard interface can finally obtained from [121] by integrating the third-order polynomial function $\hat{h}_{Ia}$:

$$P = \frac{S_{FF}^{0}}{2M} \frac{k^2 Q_{MD} R_L C_0 \omega_{0D}}{1 + \left(\frac{1}{Q_{MD}} + k^2 Q_{MD}\right) R_L C_0 \omega_{0D} + \left(R_L C_0 \omega_{0D}\right)^2}. \tag{3.73}$$

Table 3.1: Model parameters for simulation based on stochastic modeling

Lumped mass	M	200 g
Short-circuit stiffness	K_E	3000 Nm^{-1}
Capacitance	C_0	20 nF
Inversion coefficient	γ	0.75
Harvester short-circuit resonant frequency	f_{0E}	19.49 Hz

3.4 Numerical Results

The primary quantity of interest is the harvested power. In this section, the harvested power at optimal load will be presented at different switching frequencies. The effect of variations in coupling factor k^2 and mechanical quality factor Q_M will also be discussed to provide a reference for harvester system design. Then, in order to show the effectiveness of the stochastic model, different spectral distributions will be used for the external excitation.

3.4.1 The effect of coupling coefficients and switching frequency

The harvested power is decided by the spectral cross-correlation density function of the harvester velocity, which can be obtained by solbing a set of coupled equations depending on the mechanical quality factor Q_M and electromechanical coupling factor k^2. From equations (3.43) and (3.17), it is clear that the mechanical quality factor $Q_M = 1/(2\xi)$ and the electromechanical coupling factor $k^2 = \alpha^2/(C_0 K_\mathrm{E} + \alpha^2)$ influence the harvested power. So, different values of k^2 and Q_M should be investigated as figures of merit for the random-vibration-driven energy harvester with switching circuitry. In the numerical calculations, realistic, moderate k^2 and Q_M values are chosen. Numerical results reported in this section are calculated from the stochastic model stated in the previous section, the model parameters listed in Table 3.1, which is obtained from [54] and a white-noise force spectrum S_{FF}.

The harvested power as a function of switching frequency ω_s is shown in Figure 3.3 for a harvester with a moderate mechanical quality factor $Q_M = 122.475$ and different k^2 ranging from 0.067 % to 6.25 %. The harvested power is normalized with respect to the input power spectral density S_{FF} and the mass M; the switching frequency ω_s is normalized with respect to the harvester short-circuit resonant angular frequency ω_{0E}. The load resistance R_L is optimized at each value of ω_s/ω_{0E}. As expected, curves for different coupling factors k^2 as $\omega_s \to 0$ all approach the value for the standard interface with optimal resistive load $R_{opt} = 1/(C_0\omega_{0D})$ [121], and as the electromechanical coupling factor k^2 increases to around 6.25%, the switching strategy no longer beneficial, having an inferior performance compared to the standard AC interface. For all curves, a similar behavior showing a notch near $\omega_s = 2\omega_{0E}$ is observed, and as k^2 increases, the notch becomes more pronounced. For higher k^2 cases, for example (the two higher k^2 curves in figures) the notch even appears at other frequencies approximately given by $2\omega_{0E}/p$, $p \in \mathbb{N}$ giving that the notch phenomenon depends on the integer multiples of harvester's half-period. This might be because the switching electrical system has a strong influence on the mechanical system at the notch frequency, especially at $2\omega_{0E}$, which is harvester's half period. The details of why this notch phenomenon occurs and why it has a destructive effect needs further investigation. The best switching frequency for optimal power harvesting falls within the range from $1.5\omega_{0E}$ to $2\omega_{0E}$ depending on the harvester electromechanical coupling factor k^2 when PSHI AC technique still holds a better performance. With a higher k^2, the optimal switching frequency decreases ($\omega_s = 1.62\omega_{0E}$ for $k^2 = 2.34\%$, $1.74\omega_{0E}$ for $k^2 = 1.64\%$, $1.9\omega_{0E}$ for $k^2 = 0.415\%$ and $1.95\omega_{0E}$ for $k^2 = 0.067\%$). A factor that can contribute to this, is that when the electromechanical coupling is high, the inversion loss due to the switching process is larger, and a lower switching rate reduces the losses [136].

To look into more details, the following paragraph describes the scaled output power over different combination of k^2 and Q_M showing the effect of k^2 and Q_M separately. The output power at optimal load and switching frequency is illustrated in Figure 3.4 with several coupling factors $k^2 = 1.67\times10^{-4}$ %, 0.0167 %, 0.415 % and 1.64 % as a function of the mechanical quality factor Q_M. The range of Q_M is kept from 4.899 to 489.9 to reflect realistic cases. It is interesting to find that when k^2 is extremely small as in weak-coupling systems, the scaled output power collapses to a common value; and with a larger k^2 the scaled output power decreases after reaching an optimal value. Additionally, with the same Q_M, the scaled output power decreases with increase of k^2; the k^2-dependence is stronger for higher Q_M, which can be explained by that fact that the with high Q_M, the k^2-dependent damping effect due to energy conversion dominates easily the overall damping. In Figure 3.4(b), it is shown that the scaled optimal power

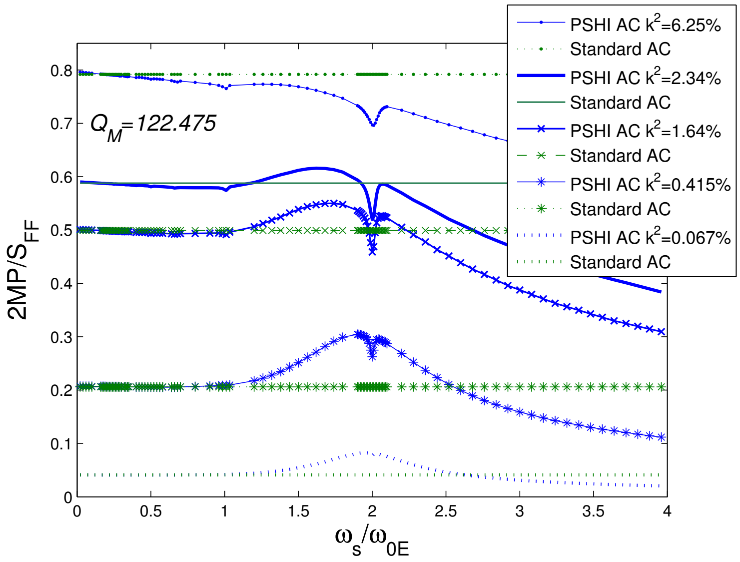

Figure 3.3: Normalized output power at optimal load versus switching frequency with $Q_M = 122.475$ and different k^2. The horizontal lines correspond to the optimal output powers for standard AC interface

is different even with the same value of k^2Q_M with switching electronic interface when k^2 is small. For example, when $k^2 = 1.67\times10^{-4}$ %, $Q_M = 489.9$ and $k^2 = 0.0167$ %, $Q_M = 4.899$ ($k^2Q_M = 8.181\times10^{-4}$), the scaled optimal power are 1.159 and 0.7787 respectively; with a larger k^2, scaled optimal powers would approach the same value, for example when $k^2Q_M = 2.009$. With a standard interface, the scaled optimal power with the same k^2Q_M-value but different combinations are slightly different for a very small k^2Q_M. However, it approaches a single value for higher k^2Q_M. It is interesting to note that under a broadband excitation with a switching electronic interface, the harvester performance can vary considerably among different choices of k^2 and Q_M even though k^2Q_M is held fixed. With a monochromatic excitation that is not the case [137]. For monochromatic force excitation case, the lack of energy conversion capability, presented by k^2, can be compensated by extracting more mechanical energy from the excitation force with a harvesting system having higher Q_M value; however, for a white noise excitation cases, except the mechanical loss coming from mechanical damping effect, there is also the loss due to deviation of excitation force from the harvester resonant frequency.

For a weak-coupling harvester, the simplified model (3.64) makes the calculation much faster. The validation of weak-coupling model is shown in Figure 3.5 with $k^2Q_M = 0.0068$. The curves obtained from the general stochastic model and the

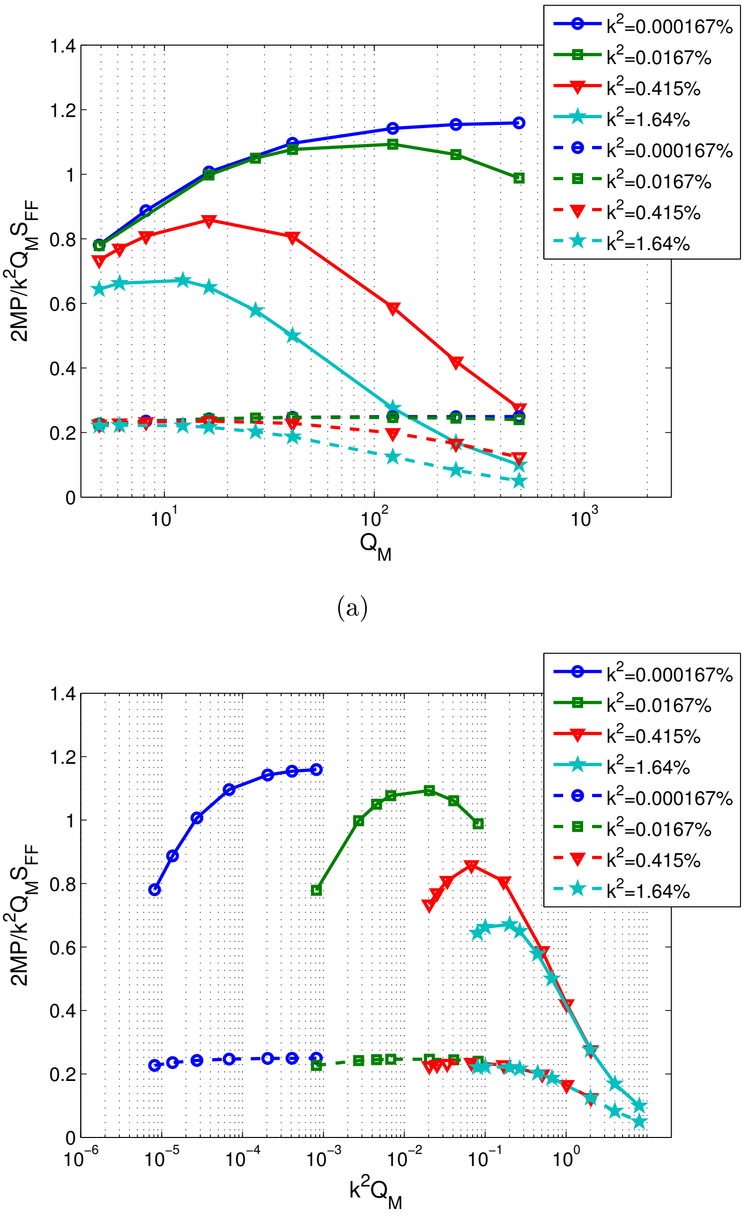

(a)

(b)

Figure 3.4: Scaled output power at optimal load and optimal switching frequency when $k^2 = 1.67 \times 10^{-4}$ %, 0.0167 %, 0.415 % and 1.64 % for several Q_M values. (a) Scaled optimal power over mechanical quality factor Q_M; (b) Scaled optimal power over $k^2 Q_M$. Solid lines for switching electronic interface; dashed line for standard case

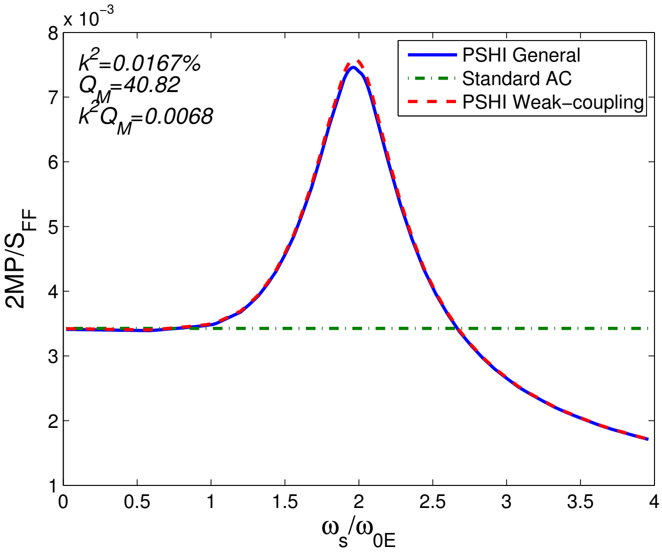

Figure 3.5: Validation of weak-coupling stochastic model. Scaled output power at optimal load versus switching frequency with $\gamma = 0.75$, $Q_M = 40.82$ and $k^2 = 0.0167\%$. The horizontal lines correspond to the scaled optimal output powers for standard AC interface

simplified model correspond well, and they all tend toward standard interface when switching frequency is very low. In 3D surface plot (Figure 3.6), the optimized power is plotted as a function of resistive load and switching frequency for a harvester with relatively high coupling $k^2Q_M = 2.0086$. It is shown that the optimal load depends strongly on the switching frequency as it is higher when the switching frequency is approaching twice the resonant frequency.

3.4.2 Excitations with Different Spectral Cross-Correlation Densities (SCD) Functions

With the mathematical formulation of the stochastic model we have now developed, different spectral densities of the excitation signal can be treated with the same algorithm and comparable computational effort. In this section, we compare band-limited spectra with different frequency bands (Figure 3.7). For the band-limited spectra, we choose bell curve shaped spectral densities in a form of Gaussian distribution as $S_{FF}(\omega) \propto e^{-(\omega/2\pi - f_{0E})^2/(2f_r)}/\left(\sqrt{2\pi}\right) + e^{-(\omega/2\pi + f_{0E})^2/(2f_r)}/\left(\sqrt{2\pi}\right)$, where f_r controls the width of the “bell". The harvested power is optimized over the resistive load and normalized with respect to the mean square force ${F_{\mathrm{rms}}}^2 = \frac{1}{2\pi}\int_{-\infty}^{\infty} S_{FF}(\omega)\mathrm{d}\omega$ of the excitation. It is clearly shown that the harvester is more effective when the spectral

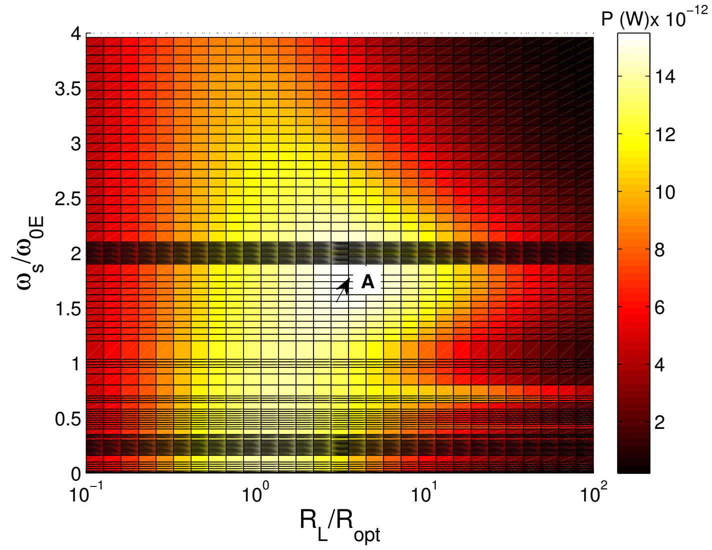

Figure 3.6: Output power as a function of resistive load and switching frequency with $Q_M = 122.4745$, $k^2 = 1.64\%$. Point **A** shows the optimal power output $P = 1.55\times10^{-5}\mu$W at $\omega_s = 1.74\omega_{0E}$, $R_L = 3.562 \times R_{opt} = 1.45$ MΩ

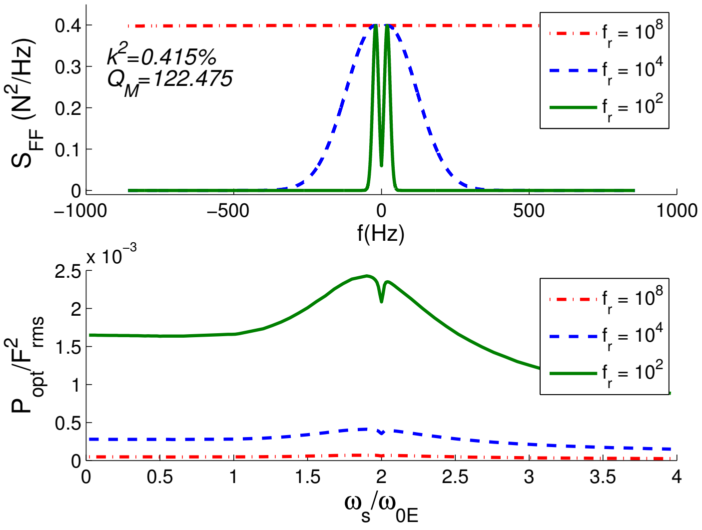

Figure 3.7: External excitation signal with Gaussian distribution in different frequency bands ($f_r = 10^2, 10^4, 10^8$), $k^2Q_M = 0.508$, $f_{0E} = 19.49$ Hz

distribution is like a monochromatic excitation (i.e., when it has a narrower frequency band) as less of the power is filtered out by the narrow response of the harvester. When the frequency band of the Gaussian distribution is wide enough, the shape of distribution is flat over a wide frequency range, and the normalized power at each switching frequency approaches the white-noise value.

When the linewidth of the Gaussian-shaped SCD is narrow (Figure 3.8(a)) and the harvester performance is more like that under a monochromatic excitation, the match between resonant frequency and the vibration spectrum becomes an issue. Here we consider three out-of-resonance cases when frequency shift Δf is 1.3Hz, 2.6Hz and -2.6Hz. The effect of out-of-resonance is clearly shown in Figure 3.8(b). When the frequency shift Δf is around 7% of the resonance frequency (Δf = 1.3 Hz), the harvested power decrease is around 8%; and when Δf is around 13% of resonance frequency (Δf = 2.6 Hz), a decrease of more than 25% in harvested power is observed. In addition, in this case, the slight difference in harvested power for negative frequency shift Δf = -2.6 Hz and positive frequency shift Δf = 2.6 Hz is explained by the asymmetry of the harvester transfer function.

3.5 Experimental Validation

The experimental setup is shown in Figure 3.9. The switching circuit and force excitation are controlled with a dSPACE box digital-to-analog converter (DAC) through Matlab Simulink environment. ControlDesk interface is used in realtime to feed the band-limited white noise signal to the shaker and command the switching device with a switching frequency f_s. Acquisition of measured signal is done through the dSPACE analog-to-digital converter (ADC) and ControlDesk interface. An unimorph type piezoelectric harvester is mounted on the shaker and two laser vibrometers (sensitivity = 25 mm/s/V and 50 mm/s/V) are monitoring the velocity on the cantilever beam clamped-end and the free-end respectively.

The harvester parameters are identified through measurements (without switching) of open-circuit frequency f_{0D}, short-circuit frequency f_{0E}, piezoelectric open circuit voltage to the beam free-end displacement ratio λ, -3dB bandwidth Δf in terms of deflection and clamped capacitance C_0 of the piezoelectric material. With these mea-

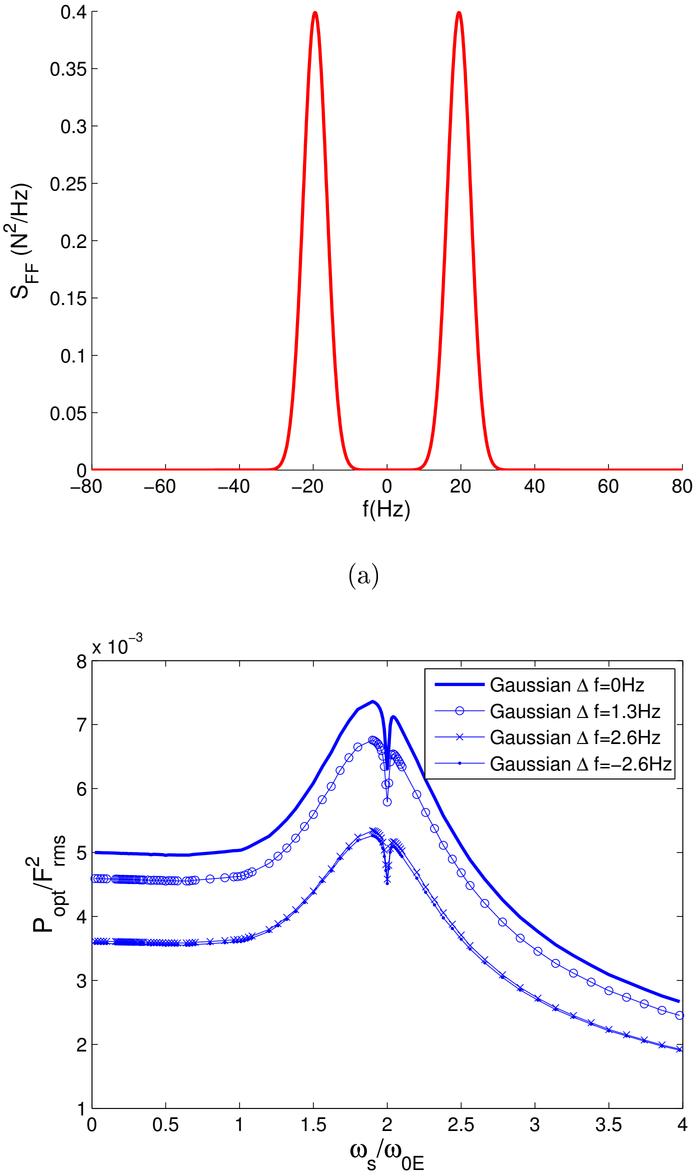

(a)

(b)

Figure 3.8: The effect of out-of-resonance with Gaussian distributed S_{FF}. (a) Gaussian distributed S_{FF} when $f_r = 10$; (b) Harvested power under different frequency shifts. $f_{0E} = 19.49$ Hz, $k^2 Q_M = 0.508$

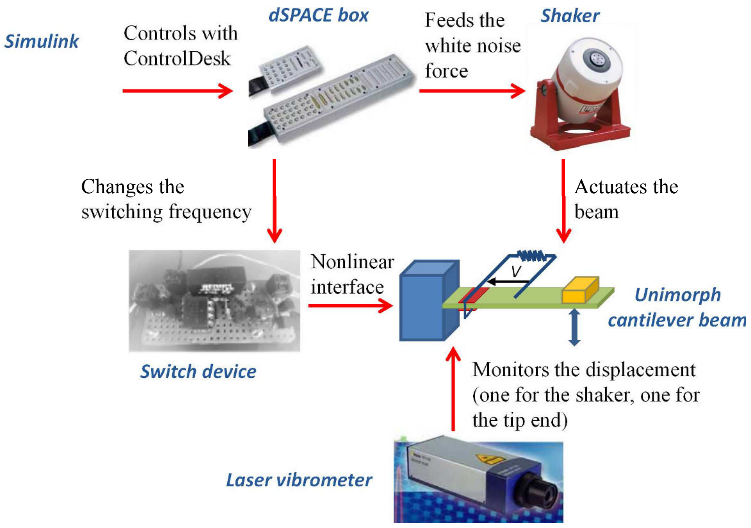

Figure 3.9: Experimental setup for PSHI technique under a band-limited white noise excitation

surements, the parameters could be obtained from [54]:

$$\alpha = \lambda C_0, \quad K_E = \alpha\lambda \frac{{f_{0E}}^2}{{f_{0D}}^2 - {f_{0E}}^2}, \quad M = \frac{K_E}{4\pi^2 {f_{0E}}^2},$$
$$C = \frac{2\pi M f_{0D}}{Q_{MD}}, \quad Q_{MD} = \frac{f_{0D}}{\Delta f}, \quad k^2 = \frac{{f_{0D}}^2 - {f_{0E}}^2}{{f_{0D}}^2}. \tag{3.74}$$

These identified parameters of the harvester are listed in Table 3.2.

A bandpass-filtered white noise acceleration is applied to the clamped end of the harvester through the shaker. The force is obtained by multiplying the base acceleration a with the proof mass M (Figure 3.10(a)). The bandpass filter for force excitation has a center frequency of 42.5 Hz and a frequency band of 80 Hz. For each measurement, the force is applied on the harvester for 17 s (as there is a storage limitation with ControlDesk). The piezoelectric power output is optimized with a 110 $k\Omega$ load, which is the experimental optimal load for monochromatic excitation with standard AC interface.

The performance of the piezoelectric harvester with a PSHI interface is shown in Figure 3.10(b) under different switching frequencies. In the experiment, 22 values of switching frequency from $f_s = 0.01 f_{0E}$ to $f_s = 3.9 f_{0E}$ have been investigated. For each switching frequency, the harvested power is averaged over 20 measurements. Error bars representing the standard error of the mean power is plotted in the figure showing that the discrepancy of data is relatively large around the notch point such as ω_{0E} and $2\omega_{0E}$. In addition, it should be noted that the mean value of the power is still very well represented by the stochastic model. It is clearly seen from Figure 3.10(b) that

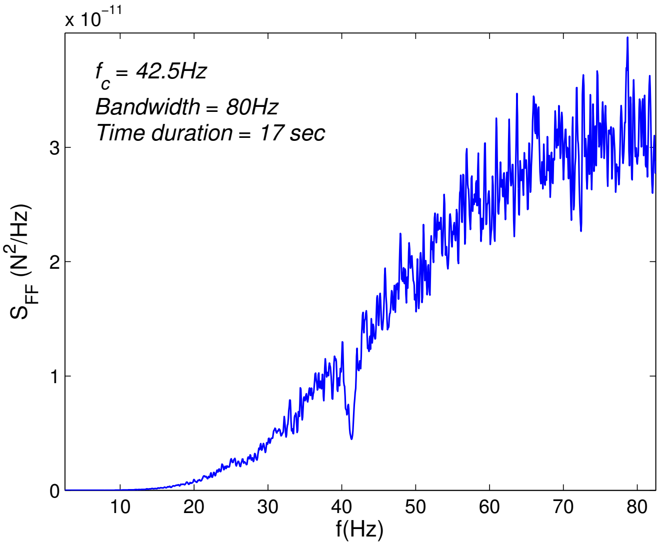

(a)

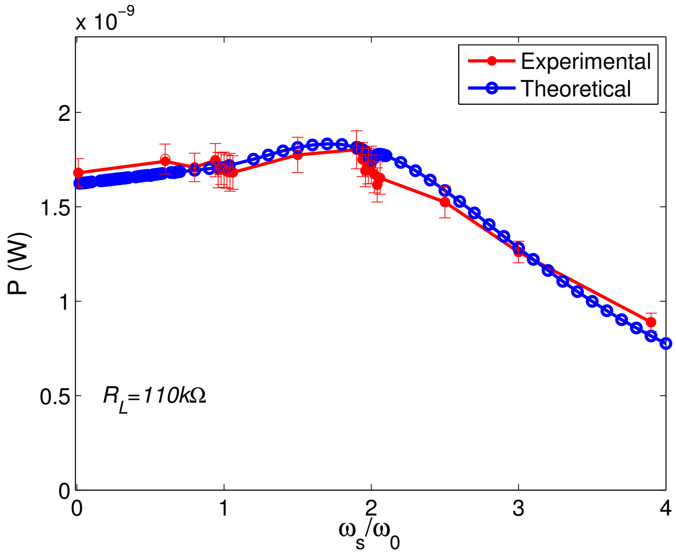

(b)

Figure 3.10: Experimental results. The harvested power is optimized with a 110 $k\Omega$ load resistance. (a) Autocorrelation of the input force; (b) Harvested power under different switching frequencies

Table 3.2: Experimental parameters for PSHI interfaced harvester under band-limited white noise force excitations

f_{0E}	$40.45\ Hz$
f_{0D}	$40.56\ Hz$
$\triangle f$	$0.944\ Hz$
λ	$1550\ V/m$
C_0	$50.3\ nF$
γ	0.694
Q_{MD}	43
k^2	0.543%
α	$7.7744 \times 10^{-5}\ N/V$
M	$0.3416\ g$
K_E	$22.06\ Nm^{-1}$
C	$0.0020\ Nm^{-1}s^{-1}$

the harvested power has the maximum value when the switching frequency is slightly less than $f_s = 2f_{0E}$ and has obvious drops when it is around $f_s = 1f_{0E}$ and $f_s = 2f_{0E}$, which is matching quite well with the simulation result. In general, the harvested power decreases when the switching frequency is getting higher. However, it should be noted that the simulation result with experimental model parameters showing that the optimal power is obtained when resistive load is around 450 $k\Omega$ and the real optimal power is about 1.4 times more than the experimental power (Figure 3.11). The increase of optimal load could be caused by the excitation not being monochromatic while the switching is not synchronized to the vibration waveform. There will generally be a time-shift between switching instants and maximum displacement points which have previously been shown to cause an increased optimal load for the parallel SSHI with small k^2Q_{M} [42]. Although the experimental results shown in the work is not the optimized case, it shows a very good correspondence with the theoretical modeling.

3.6 Comparison of SSHI AC and PSHI AC Interfaces

In this section, another validation of stochastic modeling through comparing with time-domain iterative calculations will be proposed. In addition, the comparison between using SSHI AC and PSHI AC techniques will also be presented under several excitation cases and for harvesting systems with different electromechanical coupling factors,

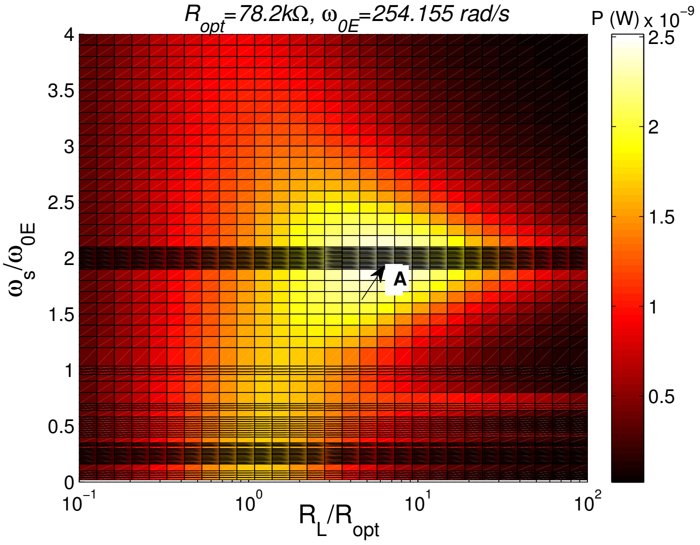

Figure 3.11: Harvested power as a function of switching frequency and resistive load with experimental parameters. Resistive load is normalized with the optimal load of standard case $R_{opt} = 78.2\ k\Omega$ and switching frequency is normalized with the harvester short-circuit resonance ω_{0E}. Point **A** shows the optimal harvested power $P_{opt} = 2.51 \times 10^{-3}(\mu)$W at $\omega_s = 1.9\omega_{0E}$ and $R_L = 5.5R_{opt} = 430$kΩ

which can be achieved by connecting different portion of piezoelectric inserts on a cantilever beam such as in [54].

The first excitation example going to be introduced is the filtered white noise force excitation with a center frequency at 4.6 Hz and a bandwidth of 20 Hz, which is shown in Figure 3.12. The excitation is also limited with a time-window to prevent time-domain aliasing effect. Also, a large enough frequency range is considered to assure all the frequency information is taken in the calculation. The simulation is calculated with the model parameter listed in Table 3.1. The mechanical quality factor Q_M is fixed with a medium value of 122.475. The validation of stochastic modeling is proved with the time-domain iterative calculation under two electromechanical coupling factors, $k^2 = 0.00167\%$ (Figure 3.13) and 3.164% (Figure 3.14) for weakly-coupled and highly-coupled cases respectively. Simulation results obtained from time-domain iterative calculations are averaged with 30 sets of calculations in order to get a representative result. A very good agreement is shown in the comparison between the time-domain calculation and the stochastic modeling for both standard AC technique ($\omega_s = 0\omega_{0E}$ in stochastic modeling) and PSHI AC technique. However, as the electromechanical coupling factor increases, the discrepancy between the two calculation methods becomes more evident. This can be solved by increasing both time and frequency resolutions,

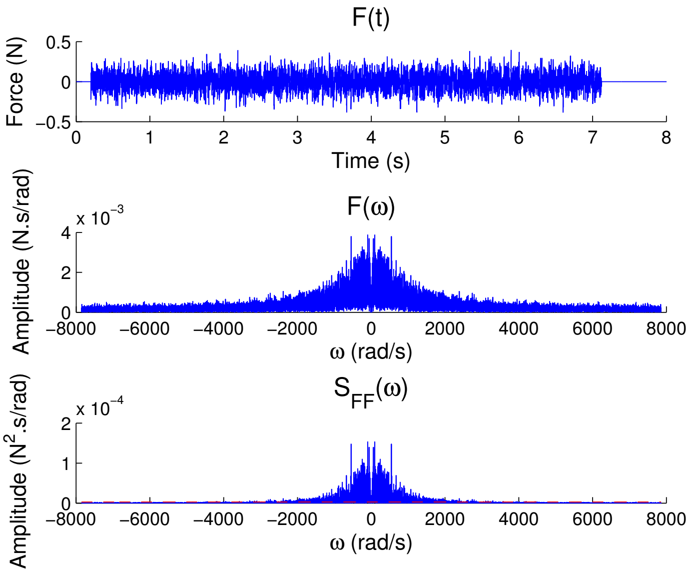

Figure 3.12: Filtered white noise force

but it is however very difficult to achieve in numerical calculation as there is a trade-off between the two resolutions. The comparison between SSHI AC, PSHI AC and standard AC techniques for filtered white noise force excitation is clearly presented in Figure 3.15. Simulation results are optimized with the resistive load, and for PSHI AC technique, optimal switching frequencies are chosen to permit optimal performances. It is worth noticing that when the electromechanical coupling factor is increasing, the optimal resistive load tends to decrease for all the connecting interfaces. In addition, SSHI AC and PSHI AC techniques can have a better improvement than using standard technique under a filtered white noise force when the electromechanical coupling factor k^2 is between very low value around 0.0167 % to 0.5 %, which is similar than under a monochromatic force excitation [52]. In addition, with a higher electromechanical coupling factor, the performance of PSHI AC technique approaches to SSHI AC technique with a lower switching frequency around $1.5\omega_{0E}$.

Another excitation example to be shown is the pulsed force excitation. A pulsed force contains more than one frequency information and is commonly seen in the real application, such as collision or ball striking. A pulsed force is applied on the harvester at $t = 0.01$ s with an amplitude of 0.01 N. The validation of stochastic modeling is also shown with the comparison of time-domain iterative calculation for two k^2 values. Instead of the harvested power, for an impulse response, the harvested energy is more

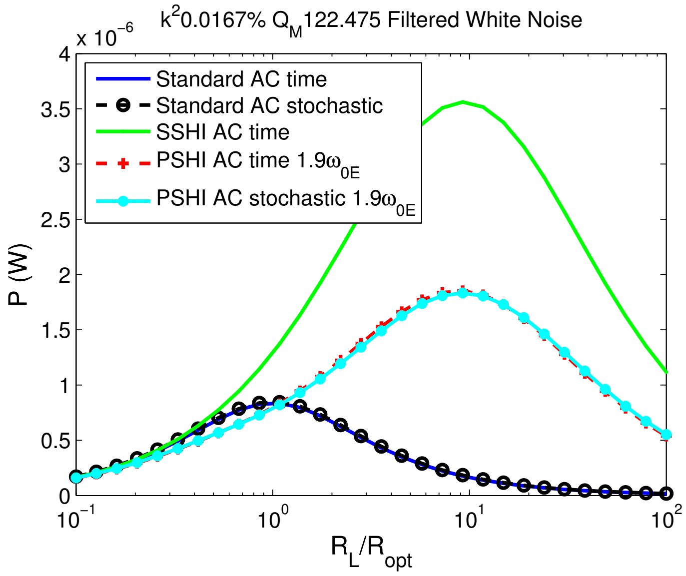

Figure 3.13: Validation of stochastic modeling with time-domain iterative calculations for weakly-coupled harvester under a filtered white noise force excitation

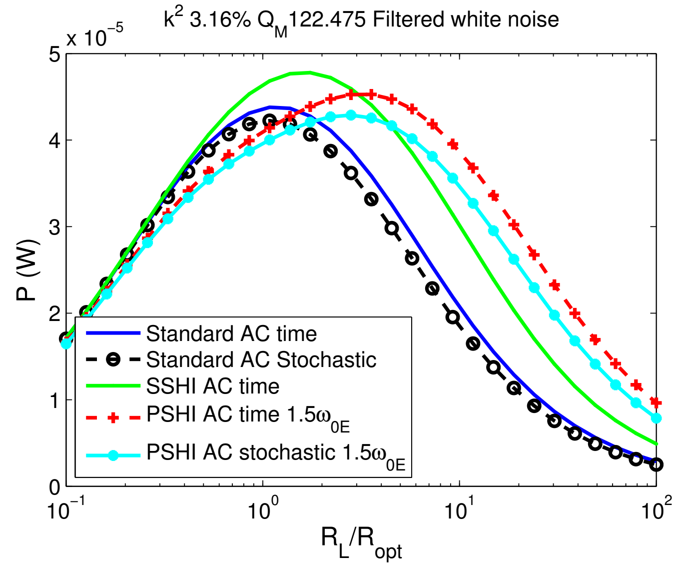

Figure 3.14: Validation of stochastic modeling with time-domain iterative calculations for highly-coupled harvester under a filtered white noise force excitation

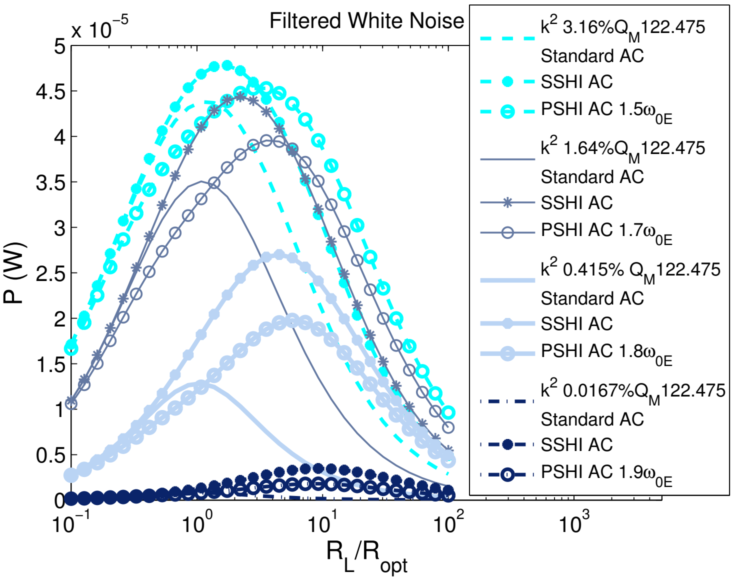

Figure 3.15: Comparison between SSHI, PSHI and standard techniques under a filtered white noise force excitation for several electromechanical coupling factors

important in the analysis. Through the comparison with time-domain calculation, the effectiveness of stochastic modeling on impulse response is proved. Very similar to under filtered white noise excitation, the optimal resistive load gets lower when electromechanical coupling factor increases and the performance of PSHI AC technique approaches to SSHI AC technique. The performance of PSHI AC technique under a pulsed force excitation is still less better than with SSHI AC technique even k^2Q_M value is already around 7.65. In addition, with a very high coupling factors, the benefit of using switching techniques no longer exists as the standard interfaced harvester performance can have similar or even better performances, and this can be found in Figure 3.18 when $k^2 = 6.25\%$ that the optimal switching frequency of PSHI technique approaches to zero.

The last excitation example to be shown is the multimodal force excitation, $F = 0.01 \times (1/2\cos(\omega_{0E}t) + \cos(2\omega_{0E}t) + \cos(4\omega_{0E}t) + 2\cos(12\omega_{0E}t))$, including both moderate and high frequency modes. The waveform of multimodal force can be referenced to Figure 3.19. The effectiveness of stochastic modeling under a multimodal force excitation is also validated through the comparison with time-domain iterative calculations for two electromechanical coupling factors showing weakly-coupled and highly-coupled cases in Figures 3.20 and 3.21 respectively. Similar to pulse and white-noise excitation cases, some discrepancies between the two calculation methods exist for highly-coupled systems because of insufficient resolutions in both time and frequency domains. Com-

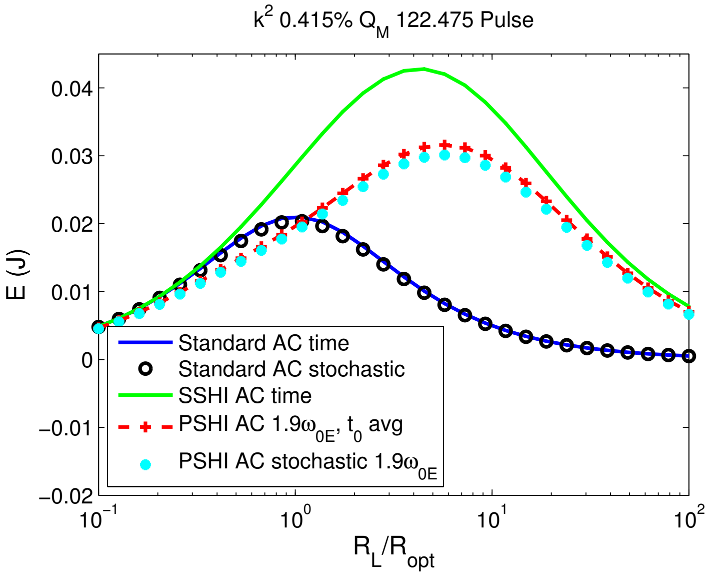

Figure 3.16: Validation of stochastic modeling with time-domain iterative calculations for weakly-coupled harvester under a pulse force excitation

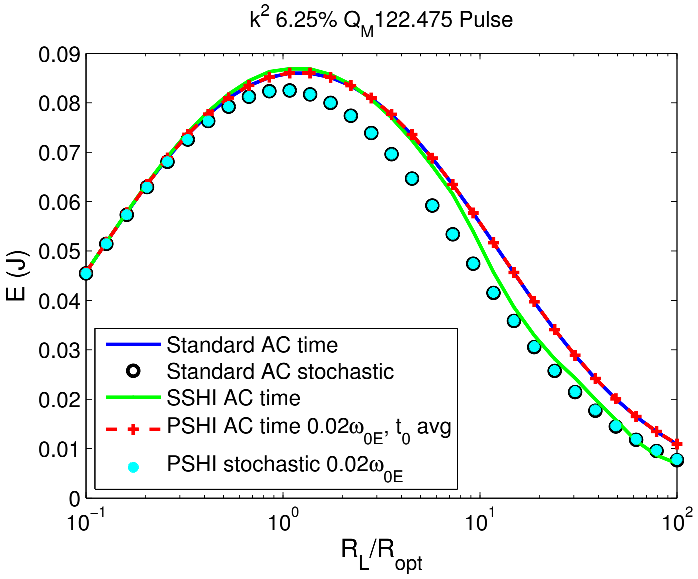

Figure 3.17: Validation of stochastic modeling with time-domain iterative calculations for highly-coupled harvester under a pulse force excitation

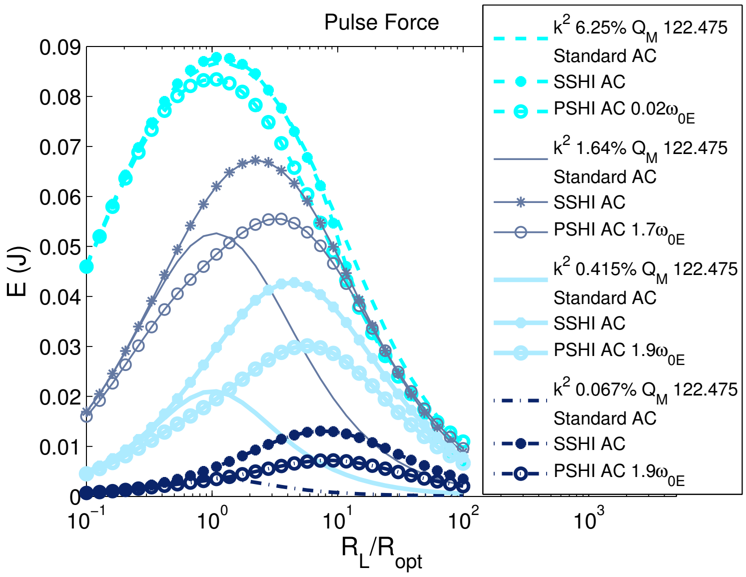

Figure 3.18: Comparison between SSHI, PSHI and standard techniques under a pulse force excitation for several electromechanical coupling factors

pared to pulse and filtered white noise excitation, under a multimodal force excitation, the harvester performance increases faster with the increase of electromechanical coupling factor, but the optimal resistive load however first decreases and then increases (Figure 3.22) as the standard interface works better for highly-coupled harvester. In addition, when the electromechanical coupling factor reaches around 1.6%, the performance of PSHI AC technique enhanced a lot and even better than using SSHI AC technique as the optimal switching frequency decreases, and this can be explained by the fact that less switching events reduce the inversion loss especially for highly-coupled harvesting system. A turning point for standard interface and switching interfaces occurs when $k^2 = 1.64\%$ as for PSHI AC technique with $\omega_s = 1.5\omega_{0E}$ (Figure 3.23), it already has a better performance than with SSHI AC interface although the optimal switching frequency approaches to zero. In addition, with a highly-coupled harvester, switching techniques become less efficient than the standard technique and the optimal switching frequency of PSHI AC technique approaches to zero. It can be also explained by the harvester displacement and voltage responses in Figure 3.23 that when the electromechanical coupling is large, the switching process leads large losses during the inversion process, and therefore decreases the vibration level and voltage output than using a classical standard AC or PSHI AC interfaces. For highly-coupled cases, simulation results from PSHI AC and standard AC ideally should be very similar in Figure 3.22 as the switching frequency is approaching to zero; the discrepancy is

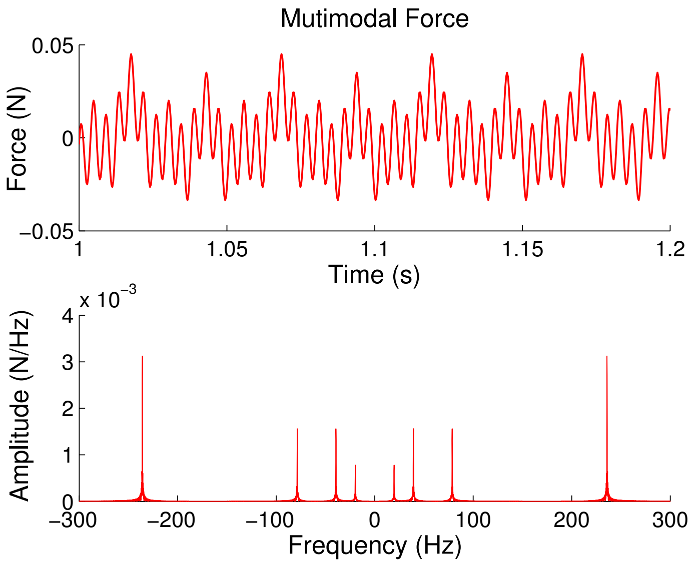

Figure 3.19: Multimodal force

however due to the numerical calculation.

3.7 Conclusion

The stochastic modeling of a switching-interfaced piezoelectric harvester under broadband force excitation based on stochastic processes and cyclostationary theory has been presented with a system working at a specific angular frequency ω_s. The stochastic modeling has been successfully validated with the result of standard AC interfaced harvester when ω_s approaches zero and with experimental results. A notch phenomenon (a sharp decrease in harvested power) is observed when switching frequency is around twice the system resonance frequency. A simplified model for weak-coupling harvester was also presented and verified. The stochastic modeling proposed in this work provides frequency-domain formula for analyzing the performance of a piezoelectric harvester with a periodic switching interface under a broadband force excitation of arbitrary force spectral density. The stochastic modeling introduced in this chapter works under any excitation spectrum given by a power spectral density and serves as a realistic design tool for this type of switched-interface piezoelectric harvesters. The stochastic modeling is validated both with the experimental measurement and the time-domain iterative calculation.

Using the derived mathematical model, the effect of different combinations of cou-

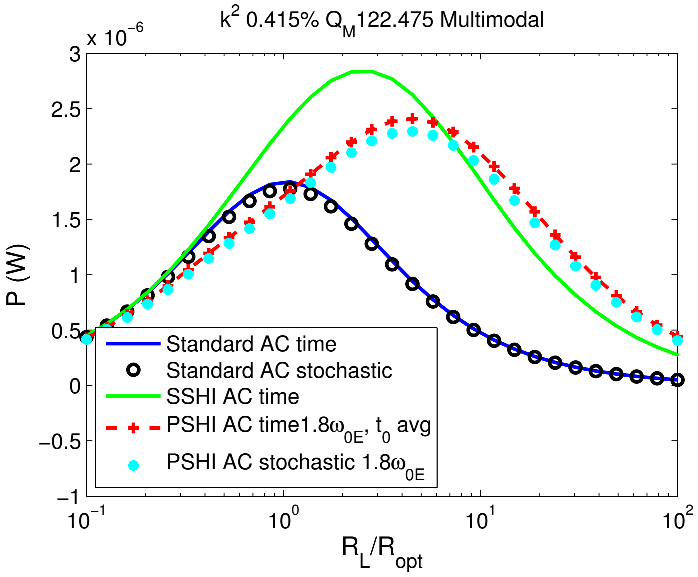

Figure 3.20: Validation of stochastic modeling with time-domain iterative calculations for weakly-coupled harvester under a multimodal force excitation

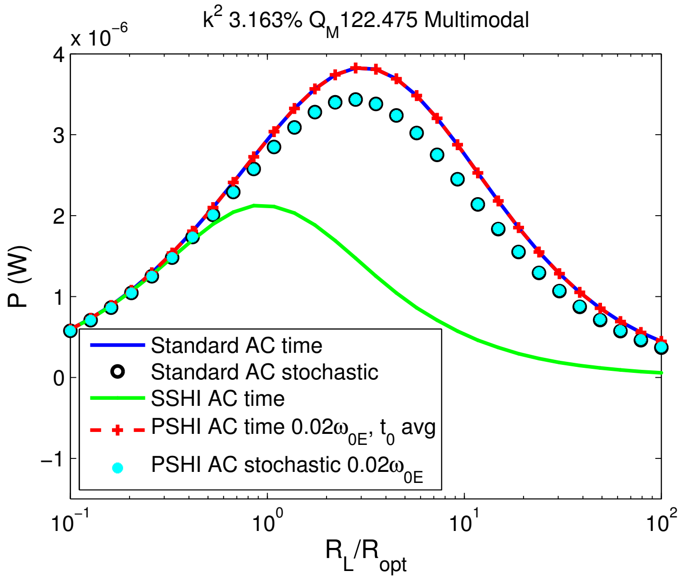

Figure 3.21: Validation of stochastic modeling with time-domain iterative calculations for highly-coupled harvester under a multimodal force excitation

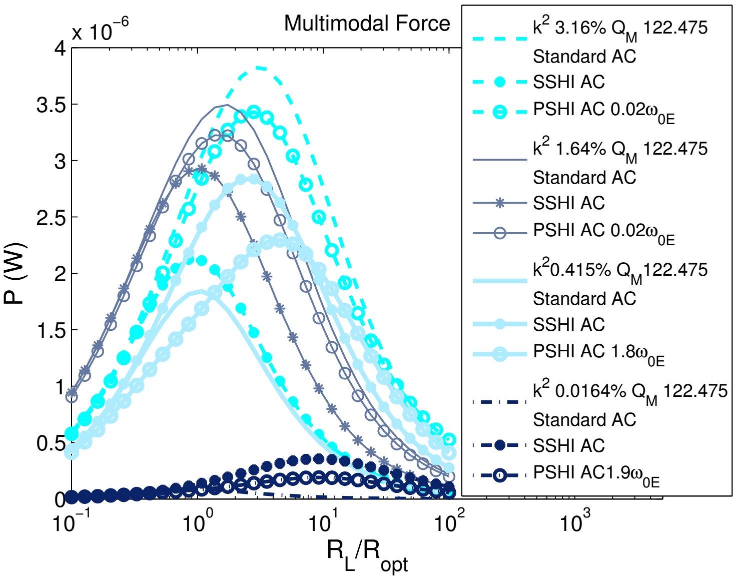

Figure 3.22: Comparison between SSHI, PSHI and standard techniques under a multimodal force excitation for several electromechanical coupling factors

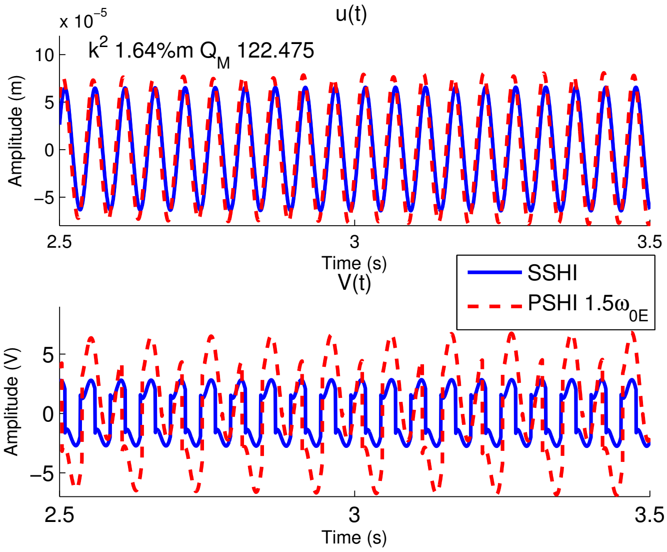

Figure 3.23: Highly-coupled harvester displacement and voltage responses under a mutimodal force excitation

pling coefficients k^2 and Q_M was discussed for a fixed range of Q_M and showed that when k^2 is very small, the very weakly coupled harvester will have an improved performance when increasing Q_M; however, for a harvester with larger k^2, the optimal scaled power output exhibits a maximal value then decreases with the increase of Q_M. It is also important to note that with a broadband force excitation, the harvester would have different power as a function of the product of k^2 and Q_M, which is not similar than the monochromatic force excitation case, which always has the same power for the same k^2Q_M. For a fixed Q_M, the harvester performance would improve with the increase of k^2 and the notch phenomenon around $2\omega_{0E}/p$, $p \in \mathbb{N}$ would be more pronounced. The harvester is proved to have best performance when the switching frequency is slightly less than twice the resonance frequency, which however depends on the coupling coefficient of the harvester, the higher coupling coefficient, the lower best switching frequency with respect to the natural frequency of the harvester.

Different spectral cross-correlation densities (SCDs) were also discussed. When the Gaussian lineshape of the SCD gets narrower, the excitation approaches the monochromatic excitation, and the normalized output power is better than when it has a large frequency band, where the normalized optimal power output will be approximately the same as with white noise SCD. The frequency shift between the center frequency of the Gaussian SCD and the harvester resonance frequency results in a decrease of the harvested power when the Gaussian SCD is narrow; however, a frequency shift within 7 % of the resonance frequency would only result in a decrease of the harvested power by no more than 10 %, which holds the similar result than using standard AC interface.

In the final part of this chapter, the stochastic modeling is validated with another method through the comparison with time-domain iterative calculation, and the performance of PSHI AC technique is compared with the SSHI AC and standard AC techniques. It is showing that for a highly-coupled case, a discrepancy exists between the numerical calculation with stochastic modeling and the time-domain iterative calculation because of the trade-off between frequency and time domain resolutions in numerical calculations. The discrepancy is however within 10% of error. The comparison between PSHI AC, SSHI AC and standard AC techniques is presented under filtered white noise, pulsed and multimodal force excitations. It can be found that with SSHI AC interface, the synchronized approach for the voltage inversion always has the best performance especially for weakly-coupled system. The SSHI AC technique can perform better than with standard AC and PSHI AC technique, especially for pulsed and filtered white noise excitation cases. However, for a highly-coupled harvester, the standard AC interface can have similar and even better performances than using SSHI AC interface no matter under what kind of excitations. Compared to SSHI AC interface, PSHI AC interface has less better performance in general as the phase delay between the real and the best switching instants is naturally taken into account in PSHI AC technique; it however might be easier to utilize as the optimal switching frequency is always fixed for a given excitation, and in some cases, for example, under a multimodal force excitation, the highly-coupled harvester might perform better with PSHI AC interface.

The further work of stochastic modeling could be extended to SSHI AC technique considering the nonlinear effect and phase effect by applying a time-window on the signal, and SSHI DC technique which introduces another nonlinear effect with the AC-DC converter. In addition, the mechanical coupling effect between the host structure and the harvester might be controlled using PSHI AC technique rather than SSHI AC technique for medium and highly-coupled harvesters.

4 The Effect of Seismic Energy Scavenging on Host Structure and Harvesting Performance

Considering the case of realistic applications of a seismic harvesting system, the purpose of this chapter is to study the effect of microgenerator on the host structure. The modeling of micro-generators has progressed from a constant displacement excitation to a constant force excitation, which takes into account the electromechanical damping induced by the harvesting process and limiting the power that can be delivered. Therefore, considering the mechanical coupling between the harvester and host structure on which it is installed is an extra step that can help us in designing harvesters with the entire chain of energy conversion process. For the sake of brevity and clarity, the modeling is restricted to the classical standard interface; the implementation of nonlinear interfaces can nevertheless be combined based on the modeling established in preceding chapters.

4.1 History of Modeling a Seismic or an Indirect-Coupled Harvesting System

Cantilevered piezoelectric energy harvesters have been studied extensively in recent years because it has benefits of easy maintenance and easy implementation in existing systems. Numerous techniques have been investigated to achieve optimal power output. However, extracting electrical energy from mechanical vibration leads to a reduction of the vibration magnitude of the harvester because of the electromechanical coupling effect [57, 58], and so a model considering constant vibration magnitude [56, 59] is no longer valid. Thus, an energy harvesting model excited with a constant force or accel-

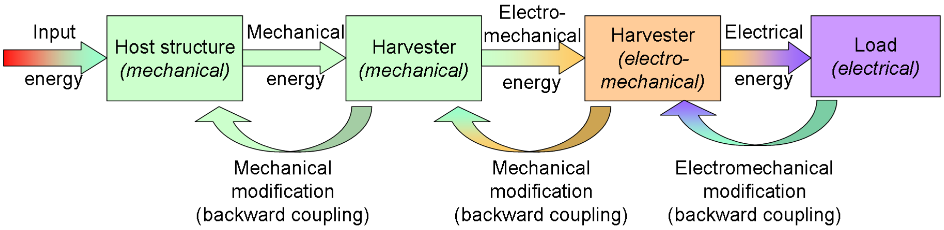

Figure 4.1: Energy flow in the whole system

eration magnitude has been adopted to take into account the damping effect induced by the energy harvesting process due to the electromechanical coupling. However, a SDOF model cannot reflect the mechanical to mechanical coupling effect in many practical applications using seismic piezoelectric harvesters. The mechanical to mechanical coupling effect would indeed result in an additional damping of the host structure due to the mechanical to mechanical energy conversion between the host structure and the harvester (Figure 4.1), and thus a decreased output power. With the concept of energy balance between the host structure and the harvester and the electromechanical coupling of the harvester itself and between the harvester and the adaptive load, the proportional tendency of the harvested power and the harvester mass proposed in the work of Roundy *et al* [63] might be no longer valid. The purpose of this chapter is therefore to study the mechanical backward coupling of seismic energy harvesting, hence extending the constant acceleration magnitude case and providing an improved model in designing efficient harvesters for given host structures. It has to be noted that the scope of this work is not to optimize the whole TDOF system by considering that the host structure is a part of the harvester, as exposed in [101, 104, 138, 139], but, for a given and fixed host structure, to demonstrate that the constant acceleration magnitude case may no longer be valid because of the mechanical backward coupling, and to discuss the impact on the power optimization of the harvester.

Theoretical developments are presented as a dynamic problem of an electromechanically coupled two-degree-of-freedom (TDOF) spring-mass-damper system. Then experimental measurements and computations based on Finite Element Modeling (FEM) are carried out to validate theoretical predictions. It is shown that the extracted power obtained from the TDOF model would reach a maximal value by tuning the mass ratio between host structure and harvester and optimizing the electric load. The mechanical to mechanical coupling effect due to the harvester leads a trade-off between the mechanical energy of the host structure and the harvested energy, showing that the coupling between two mechanisms, the host structure and the harvester has to be discussed carefully. In addition, the harvested power calculated with the classical SDOF model under a constant acceleration magnitude overestimates the power output as the SDOF model does not consider the backward damping effect due to mechanical to mechanical coupling. The work proposed in this chapter provides a quick idea in designing a seismic piezoelectric harvester for a specific host structure.

The detailed discussion of the effect of seismic energy harvesting on the host structure and the harvesting performance is arranged into six sections. The theoretical modelings with a TDOF model and a FEM model will be presented in Section 4.2 and validated in Section 4.3 with an experimental validation and a practical application on the Structural Health Monitoring (SHM) system. Then the coupling effect between the host structure and the harvester during the harvesting process will be discussed in Section 4.4. In Section 4.5, the TDOF modeling is extended with the stochastic modeling considering practical excitations which include more frequency information such as white noise, random vibration and etc.. The effect of frequency detuning between the harvester and host structure resonant frequency on the harvester performance will be discussed in Section 4.6 and in the final section, a conclusion to summarize this chapter work will be presented.

4.2 Theoretical Modeling

4.2.1 Two-Degree-of-Freedom (TDOF) Model

The harvester is composed of a cantilever beam with bimorph piezoelectric layers attached on its top and bottom sides and connected in parallel. To reveal the mechanical to mechanical coupling effect, a two degree of freedom model consisting in a seismic energy harvester attached on the host structure (Figure 4.2) is introduced. A variable resistor R_L is considered as the electric load representing the next stages of the harvesting chain.

According to Newton's second law of motion, the equations of motion Eq. (4.1) for a two degree of freedom system can be found as:

$$\begin{aligned}
&M_1\ddot{u}_1(t) = -K_1u_1(t) - C_1\dot{u}_1(t) + K_2\left[u_2(t) - u_1(t)\right] + C_2\left[\dot{u}_2(t) - \dot{u}_1(t)\right] + \alpha V(t) + F(t)\\
&M_2\ddot{u}_2(t) = -K_2\left[u_1(t) - u_2(t)\right] - C_2\left[\dot{u}_2(t) - \dot{u}_1(t)\right] - \alpha V(t),
\end{aligned} \tag{4.1}$$

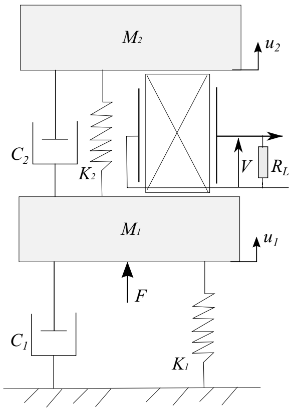

Figure 4.2: Equivalent TDOF mechanical model for energy harvesting system

where u_1 and u_2 are the absolute displacements of the dynamic mass M_1 of the host structure and harvester mass M_2 respectively; F is the external force acting on the mass M_1, αV is the piezoelectric force (with V the voltage and α the force factor), K_1, K_2 and C_1, C_2 are given as effective stiffness and structural damping coefficients, respectively. The piezoelectric patch is characterized by its effective piezoelectric coupling coefficient k, force factor α and clamped capacitance C_0.

The equations of motion can be also expressed in matrix form using mass matrix **M**, stiffness matrix **K** and damping matrix **b**, as well as displacement vector **u**, force vector **F** and piezoelectric force factor vector **A**:

$$\mathbf{M\ddot{u}(t)} + \mathbf{C\dot{u}(t)} + \mathbf{Ku(t)} = \mathbf{F(t)} + \mathbf{A}V(t), \tag{4.2}$$

where:

$$\mathbf{u}(t) = \begin{bmatrix} u_1(t) \\ u_2(t) \end{bmatrix}, \mathbf{F}(t) = \begin{bmatrix} F(t) \\ 0 \end{bmatrix}$$
$$\mathbf{M} = \begin{bmatrix} M_1 & 0 \\ 0 & M_2 \end{bmatrix}, \mathbf{K} = \begin{bmatrix} K_1 + K_2 & -K_2 \\ -K_2 & K_2 \end{bmatrix}, \mathbf{C} = \begin{bmatrix} C_1 + C_2 & -C_2 \\ -C_2 & C_2 \end{bmatrix}, \mathbf{A} = \begin{bmatrix} \alpha \\ -\alpha \end{bmatrix}.$$

Assuming that the excitation applied on the host structure is a periodic force with an angular frequency ω and a constant magnitude F_M, the displacement vector $\mathbf{u(t)}$ can be then solved by supposing the form $\mathbf{u(t)} = \text{Re}\left[\tilde{\mathbf{U}}e^{i\omega t}\right]$, $V(t) = \text{Re}\left[\tilde{V}e^{i\omega t}\right]$, where $\tilde{U_1} = U_1 e^{j\phi_1}$, $\tilde{U_2} = U_2 e^{j\phi_2}$ and $\tilde{V} = |\tilde{V}|e^{j\phi_V}$; U_1, U_2 and $|\tilde{V}|$ being respectively displacement and voltage magnitudes, and ϕ_i is the phase shift reference to the force excitation. Accordingly, the host structure and the harvester would have the following displacement response:

$$\left\{ \begin{array}{c} \tilde{U_1}(\omega) \\ \tilde{U_2}(\omega) \end{array} \right\} = \mathbf{T}(\omega) \left\{ \begin{array}{c} F_M + \alpha\tilde{V}(\omega) \\ -\alpha\tilde{V}(\omega) \end{array} \right\} = \mathbf{T}(\omega) \left\{ \begin{array}{c} F_M \\ 0 \end{array} \right\} + \mathbf{T}(\omega) \begin{bmatrix} 1 \\ -1 \end{bmatrix} \alpha\tilde{V}(\omega). \quad (4.3)$$

with:

$$\mathbf{T}(\omega) = \begin{bmatrix} -M_1\omega^2 + (C_1 + C_2)j\omega + (K_1 + K_2) & -C_2 j\omega - K_2 \\ -C_2 j\omega - K_2 & -M_2\omega^2 + C_2 j\omega + K_2 \end{bmatrix}^{-1}. \quad (4.4)$$

The voltage magnitude across the piezoelectric patch may be derived from the constitutive equations of piezoelectricity [140] as:

$$\tilde{V}(\omega) = \frac{\alpha R j\omega}{1 + C_0 R j\omega}(\tilde{U_2}(\omega) - \tilde{U_1}(\omega)) = g(\omega) \begin{bmatrix} -1 & 1 \end{bmatrix} \left\{ \begin{array}{c} \tilde{U_1}(\omega) \\ \tilde{U_2}(\omega) \end{array} \right\} \quad (4.5)$$

$$\text{with } g(\omega) = \frac{\alpha R j\omega}{1 + C_0 R j\omega}, \quad (4.6)$$

so that Eq. (4.3) may be rewritten as:

$$\left\{ \begin{array}{c} \tilde{U_1}(\omega) \\ \tilde{U_2}(\omega) \end{array} \right\} = \mathbf{T}(\omega) \left\{ \begin{array}{c} F_M \\ 0 \end{array} \right\} + \mathbf{G}(\omega) \left\{ \begin{array}{c} \tilde{U_1}(\omega) \\ \tilde{U_2}(\omega) \end{array} \right\}, \quad (4.7)$$

where

$$\mathbf{G}(\omega) = \alpha g(\omega)\mathbf{T}(\omega) \begin{bmatrix} -1 & 1 \\ 1 & -1 \end{bmatrix}. \quad (4.8)$$

so that the global displacement response is given as:

$$\left\{ \begin{array}{c} \tilde{U_1}(\omega) \\ \tilde{U_2}(\omega) \end{array} \right\} = \mathbf{L}(\omega) \left\{ \begin{array}{c} F_M \\ 0 \end{array} \right\}, \quad (4.9)$$

with:

$$\mathbf{L}(\omega) = (\mathbf{I}_2 - \mathbf{G}(\omega))^{-1} \mathbf{T}(\omega), \quad (4.10)$$

where $\mathbf{I}_n$ denotes the identity matrix of size n. From the voltage response Eq. (4.5) and displacement response Eq. (4.9), the expression of the average harvested power is then given by:

$$P = \frac{1}{2}\frac{\tilde{V}(\omega)\tilde{V}^*(\omega)}{R_L}, \quad (4.11)$$

* denoting the complex conjugate.

4.2.2 Finite Element Method (FEM) Modeling

In this section, the modeling of the harvester and host structure system based on Finite Element Method is proposed in frequency domain as an alternative method to validate the results from TDOF model. In order to simplify the approach, the following assumptions are made:

1. The structure acts as a pure Euler-Bernoulli beam (*i.e.* $T_3 = 0$) for both the harvester and the host structure.
2. The strain is 2D plane only (*i.e.* $S_2 = 0$).
3. The electric field is constant along the thickness of the piezoelectric element (x_3).
4. The piezoelectric material is assumed as a transversely isotropic material.

With the plane strain assumption and based on the material constitutive equations, for the beams (harvester substrate and host structure), the longitudinal stress T_1 is linked with the strain S_1 by:

$$T_1 = c_b S_1 = \frac{\psi}{1-\upsilon^2} S_1, \tag{4.12}$$

where ψ is the Young's modulus and υ is the Poisson's ratio of the beam. The general expression of the strain S_1 and S_2 in the piezoelectric elements along the x_1 axis and the x_2 axis and the electrical displacement D_3 could be linked using the piezoelectric constitutive equations considering isotropic material as:

$$\begin{cases} S_1 = s_{11}^E T_1 + s_{12}^E T_2 + s_{13}^E T_3 + d_{31} E_3 \\ S_2 = s_{12}^E T_1 + s_{11}^E T_2 + s_{23}^E T_3 + d_{31} E_3 \\ D_3 = d_{31} T_1 + d_{31} T_2 + d_{33} T_3 + \varepsilon_{33}^T E_3, \end{cases} \tag{4.13}$$

where s_{ij}^E corresponds to the mechanical compliance tensor of the piezoelectric element in short-circuit condition, d_{kl} are the piezoelectric constants, ε_{33}^T is defined as the permittivity under constant stress, and E_3 is the electric field in x_3 direction. With the plane-strain condition, $S_2 = 0$, and with the pure bending assumption, $T_3 = 0$. Hence, the longitudinal stress of the piezoelectric element is thus obtained as:

$$T_1 = \frac{s_{11}^E}{{s_{11}^E}^2 - {s_{12}^E}^2} S_1 - \frac{d_{31}}{s_{11}^E + s_{12}^E} E_3 \tag{4.14}$$

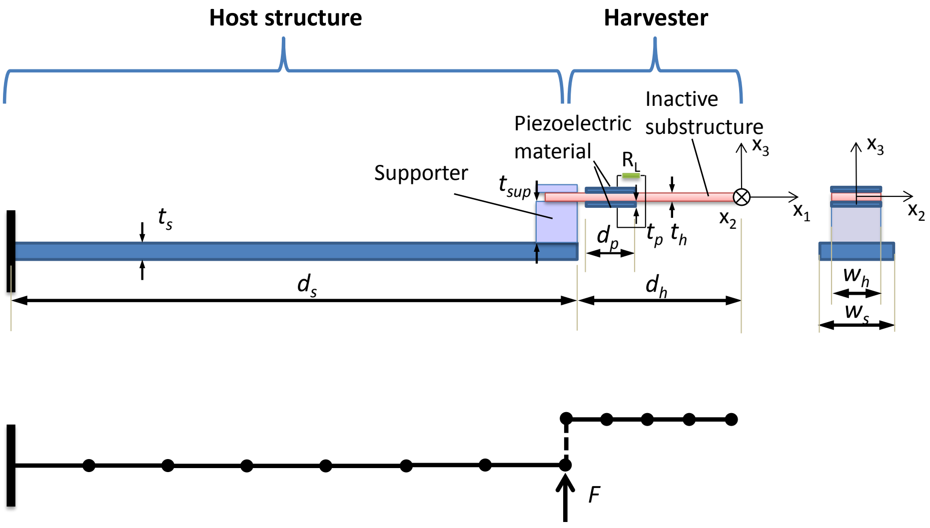

Figure 4.3: Layout and geometric parameters of the host structure and the cantilevered vibration energy harvester

Assuming a thin piezoelectric layer, the electric field E_3 can be expressed as a function of the potential difference V across the thickness t_p of the piezoelectric element:

$$E_3 = -\frac{V}{t_p}. \tag{4.15}$$

In bimorph configuration and according to the polarization direction in the piezoelectric materials, the electric field for the upper element is $E_{3up} = V/t_p$ and for the lower element is $E_{3low} = -V/t_p$ as the voltage is referenced to the substructure. The strain in x_1 axis (S_1) has the general expression of the product of the curvature of the beam by the distance from the neutral axis x_c to a point of interest:

$$\begin{aligned} S_1 &= -\left(u_3 - x_c\right)\frac{\partial^2 u_3}{\partial {x_1}^2}, \\ x_c &= 0, \text{ for piezoelements and inactive substrate} \\ x_c &= \frac{-t_h}{2} - t_{sup} + \frac{-t_H}{2}, \text{ for the host beam,} \end{aligned} \tag{4.16}$$

where u_3 is given as the deflection, t_h, t_{sup} and t_H are respectively the thickness of the inactive substrate, the supporter and the host structure. The coordinate origin is shown in Figure 4.3. The schematic FEM model is plotted in Figure 4.3, where the free end of the host structure and the clamped-end of the harvester share a common node; nevertheless, the neutral axis for each structures is different.

As the bending moment could be expressed as the area integral of the product of the longitudinal force and the deflection reference to the neutral axis:

$$\mathrm{M} = \int_A T_1 \left(u_3 - x_c\right) dA, \tag{4.17}$$

the overall bending moment of the harvester $\mathrm{M}_{harvester}$ is the combination of the bending moment of the piezoelectric layers M_{piezo} and the inactive beam M_{beam}, yielding:

$$\begin{aligned}
\mathrm{M}_{harvester} &= \mathrm{M}_{piezo} + \mathrm{M}_{beam} \qquad (4.18)\\
\mathrm{M}_{piezo} &= -E_p J_p \frac{\partial^2 u_3}{\partial x_1^2} - \frac{d_{31} w_p}{s_{11}^E + s_{12}^E} E_{3j} \int_{-\frac{t_h}{2}-t_p}^{-\frac{t_h}{2}} u_3 dx_3 \\
&\quad - E_p J_p \frac{\partial^2 u_3}{\partial x_1^2} - \frac{d_{31} w_p}{s_{11}^E + s_{12}^E} E_{3i} \int_{\frac{t_h}{2}}^{\frac{t_h}{2}+t_p} u_3 dx_3 \\
\mathrm{M}_{beam} &= -E_h J_h \frac{\partial^2 u_3}{\partial x_1^2},
\end{aligned}$$

where J_p and J_h are the second moment of inertia for the piezoelectric plate and the inactive substructure:

$$\begin{aligned}
J_h &= w_h \int_{-\frac{t_h}{2}}^{\frac{t_h}{2}} \left(u_3 - x_c\right)^2 dx_3 \\
J_p &= w_p \int_{-\frac{t_h}{2}-t_p}^{-\frac{t_h}{2}} \left(u_3 - x_c\right)^2 dx_3 = w_p \int_{\frac{t_h}{2}}^{\frac{t_h}{2}+t_p} \left(u_3 - x_c\right)^2 dx_3 \qquad (4.19)\\
x_c &= 0.
\end{aligned}$$

From the expression of M_{piezo} (Eq. (4.18)), it is clearly shown that for a bimorph piezoelectric patch, the mechanical effect is doubled as the second moment of inertia J_p for the upper layer and the lower layer are identical. The bending moment on the host structure M_{host} is the same as stated above, except that the position of neutral axis is along the middle axis of the host structure,

$$\begin{aligned}
\mathrm{M}_{host} &= -E_H J_H \frac{\partial^2 u_3}{\partial x_1^2} \qquad (4.20)\\
J_H &= w_H \int_{-\frac{t_h}{2}-t_{sup}-t_H}^{-\frac{t_h}{2}-t_{sup}} \left(u_3 - x_c\right)^2 dx_3 \\
x_c &= \frac{-t_h}{2} - t_{sup} + \frac{-t_H}{2}
\end{aligned}$$

For a dynamic Euler-Bernoulli beam, the Euler-Lagrange equation for beams is given by:

$$\frac{\partial^2}{\partial {x_1}^2} \left(-M_{overall}\right) = -\bar{m} \frac{\partial^2 u_3}{\partial {x_1}^2} + q\left(x_1, t\right), \tag{4.21}$$

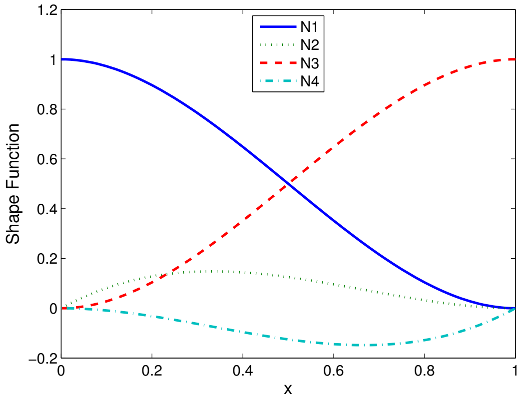

Figure 4.4: The Hermite Cubic Shape functions

where $q(x_1,t)$ denotes the external force applied at position x_1 and $\bar{m}$ is the mass per unit length of the structure. Based on the theory of Finite Element Method, the deflection and the slope of the beam could be expressed in terms of the nodal variables and the Hermitian polynomial as the cubic shape function $\mathbf{N}(x) = \{\ N_1(x) \quad N_2(x) \quad N_3(x) \quad N_4(x)\ \}$, which are defined as:

$$\begin{matrix} N_1(x) = 1 - \frac{3x^2}{l^2} + \frac{2x^3}{l^3}, & N_2(x) = x - \frac{2x^2}{l} + \frac{x^3}{l^2} \\ N_3(x) = \frac{3x^2}{l^2} - \frac{2x^3}{l^3}, & N_4(x) = -\frac{x^2}{l} + \frac{x^3}{l^2} \end{matrix}, \tag{4.22}$$

and with graphs depicted in Figure 4.4. The equation of motion is then written as:

$$[\mathbf{M}]\{\ddot{d}(t)\} + [\mathbf{C}]\{\dot{d}(t)\} + [\mathbf{K}]\{d(t)\} - B_1 V(t) = \{\mathbf{F}(t)\}, \tag{4.23}$$

where the damping matrix $\mathbf{C}$ is commonly defined by the Rayleigh equation:

$[\mathbf{C}] = \chi[\mathbf{M}] + \beta[\mathbf{K}]$,

χ and β are multiplication factors defined by damping ratio ζ and natural frequencies ω_1, ω_2,

$\chi = \zeta\dfrac{2\omega_1\omega_2}{\omega_1+\omega_2}$, $\beta = \zeta\dfrac{2}{\omega_1+\omega_2}$,

and nodal degree of freedom $\{d\} = \{\ u_i \quad \theta_i\ \}^T$, where $\theta_i = \dfrac{\partial u_{3i}}{\partial x_1}$.

Applying the bending moments stated in Eq. (4.18) and Eq. (4.20) into the Euler-Lagrange equation (4.21), and applying the shape functions, the mass matrix $\mathbf{M}$, stiffness matrix $\mathbf{K}$ and force vector $\mathbf{B}_1$ can be found as:

$$[\mathbf{M}] = \int_0^l m[\mathbf{N}]^T[\mathbf{N}]dx_1 \tag{4.24}$$

$$[\mathbf{K}] = \int_0^l [\mathbf{N}'']^T EJ[\mathbf{N}'']dx_1 \tag{4.25}$$

$$\mathbf{B}_1 = \frac{d_{31}(t_p+t_h)}{({s_{11}}^E+{s_{12}}^E)} w_p \int_0^l [\mathbf{N}'']^T dx_1, \tag{4.26}$$

Accordingly, the overall mass matrix is written as:

$$[\mathbf{M}] = \begin{bmatrix} {M_H}^{\mathrm{i}}{}_{22}+{M_H}^{\mathrm{ii}}{}_{11} & {M_H}^{\mathrm{ii}}{}_{12} & 0 & 0 & 0 & 0 \\ {M_H}^{\mathrm{ii}}{}_{12} & {M_H}^{\mathrm{ii}}{}_{22}+{M_H}^{\mathrm{iii}}{}_{11} & {M_H}^{\mathrm{iii}}{}_{12} & 0 & 0 & 0 \\ 0 & {M_H}^{\mathrm{iii}}{}_{21} & \ddots & {M_H}^{\mathrm{j}}{}_{12} & 0 & 0 \\ 0 & 0 & M_{H21}^{\mathrm{j}} & M_{H22}^{\mathrm{j}}+M_{h11}^{\mathrm{i}} & M_{h12}^{\mathrm{i}} & 0 \\ 0 & 0 & 0 & M_{h21}^{\mathrm{i}} & \ddots & M_{h12}^{\mathrm{l}} \\ 0 & 0 & 0 & 0 & M_{h21}^{\mathrm{l}} & M_{h22}^{\mathrm{l}} \end{bmatrix}_{(n+L)*2}. \tag{4.27}$$

The host structure is assumed to have n elements, and the harvester has L elements. For the notation in $\mathbf{M}$ matrix; for example, M_{H22}^{i} means the second-row-second-column element in the mass matrix of the ith element and the subscript H defines the element mass of the host structure. In the mass matrix $\mathbf{M}$, the part belonging to the harvester M_h (subscript h defining the harvester) is constructed with the same rule with the inactive substructure and the piezoelectric material; the overall stiffness matrix $\mathbf{K}$ could be also formed with the same principle presented above. The beam element mass matrix $\mathbf{M_e}$ and stiffness matrix $\mathbf{K_e}$ are expressed as:

$$\mathbf{K_e} = E_eJ_e \begin{bmatrix} \frac{12}{{l_e}^3} & \frac{6}{{l_e}^2} & \frac{-12}{{l_e}^3} & \frac{6}{{l_e}^2} \\ \frac{6}{{l_e}^2} & \frac{4}{l_e} & \frac{-6}{{l_e}^2} & \frac{2}{l_e} \\ \frac{-12}{{l_e}^3} & \frac{-6}{{l_e}^2} & \frac{12}{{l_e}^3} & \frac{-6}{{l_e}^2} \\ \frac{6}{{l_e}^2} & \frac{2}{l_e} & \frac{-6}{{l_e}^2} & \frac{4}{l_e} \end{bmatrix}, \quad \mathbf{M_e} = \frac{\rho_eA_el_e}{420} \begin{bmatrix} 156 & 22l_e & 54 & -13l_e \\ 22l_e & 4{l_e}^2 & 13l_e & -3{l_e}^2 \\ 54 & 13l_e & 156 & -22l_e \\ -13l_e & -3{l_e}^2 & -22l_e & 4{l_e}^2 \end{bmatrix}, \tag{4.28}$$

where the subscript $_e$ denotes the beam element. The host structure is clamped at one end, and the external force is applied in the other end (Figure 4.3). The harvester is attached to the host structure free-end with an U-shape supporter ($0.46 \times 15 \times 17.5 \times 20 \times 10^{-9}\ \ m^3 \times 2700\ \ kg/m^3$, where the coefficient 0.46 is used to approximate the U-shape volume), and two magnets ($2 \times 3.8 \times 1.74 \times 3.8 \times 10^{-9}\ \ m^3 \times 7800\ \ kg/m^3$) are placed in the harvester free-end as a seismic mass.

From the expression of electrical displacement D_3 (Eq. (4.13)), the electrical charge Q can be obtained by taking the integration of D_3 over the longitudinal length:

$$Q = w_p \int D_3 dx_1. \tag{4.29}$$

The electrical charge Q_i distributed on each piezoelectric element i (here the element states the elements in the FEM model) is then expressed as:

$$\begin{aligned} Q_i(t) &= -\frac{w_p d_{31} t_p}{\left(s_{11}^E + s_{12}^E\right)} \left.\frac{\partial u_3(t)}{\partial x_1}\right|_{x_{i0}}^{x_{i0}+L_{pi}} - \frac{w_p L_{pi} \left[\varepsilon_{33}^T \left(s_{11}^E + s_{12}^E\right) - 2{d_{31}}^2\right]}{t_p \left(s_{11}^E + s_{12}^E\right)} V_i(t) \\ &= -\frac{w_p d_{31} t_p}{\left(s_{11}^E + s_{12}^E\right)} \theta(t)|_{x_{i0}}^{x_{i0}+L_{pi}} - \frac{w_p L_{pi} \varepsilon_{33}^S}{t_p} V_i(t), \end{aligned} \tag{4.30}$$

where L_{pi} is the element length and ε_{33}^S is the permittivity coefficient under constant strain. For a bimorph harvester connected in parallel, the overall charge is twice the value obtained from Eq. (4.30), and the upper plate and the lower plate have equal voltage:

$$\begin{aligned} \dot{Q}(t) &= \dot{Q}_{up}(t) + \dot{Q}_{up}(t) = 2\dot{Q}_{up}(t) = \frac{V(t)}{R_L}, \\ V_{up}(t) &= V_{low}(t) = V(t). \end{aligned} \tag{4.31}$$

The voltage derivative is then given by:

$$\begin{aligned} \dot{V}(t) &= -\frac{d_{31} {t_p}^2}{L_p \left(s_{11}^E + s_{12}^E\right) \varepsilon_{33}^S} \left.\dot{\theta}(t)\right|_{x_0}^{x_0+L_p} - \frac{t_p}{w_p L_p \varepsilon_{33}^S R_L} V(t) \\ &= B_2 \left.\dot{\theta}(t)\right|_{x_0}^{x_0+L_p} + B_3 V(t), \end{aligned} \tag{4.32}$$

where R_L is the load resistance. The system of equations in frequency domain will then lead to:

$$\begin{bmatrix} \left([\mathbf{K}] - \omega^2 [\mathbf{M}]\right) + j [\mathbf{C}] \omega & -B_1 \\ j\omega \mathbf{B}_2 & B_3 - j\omega \end{bmatrix} \begin{bmatrix} \tilde{\mathbf{d}}(\omega) \\ \tilde{V}(\omega) \end{bmatrix} = \begin{bmatrix} \tilde{\mathbf{F}}(\omega) \\ 0 \end{bmatrix}. \tag{4.33}$$

Frequency response of voltage $\tilde{V}(\omega)$ and harvested power $P(\omega)$ at a particular frequency could then be expressed as:

$$\tilde{V}(\omega) = [B_3 - j\omega]^{-1} [j\omega \mathbf{B}_2] \times \tilde{\mathbf{d}}(\omega) \tag{4.34}$$

$$P(\omega) = \frac{\tilde{V}(\omega) \tilde{V}^*(\omega)}{2R_L}. \tag{4.35}$$

Table 4.1: Host and harvester beam characteristics for FEM model

Length, d_H	0.104 m	**Thickness**, t_H	0.52 m
Width, w_H	0.04 m	**Young's modulus**, E_H	210 Gpa
Poisson's ratio, ν_H	0.3	**Density**, ρ_H	7450 kg/m^3
Damping ratio, ζ_H	0.007		
Length, d_h	0.033 m	**Thickness**, t_h	49.4 μm
Width, w_h	0.02 m	**Young's modulus**, E_h	210 Gpa
Poisson's ratio, ν_h	0.3	**Density**, ρ_h	7480 kg/m^3
Damping ratio, ζ_h	0.0658		
Length, d_p	0.022 m	**Thickness**, t_p	55 μm
Width, w_p	0.02 m	**Location**, x_p	0.0033 m
Density, ρ_p	7900 kg/m^3	**Thickness**, t_{sup}	0.00175 m
Piezoelectric constant, d_{31}	-152.5 $pC.N^{-1}$	**Permittivity**, ε_{33}^S	15.5 $nF.m^{-1}$
Mechanical compliance tensor, ${s_{11}}^E$	15.27 $\times 10^{-12}$ Pa^{-1}	${s_{12}}^E$	-5.46 $\times 10^{-12}$ Pa^{-1}

In Figure 4.5, an example of harvester system beam tip frequency responses and beam mode shapes are shown and predicted using the FEM model. The response is obtained with the beam system characteristics stated in Table 4.1 and at a resistive load $R_L = 1380$ k Ω (which corresponds to the optimal load). The host beam and the harvester beam mode shapes are predicted at the first frequency peak and the second frequency peak from global frequency response (Figure 4.5(a)) and normalized with the beam tip displacement for each beams. At the first frequency peak, both the host beam and the harvester beam are in their first mode; however, at the second frequency peak, the host beam is still in its first mode and the harvester beam turns into another mode.

4.3 Experimental Validation

In this section, the experimental setup and results will be introduced to validate the TDOF and FEM modeling stated in 4.2. It is very difficult to implement a very small scale harvester or a huge host structure in the lab. Accordingly, an experimental setup with a moderate mass ratio around 0.02 will be presented in order to validate the previous models and to expose the mechanical to mechanical coupling effect on the host structure that leads to the non validity of constant acceleration magnitude hypothesis in SDOF models and an overestimation of the power output that can be

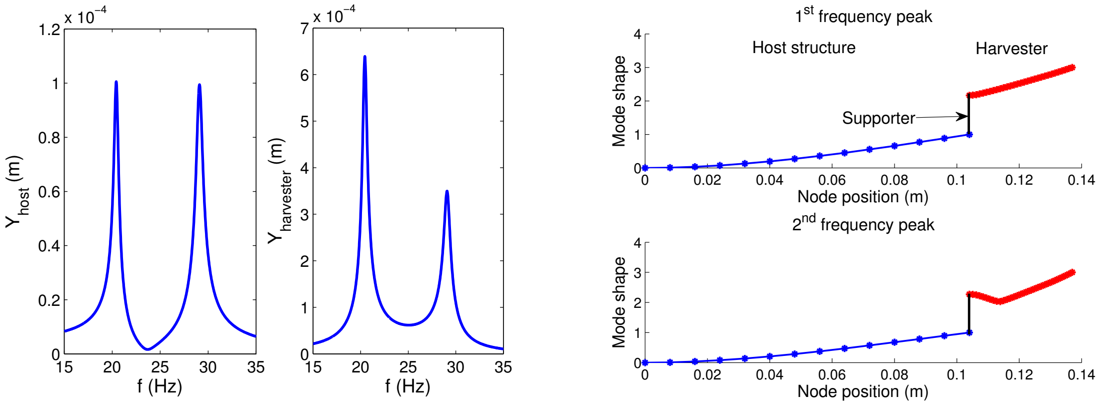

(a) (b)

Figure 4.5: Harvester system responses predicted with the FEM model: (a) frequency response; (b) host and harvester beam mode shapes at the first and the second frequency peaks

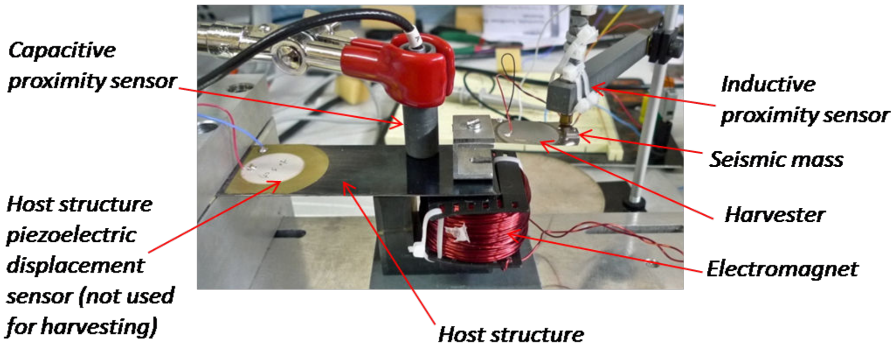

Figure 4.6: Experimental setup

expected. For convenience purpose, the host structure is taken as a cantilever beam, although it can be any other structures (*e.g.*, rotating machinery, car engine, wing...).

The harvester is composed by a bimorph buzzer and it is attached on the host beam through a self-made supporter and permanent magnets. Two small magnets are also placed at the free end of the harvester to form a proof mass. The external excitation is applied at the free end of the host structure with an electromagnet. The experimental setup is depicted in Figure 4.6.

The harvester parameters are identified with the experimental measurements of the open-circuit frequency f_{1h}, the short-circuit frequency f_{0h}, the open circuit piezovoltage to the beam free-end displacement ratio λ, the -3 dB displacement bandwidth Δf and the clamped capacitance of the piezoelectric material C_{0h}. A piezoelectric buzzer is also bonded on the host structure for identifying its parameters and is not used in the harvesting experiment. It is furthermore considered as negligible in the modeling because of its low product of thickness by Young's modulus compared to the host structure. It is also important to note that when identifying the harvester, the harvester is attached on the host structure and the host structure is blocked to make no boundary condition change for the harvester. With these measurements, the parameters are identified as [52]:

$$\alpha_h = \lambda C_{0h}, \ \ \mathrm{K_h} = \alpha_\mathrm{h}\lambda\frac{\mathrm{f_{1h}}^2}{\mathrm{f_{1h}}^2 - \mathrm{f_{0h}}^2}, \ \ \mathrm{M_h} = \frac{\mathrm{K_h}}{4\pi^2\mathrm{f_{1h}}^2}, \ \ \mathrm{k_h}^2 = \frac{\mathrm{f_{1h}}^2 - \mathrm{f_{0h}}^2}{\mathrm{f_{1h}}^2}, \ \ \mathrm{Q_{Mh}} = \frac{\mathrm{f_{1h}}}{\Delta \mathrm{f}},$$
$$b_h = \frac{2\pi M_h f_{1h}}{Q_{Mh}}. \tag{4.36}$$

The model parameters are listed in Table 4.2 and the dimension and the physical properties are given in Table 4.1.

The responses with varying resistive load by TDOF modeling, FEM simulation and experimental measurements are shown in Figure 4.7. The experimental results are obtained by tracking the optimal frequency response whenever the resistance is changed. However, the frequencies where the optimal response occurs varies very little and is always around 30.2 Hz. The FEM model is obtained with 13 elements for the host structure and 30 elements for the harvester. In Figure 4.7, the measured responses correspond well with FEM model and TDOF simulation. The displacement of host structure has an evident decrease when the harvested power reaches its maximum value 1.44 μW (when $R_L \cong 16.7$ kΩ), which shows that when the harvester converts the energy from the host structure, it also induces a damping effect on the host structure; and this reduction could be more than 3 dB. In Figure 4.7, the voltage and harvested power are also plotted with a SDOF model, which is obtained considering a constant acceleration magnitude applied to the clamped end of the harvester, and

Table 4.2: Experimental parameters for validating the host-harvester TDOF model

f_{1H}	26.3 Hz	f_{0H}	26.256 Hz
C_{0H}	40.2 nF	Q_{MH}	142.23
α_H	2.07×10^{-4}	M_H	0.0115 kg
K_H	314.4 Nm^{-1}	b_H	0.0134 $Nm^{-1}s^{-1}$
f_{1h}	24.05 Hz	f_{0h}	23.45 Hz
C_{0h}	360 nF	Q_{Mh}	36.92
α_h	3.102×10^{-4} N/V	M_h	2.39×10^{-4} kg
K_h	5.467 Nm^{-1}	b_h	9.792×10^{-4} $Nm^{-1}s^{-1}$
F_m	6.2×10^{-4} N	${k_h}^2$	4.89%

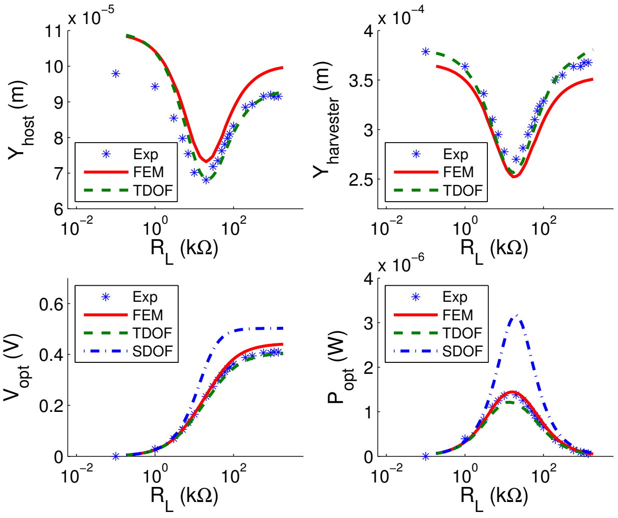

Figure 4.7: Experimental validation when the dimension of the host structure is close to the harvester (mass ratio=0.0208); the response is optimized with the frequency response for varying resistance

this acceleration is taken from the second derivative of the host structure displacement when it is in short circuit. It is clearly shown that with a SDOF model considering a constant acceleration excitation, the harvester response (both in terms of displacement and output power) is overestimated, as it does not consider the mechanical to mechanical backward coupling to the host structure and thus the host structure damping effect is neglected, yielding an inaccurate estimation.

Although in the lab scale, the mass ratio chosen in the experiment is not the optimal case (Figure 4.8) predicted with the TDOF modeling and could only achieve less than half the optimal power output, the validation of the TDOF modeling is shown by the experimental measurement.

4.4 Coupling Effect between Host Structure and Harvester and a Practical Application Example

This section details the coupling effect between the harvester and the host structure under a monochromatic force excitation using the TDOF model explained in section section 4.2.1. Then a practical example with a self-powered bridge SHM system will be analysis using the TDOF modeling.

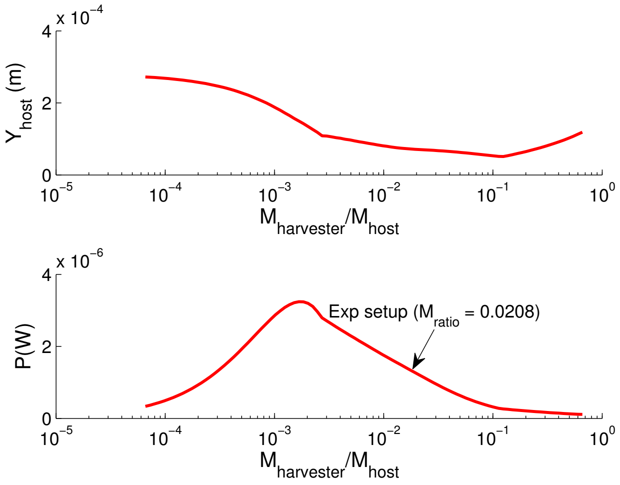

Figure 4.8: Optimal performance predicted with TDOF modeling for the experimental setup

4.4.1 Coupling Effect between Host Structure and Harvester

The analysis of the coupling effect between the host structure and the harvester is based on model parameters listed in Table 4.3; these parameters are chosen based on the experimental measurements of Section 4.3. In order to maintain the resonance frequency of the harvester, the harvester stiffness is changing with the harvester mass (the host structure is always maintained as the same structure). The resistive load is varying from 18.38 Ω to 1838.2 kΩ.

For a fair comparison, a design criterion with a constant piezoelectric force factor $\alpha = 5.5 \times 10^{-5}$ as well as the constant mechanical quality factor $Q_M = 36.92$ have been ensured for each iteration, and the damping coefficient C_2 and the electromechanical coupling factor k are changing with the stiffness and the mass of the harvester. Q_M is chosen according to the experimental measurement and the value of α is selected to ensure a rational range of electromechanical coupling factor k^2, as k^2 depends on the

Table 4.3: Model parameters for TDOF model simulations

Host resonance frequency	f_1	26.3 Hz
Host dynamic mass	M_1	0.0115 kg
Host stiffness	K_1	314.4 N.m^{-1}
Host damping coefficient	b_1	0.0134 N.m^{-1}.s^{-1}
Harvester resonance frequency	f_2	24.05 Hz
Piezoelectric clamped capacitance	C_0	360 nF
Force magnitude	F_m	6.2000×10^{-4} N

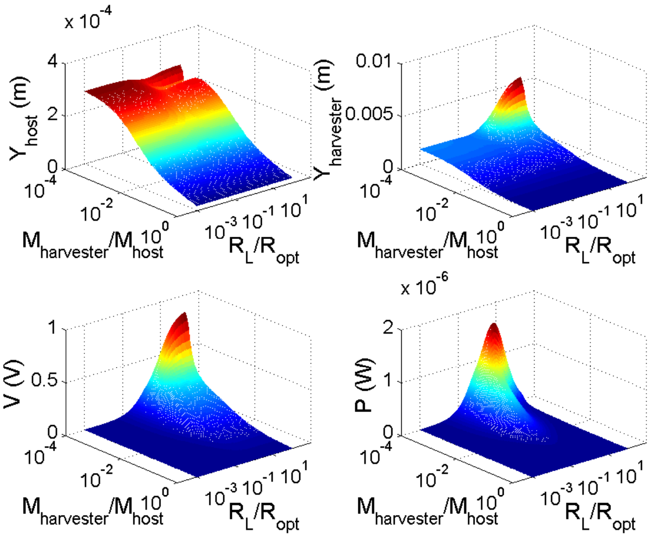

Figure 4.9: Responses of host structure and harvester under different mass ratios and resistive loads; the performance is optimized with frequency and the resistive load is normalized with the optimal load for standard AC technique

open or short circuit stiffness, clamped capacitance and α. Displacement, voltage and power responses at the resonance frequency as a function of the mass ratio (harvester dynamic mass over host dynamic mass - the latter being fixed) and the resistive load are depicted in Figure 4.9; optimal host displacement and associated maximum power for varying mass ratios are detailed in Figure 4.10. These figures clearly show that the mechanical to mechanical coupling effect (see Figure 4.1) increases (host displacement Y_{host} decreases) with the increase of harvester mass, and actually becomes non negligible for even a very small mass ratio ($M_2/M_1 \approx 1.6 \times 10^{-4}$). Around this particular mass ratio, the electromechanical coupling due to the energy harvesting process actually leads to a significant change in the mechanical to mechanical coupling as well, as the load adaption modifies the mechanical behavior of the harvester which in turns also modifies the mechanical behavior of the host (Figure 4.1). With a higher resistive load, the host structure displacement Y_{host} would have a slight increase after the displacement decrease and the harvester displacement $Y_{harvester}$ would have an optimal value (Figure 4.9), denoting the needs of taking the mechanical to mechanical coupling to optimize the power harvesting abilities.

Around the sharp decrease of host structure displacement with the mass ratio $M_2/M_1 \approx 1.6 \times 10^{-4}$, the harvested power reaches its maximal value of 1.695 μW. To look it more detail around the optimal mass ratio in Figure 4.11, the trade-off between the host dis-

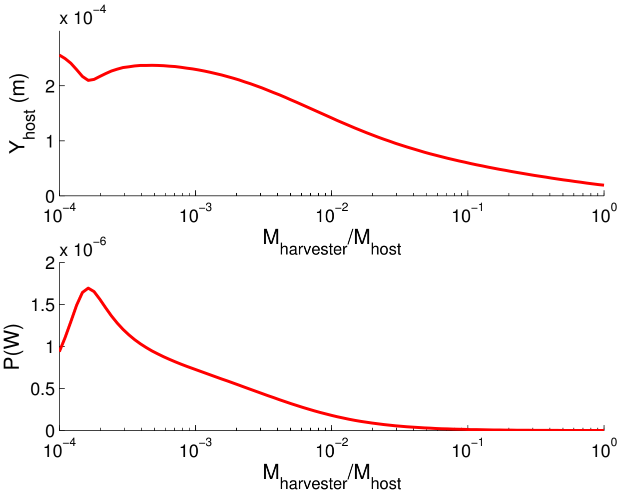

Figure 4.10: Mechanical to mechanical coupling effect on host structure displacement and harvested power versus different mass ratios; the results are optimized with resistive load and frequency

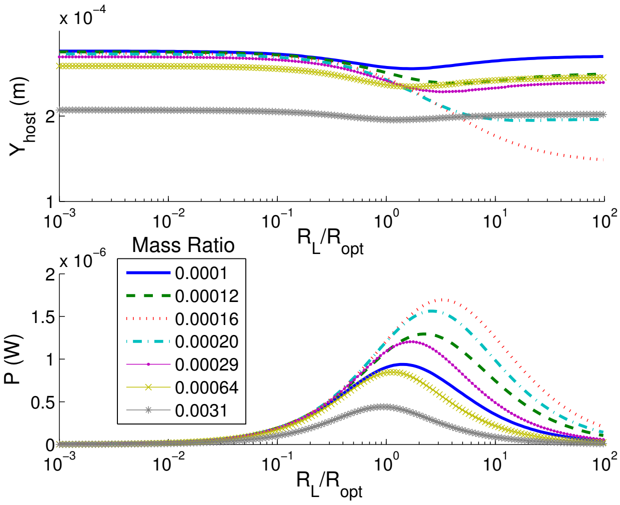

Figure 4.11: The host displacement and harvested power as function of normalized resistive load for picked mass ratios

placement and the harvested power can be explained more clearly as there are strong coupling effects (both electromechanical and mechanical to mechanical) for the energy conversion between the host structure and the harvester, and for the piezoelectric element. Before the harvested power reaches its optimum value, when mass ratio increases, the optimal value of resistive load also increases. After obtaining the optimal power as a function of the mass ratio, the optimal resistive load decreases with the increase of the mass ratio. Such a phenomenon may be explained by the strong mechanical to mechanical coupling between the host structure and the harvester, and the electromechanical coupling effect of the harvester itself (between the electrical part of the piezoelectric element and the mechanical part); the coupling effect on the optimal resistive load has been shown for example in the work of Guyomar *et al* [54], and it is therefore not surprising that the mechanical to mechanical coupling also affects the optimal load. The phenomenon can be explained by the fact that the harvesting process modifies the mechanical behavior of the harvester which in turns changes the behavior of the host structure because of the mechanical to mechanical coupling. In other words, in order to have a significant harvested energy, the available energy in the host structure should not be totally eliminated by preventing the energy entering into it due to the mechanical to mechanical coupling with the harvester. With the decrease of host structure displacement, in order to have a higher harvested power, the resistive load tends to increase; after reaching an optimal harvested power, the resistive load decreases to maintain the host displacement level. In addition, the coupling between the harvester and the host structure can be explained with Figure 4.12. The frequency responses for several mass ratio cases are exposed in Figure 4.12 when the displacement of the host goes through the local minimum corresponding to the optimal mass ratio value with the load chosen as the optimal resistive load $R_L = 61.8k\Omega$ for optimal mass ratio. The arrow shows the direction of the increase of the mass ratio. When the mass ratio is small, the host structure displacement has only one peak value because of weak mechanical to mechanical coupling effect and its magnitude decreases as the mass ratio increases. When the host structure displacement reaches the optimal mass ratio region, the motions of the harvester and the host structure become strongly coupled and the harvester frequency response peak is doubled.

Another design criterion can be considered which consists in a constant electromechanical coupling factor k^2 (where α varies with k^2 and harvester stiffness) instead of a fixed force factor α. In the case of a simple SDOF modeling considering constant

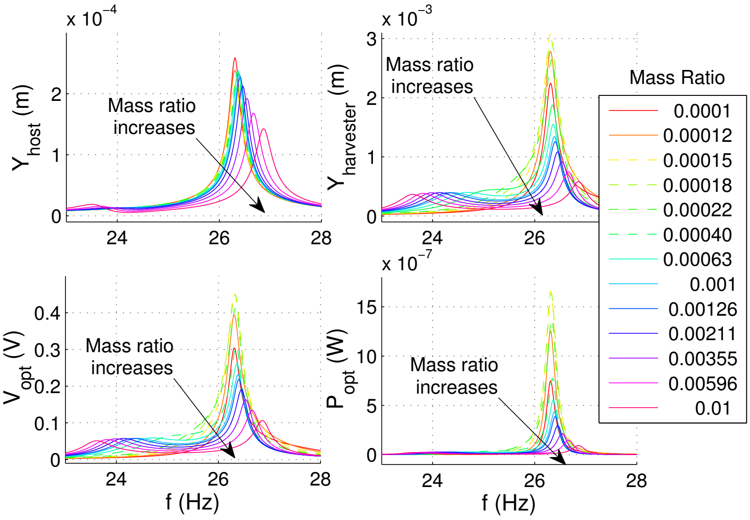

Figure 4.12: Frequency response for several mass ratio cases; displacements, output voltage and harvested power are calculated for the optimal load at optimal mass ratio $R_L = R_{opt}|_{(M_2/M_1)_{opt}} = 61.8$ kΩ

acceleration magnitude (*i.e.*, without considering the host structure and mechanical to mechanical backward coupling from the harvester), the harvested power depends on the multiplication of k^2 and Q_M [48] and will reach a power saturation. However, with a TDOF model, the performance is found depending on k^2 and Q_M separately. Simulation results shown in Figure 4.13 present the harvester performance under three k^2 values (k^2=0.25%, 4%, 10%) for several Q_M values ranging from 36.92 to 1600, optimized with global frequency response and frequency responses around the first and second frequency peaks. The performance is also optimized with the resistive load (in the case when two optimal loads exist - which appears for strongly coupled and lightly damped systems - the first one is chosen as the displacement and power responses are the same for the two optimal loads [86,141]). From the three subfigures in Figure 4.13, it is found that for a lighter harvester mass, the harvester performance depends more on the responses around second frequency peak, which is closer to the host structure natural resonance frequency, except for very weakly-coupled harvesters when $k^2 = 0.25\%$ (with very low k^2, the harvester open-circuit and short-circuit resonance frequencies are almost identical and the harvester frequency response are rather sharp) and a very lightly-damped harvester ($Q_M = 1600$) with moderate coupling $k^2 = 4\%$ (with very high Q_M, the frequency response of the harvester is also rather sharp). For a heavier harvester, it depends more on the first frequency peak response as when the mass

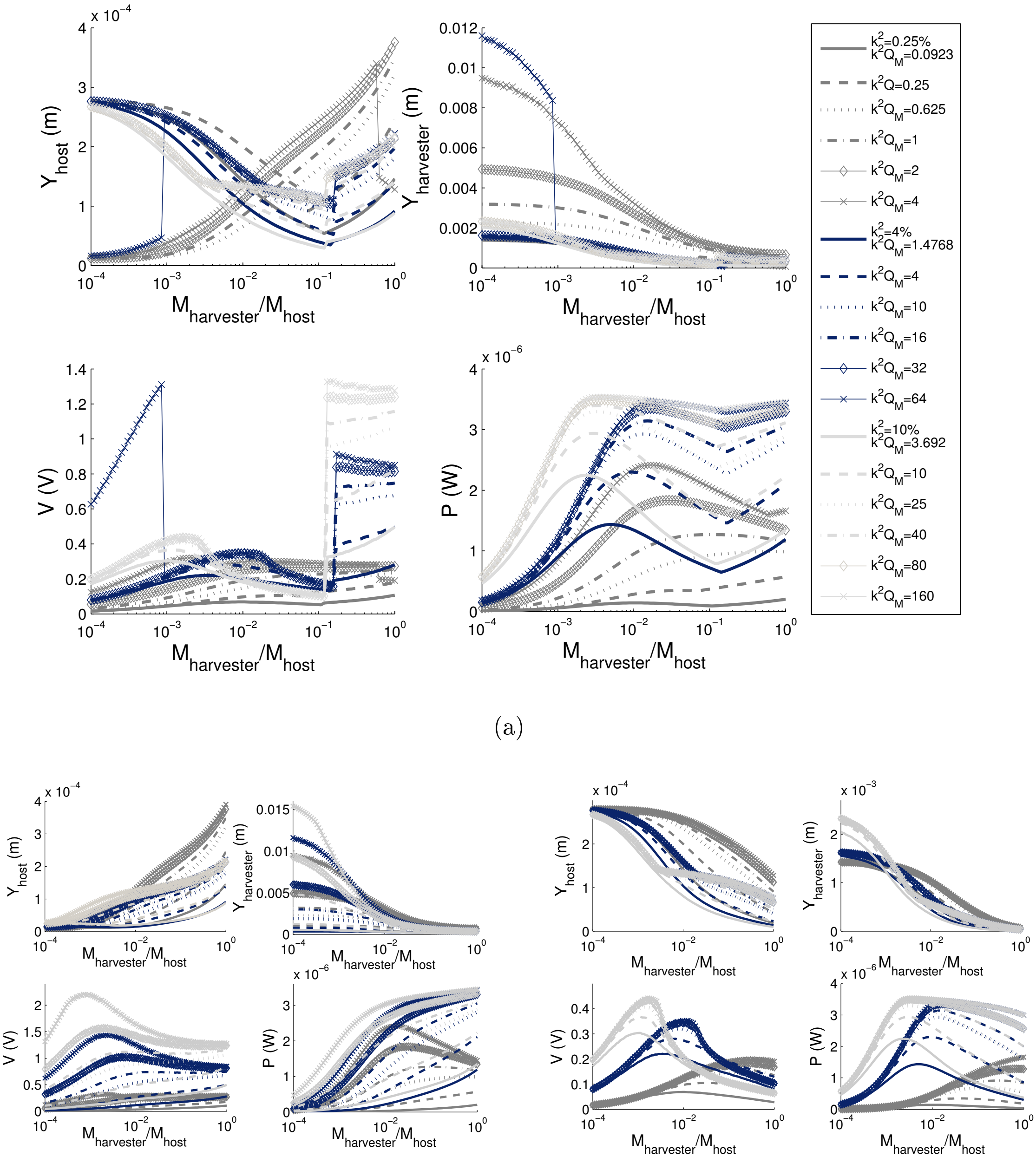

(a)

(b)

(c)

Figure 4.13: Optimal performance of host structure and harvester versus mass ratio under different k^2 and Q_M values; optimized with (a) global frequency responses; (b) responses around first frequency peak; (c) responses around second frequency peak

ratio increases, the frequency peak value shifts to the lower frequency. In the figure, the decrease of host structure displacement at the optimal mass ratio is more evident with higher k^2. The harvested power increases with the increase of k^2 and Q_M, and reaches a power saturation at the optimal mass ratio; however, with a higher k^2, the power increases more rapidly. The dependance of the multiplication k^2 and Q_m and the power output is validated only when k^2Q_M is very small, but the optimal mass ratio is always different even with an identical and very small k^2Q_M value. Moreover, the mass ratio for obtaining the optimal harvested power is lower with a higher k^2, which shows that there exists a trade-off between the strong electromechanical coupling and the mechanical to mechanical coupling (Figure 4.1).

Although in some cases the value of Q_M is not really realistic for millimeter scale devices (which however can be obtained under particular conditions, e.g. MEMS piezoelectric harvester in the vacuum condition [142]), these results point out the need of a careful design for ensuring a good matching between the host structure and the harvester to optimize the energy harvesting abilities. Such an issue is of significant importance when designing the harvester, especially for a highly-coupled harvesting system.

4.4.2 Practical Application on a SHM System

To face the problem of supplying power to wireless sensors and preventing maintenance problems of batteries for a SHM system, energy harvesting from ambient sources becomes more and more popular. A piezogenerator is nowadays well-utilized for Wireless Sensor Networks (WSN) as the power output is fairly enough for a WSN system and as it has adequate lifetime and low maintenance. The autonomous WSN system could be embedded or retrofitted to monitoring sensor systems with an appropriate lifetime for fixed civil infrastructures such as buildings, bridges, tunnels, dams, mines, pipelines, embankments, offshore, oil platforms and so on or structures with difficult and expensive maintenance such as aircrafts and railroads. However, most designs of the harvester consider only the harvester performance and these harvesting system might perform well only when the mechanical coupling between the harvester and the host structure is very weak, which limits the harvested power. In this section, a quick analysis based on the TDOF modeling stated in previous paragraphs will be presented to provide us a concept in piezoelectric harvester design for a given host structure; here we take a moving bridge as our host structure. The model parameters of the bridge and the harvester are specified in the work of Yang *et al* [143] and Ali *et al* [144] respectively listed in Table 4.4. The bridge stiffness is calculated with the formula $K_{bridge} = 3EI/L^3$, and the bridge dynamic mass is obtained from the relation linking resonance frequency and the stiffness, $\omega_{bridge} = \sqrt{K_{bridge}/M_{bridge}}$.

The harvester and host structure performance under different resistive loads and mass ratio $(M_{harvester}/M_{host})$ are shown in Figure 4.14. The performance are optimized with the frequency response. Under a force magnitude 33.26 N, the optimal power output would have about 19 μW at the optimal mass ratio around 2.29×10^{-5} and the optimal load around 26 MΩ. Compared to the work of Ali *et al* [144] (mass ratio is around $6.76{\times}10^{-7}$), it could achieve more than 1.5 times harvested power with a higher harvester mass under a similar resistive load. In addition, as the harvester mass is so small compared to the bridge mass, the harvester has almost no influence on the bridge vibration before the optimal mass ratio obtained.

4.5 Optimization of Harvester Performance with TDOF Model under a Broadband Force Excitation

So far the analysis of piezoelectric harvester has usually been discussed under a monochromatic excitation in order to simplify the problem. However, in practical and realistic environments, the real-world vibration contains more than single frequency information and is usually broadband. In this section, the TDOF model stated in previous paragraphs will be extended to consider a more general case with a broadband and/or random force excitation. The modeling is based on the stochastic theory and the harvester performance can then be simply expressed with the power spectral density of

Table 4.4: Model parameters for a self-powered bridge SHM system

f_{bridge}	2.084 Hz	$f_{harvester}$	2.084 Hz
ζ_{bridge}	0.02	$\zeta_{harvester}$	0.038
E_{bridge}	27.5 Gpa	$C_{0harvester}$	2.866 nF
L_{bridge}	25 m	$\alpha_{harvester}$	$7.501{\times}10^{-6}$ N·V^{-1}
I_{bridge}	0.12 m^4	a_{bridge}	0.02 m·s^{-2}

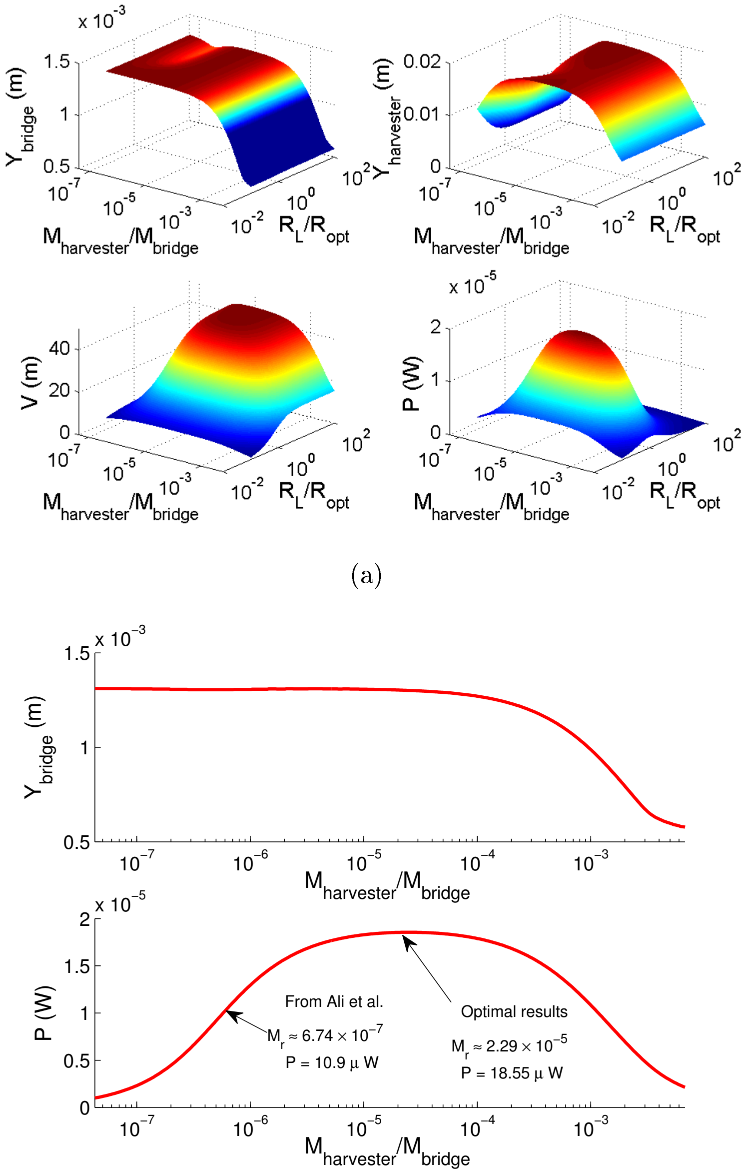

(a)

(b)

Figure 4.14: Optimal performance of harvester versus the mass ratio in a practical case taken from the literatures [143, 144]: (a) responses of host structure and harvester under different mass ratios and resistive loads; the performance is optimized with frequency responses and the resistive load is normalized with the optimal load for standard AC technique; (b) mechanical to mechanical coupling effect on host structure displacement and harvested power; the results are optimized with the resistive load and frequency response

the input excitation.

4.5.1 Stochastic Modeling with TDOF Model

Recalling from Section 4.2.1, the host structure and harvester displacement response can be expressed as the following expression:

$$\tilde{V}(\omega) = \mathbf{g}s(\omega)\tilde{\mathbf{U}}(\omega) \text{ with } g(\omega) = \frac{\alpha R j\omega}{1 + C_0 R j\omega}, \tag{4.37}$$

$$\tilde{\mathbf{U}}(\omega) = \mathbf{L}(\omega)\mathbf{F}(\omega), \tag{4.38}$$

with:

$$\mathbf{L}(\omega) = \left(\mathbf{I}_2 - \mathbf{G}(\omega)\right)^{-1}\mathbf{T}(\omega). \tag{4.39}$$

The power spectral density (PSD) of a signal is defined as the Fourier transform of its autocorrelation function. Accordingly, the PSD of the global displacement response can then be found from the PSD of the force excitation:

$$S_{\mathbf{uu}}\left(\omega\right) = \left|\mathbf{L}\left(\omega\right)\right|^2 S_{\mathbf{FF}}\left(\omega\right). \tag{4.40}$$

As the average power delivered into the load resistance can be expressed as the area under the PSD function, it can easily be obtained from the force excitation PSD function $S_{\mathbf{FF}}(\omega)$:

$$\begin{aligned} P &= \frac{\left\langle V^2\left(t\right)\right\rangle}{R_L} = \frac{1}{2\pi}\int_{-\infty}^{\infty} S_{VV}\left(\omega\right)d\omega \\ &= \frac{1}{R_L}\frac{1}{2\pi}\int_{-\infty}^{\infty}\left|\mathbf{gL}\left(\omega\right)\right|^2 S_{\mathbf{FF}}\left(\omega\right)d\omega. \end{aligned} \tag{4.41}$$

For a monochromatic force excitation ($F = F_M \cos\left(\omega_0 t\right)$), the PSD function has nonzero values at two sharp peaks in the frequency domain as:

$$S_{FF}(\omega) = \frac{\pi}{2}{F_M}^2\left[\delta\left(\omega - \omega_0\right) + \delta\left(\omega + \omega_0\right)\right], \tag{4.42}$$

and the power output is simplified as:

$$P = \frac{1}{2R_L}\left|\mathbf{gL}\left(\omega_0\right)\right|^2{F_M}^2, \tag{4.43}$$

which is identical as expressed in the previous work [52]. For a white noise force excitation with a constant power spectral density function S_{FF}, the power expression can be simplified by taking S_{FF} outside the integration:

$$P = \frac{1}{R_L}\frac{1}{2\pi}S_{FF}\int_{-\infty}^{\infty}\left|\mathbf{gL}\left(\omega\right)\right|^2 d\omega. \tag{4.44}$$

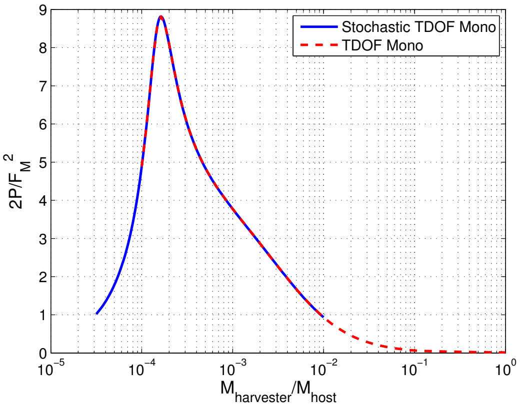

Figure 4.15: Comparison of stochastic TDOF modeling and TDOF modeling under a monochromatic force excitation

4.5.2 Case Study

In this subsection, the stochastic TDOF modeling expressed with the power spectral density (PSD) of the input excitation will first be validated with the TDOF modeling (Section 4.2.1) under a monochromatic force excitation ($F = F_M \cos(\omega_0 t)$); then different noise force excitation cases will be applied on the harvester-host structure system and discussed. The harvester and host structure performance are discussed with the stochastic TDOF modeling through numerical calculations.

The comparison of the harvester performance under a monochromatic force excitation with TDOF modeling and stochastic TDOF modeling (Eq. (4.43)) is provided in Figure 4.15 to validate the stochastic TDOF modeling. The simulation is done with the parameters stated in Table 4.3 ($\alpha = 5.5 \times 10^{-5}$, $Q_M = 36.92$) and the harvested power is normalized with ${F_M}^2/2$ to show a fair comparison. A perfect correspondence between the two simulation results shows the validation of the stochastic TDOF modeling. The harvested power output is plotted in Figure 4.16 as a function of the harvester to host structure mass ratio for the case of white noise force excitation ($S_{FF} = 10^{-8}$ N^2/Hz). The model parameters are also acquired from Table 4.3 and with $\alpha = 5.5 \times 10^{-5}$ and $Q_M = 36.92, 100, 200, 400$ and 800. The harvested power is optimized with the resistive load at each mass ratio and the optimal power output is obtained around a mass ratio of 1.68×10^{-4} when $Q_M = 36.92$, which is very close to the result when it is under a monochromatic force excitation (Figure 4.15). However, the decrease in power output with the increase of mass ratio is slower. With the increase of mechanical quality factor Q_M, the harvested power approaches a power limit around 0.25mW, and the optimal

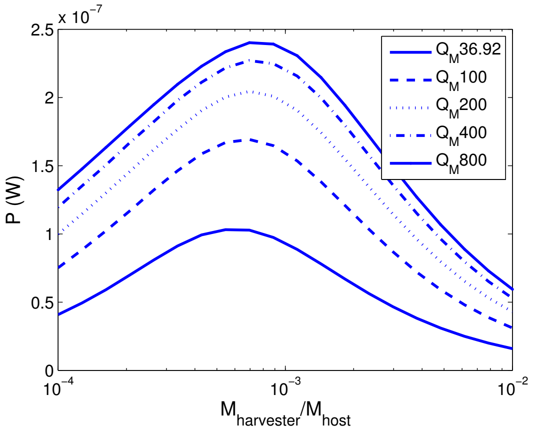

Figure 4.16: Harvested power versus mass ratio under a white noise force excitation at optimal resistive load for several mechanical quality factors

mass ratio tends to be larger.

Instead of having a constant force factor α, a constant electromechanical coupling factor k^2 representing a fixed ratio in mechanical to electrical energy conversion within the harvester is considered in the following simulation. In Figure 4.17, the effect of coupling coefficients (k^2 and Q_M) on the harvester-host structure system is discussed under a white noise excitation. The analysis is evaluated with the same model parameters (Table 4.3) and three electromechanical coupling factor cases ($k^2 = 10\%,\ 4\%,\ 0.25\%$); in each k^2 value, the mechanical quality factor Q_M are taken as 50, 200 and 400. As shown in the previous work [145] for monochromatic excitation case, the harvested power improves with the increase of k^2 and Q_M and finally reaches a power limit, and the optimal mass ratio decreases with the increase in k^2. In addition, the harvester performance considering the mechanical to mechanical coupling between the host structure and the harvester depends on the electromechanical coupling factor k^2 and mechanical quality factor Q_M separately but not the multiplication of k^2 and Q_M as in the classical SDOF system under a monochromatic excitation. However, with a white noise excitation, optimal mass ratios are around 10^{-1}, which are relatively larger than under a monochromatic force excitation as the harvester mass is not necessary to be very small to have the matched frequency peak with the excitation frequency, which is also the host structure resonant frequency. In addition, with a constant k^2, the range of mass ratio for optimal output power is in two orders of magnitude from 10^{-2} to 1, which is larger than the result from a constant α design criterion. This might be because with a constant α, the energy conversion process is a trade-off between

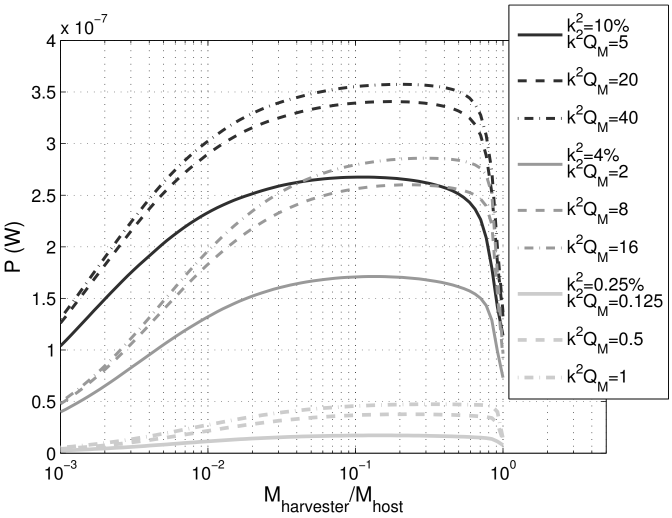

Figure 4.17: The effect of coupling coefficients on the harvested power versus mass ratio under a white noise force excitation

the mechanical energy which flows from the host structure to the harvester and the electromechanical energy flowing within the harvester and the adjustable range of the mass ratio is then limited.

Another noise excitation example to be introduced is a band-limited random noise with "bell-curve" shaped spectral density. The spectral density function is in the form of Gaussian function $e^{-(f-f_H)^2/(2f_r)} + e^{-(f+f_H)^2/(2f_r)}$ with the center frequency at the host structure resonance frequency f_H; f_r controls the bandwidth of the "bell" shape. Through the control of the bell-curve width, the excitation spectral density function can approach the monochromatic excitation with a very small f_r or a white noise excitation with a very large f_r (Figure 4.18). The harvester performance versus the harvester to host structure mass ratio is depicted in Figure 4.19 when the harvester resonance frequency equals to the host structure resonance frequency and the harvested power is normalized with the mean square force of the excitation $F_{\text{rms}}^2 = \frac{1}{2\pi}\int_{-\infty}^{\infty} S_{FF}(\omega)\mathrm{d}\omega$. The analysis is done under two design criteria as previously: constant force factor α and constant electromechanical coupling factor k^2. The constant α permits the piezoelectric patch a fixed capability in converting the strain to charges; and the constant k^2 permits the constant energy conversion in the harvester from the mechanical energy to electrical energy. In the constant α design criterion, $\alpha = 2 \times 10^{-5}$ and in k^2 constant case, $k^2 = 0.25\%$; in both cases, the mechanical quality factor is set to $Q_M = 50$ to have a fair comparison. In both cases (Figure 4.19(a) and Figure 4.19(b)), a reasonable result has been shown that as the PSD of the excitation is approaching to a monochromatic

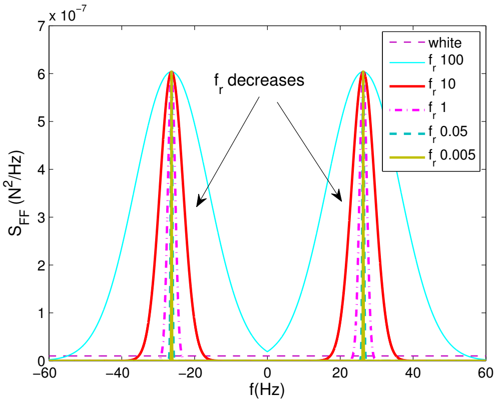

Figure 4.18: Bandlimited noise excitation with bell-curve shape PSD function in different frequency bands

excitation with very small f_r, the harvester works in a higher efficiency, and with a higher f_r, the harvester performance approaches to the result under a white noise excitation. In addition, it is interesting to note that when the excitation is more like a monochromatic excitation, the optimal mass ratio tends to decrease to have less effect on the frequency peak shift and to have a higher power output as there is a stronger mechanical to mechanical coupling effect between the host structure and the harvester. Compared to the constant α design criterion, with a constant k^2, the optimal mass ratio shifts a lot to a smaller value and the harvester is more sensitive to the mass ratio when the width of bell shape PSD function decreases. With a constant k^2, the energy conversion between the host structure and the harvester and within the harvester itself through the electromechanical coupling effect can only be adjusted through the mechanical energy poured into the harvester from the host structure; with a constant α, the energy conversion process is however a compensation between the mechanical energy conversion between the host structure and the harvester and the mechanical to electrical energy within the harvester, and therefore, the optimal mass ratio changes very little with the change of excitation bandwidth. When the excitation power spectral density function becomes flat (f_r increases), the mass ratio between the harvester and the host structure has less effect on the harvested power with both a constant k^2 and α design criterion as there is no much need in tuning the frequency through the mass ratio to make it matched with the excitation frequency; the harvester works in a larger tolerance of harvester to host structure mass ratio.

The vibration frequency variation due to the surrounding disturbances such as temperature change, strong wind and etc. is always a serious problem resulting in a

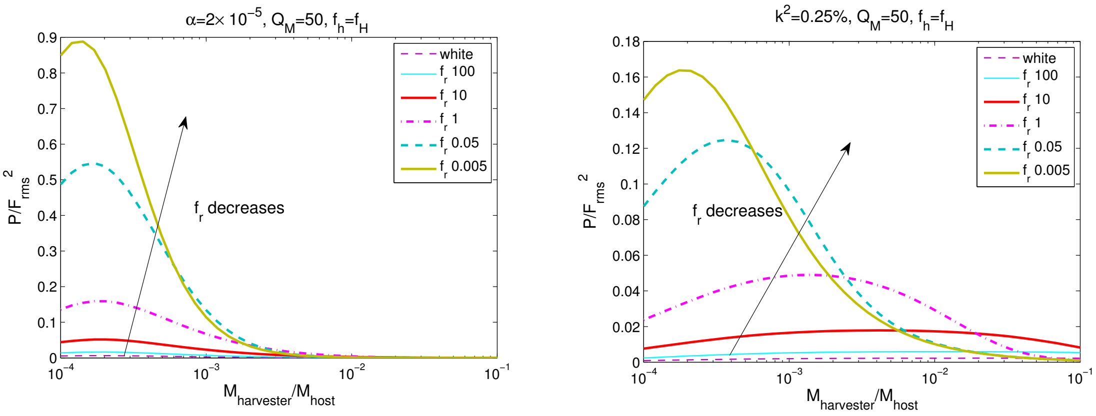

(a) (b)

Figure 4.19: The effect of frequency bands of a bell-curve shape bandlimited noise excitation on the harvester-host structure system: (a) constant α design criterion; (b) constant k^2 design criterion

decrease in harvester efficiency. In Figure 4.20, the excitation signal with narrow band is assumed to have a center frequency shift Δf from the resonance frequency of the host structure f_H. The normalized power output versus the mass ratio is depicted in Figure 4.21 with constant α and constant k^2 design criteria and it is clearly shown that with only a 5 % mismatch with excitation peak frequency, the harvester performance would have a 50 % drop. For negative and positive frequency shifts, the harvester would possess a very similar performance. However, very similar to the effect of the excitation bandwidth, the frequency shift between the excitation center frequency and the host structure resonant frequency under a constant k^2 design criterion causes a large shift in optimal mass ratio as shown in Figure 4.21(b). When the frequency shift Δf increases, the energy input to the host structure from the excitation decreases and in order to compensate this decrease, the optimal mass ratio between the harvester and host structure tends to increase to have a higher mechanical energy poured into the harvester from the host structure. In addition, through this compensation process having an increase in optimal mass ratio, the decrease in power output because of the frequency mismatching can be efficiently halted.

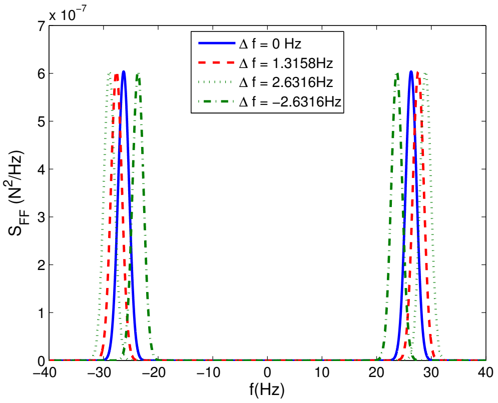

Figure 4.20: Narrow-band noise excitation with a center frequency shift Δf respecting to the host structure resonance frequency

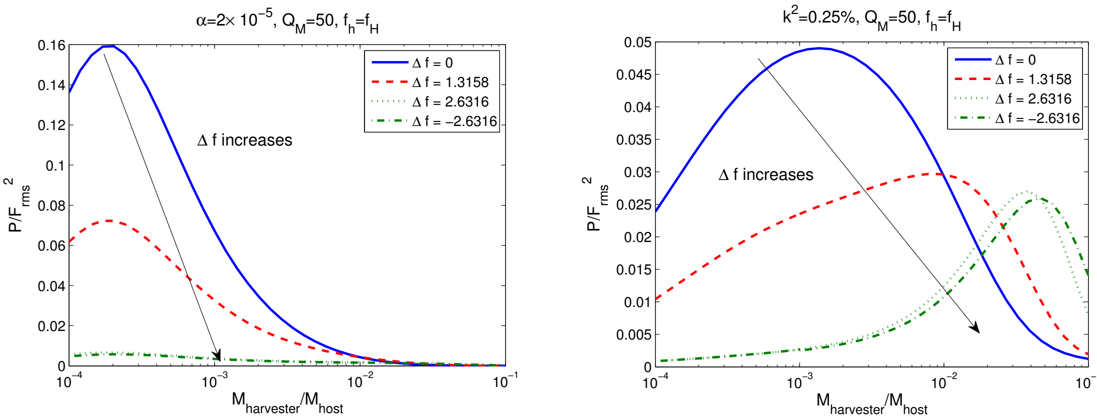

(a) (b)

Figure 4.21: Frequency detuning between the narrow-band noise excitation center frequency and the host structure resonance frequency on the harvester performance: (a) constant α design criterion; (b) constant k^2 design criterion

4.6 Issue of Frequency Detuning between Harvester and Host Structure

Currently, most vibration based energy harvesters are designed as linear resonators which work efficiently only with a limited bandwidth near their resonant frequencies. However, in the practical scenarios, ambient vibrations are usually random with energy distributed over a wide frequency range or are frequency-varying due to environmental disturbances, for example the temperature variation, the wind, aging, etc.. Accordingly, the frequency matching between the host structure or the vibration source and the harvester is also a issue in vibration based energy harvesting. In this section, the effect of frequency mismatching between the harvester and the host structure will be discussed with simulation results calculated with the TDOF model considering the relation between the host structure and the harvester.

4.6.1 Constant Force Factor Design Criterion

The first analysis of frequency detuning effect between the host structure and the harvester resonant frequencies will be discussed with a constant α design criterion under a monochromatic force and white noise excitations. With a constant force factor ($\alpha = 5.5 \times 10^{-5}$), the energy conversion process can be optimized through both the electromechanical coupling of the harvester itself and the mechanical to mechanical coupling between the host structure and the harvester. The frequency detuning problem is discussed by setting a ratio between the harvester resonant frequency f_h and the host structure resonant frequency f_H. The frequency mismatch effect for two excitation cases and two mechanical quality factors are exposed in Figure 4.22. The harvested power is optimized in two ways under a monochromatic excitation; one is the optimal power over the whole frequency range, which is called "global fmax" in the figure, and another is the optimal power in the frequency range closed to the host structure resonant frequency, which is called "local fmax". In the simulation, the electromechanical factor k^2 is varying with the harvester stiffness as the force factor α and the piezoelectric internal capacitance C_0 are fixed. It is shown in the figure that with a higher mechanical quality factor Q_M, there exist two optimal mass ratios for the same optimal power output when resonant frequencies of the harvester and the host structure are very close. In Figures 4.22(e) and 4.22(f), the power is normalized with the optimal value in each cases and it is clearly shown that the optimal power reaches the maximum value when the harvester resonant frequency f_h is equal to the host structure resonant frequency f_H. When $f_h < f_H$, the optimal power would have a slight decrease, and for $f_h > f_H$, the decrease in optimal power is faster as with a constant α, the electromechanical coupling factor k^2 decreases with the increase of the open-circuit stiffness K_D, which is proportional to the harvester resonant frequency and inversely proportional with the mass ratio, and the power decrease faster when k^2 is small because when k^2 is small, the difference between the open- and short-circuit resonant frequency is less and the range of frequency tuning is therefore less. However, it is interesting to note that for a white noise excitation, when $f_h < f_H$, the optimal power decreases faster than under a monochromatic excitation as the optimal mass ratio for white noise case is slightly larger under the same frequency ratio.

4.6.2 Constant Electromechanical Coupling Design Criterion

Another design criterion is to fix the electromechanical coupling factor k^2, which means the harvester has a fixed capability (in a ratio) in converting mechanical energy to electrical energy. In the simulation, the force factor α varies with the harvester stiffness, and the stiffness varies with the harvester mass as the harvester resonant frequency f_h is fixed. The capacitance C_0 is set as 360 nF. As an excitation containing more frequency information reflects a more practical case, in the simulation, a white noise force is applied on the host structure as the external force excitation.

In Figure 4.23, 6 values of k^2 have been taken in the simulation. It can be clearly shown in Figure 4.23(c) that the power output improves when the electromechanical factor increases. The increasing speed of the harvested power is very fast when k^2 is small and finally the power reaches a saturation value when k is around 30 %. It is different than the results from constant α design criterion; with fixed k^2, the harvester performance changes very little due to the frequency mismatching between the host structure and the harvester (with less than 50 % for a two times frequency mismatching). As the electromechanical factor k^2 is fixed, the ratio of the output electrical energy to the mechanical energy is fixed within the harvester. Accordingly, the performance reduction due to the frequency mismatching can only be compensated by the mechanical to mechanical coupling between the host structure and the harvester. When the two frequencies are detuned, the harvester mass tends to be bigger to convert more mechanical energy from the host structure. However, when the harvester resonant frequency is perfectly matched with the host structure resonant frequency ($f_h/f_H = 1$),

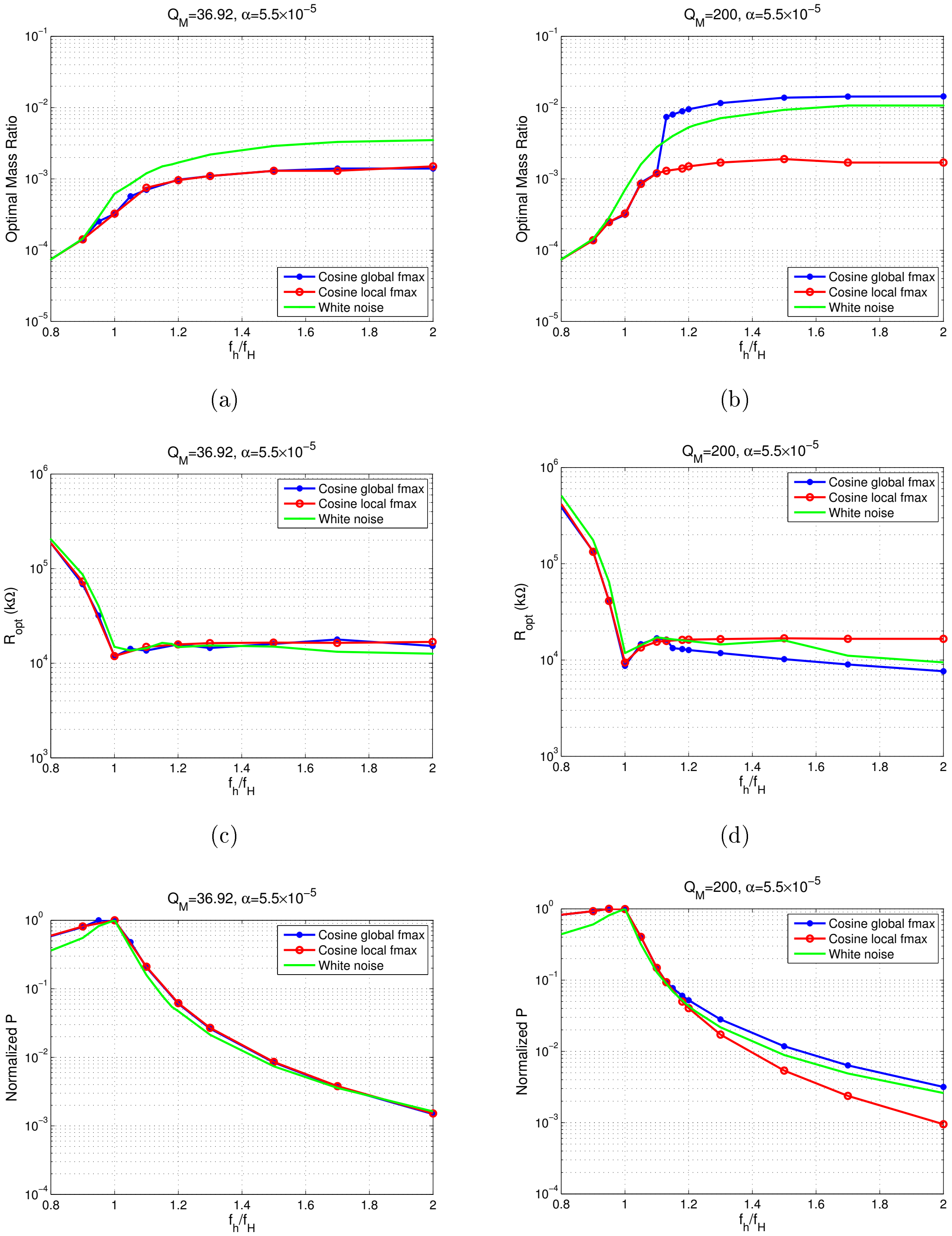

(a) (b)

(c) (d)

(e) (f)

Figure 4.22: Effect of frequency mismatch between the harvester and the host structure under a constant α design criterion: optimal mass ratio at (a)$Q_M = 36.92$; (b)$Q_M = 200$; optimal resistive load (c)$Q_M = 36.92$; (d)$Q_M = 200$; optimal power output at (e)$Q_M = 36.92$; (f)$Q_M = 36.92$

for a very weakly electromechanical coupled harvester (k^2 is very small), the optimal mass would have a sudden decrease. It is because when k^2 is very small, the whole system is considered to have only mechanical coupling effect. In order to ensure the frequency response of the whole system is with only one frequency peak which is very close to the host structure resonant frequency, the harvester mass will be very small. In addition, when the mismatching ratio between the two frequencies exceeds 1.5, the optimal mass ratio tends to decrease to make the two frequency peaks of the whole system as close as possible and be as close to the host structure resonant frequency. Nevertheless, the frequency mismatching does not have much influence on the optimal resistive load, especially for large k^2 harvester. For a weakly-coupled harvester, the optimal resistive load decreases with the increase of frequency mismatching, and this load decreasing ratio is about the same as the increasing ratio in frequency mismatching as the optimal resistive load is inversely proportional to the frequency. For a weakly-coupled harvester, the whole system is purely mechanical coupled. So, when frequency mismatching ratio increases, to keep the mechanical energy level, where the resistive load tends to decrease, which is not like the highly-coupled harvester case, the decrease in mechanical energy conversion due to the frequency mismatching can be compensated by the high electromechanical energy conversion from the harvester to the resistive load.

Another simulation result presented in this subsection aims at discussing the effect of the piezo internal capacitance C_0. In the simulation, three capacitances $C_0 = 360, 180, 90$ nF have been used for a highly-coupled harvester with $k^2 = 10\%$, $Q_M = 200$ under a white noise force excitation. From Figure 4.24, we can see that as the capacitance C_0 is a pure electronic component, the only influence is on the final stage of the energy harvesting process (energy transfer between the harvester and the resistive load) and the influence of C_0 will be corrected by the resistive load to optimize the harvester performance.

4.7 Conclusion

This work provides a further step in the modeling of seismic piezoelectric microgenerators by providing a detailed discussion to describe the mechanical to mechanical coupling induced on a given host structure from the piezoelectric harvester with a TDOF model. In the first case, we consider a constant magnitude force applied to the

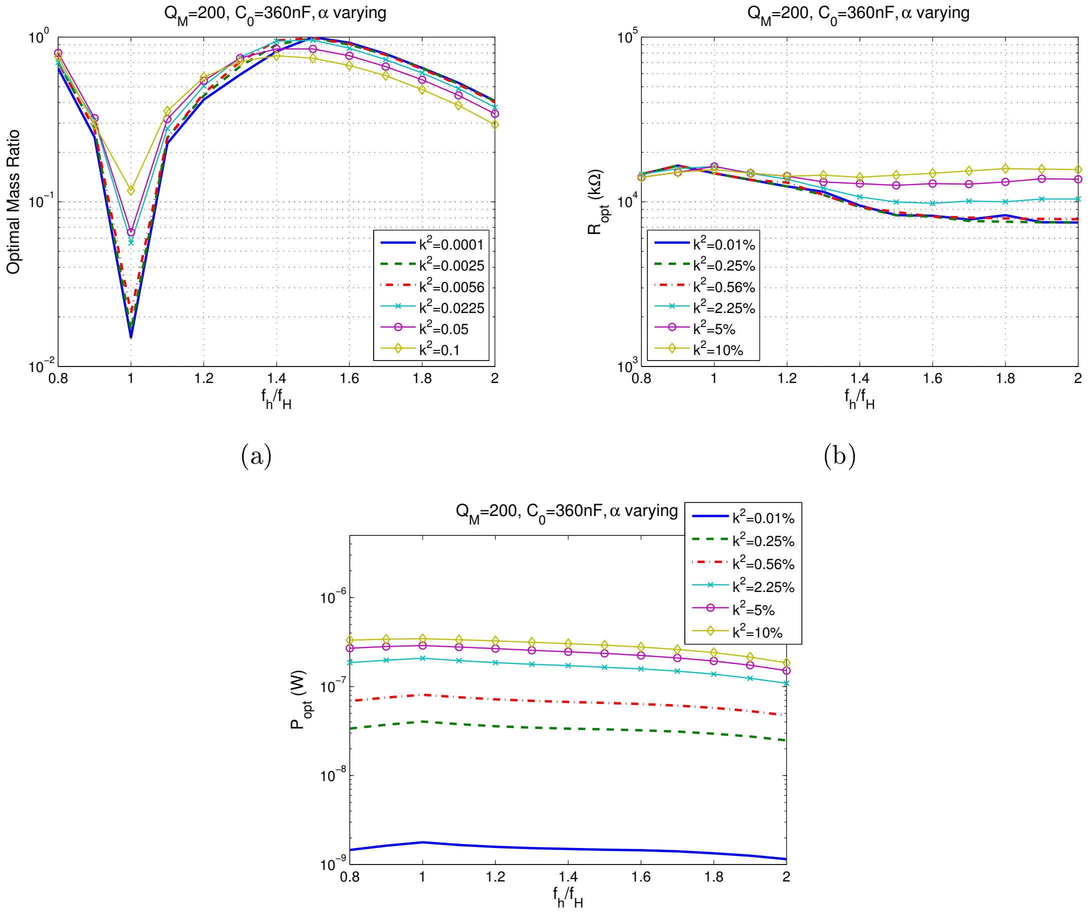

(a) (b)

(c)

Figure 4.23: Effect of frequency mismatch between the harvester and the host structure under a constant k^2 design criterion and a white noise excitation with $Q_M = 200$ and different k^2: (a) optimal mass ratio; (b) optimal resistive load; (c) optimal power output

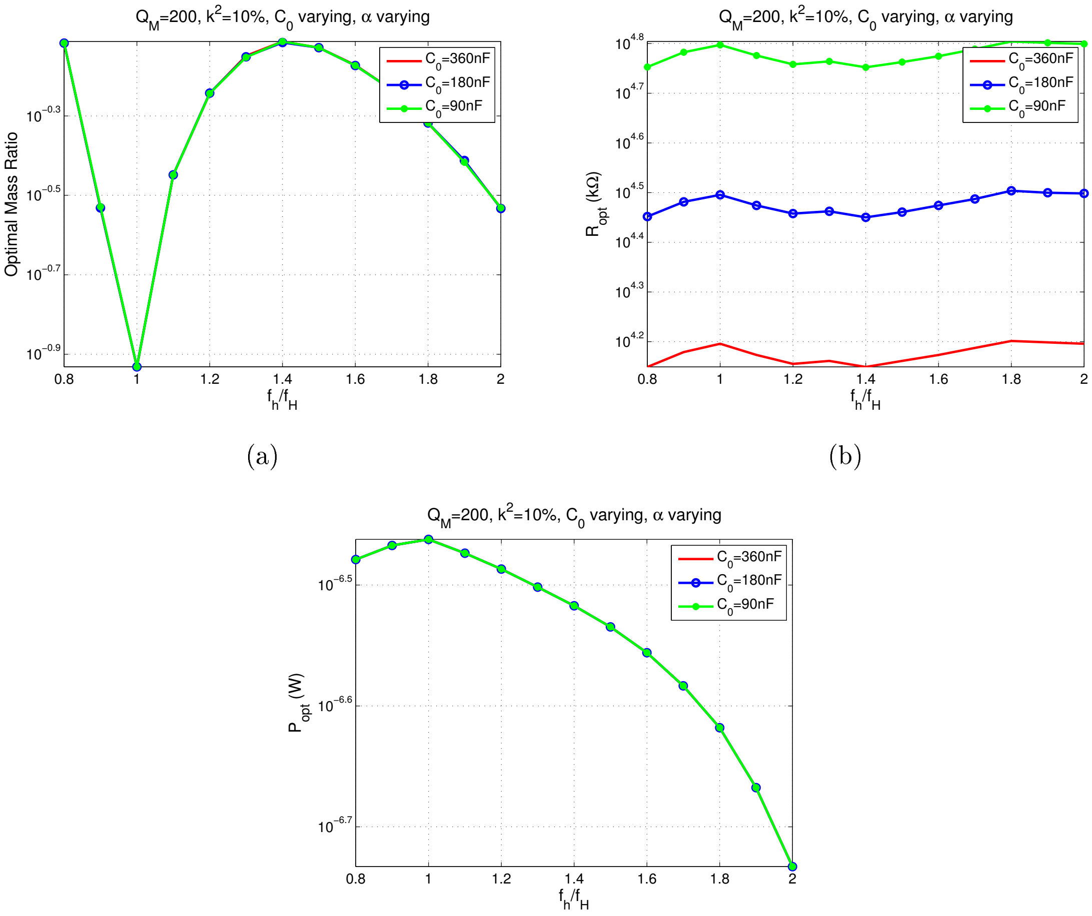

(a)

(b)

(c)

Figure 4.24: Effect of frequency mismatch between the harvester and the host structure under a constant k^2 design criterion and a white noise excitation with $Q_M = 200$, $k^2 = 0.1$ and different block capacitances C_0: (a) optimal mass ratio; (b) optimal resistive load; (c) optimal power output

host structure. FEM simulation and experimental results are presented to validate the TDOF modeling under a single frequency excitation. The resonance frequency of the harvester is tuned to be very close to one of the host structures resonance frequencies, although a frequency peak doubling effect may occur. An optimal ratio of the harvester dynamic mass to the host structure dynamic mass has been proved to allow a maximum harvested power output, whereby the host structure displacement has a sudden reduction due to the mechanical to mechanical coupling effect. For a constant electromechanical coupling factor k^2 case, an optimal mass ratio has also been reported; this mass ratio decreases as k^2 increases. The harvested power also increases with increase of Q_M. However, it eventually reaches a power limit. Experimental measurements confirmed the non-validity of the constant acceleration magnitude assumption without considering the coupling effect between the harvester and the host structure, even for a mass ratio as low as 0.02, for which the displacement of the host structure is damped by more than 3 dB at the maximum power. Comparison with the classical SDOF model that considers a constant acceleration excitation showed an overestimation of the harvested power by a factor of 2, as the mechanical to mechanical coupling is not taken into account in the SDOF model and thus the backward damping effect on the host structure is neglected and therefore the harvested power is overestimated.

Then the work is extended to consider a more practical case with a random and/or broadband force excitation. In the second part of the work, the stochastic modeling is introduced for analyzing the effect of seismic energy scavenging on the host structure and the harvester and the frequency detuning effect between the structures under a broadband force excitation. With the stochastic modeling, the harvester performance can be expressed with the power spectral density (PSD) function of the excitation force S_{FF}. The analysis is also discussed under two design criteria, fixed force factor α, which introduces the trade-off between the electromechanical coupling within the piezoharvester and the mechanical to mechanical coupling between the harvester and the host structure, and with fixed electromechanical coupling k^2, which presents the energy compensation process by extracting more mechanical energy from the host structure for a harvester with fixed abiblity in converting mechanical energy to electrical energy. The stochastic modeling is first applied under a white noise force excitation and then a band-limited random excitation with the two design criteria. The resonant frequencies of the harvester and the host structure are set to be very close. It is found that with a fixed α, the adjustable range of mass ratio is narrower as the energy conversion process is a trade-off between the electromechanical energy conversion within the harvester and the mechanical to mechanical energy conversion between the harvester and the host structure. With a fixed k^2, it however owns a larger adjustable range in mass ratio as the harvester performance strongly depends on the mechanical energy poured into the harvester from the host structure. When the force factor is decreasing with the increase of harvester stiffness, the decrease in energy conversion within the harvester can be compensated by pouring more mechanical energy from the host structure.

Then, the stochastic modeling is used for discussing the frequency detuning problem. The analysis is also done under the two design criteria to show two different energy conversion processes. The external excitation is considered with a white noise force excitation to show a practical example. The harvester performance is found to be very sensitive to the frequency ratio of harvester to host structure resonant frequencies with fixed α. When the harvester resonant frequency is slightly less than the host structure resonant frequency, the harvester performance is less sensitive to the frequency ratio as the harvested power varies more slowly when the electromechanical coupling factor k^2 is higher. When the harvester resonant frequency is slightly larger than the host structure resonant frequency, the optimal mass ratio tends to increase to hold a higher poured-in mechanical energy from the host structure and the resistive load is nevertheless decreasing to slow down the energy harvesting process to hold the vibration level of the host structure, and as the harvester resonant frequency is getting larger, the two parameters (mass ratio and resistive load) are kept constant to hold the energy level in every stages. With a constant k^2, the harvester performance is surprisingly very little changed due to the mismatching in the two resonant frequencies (with even less than 50 % for two times frequency mismatching). When the two frequencies are detuned, the mass ratio (harvester mass to host structure mass) tends to be larger to convert more mechanical energy from the host structure; when the two frequencies are perfectly matched, the optimal mass ratio would have a sudden decrease for a weakly-coupled harvester (which means the whole system becomes pure mechanical coupled) to ensure the whole system is with a single frequency peak and it is very close to the host structure resonant frequency.

5 Conclusion

This work provided a detailed analysis on piezoelectric harvesters with practical aspects. The performance of nonlinear interfaced piezoelectric harvesters under a broadband and/or random vibration is discussed with two approaches: broadband modeling and stochastic modeling. In addition, the interaction between the host structure and the harvester is also discussed with a TDOF model under broadband excitations. The nonlinear interface discussed in the broadband modeling and stochastic modeling consists in a periodically switched circuit, which is called “Periodic Switching harvesting on Inductor" (PSHI) technique, providing another switching strategy and simplifying the harvester performance to a cyclostationary process.

The broadband modeling, which serves as an introductory chapter of how the PSHI interfaced piezoelectric harvester works under broadband excitations, is derived with the self-sampling and self-aliasing theories. The modeling is introduced step by step from the periodic switching process, which does not include a resistive load representing the harvesting process, to the periodic switching harvesting process, which introduces an exponential decayed effect due to the energy dissipation on the resistive load. The working principle of PSHI interfaced piezoelectric harvester is clearly presented with a very simple monochromatic excitation case that the periodic switching processes acts as a self-sampling process on the harvester response. Accordingly, with a switching frequency chosen as twice the excitation frequency and a proper switching delay, a constructive interference will lead due to self-aliasing effects and improve the harvester performance. Several well-known excitations are applied on the harvester and discussed with the broadband modeling to show its effectiveness. The simulation results calculated with the broadband modeling in frequency domain are also validated with time domain iterative calculations.

Based on this broadband modeling, the stochastic approach consisting in the probabilistic theory and being commonly utilized in analyzing broadband signals is further introduced in Chapter 3. With the stochastic modeling, the performance of PSHI interfaced piezoelectric harvester can be directly expressed with the power spectral density (PSD) function of the excitation signal. As the switching process is periodic, the harvester performance can be seen as a cyclostationary process. The stochastic modeling is derived from the state-space form of equation of motion and piezoelectric equation. With the expression linking the cyclic autocorrelation function R_{XX} and spectral correlation density function (SCD) and by solving a set of coupled equations expressed with cross-correlation functions, the PSD function of harvester performance can be expressed with the excitation PSD function. The stochastic modeling is validated with experimental measurements under a filtered white noise force excitation and compared with time-domain iterative calculations. The harvester performance is discussed under several coupling factors (mechanical quality factor Q_M and electromechanical coupling factor k^2) and different switching frequencies. The harvester performance is also optimized with the resistive loads. Under a white noise force excitation, a power drop has been found when the switching frequency is around twice the harvester resonant frequency especially for highly coupled harvester, and an optimal switching frequency is found to be slightly less than twice the harvester resonant frequency. The optimal switching frequency locates farther to twice the harvester resonant frequency as the electromechanical coupling factor k^2 increases, but it is however usually within the range between $1.5\omega_0$ and $2\omega_0$ for harvesters with low to medium electromechanical coupling factors ($k^2 < 3\%$ with $Q_M = 122.475$). Also, it is interesting to notice that under a broadband excitation with a switching electronic interface, the harvester performance varies with different choice of k^2 and Q_M even when $k^2 Q_M$ is held constant, and this is contrary to the case under a monochromatic excitation. Except white noise excitation, the harvester performance under a colored noise is also discussed with a PSD function in the form of Gaussian distribution function by considering excitations with different frequency bands and center frequencies which is detuned from the harvester resonant frequency. Finally, a comparison between the SSHI AC interface and PSHI AC interface proposed in this work is calculated with time-domain iterative calculation and stochastic modeling in frequency domain respectively. With the SSHI AC technique, the switching process happens on the extremum displacements and permits the better inversion for the system having a larger response at the harvester resonant frequency, such as under monochromatic or pulse excitation. With the PSHI AC technique, the switching process conducts periodically and naturally includes the phase delay between the best inversion instant and the switching instant and therefore holds a less better performance than using SSHI AC technique for a resonant frequency response weighted system. Nevertheless, for multimodal excitation case, the system responses are spread at other frequencies, and in this case the optimal inversion instants become less important and the PSHI technique will permit a similar or even better performance than SSHI AC technique with a smaller switching frequency especially for harvesters hold moderate coupling factors. In addition, with a highly-coupled harvester, the standard AC interface is proved to be more efficient than using switching interfaces as the strong electromechanical coupling leads a larger inversion loss in switching processes, and accordingly, decrease the vibration level and voltage output.

Other practical perspectives considered in the work for piezoelectric harvesters are the backward damping effect on the host structure due to the harvesting process and the frequency mismatching issue between the host structure and the harvester resonant frequencies. In order to focus on the harvester performance itself or to simplify the problem, a single-degree-of-freedom (SDOF) system is usually considered in the existing works. Nevertheless, based on the principle of energy balance for a force excited system, there will be a backward mechanical to mechanical coupling effect on the host structure because the mechanical energy is transferred from the host structure to the harvester and might degrade the harvester performance. Two analysis criteria are provided in the work to consider different energy conversion process: constant force factor α and constant electromechanical coupling factor k^2. With a constant force factor, the energy conversion process can be tuned by both the electromechanical coupling within the harvester and the mechanical to mechanical coupling between the host structure and the harvester. With a constant electromechanical coupling factor, the energy conversion however can be only tuned by the mechanical energy poured in from the host structure. With both design criteria, an optimal mass ratio between the harvester mass to the host structure mass has been proved to have the best power output. However, the adjustable mass ratio is narrower for a constant force factor design under both monochromatic force and white noise force excitations. This might be because the energy conversion process under a constant force factor is a trade-off between the electromechanical energy within the harvester and the mechanical energy flowing between the host structure and the harvester, which limits the adjustable range of mass ratio. The effect of frequency detuning of host structure and harvester resonant frequencies is analyzed under a white noise force excitation with both design criteria for two mechanical quality factors. It is interesting to find that the optimal power output will be obtained only when the two resonant frequencies are exactly matched for constant force factor consideration, and with a constant electromechanical coupling factor, the frequency mismatching is however less important or even can be neglected (with a twice frequency matching, less than 50 % power drop will be induced).

The work proposed in this thesis is based on the practical perspective of utilizing piezoelectric harvesting systems and makes the analysis much closer to the real situation. For the future work, an AC-DC converter, which introduces another nonlinear effect can be taken into account in the modeling for a more practical consideration. A stochastic modeling for SSHI interfaced harvesting system is necessary as SSHI technique permits a better harvesting performance for weakly-coupled harvesting system compared to PSHI technique. The modeling of SSHI technique under broadband excitations could be extended from the stochastic modeling of PSHI technique, for example by modeling the SSHI technique with PSHI technique in different given time-windows. The backward coupling effect of nonlinear harvesters (the nonlinearity here is in terms of both mechanical and electrical) on the host structure can be also an interesting topic to be explored.

French Part

1 Etat de l'art - généralité sur la récupération d'énergie

1.1 Motivations

La prolifération des dispositifs de récupération d'énergie a été promue par la décroissance rapide de la consommation des dispositifs électroniques, suivant plus ou mois une loi de Moore. Désormais, de nombreux dispositifs nécessitent très peu d'énergie pour pouvoir fonctionner (Tableau 1.1). Néanmoins, la limitation des batteries en termes d'auto-décharge, de maintenance (remplacement) et de recyclage devient de plus en plus un frein au développement des systèmes autonomes. Les systèmes de récupération d'énergie permettent ainsi de palier à ce problème, permettant une durée de vie du système global grandement étendue, voire quasi-infinie. Une application typique consiste en l'utilisation de réseaux de capteurs autonomes qui, une fois déployé, ne nécessitent aucune maintenance et peuvent fonctionner de manière totalement autonome (Figure 1.1).

Nous proposons ici une rapide présentation des sources d'énergies et moyens de conversion pouvant être exploités pour alimenter des systèmes électroniques en puisant

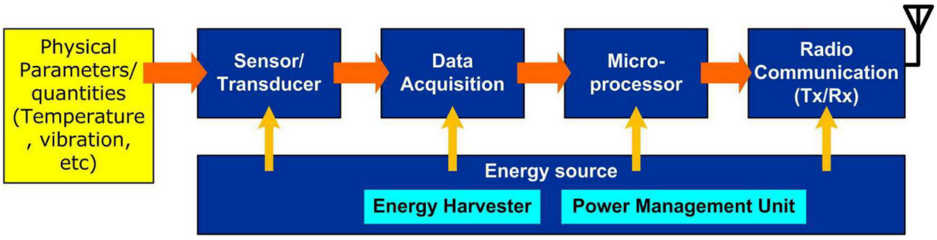

Figure 1.1: Schéma-bloc d'un système de réseau de capteurs sans fils auto-alimentés [2].

Tableau 1.1: Consommation moyenne de dispositifs domestiques électroniques communs

Produit	*Puissance moyenne consommée*
Ecran LCD (21 pouces)	30-80 W
Ordinateur portable (allumé, chargé)	30 W
Ampoule fluorescente	14 W
Lecteur DVD (en lecture)	10 W
Ipad (wifi et lecture vidéo)	2.5 W
Iphone 5 (communication/en veille)	680 mW/24 mW
Smartphone HTC One S ((communication/en veille))	630 mW/170 mW
Liseuse numérique Kindle touch (mode lecture)	210 mW
Télécommande de télévision	100 mW
Radio FM portable	30 mW
Montre quartz	1 μW

l'énergie dans l'environnement immédiat, avec une attention toute particulière aux systèmes de récupération mécanique utilisant l'effet piézoélectrique.

1.2 Sources d'énergie et mécanismes de conversion

1.2.1 Energie thermique

L'énergie thermique est présente, sous une forme ou une autre, dans tout système, mais est généralement disponible selon deux manières : gradient spatial ou variation temporelle. Pour la première, l'effet thermoélectrique (également connu sous le nom d'effet Seebeck), obtenu à partir d'éléments semi-conducteurs dopés (par exemple avec du Bi_2Te_3 - ce dernier permettant d'obtenir jusqu'à 18% du rendement de Carnot), est le plus connu et utilisé pour convertir l'énergie thermique sous forme électrique (Figure 1.2). Les éléments thermoélectriques sont fiables et peu sensibles au bruit, mais leur efficacité est assez limitée, notamment du fait d'un interfaçage thermique délicat pour assurer un gradient thermique suffisant au sein de l'élément lui-même. Malgré cela, les microgénérateurs thermoélectriques peuvent produire jusqu'à plusieurs milliwatts sous un gradient de 10 à 30 $^\circ$K. Néanmoins, une possibilité pour améliorer le rendement des microgénérateurs thermoélectriques est l'utilisation de structures hybrides [10].

Dans le cas de fluctuations temporelles de la température, l'effet pyroélectrique, semblable à l'effet piézoélectrique mais couplant les domaines de la thermique et de l'électricité, peut être utilisé. Etant basé sur une variation temporelle de la tem-

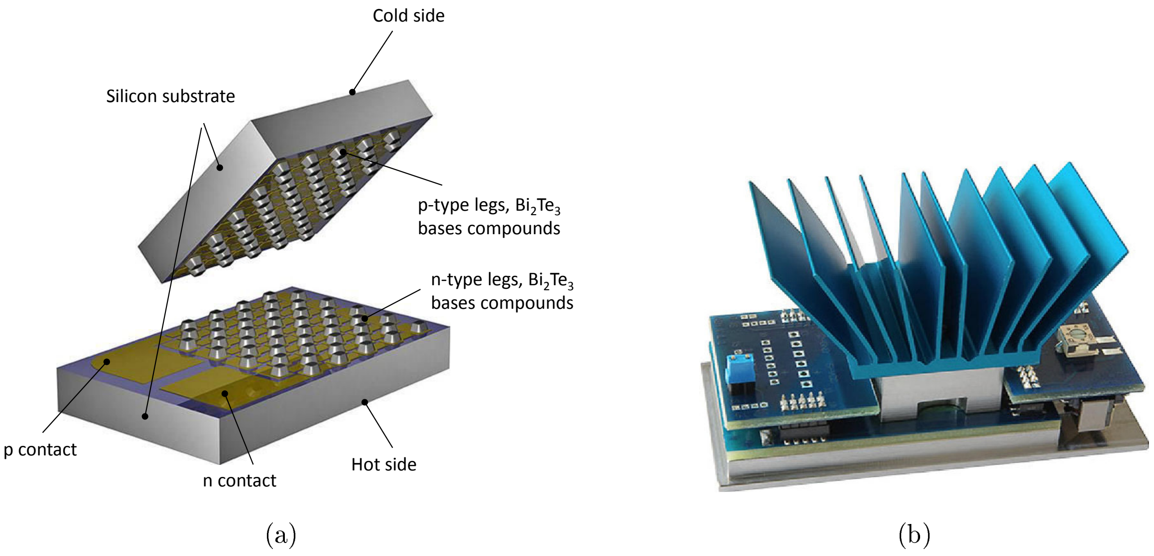

(a) (b)

Figure 1.2: Thermogénérateur Micropelt : (a) Thermogénérateur ; (b) TE-Power PLUS (source: www.micropelt.com).

pérature, la récupération d'énergie par effet pyroélectrique se fait par l'utilisation de cycles énergétiques (par exemple un cycle d'Olsen ou d'Ericsson - [12]), pouvant récupérer jusqu'à plus de 100 mJ/cm^3/cycle pour une température variant entre 100 et 130 $^\circ$C. Les éléments pyroélectriques peuvent par ailleurs outrepasser les performances de générateurs thermoélectriques pour de très faibles fréquences de variation (de l'ordre de 10^{-4} Hz - [9]). L'utilisation des non-linéarités intrinsèques du matériau (par des transitions de phase) peut par ailleurs conduire à des énergies générées bien plus importantes qu'en mode linéaire [?]. Par ailleurs, la transformation d'un gradient de température en variation temporelle de température peut se faire par l'intermédiaire de structures bistables [?].

1.2.2 Energie radiative

La prolifération des dispositifs de communications sans fils et des émissions radiofréquences a conduit à une saturation des bandes fréquentielles dans de nombreuses zones. L'énergie associée, bien que très faible (de l'ordre de 0,26 μW/m^2), est ainsi néanmoins très communément disponible. L'émission d'ondes radiofréquences pour l'alimentation électriques de dispositifs peut aussi être délibérément effectuée, comme dans le cas de systèmes RFID ("Radio Frequency IDentification"). Néanmoins, la forme la plus commune dans la vie quotidienne de récupération d'énergie rayonnante est l'utilisation de cellules et panneaux photovoltaïques, qui convertissent l'énergie de photons incidents sous forme électrique par l'utilisation de jonctions semi-conductrices de silicium. A l'heure actuelle, la plupart des cellules photovoltaïques commercialement disponibles présentent des rendements de conversion de l'ordre de 15%, mais leurs performances restent très dépendent des conditions d'ensoleillement. La combinaison d'éléments photovoltaïques et thermoélectriques est également très prometteuse, les panneaux chauffant énormément sous l'effet des radiations solaires. L'énergie radiofréquence et rayonnante peut aussi être récupérée à l'échelle microscopique par l'utilisation de "rectennas" (compression du mot "rectifying antenna" - antenne redresseuse) mise en réseau, voire de l'utilisation de nantenna ("nano antenna") qui peuvent absorber les rayonnements dans la gamme de longueur d'onde entre 3 et 15 μm (Figure 1.3).

1.2.3 Energie vibratoire

Les vibrations mécaniques sont très communément disponibles dans de nombreux environnements. Elles vont des vibrations du sol lorsqu'une personne marche, d'une carcasse d'une machine rotative jusqu'aux charges que supportent les bâtiments, infrastructures et moyens de transport (avions...). Les vibrations sont disponibles sur une large gamme de fréquences (de quelques Hertz voire moins à plusieurs centaines de kiloHertz mais typiquement entre 1 et 1000 Hz - Tableau 1.2), et ne souffrent que de peu de restriction de l'environnement. Ainsi cette énergie peut être récupérée pour alimenter des dispositifs autonomes.

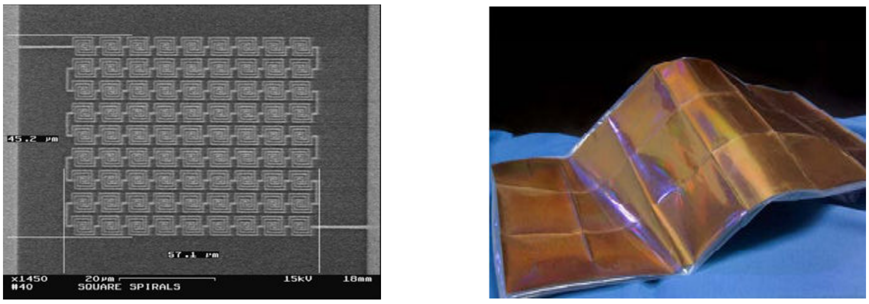

(a) (b)

Figure 1.3: Nantenna de l'Idaho National Laboratories: (a) Un réseau de nantennas, imprimé sur or et imagé avec un microscope à balayage ; (b) Feuille de nantenna, assemblées à partir de 18 éléments.

Tableau 1.2: Amplitude et fréquence d'accélération de sources vibratoires potentielles parmi des dispositifs commerciaux typiques [25]

Source de vibration	*Accélération* (m.s^{-2})	*Fréquence (pic)* (Hz)
Compartiment de moteur de voiture	12	200
Base d'une machine-outil 3 axes	10	70
Boitier d'un mixeur de cuisine	6.4	121
Sèche-linge	3.5	121
Personne tapant ses talons	3	1
Tableau de bord de voiture	3	13
Enceinte de porte juste après la fermeture de cette dernière	3	125
Petit four à micro-ondes	2.5	121
Events de climatiseur dans un immeuble commercial	0.2-1.5	60
Fenêtre proche d'une route fréquentée	0.7	100
CD dans un ordinateur portable	0.6	75
Plancher d'un étage d'un immeuble commercial fréquenté	0.2	100

En plus de l'optimisation de la structure elle-même (poutre encastrée-libre trapézoïdale...), la récupération d'énergie mécanique peut se faire par l'utilisation de nombreux effets de conversion, dont les principaux sont l'électromagnétisme, l'électrostatique, la piézoélectricité (qui sera détaillée dans un paragraphe dédié) et l'électrostriction.

L'effet électromécanique par l'utilisation du magnétisme se traduit par un changement de flux magnétique (provoqué par le mouvement) qui entraîne une variation de tension électrique lorsqu'un enroulement de fils électriques (bobine) est placé à l'intérieur. De nombreuses applications utilisent cet effet, dont le rendement devient cependant relativement faible lorsque les dimensions sont réduites. Un autre effet qui utilise le magnétisme est la magnétostriction. Les matériaux magnétostrictifs sont des éléments capables de changer leur forme sous l'effet d'un champ magnétique, ou, de manière réciproque, changer leur magnétisation sous l'effet d'une déformation (effet Villari). Ces dispositifs, ainsi contrôlés par un champ magnétique, peuvent ainsi être associés avec un autre effet (par exemple piézoélectrique) afin de récupérer l'énergie.

Les dispositifs électrostatiques exploitent quant à eux les variations de capacité afin de récupérer de l'énergie à partir de vibrations (ces dernières modulant la capacité - Figure 1.4). Néanmoins, étant des systèmes passifs, il convient de pré-charger le système pour l'accomplissement des cycles de récupération (typiquement à tension constante - Ericsson - ou à charge constante - Stirling), ce qui peut conduire à une électronique de contrôle relativement complexe. Le système étant chargé lorsque la valeur de la capacité est maximale, lors de la déformation (conduisant à une diminution de la capacité), de l'énergie mécanique est convertie sous forme électrostatique, et ensuite récupérée. Malgré la nécessité de devoir contrôler la charge ou la tension à chaque instant (ce qui peut néanmoins être facilité par l'utilisation d'électrets), des tels dispositifs présentent des capacités d'intégration très élevées. La variation de capacité peut par ailleurs être obtenue selon plusieurs configurations mécaniques (Figure 1.5).

Enfin, par analogie avec la magnétostriction, l'électrostriction peut être envisagée pour récupérer de l'énergie. De façon similaire, l'application de cycles énergétiques permet d'assurer la conversion d'énergie, mais il est également possible d'appliquer un champ électrique de polarisation afin d'avoir un comportement pseudo-piézoélectrique.

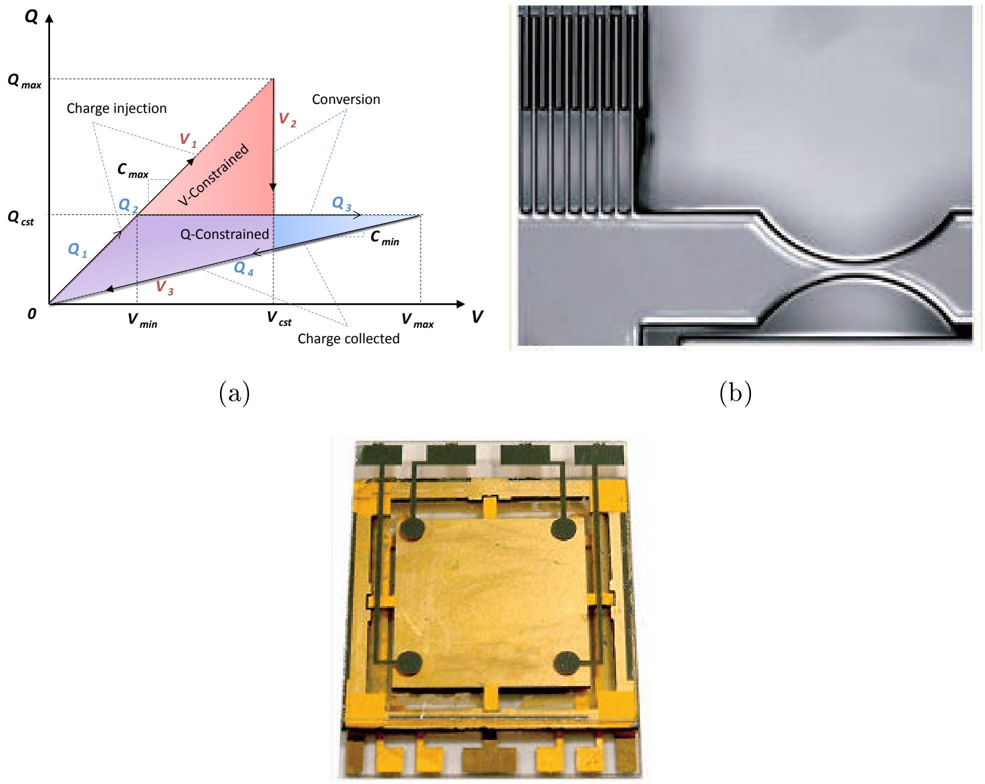

(a)

(b)

(c)

Figure 1.4: Cycles et dispositifs électrostatiques : (a) Cycles typiques de récupération d'énergie [?] ; (b) exemple d'un microgénérateur électrostatique de 1 cm^2 fabriqué au MIT ; (b) exemple d'un microgénérateur électrostatique de 2 cm^2 fabriqué à l'Imperial College [4].

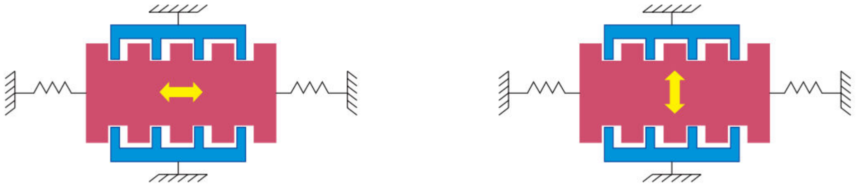

ⓐ convertisseur dans le plan à entrefer variable (*In Plane Gap Closing*) : structure à peignes interdigités à entrefer variable entre doigts et mouvement dans le plan

ⓑ convertisseur dans le plan à chevauchement variable (*In Plane Overlap*) : structure à peignes interdigités avec chevauchements variables des doigts et mouvement dans le plan

ⓒ convertisseur hors plan à entrefer variable (*Out of Plane Gap Closing*) : structure plane à entrefer variable par mouvement relatif au plan

ⓓ convertisseur dans le plan à surface variable : structure à bosses en vis-à-vis à surface variable à mouvement dans le plan

Figure 1.5: Topologies des systèmes électrostatiques [?].

1.3 Récupération d'énergie vibratoire par effet piézoélectrique

Grâce à leur intégrabilité et densité de puissance relativement importante, les éléments piézoélectriques sont des choix de premier ordre pour concevoir des microgénérateurs d'énergie, et ont ainsi fait l'objet de nombreuses études dans ce domaine. Typiquement, les microgénérateurs piézoélectriques peuvent générer des puissances allant du μW à quelques mW. De même, leurs tensions de sortie relativement importante (de l'ordre du Volt) en font des candidats particulièrement intéressants pour une interface électronique aisée (pont redresseur...). Les éléments piézoélectriques capables de transformer directement une énergie mécanique (contrainte, déformation) sous forme électrique (champ électrique, induction) par divers mécanismes (par exemple par déformation d'une maille cristalline dont les barycentres des charges positives et négatives ne sont pas confondus) sont ainsi très bien adaptés à la récupération d'énergie vibratoire à petite échelle. Ils peuvent coupler les grandeurs électriques et mécaniques dans le même axe (mode 33) ou selon des axes différents, le plus commun étant l'utilisation de modes de flexion (couplage 31) permettant une utilisation à des fréquences compatibles avec les vibrations (Figure 1.6). De même, le couplage avec la structure hôte peut se faire directement (élément directement collé sur la structure) ou de manière sismique via l'utilisation d'une structure mécanique intermédiaire (Figure 1.7). Bien que cette dernière soit très sensible à l'adaptation avec la structure hôte et ne peut pas refléter

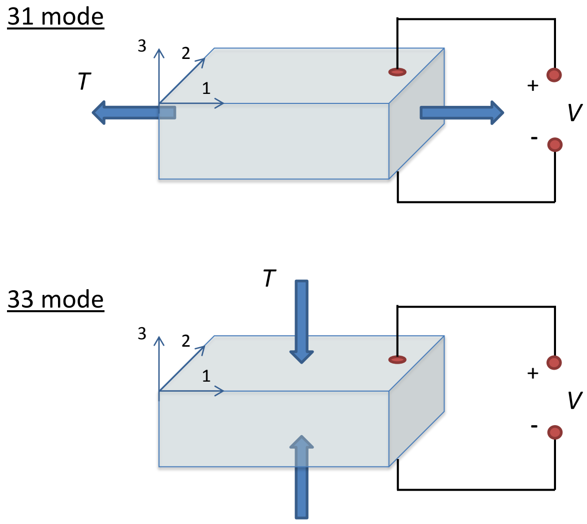

Figure 1.6: Illustration des modes 31 et 33 pour les matériaux piézoélectriques.

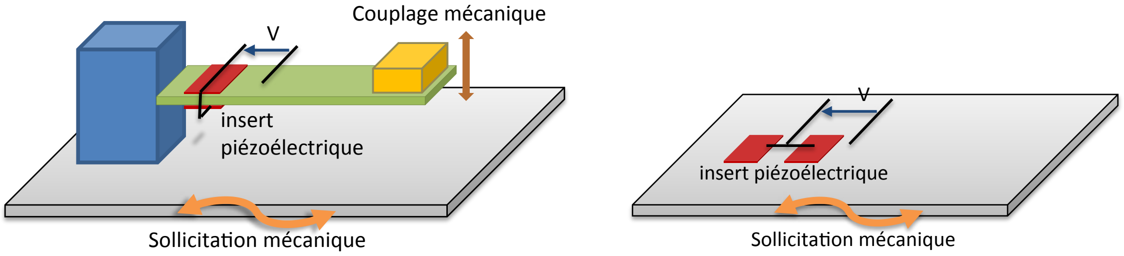

(a) (b)

Figure 1.7: Types généraux de conversion piézoélectrique [52] : (a) couplage indirect ; (b) couplage direct.

les modes de la structure hôte hors de cette fréquence d'accordage, sa maintenance aisée la rend commercialement très attractive. De par leur nature diélectrique, il est possible, en plus de l'optimisation mécanique, d'augmenter artificiellement le couplage électromécanique des éléments piézoélectriques et donc les capacités de récupération d'énergie, par l'utilisation de dispositifs de commutation adaptés [54, 74, 81, 89, 146].

1.3.1 Energie vibratoire

Bien que la grande majorité des études menées sur les dispositifs ne considèrent que des excitations sinusoïdales, le comportement du microgénérateur dans son environnement réel, où les vibrations sont généralement plus aléatoires et présentent un caractère large bande, est radicalement changé. Ceci est d'autant plus vrai lorsque des non-linéarités (mécaniques ou électriques) interviennent dans le système. De même, dans le cas de structures sismiques, les dérives de fréquence de résonance dues à des facteurs environnementaux ou au vieillissement peuvent conduire à un désaccordage qui réduit dramatiquement l'énergie récupérée. Ainsi, l'aspect large bande d'excitations réalistes et la nécessité d'adapter le système en conséquence a récemment attiré l'attention de la communauté scientifique. Diverses solutions ont été proposées, comme l'utilisation de réseaux de résonateurs légèrement désaccordés les uns des autres, de structures bistables, d'impacteurs, ou de composants non-linéaires (comme par exemple des rigidités cubiques).

De même, en termes d'analyse, peu de travaux ont évalué l'impact de vibrations large bande sur les performances des microgénérateurs. Parmi eux, beaucoup se basent sur l'expérimentation ou l'analyse numérique (par exemple, les éléments finis) du fait du manque d'outils théoriques d'analyse. Il convient cependant de noter que quelques recherches ont proposé l'utilisation d'approches stochastiques pour évaluer théoriquement les niveaux d'énergie récupérée qui peuvent être espérés.

2 Modélisation large bande de la récupération d'énergie non-linéaire

Le chapitre précédent a montré que la récupération d'énergie vibratoire à l'aide d'éléments piézoélectriques peut être grandement améliorée par l'intermédiaire d'interfaces électroniques non-linéaire. Dans ce chapitre, la modélisation du comportement d'une technique similaire sous des conditions d'excitation quelconque et possiblement large bande sera exposée, et formera une première étape à l'évaluation des performances de récupération d'énergie large bande qui sera poursuivie dans le chapitre suivant. La méthode de traitement non-linéaire envisagée consiste à commuter à intervalle régulier l'élément piézoélectrique sur un circuit d'inversion de la tension de ce dernier. Cette approche diffère légèrement de la technique SSHI classique qui consiste à inverser la tension de l'élément sur des extrema de déplacement. La commutation périodique, baptisée PSHI ("Periodic Switch Harvesting on Inductor" - Récupération par commutation périodique sur une inductance), permet d'aborder le dispositif comme un système "auto-échantillonné", en ce sens que la commutation périodique, conduisant à une inversion quasi-instantanée de la tension, peut être vue comme la réinjection dans le système de ses propres valeurs échantillonnées (Figure 2.1).

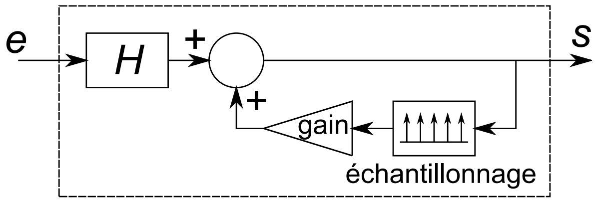

Figure 2.1: Principes de l'"auto-échantillonnage".

2.1 Processus de commutation périodique sans récupération d'énergie

Avant d'aborder l'application de la technique PSHI à la problématique de récupération d'énergie vibratoire, cette partie expose l'utilisation de la technique synchronisée dans le cas où aucune charge électrique n'est connectée au système. Ceci permettra d'établir la démarche adoptée de manière plus claire, tout en pouvant être adaptée au cas du contrôle vibratoire. Le principe de l'approche par "auto-échantillonnage" peut être illustré par la Figure 2.2. En considérant le cas simple d'un signal sinusoïdal de fréquence f_0 (qui contient donc que deux composantes fréquentielles à $\pm f_0$), l'échantillonnage du signal par un peigne de Dirac dont la période est la moitié de celle du signal sinusoïdal conduit à la convolution du signal original par un peigne de Dirac fréquentiel de fréquence $2f_0$. Ensuite, la superposition dans le domaine fréquentiel du signal original avec sa version échantillonnée conduit à un processus cumulatif qui amplifie le signal original (si la phase est correctement choisie) par "auto-repliement", tout en générant des harmoniques supplémentaires. Dans cette partie, il sera d'abord envisagé par soucis de clarté le cas où la tension est seulement annulée périodiquement (et non inversée).

2.1.1 Commutation sur un court-circuit

Ce paragraphe a pour but d'introduire le concept de modélisation des performances de la technique de commutation en utilisant le concept d'"auto-échantillonnage" sur un cas relativement simple consistant en un élément piézoélectrique dont la tension est annulée périodiquement (Figure 2.3), par exemple pour l'application au contrôle de vibrations (technique PSDS : "Periodic Switch Damping on Short-circuit" - Amortissement par Commutation Périodique sur Court-circuit).

Dans ce cas, en considérant un modèle masse-ressort-amortisseur couplé électromécaniquement (Figure 2.4) et dont les équations mécanique et électrique sont données par :

$$\begin{array}{l} M\ddot{u} = F - K_{\mathrm{E}}u - \alpha V - C\dot{u} \\ I = \alpha\dot{u} - C_0\dot{V} \end{array}, \tag{2.1}$$

avec u, F, V et I le déplacement, la force d'entrée, la tension et le courant sortant de l'élément actif et M, C, K_E, α et C_0 la masse dynamique, le coefficient d'amortissement

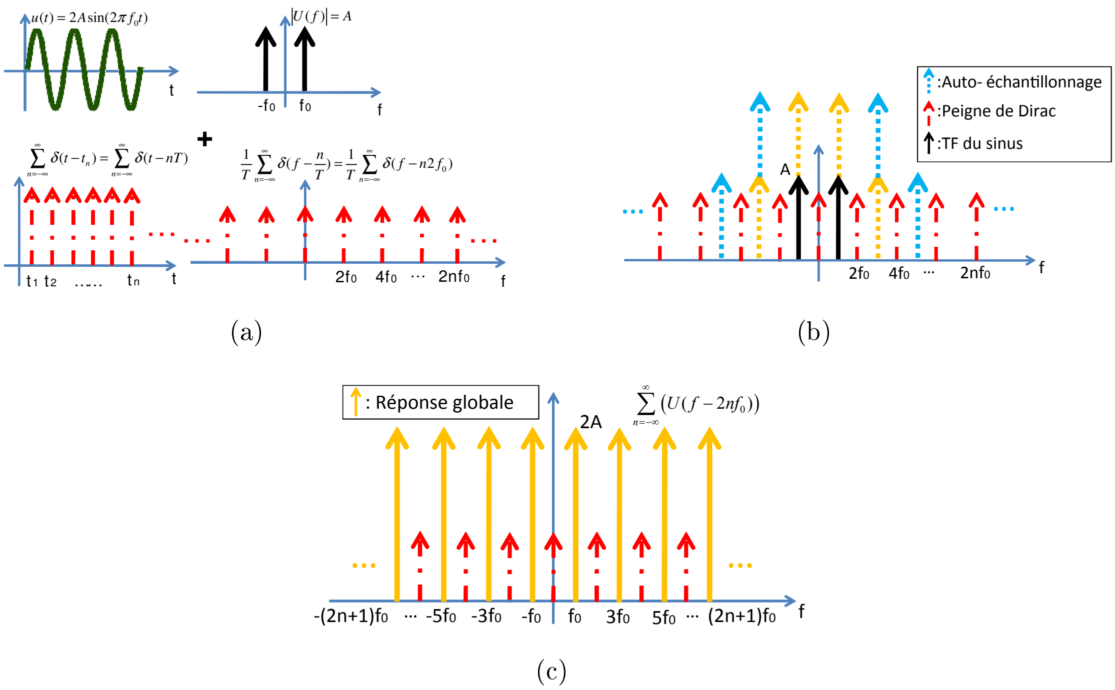

(a) (b)

(c)

Figure 2.2: Concept de l'"auto-échantillonnage" et de l'"auto-repliement" pour un signal sinusoïdal : (a) somme du signal sinusoïdal et du peigne de Dirac ; (b) signal sinusoïdal subissant l'"auto-échantillonnage" ; (c) réponse global après le processus d'échantillonnage.

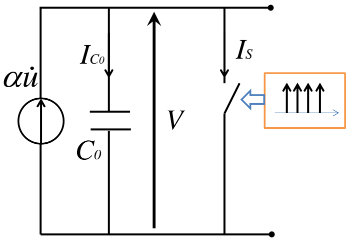

Figure 2.3: Commutation périodique sur court-circuit.

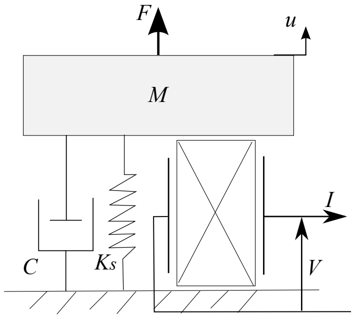

Figure 2.4: Modélisation par système masse-ressort-amortisseur électromécaniquement couplé.

structural, la raideur en court-circuit, le facteur de force et la capacité bloquée, la tension aux bornes de l'élément piézoélectrique peut être exprimée par :

$$V(t) = \frac{\alpha}{C_0}u(t) + \kappa(t), \tag{2.2}$$

où $\kappa(t)$ est une fonction constante par morceaux. En notant t_n $(n \in N)$ les instants de commutation, la fonction $\kappa(t)$ peut être résolue. En combinant la tension ainsi obtenue avec l'équation donnant le courant I et en considérant que les commutations se font avec une période T, il est alors possible d'exprimer la tension dans le domaine fréquentiel selon :

$$V(\omega) = \frac{\alpha}{C_0}U(\omega) - \frac{1}{j\omega}\frac{a}{C_0}\frac{1}{T_s}\sum_{n=-\infty}^{\infty}\left[U(\omega - n\frac{2\pi}{T_s})\left(1 - e^{-j\left(\omega - n\frac{2\pi}{T_s}\right)T_s}\right)e^{-jn\frac{2\pi}{T_s}t_0}\right]. \tag{2.3}$$

où le terme de sommation fait clairement apparaître l'effet de l'"auto-échantillonnage". t_0 représente l'éventuel retard du peigne de Dirac non centré temporellement en zéro.

2.1.2 Inversion de la tension

Afin de progresser par étape dans l'élaboration de la méthode d'analyse des performances des techniques non-linéaires dans le cas d'excitations complexes, cette partie propose l'inclusion de l'inductance dans le circuit de commutation, comme illustré en Figure 2.5. Dans ce cas, la tension au moment de la commutation est inversée avec un facteur γ $(0 \geq \gamma \geq 1)$, conduisant au jeu d'équations :

$$-\gamma V(t_{n-1}^-) = \frac{\alpha}{C_0}u(t_{n-1}) + A_{n-1}, \tag{2.4}$$

$$V(t_n^-) = \frac{\alpha}{C_0}u(t_n) + A_{n-1}, \tag{2.5}$$

$$-\gamma V(t_n^-) = \frac{\alpha}{C_0}u(t_n) + A_n. \tag{2.6}$$

où A_n sont les constantes de la fonction $\kappa(t)$.

La relation entre les constantes A_n peut être obtenue en considérant la différence entre la constante A_n et A_{n-1} par rapport à A_{n-1} et A_{n-2}, ce qui permet d'exprimer la fonction $\kappa(t)$ et d'en déduire l'expression de la tension dans le domaine fréquentiel :

$$V(\omega) = \frac{\alpha}{C_0}U(\omega) - \frac{\alpha}{C_0}(1+\gamma)\frac{1}{j\omega}\frac{1}{T_s}\left(\frac{1}{1+\gamma e^{-jT_s\omega}}\right)\left(1 - e^{-jT_s\omega}\right)\sum_{n=-\infty}^{\infty}\left(U(\omega - n\frac{2\pi}{T_s})e^{-jn\frac{2\pi}{T_s}t_0}\right). \tag{2.7}$$

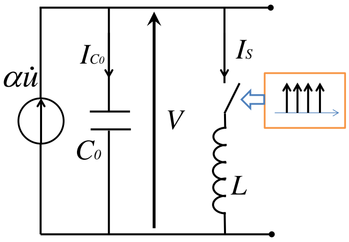

Figure 2.5: Commutation périodique sur inductance.

qui, en plus du processus d'"auto-échantillonnage", montre l'effet cumulatif d'augmentation de la tension du fait de l'inversion.

2.2 Récupération d'énergie par processus de commutation périodique

Le paragraphe précédent s'est attaché, par soucis de clarté au niveau du développement de la méthode d'analyse, au cas où aucune charge n'était connectée au système. Dans cette partie, l'étude sera étendue au cas où la récupération d'énergie se fait effectivement sur une charge résistive (représentant le circuit alimenté) connectée en parallèle avec le système.

2.2.1 Expression de la tension

Dans ce cas, la fonction $\kappa(t)$ n'est plus constante par morceaux du fait de la décharge exponentielle de la capacité de l'élément piézoélectrique dans la résistance, et la réponse en courant dépend de la convolution avec la réponse impulsionnelle décrivant ce circuit :

$$\tilde{I}_s = -(1+\gamma)\sum_{n=-\infty}^{\infty}\left[\sum_{k'=0}^{\infty}(-\gamma)^{k'}\left([(\dot{u}*h)]_{t-k'T_s}\, e^{-\frac{k'T_s}{R_LC_0}} - [(\dot{u}*h)]_{t-(k'+1)T_s}\, e^{-\frac{(k'+1)T_s}{R_LC_0}}\right)\delta(t-nT_s)\right]. \qquad (2.8)$$

Une analyse similaire au cas précédent permet ainsi d'exprimer la tension dans le domaine fréquentiel :

$$\begin{aligned}&V(\omega) = j\omega U(\omega)h(\omega)\\&-j(1+\gamma)\tfrac{C_0}{\alpha}\tfrac{1}{T_s}\frac{\left(1-e^{-T_s j\omega}e^{-\frac{T_s}{R_L C_0}}\right)}{\left(1+\gamma e^{-T_s j\omega}e^{-\frac{T_s}{R_L C_0}}\right)}h(\omega)\left[\sum_{n=-\infty}^{\infty}\left[\left(\omega-\tfrac{n2\pi}{T_s}\right)U(\omega-\tfrac{n2\pi}{T_s})h(\omega-\tfrac{n2\pi}{T_s})\right]e^{-jn\frac{2\pi}{T_s}t_0}\right]\ ,\end{aligned} \tag{2.9}$$

2.2.2 Prise en compte de l'amortissement

Du fait du couplage inverse, l'extraction d'énergie mécanique conduit à un effet d'amortissement qui réduit ainsi la quantité d'énergie récupérable dans la structure. Dans le cas d'une excitation large bande et à partir de l'équation mécanique du modèle combinée avec celle de la tension dans le cas commuté, on peut ainsi exprimer le déplacement dans le domaine fréquentiel par :

$$\lambda(\omega)^{-1}U(\omega) - F(\omega) = \eta\left(\omega\right)\sum_{n=-\infty}^{\infty}\left(\omega - n\frac{2\pi}{T_s}\right)U\left(\omega - n\frac{2\pi}{T_s}\right)h\left(\omega - n\frac{2\pi}{T_s}\right)e^{j\left(\omega-n\frac{2\pi}{T_s}\right)t_0}, \tag{2.10}$$

avec

$$\eta(\omega) = j\frac{(1+\gamma)\left(1-e^{-T_s j\omega}e^{-\frac{T_s}{RC_0}}\right)}{\left(1+\gamma e^{-T_s j\omega}e^{-\frac{T_s}{RC_0}}\right)}\frac{e^{-j\omega t_0}C_0}{T_s}h(\omega) \tag{2.11}$$

$$\lambda\left(\omega\right) = \frac{1}{-M\omega^2 + jC\omega + K_E + j\omega\alpha h(\omega)}. \tag{2.12}$$

En remarquant que la sommation introduite par l' "auto-échantillonnage" est invariante par translation d'une fréquence proportionnelle à $\omega_s = 2\pi/T$, il est alors possible d'exprimer le déplacement par :

$$\begin{aligned}U(\omega) &= \lambda(\omega)F(\omega) + \frac{\eta(\omega)\lambda(\omega)S_F(\omega)}{1-\eta(\omega)S_h(\omega)}\\&= U_1(\omega) + U_2(\omega).\end{aligned} \tag{2.13}$$

où :

$$\beta\left(\omega\right) = h\left(\omega\right)e^{-j\omega t_0}\lambda\left(\omega\right). \tag{2.14}$$

$$S_F\left(\omega\right)=\sum_{n=-\infty}^{\infty}\left[\left(\omega-n\frac{2\pi}{T_s}\right)\lambda\left(\omega-n\frac{2\pi}{T_s}\right)F\left(\omega-n\frac{2\pi}{T_s}\right)h\left(\omega-n\frac{2\pi}{T_s}\right)e^{j\left(\omega-n\frac{2\pi}{T_s}\right)t_0}\right], \tag{2.15}$$

$$S_h\left(\omega\right)=\frac{e^{j\omega t_0}}{h(\omega)}\sum_{n=-\infty}^{\infty}\left[\left(\omega-n\frac{2\pi}{T_s}\right)\beta\left(\omega-n\frac{2\pi}{T_s}\right)h\left(\omega-n\frac{2\pi}{T_s}\right)e^{j\left(\omega-n\frac{2\pi}{T_s}\right)t_0}\right], \tag{2.16}$$

et qui peut être vu comme la réponse sans commutation (U_1) plus un contre-déplacement introduit par le processus de commutation.

Ainsi, en combinant les expressions précédentes avec celle de la tension, il est possible d'évaluer la puissance totale récupérée sur la charge à partir de l'expression de la force dans le domaine fréquentiel :

$$P=\frac{1}{T_v}\frac{1}{2\pi}\int_{-\infty}^{\infty}\frac{V(\omega)V^*(\omega)}{R_L}d\omega \tag{2.17}$$

2.3 Etudes de cas

Dans cette partie, il est proposé de valider l'analyse des performances en termes de récupération d'énergie de la technique de commutation périodique, via l'utilisation d'une excitation simple (sinus), d'hypothèses simplificatrices (couplage limité), puis à un cas plus général. Pour chaque étude, une comparaison avec une résolution temporelle itérative par différences finies sera menée pour vérifier la validité de l'analyse menée.

2.3.1 Excitation monochromatique

Dans le cas où le système est excité de manière monochromatique, les techniques PSHI et SSHI se rejoignent, dès lors que la fréquence de commutation de la technique périodique est égale à deux fois la fréquence de vibration et que le déphasage entre les instants de commutation et la vitesse est nul. En négligeant le couplage inverse (faible coefficient de couplage piézoélectrique et/ou fort amortissement structurel), le déplacement peut être considéré sinusoïdal, et son expression fréquentielle est donnée par :

$$U(\omega)=\frac{u_M}{2}\left[\delta(\omega-\omega_0)+\delta(\omega+\omega_0)\right], \tag{2.18}$$

En couplant cette expression avec celles obtenues précédemment, on peut alors exprimer la tension selon :

$$V(\omega_0) = \frac{u_M}{2} j\omega_0 h(\omega_0) - j(1+\gamma)\frac{C_0}{\alpha}\frac{{\omega_0}^2}{\pi}\frac{\left(1+e^{-\frac{\pi}{R\omega_0 C_0}}\right)}{\left(1-\gamma e^{-\frac{\pi}{R\omega_0 C_0}}\right)} h(\omega_0)\frac{u_M}{2}\left[h(\omega_0) - h(-\omega_0)e^{-j2\omega_0 t_0}\right], \tag{2.19}$$

pour $m = \pm 1$ et

$$V(m\omega_0) = -j(1+\gamma)\frac{u_M}{2}\frac{C_0}{\alpha}\frac{{\omega_0}^2}{\pi}\frac{\left(1+e^{-\frac{\pi}{R\omega_0 C_0}}\right)e^{-jm\omega_0 t_0}}{\left(1-\gamma e^{-\frac{\pi}{R\omega_0 C_0}}\right)} h(m\omega_0)\left(h(\omega_0)e^{j\omega_0 t_0} - h(-\omega_0)e^{-j\omega_0 t_0}\right),$$

pour $m \neq \pm 1$ (2.20)

l'expression fréquentielle de la tension étant nulle autrement. On pourra noter que la première expression est identique à celle obtenue classiquement avec l'approximation du premier harmonique [140]. Néanmoins, la méthode d'analyse choisie ici permet d'accéder aux harmoniques de la tension et ainsi d'estimer de manière plus précise la puissance qui peut être récupérée.

Lorsque l'amortissement induit par le processus de commutation est pris en compte, c'est-à-dire que la force est considérée comme l'entrée sinusoïdale, l'utilisation des expressions précédentes en notant que les réponses aux fréquences qui ne sont pas des harmoniques sont nulles conduit aux expressions du déplacement (en ne considérant que les fréquences positives - la réponse pour la partie négative étant simplement le conjugué) :

$$U(\omega_0) = \lambda(\omega_0)F(\omega_0) + \frac{\lambda(\omega_0)\eta(\omega_0)S_F(\omega_0)}{1-\eta(\omega_0)S_h(\omega_0)}. \tag{2.21}$$

et pour $m \neq 1$:

$$U(m\omega_0) = \frac{\lambda(m\omega_0)\eta(m\omega_0)S_F(m\omega_0)}{1-\eta(m\omega_0)S_h(m\omega_0)} \tag{2.22}$$

avec

$$\eta\left(m\omega_0\right) = j\frac{(1+\gamma)}{\left(1-\gamma e^{-\frac{T_s}{RC_0}}\right)}\frac{C_0}{T_s}h(m\omega_0)e^{-jm\omega_0 t_0}\left(1+e^{-\frac{T_s}{RC_0}}\right), \tag{2.23}$$

$$S_F\left(m\omega_0\right) = \omega_0\lambda\left(\omega_0\right)F\left(\omega_0\right)h\left(\omega_0\right)e^{j\omega_0 t_0} - \omega_0\lambda\left(-\omega_0\right)F\left(-\omega_0\right)h\left(-\omega_0\right)e^{-j\omega_0 t_0}, \tag{2.24}$$

$$S_h\left(m\omega_0\right) \approx \frac{e^{jm\omega_0 t_0}}{h(m\omega_0)}\left[\omega_0\beta\left(\omega_0\right)h\left(\omega_0\right)e^{j\omega_0 t_0} - \omega_0\beta\left(-\omega_0\right)h\left(-\omega_0\right)e^{-j\omega_0 t_0}\right] \tag{2.25}$$

et pour la tension :

$$V(m\omega_0) = jm\omega_0 U(m\omega_0)h(m\omega_0) - \frac{\eta(m\omega_0)}{\alpha}\left[\omega_0 U(\omega_0)h(\omega_0)e^{j\omega_0 t_0} - \omega_0 U(-\omega_0)h(-\omega_0)e^{-j\omega_0 t_0}\right]. \tag{2.26}$$

En utilisant des paramètres inspirés de structures expérimentales présentées dans la littérature [54] et listés dans le Tableau 2.1, on obtient les résultats présentés en Figure 2.6, qui concordent très bien avec les résultats théoriques et expérimentaux obtenus dans la littérature (notamment le fait qu'un faible retard de commutation peut augmenter légèrement la puissance récupérée - [126]). Par ailleurs, les formes d'ondes obtenus par transformées de Fourier inverses et comparées à celles obtenues par résolution temporelle (Figure 2.7) confirment la précision de la méthode basée sur le principe d'"auto-échantillonnage".

2.3.2 Réponse impulsionnelle

Dans le cas intermédiaire d'une réponse impulsionnelle, l'ouverture de la bande fréquentielle et sa recopie par convolution avec le peine de Dirac dans le domaine fréquentiel (Figure 2.8) conduit à un étalement du spectre, voire même dans certains cas où l'amortissement est important à un repliement (Figure 2.9). Dans le cas d'un système très amorti et/ou peu couplé où le couplage inverse peut être négligé, il est alors possible d'approcher l'expression de la tension dans la bande fréquentielle $2k\omega_0 < \omega < 2(k+1)\omega_0$ par :

Tableau 2.1: Paramètres du modèle pour le microgénérateur

C_0	20 nF
α	0.001 N/V
K_E	3000 Nm^{-1}
M	200 g
C	0.2 $Nm^{-1}s^{-1}$
Q_I	5.6
f_0	19.49 Hz
k^2	0.0164
Q_M	122.475
k^2Q_M	2.009

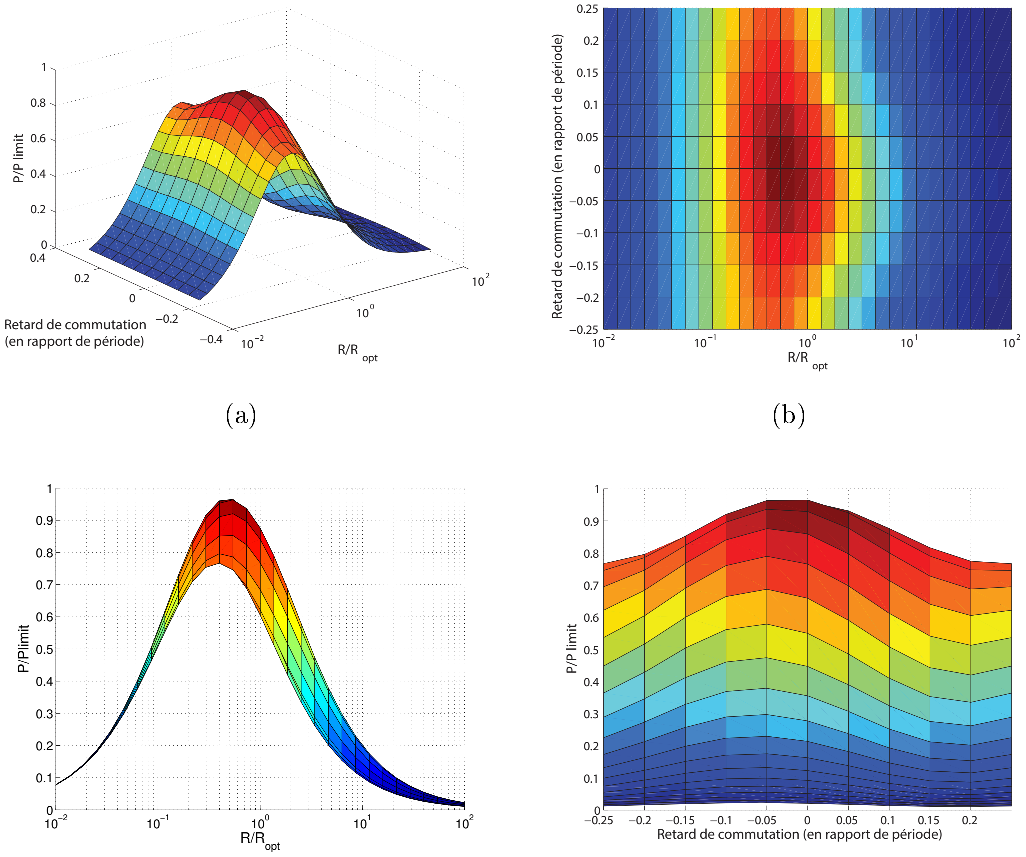

(a) (b)

(c) (d)

Figure 2.6: Puissance récupérée normalisée en fonction du retard de commutation et de la charge sous excitation sinusoïdale d'amplitude constante pour la technique PSHI : (a) vue 3D de la puissance récupérée normalisée en fonction de R/R_{opt} et du retard de commutation (en rapport de période); (b) vue de dessus de la puissance récupérée normalisée en fonction de R/R_{opt} et du retard de commutation (en rapport de période) ; (c) vue de côté représentant la puissance récupérée normalisée en fonction de R/R_{opt}; (d) vue de côté représentant la puissance récupérée normalisée en fonction du retard de commutation (en rapport de période).

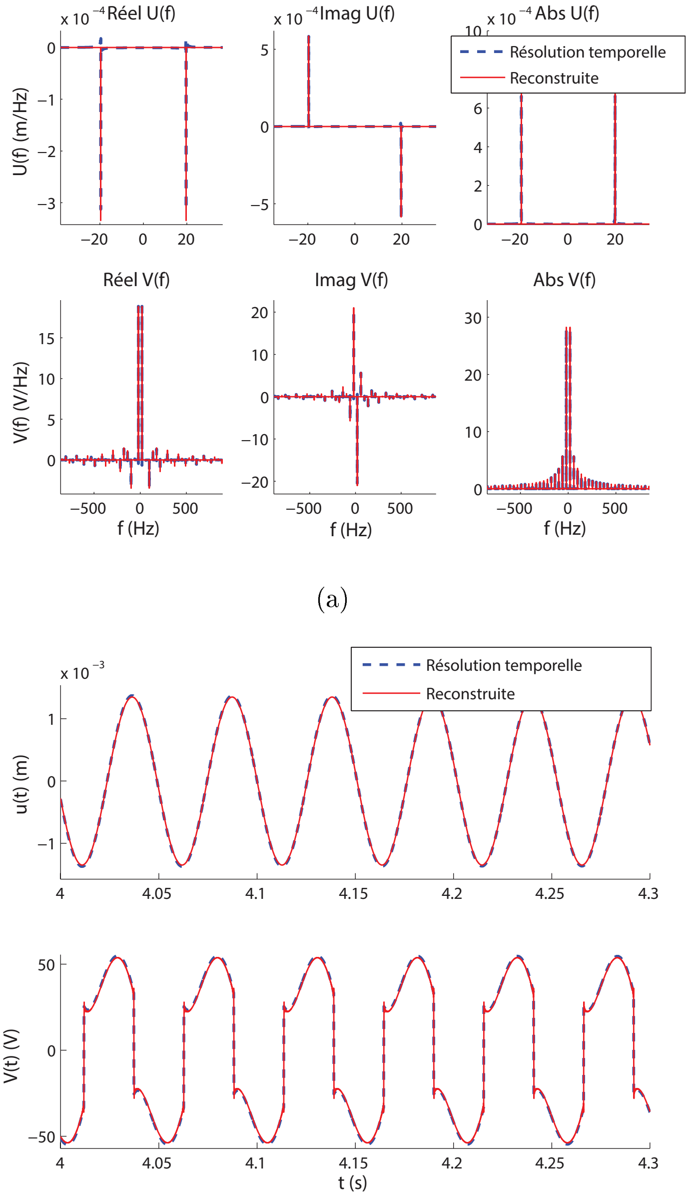

(a)

(b)

Figure 2.7: Résultats de simulation pour une excitation sinusoïdale d'amplitude constante obtenus à partir de la modélisation large bande (trait plein rouge) et d'une résolution numérique dans le domaine temporel (trait pointillé bleu) avec l'interface PSHI et un retard de commutation de 10% de la période de vibration : (a) comparaison fréquentielle ; (b) comparaison temporelle.

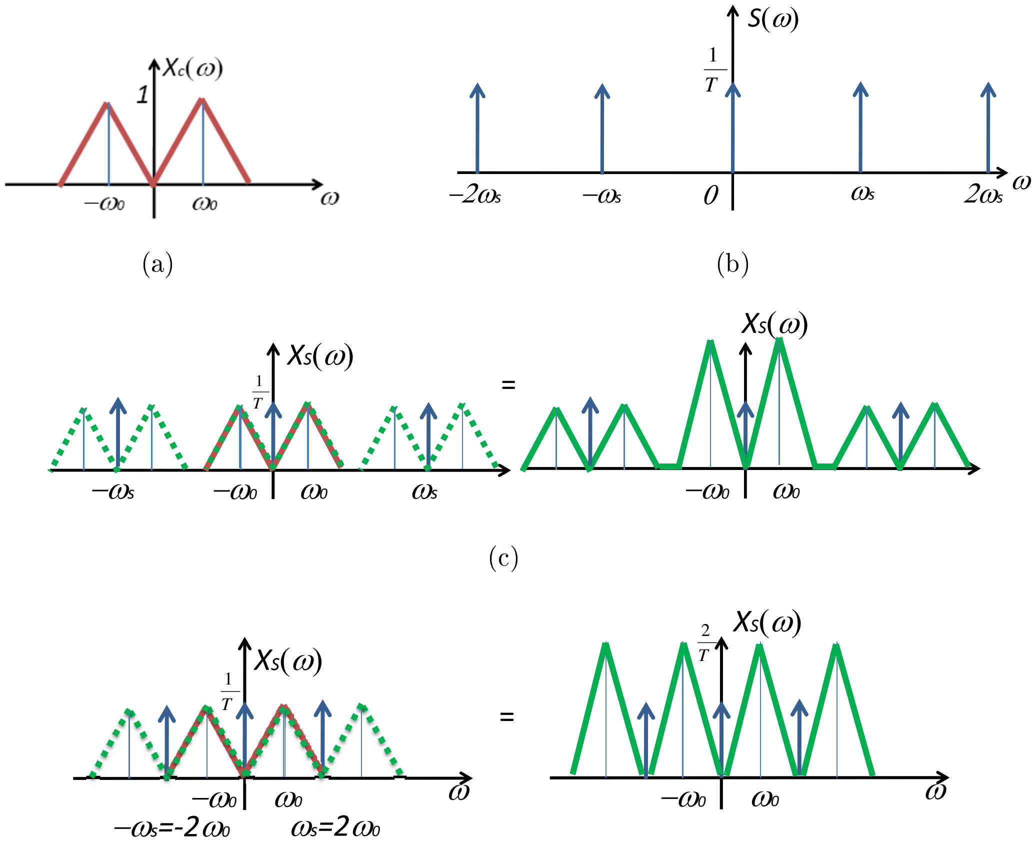

(a) (b)

(c)

(d)

Figure 2.8: Effet de l'"auto-échantillonnage" sur la réponse du système : (a) spectre du signal original ; (b) spectre de la fonction d'échantillonnage ; (c) spectre du signal échantillonné avec $\omega_s > 2\omega_0$; (d) spectre du signal échantillonné avec $\omega_s = 2\omega_0$.

$$\begin{aligned} V(\omega) =& j\omega U(\omega)h(\omega) \\ & - \left\{ \frac{\eta(\omega)}{\alpha} \lambda_0\left(\omega - 2k\omega_0\right) F\left(\omega - 2k\omega_0\right) e^{j(\omega-2k\omega_0)t_0} \right. \\ & \left. \times \left[\left(\omega - 2k\omega_0\right) h\left(\omega - 2k\omega_0\right) - \left(\omega - 2\left(k+1\right)\omega_0\right) h\left(\omega - 2\left(k+1\right)\omega_0\right) e^{-j(2\omega_0)t_0} \right] \right\}. \end{aligned} \tag{2.27}$$

avec :

$$U(\omega) = \frac{F(\omega)}{-M\omega^2 + jC\omega + K_E}. \tag{2.28}$$

et :

$$\lambda_0(\omega) = \frac{1}{-M\omega^2 + jC\omega + K_E} \tag{2.29}$$

$$\eta(\omega) = j \frac{(1+\gamma)\left(1 - e^{-T_s j\omega} e^{-\frac{T_s}{RC_0}}\right)}{\left(1 + \gamma e^{-T_s j\omega} e^{-\frac{T_s}{RC_0}}\right)} \frac{e^{-j\omega t_0} C_0}{T_s} h(\omega). \tag{2.30}$$

ce qui donne des résultats qui sont très proches des résultats par intégration numérique dans le domaine temporel (Figure 2.10)

2.3.3 Excitation aléatoire large bande

Ce dernier cas considère un force d'entrée suivant un loi de distribution gaussienne avec une moyenne nulle et un écart-type unitaire, le tout moyenné sur quelques points pour lisser la forme d'onde. Les simulations temporelle par intégration numérique et fréquentielle suivant l'analyse précédemment exposée concordent toujours parfaitement

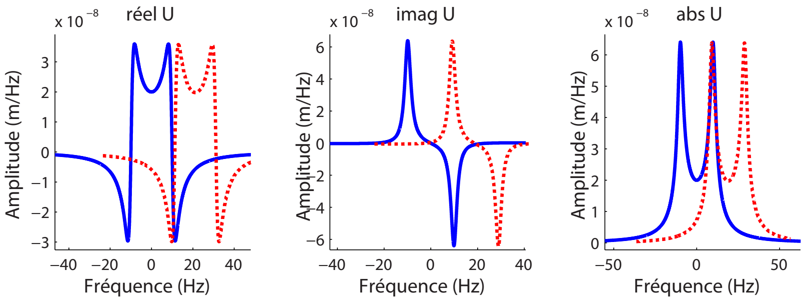

Figure 2.9: Réponse impulsionnelle auto-échantillonnée dans le cas d'un système peu amorti ; – et ··· représentent respectivement les réponses originale et échantillonnée.

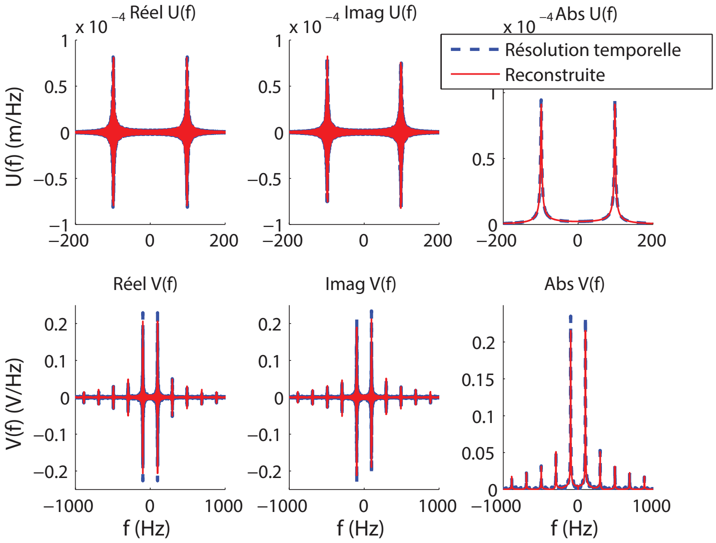

(a)

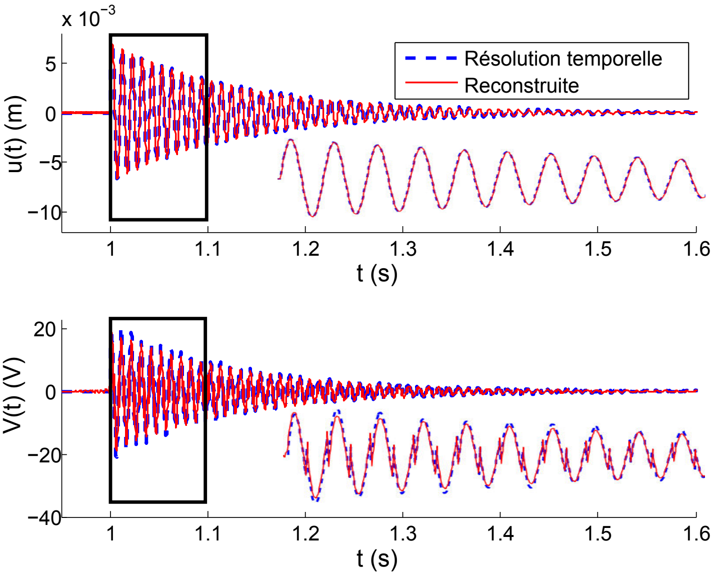

(b)

Figure 2.10: Résultats de simulation pour une excitation impulsionnelle sans couplage inverse obtenus à partir de la modélisation large bande (trait plein rouge) et d'une résolution numérique dans le domaine temporel (trait pointillé bleu) avec l'interface PSHI et un retard de commutation de 10% de la période de vibration : (a) comparaison fréquentielle ; (b) comparaison temporelle.

(Figure 2.11). La puissance récupérée dans ce cas en variant la fréquence de commutation et par moyennage de 10 simulations par point est exposée en Figure 2.12. Il est intéressant de noter la présence de creux à des fréquences particulières, notamment aux alentours de deux fois la fréquence de résonance, ce qui peut être expliqué par le fait que le retard de commutation ne peut être compensé par un battement du à une légère différence de fréquence.

2.4 Conclusion

Ce chapitre a exposé une approche de modélisation d'une technique non-linéaire de récupération d'énergie basée sur une commutation périodique de l'élément piézoélectrique. Cette nouvelle méthode, fondée sur le principe d'"auto-échantillonnage" induit par le processus de commutation, permet d'évaluer efficacement la réponse du système et l'énergie récupérée lorsque le microgénérateur est soumis à un déplacement ou une force quelconque. Bien que plus efficace et rapide qu'une analyse temporelle, cette approche nécessite une connaissance complète de l'excitation (module et phase), ce qui est rarement disponible dans l'optique d'application réaliste. Mais sa combinaison avec une approche probabiliste permettra d'évaluer efficacement les capacités de récupération d'énergie de microgénérateurs intégrant l'interface PSHI dans un environnement quelconque.

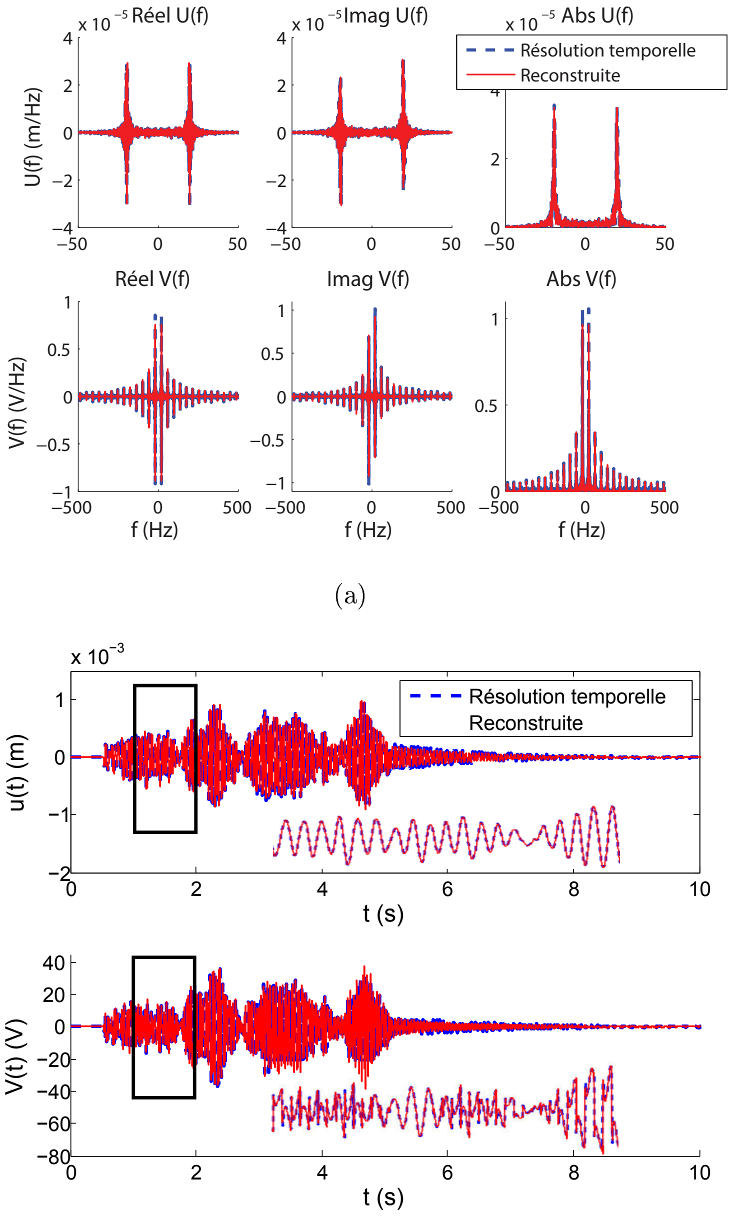

(a)

(b)

Figure 2.11: Résultats de simulation pour une excitation aléatoire pour une fréquence de commutation de $2\omega_0$ obtenus à partir de la modélisation large bande (trait plein rouge) et d'une résolution numérique dans le domaine temporel (trait pointillé bleu) avec l'interface PSHI et un retard de commutation de 10% de la période de vibration : (a) comparaison fréquentielle ; (b) comparaison temporelle.

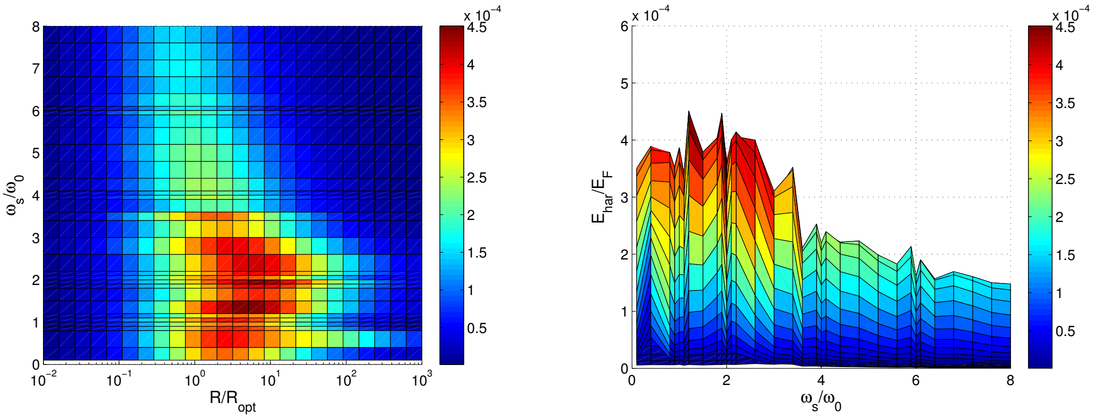

(a) (b)

Figure 2.12: Energie récupérée (moyennée sur 10 simulations) obtenue par l'analyse large bande en fonction de la charge (normalisée par rapport à la charge optimale dans le cas standard sinusoïdal) et de la fréquence de commutation (normalisée par rapport à la fréquence de résonance) pour une exictation aléatoire : (a) vue de dessus ; (b) vue de côté représentant l'énergie récupérée normalisée en fonction de de la fréquence de commutation normalisée.

3 Modélisation stochastique de la technique PSHI dans le domaine fréquentiel

Le chapitre précédent s'est attelé à la modélisation fréquentielle de la technique PSHI de commutation périodique. Bien qu'il ait été montré que cette approche s'avère particulièrement efficace pour évaluer les performances de récupération d'énergie dans le cas d'une excitation aléatoire, ce chapitre propose d'étendre l'étude en y incorporant une analyse stochastique, permettant une meilleure estimation de l'énergie qui peut être récupérée dans le cas de signaux aléatoires d'environnements réalistes à partir de la densité spectrale de puissance de l'excitation. On se bornera toujours au cas de la technique PSHI, celle-ci étant linéaire mais non temporellement invariante ; en effet, la technique SSHI étant non temporellement invariant mais également non-linéaire, ceci compromet l'utilisation des méthodes d'analyse stochastique. Cet effet de non-invariance temporelle engendrée par le processus de commutation peut être typiquement vu sur la réponse impulsionnelle donnant le courant en fonction du déplacement établie dans le chapitre 2 :

$$\begin{aligned} h_s(t,t_1) = &-(1+\gamma)\sum_{n=-\infty}^{\infty}\left[\sum_{k'=0}^{\infty}(-\gamma)^{k'}\left(h\left(t-k'T-t_1\right)e^{-\frac{k'T}{\tau_e}}\right.\right. \\ &\left.\left.-h\left(t-\left(k'+1\right)T-t_1\right)e^{-\frac{(k'+1)T}{\tau_e}}\right)\delta\left(t-nT\right)\right]. \end{aligned} \tag{3.1}$$

Ainsi, du fait de l'aspect temporellement variant de la technique PSHI, la méthode d'analyse choisie se base sur une approche cyclostationnaire, qui postule que les caractéristiques statistiques d'un signal présentent une périodicité, ce qui permet leur expression en termes de séries de Fourier.

3.1 Application à la technique PSHI

3.1.1 Cas général

Dans le cas de l'analyse menée ici, on définira $h_{xy}(t,t_1)$ les différentes réponses impulsionnelles du signal x par rapport à l'entrée y, permettant de relier les différentes fonctions de covariance K_{xy} ($K_{AB} = E[A(t)B(t')]$ avec E l'espérance et A et B deux fonctions quelconques mais stationnaires au sens large) selon le jeu minimum d'équations :

$$\begin{align}
\langle \dot{u}(t)v(t')\rangle &= \frac{\partial}{\partial t}K_{uv}(t,t') = K_{vv}(t,t') \tag{3.2}\\
\langle \dot{v}(t)v(t')\rangle &= \frac{\partial}{\partial t}K_{vv}(t,t') = -{\omega_{0E}}^2 K_{uv}(t,t') - \frac{\omega_{0E}}{Q_M}K_{vv}(t,t') \nonumber\\
&\qquad - \frac{\alpha}{M}K_{Vv}(t,t') + \frac{1}{M}K_{Fv}(t,t') \tag{3.3}\\
\langle V(t)v(t')\rangle &= K_{Vv}(t,t') = \int_{-\infty}^{\infty} h_{Vv}(t,t_1)K_{vv}(t_1,t')dt_1 \tag{3.4}\\
\langle F(t)\dot{u}(t')\rangle &= \frac{\partial}{\partial t'}K_{Fu}(t,t') = K_{Fv}(t,t') \tag{3.5}\\
\langle F(t)\dot{v}(t')\rangle &= \frac{\partial}{\partial t'}K_{Fv}(t,t') = -{\omega_{0E}}^2 K_{Fu}(t,t') - \frac{\omega_{0E}}{Q_M}K_{Fv}(t,t') \nonumber\\
&\qquad - \frac{\alpha}{M}K_{FV}(t,t') + \frac{1}{M}K_{FF}(t,t') \tag{3.6}\\
\langle F(t)V(t')\rangle &= K_{FV}(t,t') = \int_{-\infty}^{\infty} h_{Vv}(t',t_1)K_{Fv}(t,t_1)dt_1. \tag{3.7}
\end{align}$$

qui est soluble si K_{FF}, qui caractérise l'excitation appliquée sur la structure, est connue. En utilisant un temps central et une différence de temps plutôt que deux instants distincts ($R_{AB}(t,\tau) \equiv K_{t_2,t_1}$ avec $t = (t_1+t_2)/2$ et $\tau = t_2 - t_1$), il est possible d'utiliser une représentation en série de Fourier dont les coefficients sont donnés par :

$$R^n_{AB}(\tau) = \frac{1}{T_s}\int_0^{T_s} R_{AB}(t,\tau)e^{-j\omega_s nt}dt; \tag{3.8}$$

et d'introduire la densité spectrale d'interaction selon :

$$S^n_{AB}(\omega) = \int_{-\infty}^{\infty} R^n_{AB}(\tau)e^{-j\omega\tau}d\tau. \tag{3.9}$$

ce qui permet d'exprimer et de réduire le jeu minimum d'équations précédemment établi dans le domaine temporel à :

$$\frac{L\left(\omega+\frac{1}{2}\omega_s n\right)}{j\left(\omega+\frac{1}{2}\omega_s n\right)}S^n_{vv}(\omega)=-\frac{\alpha}{M}S^n_{Vv}(\omega)+\frac{1}{M}S^n_{Fv}(\omega) \tag{3.10}$$

$$\frac{L^*\left(\omega-\frac{1}{2}\omega_s n\right)}{-j\left(\omega-\frac{1}{2}\omega_s n\right)}S^n_{Fv}(\omega)=-\frac{\alpha}{M}S^n_{FV}(\omega)+\frac{1}{M}S^n_{FF}(\omega), \tag{3.11}$$

avec :

$$L(\omega)=-\omega^2+{\omega_{0E}}^2+2j\omega\zeta\omega_{0E}; \tag{3.12}$$

Où ζ dénote le coefficient d'amortissement. On pourra noter que S^n_{FF} est nul pour $n\neq 0$ pour un signal stationnaire au sens large, et que le coefficient non nul S^0_{FF} représente la densité spectrale de puissance.

La résolution de ce système se fait en considérant les densités spectrales d'interaction entre la tension V et la force F ainsi qu'entre la tension et la vitesse v :

$$S^n_{FV}(\omega)=\sum_i S^i_{Fv}(\omega+\frac{1}{2}\omega_s\,(n-i))y_{n-i}(\omega-\omega_s i+\frac{1}{2}\omega_s n). \tag{3.13}$$

$$S^n_{Vv}(\omega)=\sum_i S^i_{vv}(\omega-\frac{1}{2}\omega_s\,(n-i))y^*_{n-i}(\omega+\omega_s i-\frac{1}{2}\omega_s n). \tag{3.14}$$

Où y_k sont les coefficients de Fourier d'une fonction t-périodique $y(t,\omega)$ découlant des propriétés cyclostationnaires de la réponse impulsionnelle donnant la tension en fonction de la vitesse h_{Vv} :

$$\int_{-\infty}^{\infty} h_{Vv}(t,t_1)e^{-j\omega t_1}dt_1=e^{-j\omega t}y(t,\omega)=\sum_k y_k(\omega)e^{j(-\omega+k\omega_s)t}, \tag{3.15}$$

avec

$$y_k(\omega)=\hat{h}^*(\omega)\times\left(\delta_{k,0}-\frac{1}{T_s}\cdot\frac{1+\gamma}{-j\omega+\frac{1}{\tau}+j\omega_s k}\cdot\frac{1-e^{\left(j\omega-\frac{1}{\tau}\right)T_s}}{1+\gamma e^{\left(j\omega-\frac{1}{\tau}\right)T_s}}\right) \tag{3.16}$$

Ainsi il est possible d'en déduire la puissance récupérée à partir de la fonction de covariance K_{vv} :

$$
\begin{aligned}
P &= \frac{1}{T_s}\frac{1}{R_L}\int_{0}^{T_s}\int_{-\infty}^{\infty}\int_{-\infty}^{\infty} h_{Vv}(t,t_1)h_{Vv}(t,t_2)K_{vv}(t_1,t_2)dt_1dt_2dt \\
&= \frac{1}{R_L}\frac{1}{2\pi}\int_{-\infty}^{\infty} d\omega \sum_{n} \tilde{S}_{vv}^{n}(\omega)\Bigg(\hat{h}^{*}(\omega)\hat{h}(\omega+\omega_s n) \\
&\qquad\qquad \times\left(\delta_{n,0}+(1+\gamma)\,\frac{1}{T_s}J(\omega)\right)\Bigg), \qquad (3.17)
\end{aligned}
$$

où :

$$
\begin{aligned}
J_n(\omega) = {} & \frac{1}{\left(-j\omega-\frac{1}{\tau_{\mathrm{e}}}\right)}\frac{1-e^{\left(-j\omega-\frac{1}{\tau_{\mathrm{e}}}\right)T_s}}{1+\gamma e^{\left(-j\omega-\frac{1}{\tau_{\mathrm{e}}}\right)T_s}} + \frac{1}{\left(j\left(\omega+\omega_s n\right)-\frac{1}{\tau_{\mathrm{e}}}\right)}\frac{1-e^{\left(j\omega-\frac{1}{\tau_{\mathrm{e}}}\right)T_s}}{1+\gamma e^{\left(j\omega-\frac{1}{\tau_{\mathrm{e}}}\right)T_s}} \\
& + \frac{\tau_{\mathrm{e}}}{2}\frac{(1+\gamma)\left(1-e^{-\frac{2T_s}{\tau_{\mathrm{e}}}}\right)}{\left(1+\gamma e^{\left(j\omega-\frac{1}{\tau_{\mathrm{e}}}\right)T_s}\right)\left(1+\gamma e^{\left(-j\omega-\frac{1}{\tau_{\mathrm{e}}}\right)T_s}\right)}.
\end{aligned}
$$

3.1.2 Cas des couplages faibles

Lorsque l'on néglige l'impact de la récupération d'énergie sur la structure mécanique, il est possible d'exprimer directement et simplement la densité spectrale de puissance de la vitesse en fonction de celle de la force selon :

$$
S_{vv}^{0}\left(\omega\right) = \left|\hat{h}_{vF}\left(\omega\right)\right|^{2} S_{FF}^{0}\left(\omega\right) \ . \qquad (3.18)
$$

Dès lors, la puissance s'exprime par :

$$
P = \frac{1}{R_L}\frac{1}{2\pi}\int_{-\infty}^{\infty}\left|\hat{h}_{vF}\left(\omega\right)\right|^{2}\left|\hat{h}(\omega)\right|^{2}\left[1+\frac{1+\gamma}{T_s}J_0(\omega)\right]S_{FF}^{0}\left(\omega\right)d\omega \qquad (3.19)
$$

3.2 Résultats numériques

Cette partie présente l'effet de différents paramètres du système (couplage, amortissement,...) ainsi que de différents types d'excitation sur l'énergie récupérée. Les résultats se basent sur la structure expérimentale utilisée dans la partie suivante dont les paramètres sont donnés Tableau 3.1.

Tableau 3.1: Paramètres du modèle pour la simulation

Masse dynamique	M	200 g
Raideur en court-circuit	K_E	3000 Nm^{-1}
Capacité	C_0	20 nF
Coefficient d'inversion	γ	0.75
Fréquence de résonance en court-circuit	f_{0E}	19.49 Hz

Dans le cas d'une excitation par bruit blanc, la Figure 3.1 montre la puissance récupérée maximale (à charge optimale) normalisée en fonction de la fréquence de commutation pour plusieurs valeurs de couplage électromécanique global k^2, ainsi qu'une comparaison avec la technique sans commutation (standard). Il apparaît clairement qu'à faible valeur de k^2, l'approche non-linéaire permet un gain certain en termes d'énergie récupérée. Néanmoins, plus le couplage augmente, plus l'écart se réduit, la technique standard dépassant même la technique PSHI. Plus particulièrement, le creux déjà observé dans le chapitre précédent se confirme dans ces résultats, et apparaît même plus prononcé pour de fortes valeurs de couplage. La fréquence optimale maximisant la puissance dans le cas de la technique PSHI devient par ailleurs de plus en plus faible alors que le couplage augmente. Egalement, il est très intéressant de noter que la puis-

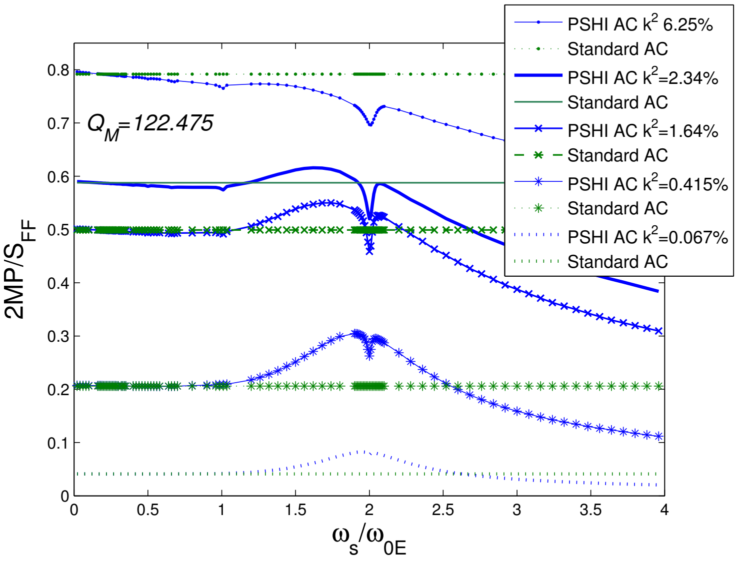

Figure 3.1: Puissance de sortie normalisée à la charge optimale en fonction de la fréquence de commutation avec le facteur de qualité mécanique $Q_M = 122.475$ et différents coefficient de couplage au carré k^2. Les lignes horizontales correspondent aux puissances optimales dans le cas de l'interface alternative standard (sans commutation).

sance récupérée dépend de manière différente du couplage électromécanique k^2 et du facteur de qualité mécanique Q_M, ainsi que montré par la Figure 3.2, ce qui est très différent du cas sinusoïdal ou seul intervient le produit de ces deux paramètres [86].

Grâce à l'approche stochastique dans le domaine fréquentiel, il est possible d'appliquer n'importe quel type d'excitation. Il est ainsi possible d'évaluer les performances du système lorsqu'est appliquée une forme présentant une densité spectrale de bande fréquentielle limitée comme par exemple une distribution gaussienne. La Figure 3.3 montre la forme de densité spectrale de force ainsi que la puissance maximale récupérée normalisée dans ce cas en variant l'ouverture de la bande (représentée par le paramètre f_r). Ces résultats montrent bien entendu que plus l'excitation a un contenu fréquentiel concentré autour de la résonance mécanique plus l'énergie récupérée est importante, mais également que le creux et la fréquence de commutation optimale dépend de la largeur du spectre. Ainsi, plus le spectre est large, plus le creux est atténué et la fréquence de commutation optimale proche de deux fois la fréquence d'excitation.

De manière similaire, il est possible d'évaluer l'effet d'un désaccordage entre l'excitation et la résonance du système (différence de fréquence Δf), représenté en Figure 3.4. Il apparaît encore une dépendance de la fréquence optimale de commutation et de l'amplitude du creux en fonction du décalage fréquentiel ; plus ce dernier est important plus la puissance diminue, mais plus le creux s'atténue et plus la fréquence optimale est proche de deux fois la fréquence de résonance.

3.3 Validation expérimentale

Afin de vérifier plus en avant les développements théoriques menés dans la partie précédente, il est proposé ici d'étudier de manière expérimentale la puissance qui peut être récupérée en moyenne sur un système sismique soumis à une accélération (qui, lorsque multipliée par la masse dynamique, devient la force appliquée au système) dont le contenu fréquentiel est plus riche qu'une simple raie (Figure 3.5(a)). Les résultats, montrés en Figure 3.5(b), obtenue en moyennant la puissance moyenne d'un jeu de 20 mesures, confirme la tendance prévue par l'analyse stochastique du système. Particulièrement, on pourra noter que le creux autour de certaines fréquences est bien observé.

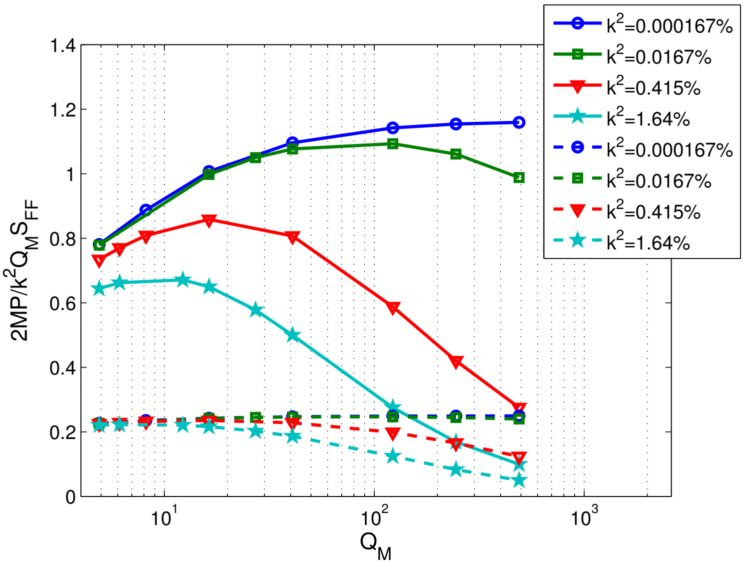

(a)

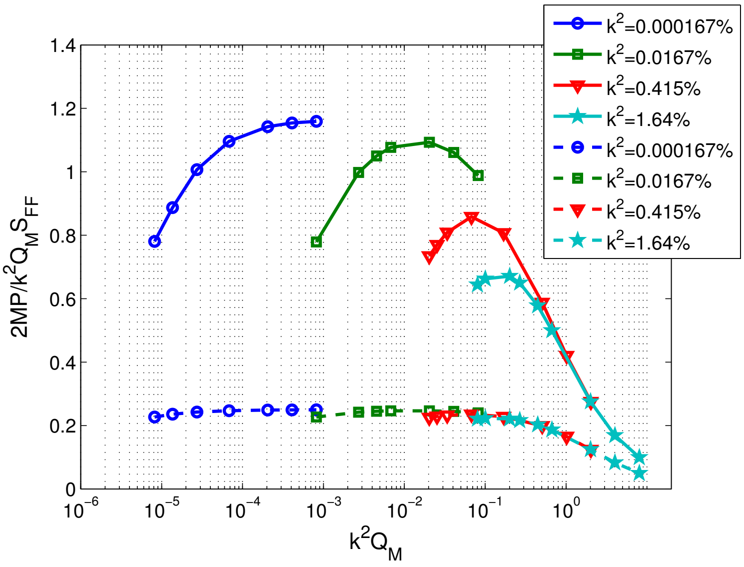

(b)

Figure 3.2: Puissance récupérée normalisée à la charge et fréquence de commutation optimales pour $k^2 = 1.67 \times 10^{-4}$ %, 0.0167 %, 0.415 % and 1.64 % et différentes valeurs de Q_M. (a) Puissance maximale récupérée normalisée en fonction du facteur de qualité mécanique Q_M; (b) Puissance maximale récupérée normalisée en fonction de k^2Q_M. Les lignes pleines représentent la technique non-linéaire PSHI ; les lignes en pointillés représentent le cas standard.

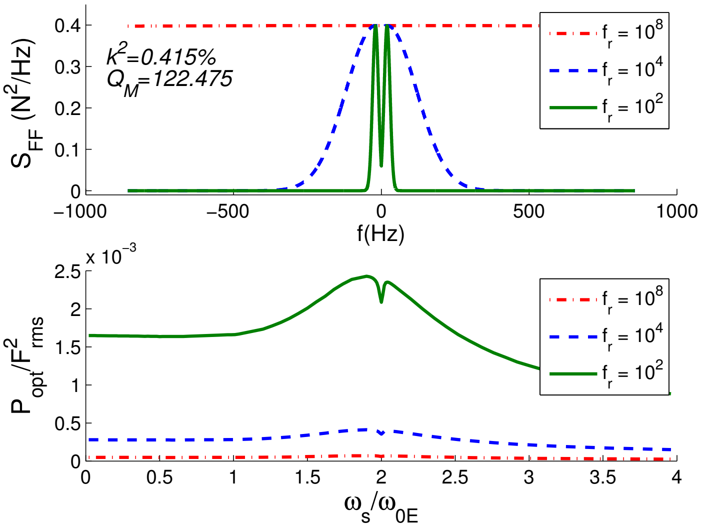

Figure 3.3: Densité spectrale de force et puissance récupérée dans le cas d'une excitation de profil gaussien de largeur de bande différente ($f_r = 10^2, 10^4, 10^8$), $k^2Q_M = 0.508$, $f_{0E} = 19.49$ Hz.

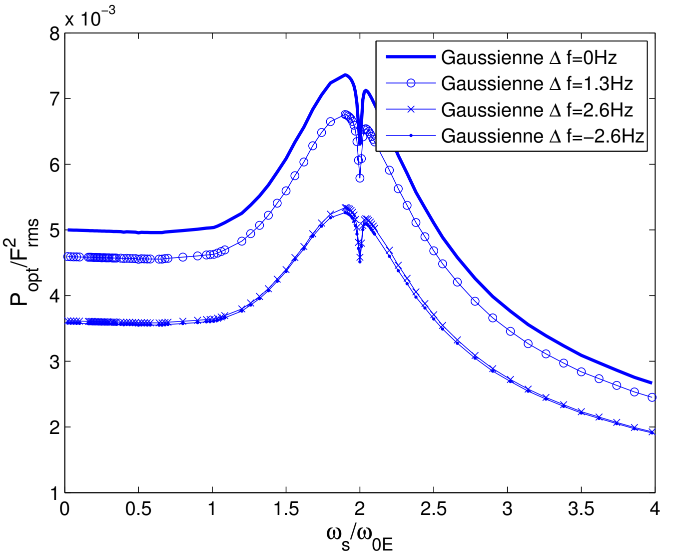

Figure 3.4: Puissance maximale récupérée en fonction de la fréquence de commutation dans le cas d'une densité de spectrale de puissance de l'excitation gaussienne non centrée sur la résonance.

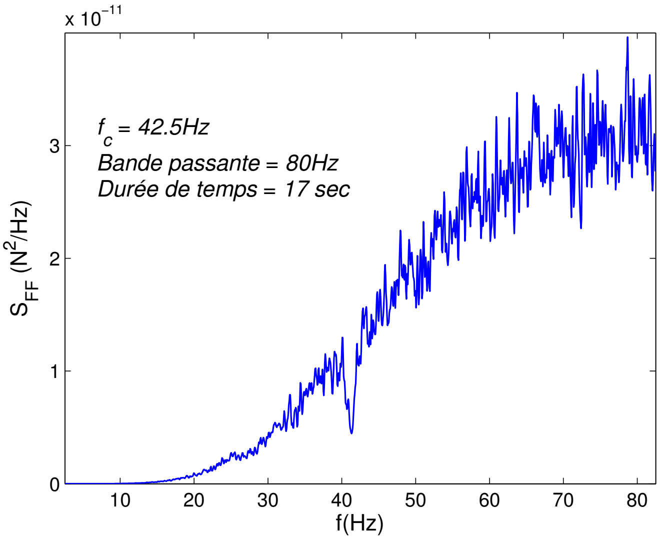

(a)

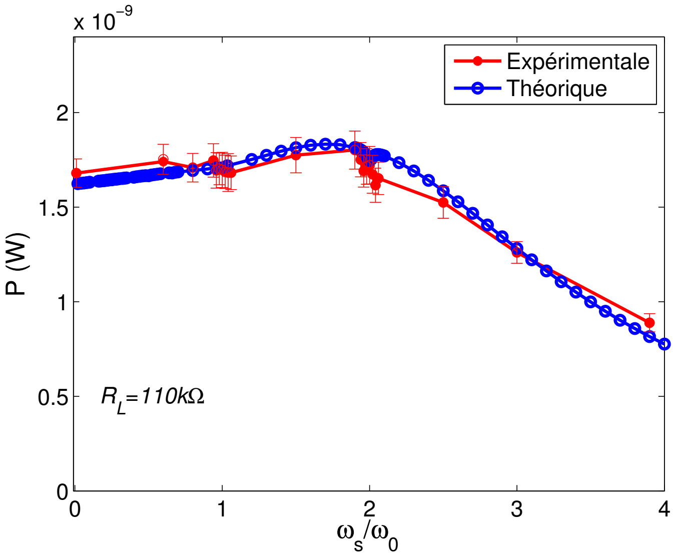

(b)

Figure 3.5: Résultats expérimentaux. La puissance récupérée est optimisée avec une charge résistive de 110 $k\Omega$. (a) autocorrélation de l'excitation d'entrée ; (b) puissance récupérée pour différentes fréquences de commutation.

3.4 Comparaison entre les techniques PSHI et SSHI

Dans cette thèse, afin de pouvoir appliquer les principes d'analyse stochastique, la technique de commutation est considérée périodique, contrairement au cas de la technique SSHI qui elle est directement synchronisée sur le déplacement. Cette partie propose de comparer numériquement les deux approches pour différents cas (faiblement ou fortement couplé) et sous différentes conditions d'excitation. Les résultats montrant les puissances récupérées par les techniques standard, SSHI et PSHI pour différentes valeurs de couplage et de facteurs de qualité mécanique sont présentés en Figure 3.6(a) dans le cas d'une excitation en bruit blanc filtré pour assurer la stabilité de la résolution, en Figure 3.6(b) pour une excitation impulsionnelle et en Figure 3.6(c) dans le cas d'une excitation quadrichromatique (à une, deux, quatre et douze fois la fréquence de résonance). Dans le cas de la technique PSHI, la fréquence de commutation est choisie de telle manière à maximiser la puissance.

Les résultats montrent qu'à faible couplage, la technique SSHI présente des performances bien supérieures à l'approche par commutation périodique, notamment dans le cas d'un bruit blanc filtré où le SSHI permet de récupérer environ deux fois plus d'énergie que le PSHI. Néanmoins, ce dernier reste très supérieur à la technique standard. Néanmoins, au fur et à mesure que le couplage et/ou le facteur de qualité mécanique augmente, ces écarts se réduisent, conduisant à des puissances récupérées similaires pour le SSHI, le PSHI et la technique standard. Il convient même de noter que pour de fortes valeurs de ces paramètres dans le cas multimodal, la technique PSHI dépasse largement le SSHI, ce qui s'explique par le fait que le SSHI se focalisant naturellement sur la plus haute fréquence détectable, les performances se retrouvent très fortement dégradées lorsque celle-ci n'est pas la plus énergétique, ainsi qu'illustré en Figure 3.7.

3.5 Conclusion

Ce chapitre a exposé l'analyse stochastique de la technique PSHI de commutation périodique pour l'évaluation des capacités de récupération d'énergie dans le cas de signaux complexes mais réalistes. Du fait de son aspect non temporellement invariant et non-linéaire, une telle approche ne peut être appliquée à la technique SSHI, alors que le comportement non temporellement invariant mais linéaire du PSHI permet d'appliquer le principe de cyclostationnarité des signaux. Il a ainsi été démontré, numériquement

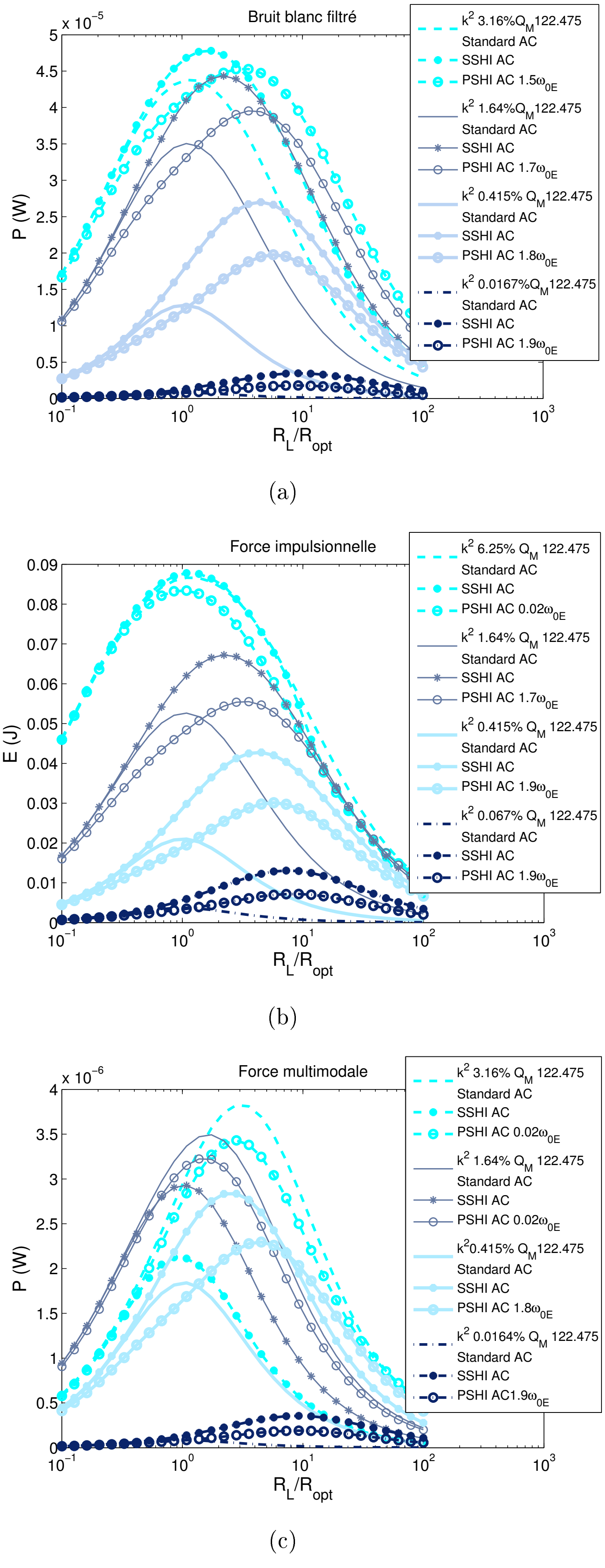

(a)

(b)

(c)

Figure 3.6: Comparaison des puissances et énergies récupérées pour les techniques standard, SSHI et PSHI pour différents profils d'excitation : (a) Bruit blanc filtré ; (b) impulsion ; (c) excitation quadrimodale.

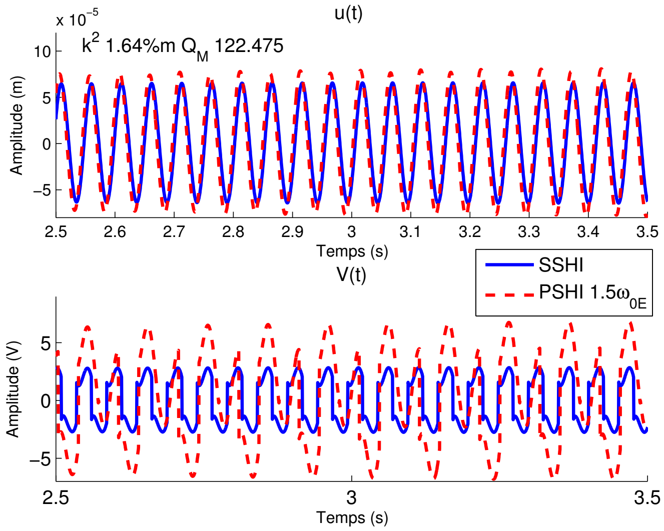

Figure 3.7: Réponses en déplacement et tension d'un récupérateur fortement couplé dans le cas d'une excitation multimodale.

mais aussi expérimentalement, que la technique PSHI présente des phénomènes de creux lorsque le système est bien couplé et/ou amorti à certaine fréquence de commutation en relation avec la fréquence de résonance du système électromécanique, l'amplitude ces creux étant étroitement relié au coefficient de couplage, tout comme la fréquence de commutation optimisant la puissance récupérée. De plus, contrairement au cas monochomatique, il a été montré que les performances de la technique PSHI varient différemment avec le coefficient de couplage global au carré et le facteur de qualité mécanique. Une comparaison avec l'approche SSHI a montré que cette dernière reste supérieure à l'approche périodique lorsque le système est peu couplé, mais que cet écart se réduit lorsque le couplage et/ou le facteur de qualité mécanique augmente. Par ailleurs, dans certains cas, les performances de la technique PSHI dépassent même celles du SSHI, car ce dernier se focalise par nature sur les fréquences les plus hautes qui ne portent pas forcément le plus d'énergie.

4 Effet de la récupération sismique sur la structure hôte et les performances de récupération

Dans le cas d'applications réalistes d'un système de récupération d'énergie sismique, ce chapitre propose d'étudier l'effet du microgénérateur sur la structure hôte. En effet, la modélisation historique des microgénérateurs est passée d'une amplitude de vibration constante de la structure électromécanique à une amplitude d'excitation constante, afin de relater l'amortissement induit par le processus de récupération qui limite la puissance qui peut être délivrée. Ainsi, prendre en compte le couplage mécanique entre le microgénérateur et la structure sur laquelle il est installé est une étape supplémentaire pouvant aider au dimensionnement du récupérateur, toute la chaîne de conversion d'énergie étant prise en compte (Figure 4.1). Par soucis de concision et de clarté, on se limitera à l'interface électrique standard alternative ; l'implémentation de dispositifs non-linéaires pouvant néanmoins être combiné à cette analyse en se basant sur les résultats établis dans les chapitres précédents.

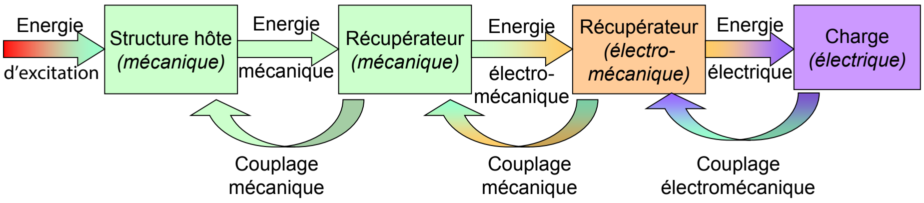

Figure 4.1: Chaîne de conversion d'énergie.

4.1 Modélisation théorique

4.1.1 Modèle à constantes localisées

Le système composé du microgénérateur et de sa structure hôte peut être vu comme un système à deux degrés de libertés mécaniques dont l'un des oscillateurs est électromécaniquement couplé (Figure 4.2), ce qui conduit à l'expression matricielle des équations mécaniques suivante :

$$\mathbf{M\ddot{u}(t)} + \mathbf{C\dot{u}(t)} + \mathbf{Ku(t)} = \mathbf{F(t)} + \mathbf{A}V(t), \tag{4.1}$$

Où $\mathbf{u(t)}$ et $\mathbf{F(t)}$ sont les vecteurs de déplacement et de force (ce dernier ayant seulement la composante appliquée sur la base qui est non nulle) :

$$\mathbf{u}(t) = \begin{bmatrix} u_1(t) \\ u_2(t) \end{bmatrix}, \mathbf{F}(t) = \begin{bmatrix} F(t) \\ 0 \end{bmatrix} \tag{4.2}$$

et $\mathbf{M}$, $\mathbf{C}$, $\mathbf{K}$ et $\mathbf{A}$ sont les matrices de masse dynamique, coefficient d'amortissement structurel, raideur en court-circuit et matrice de facteur de force définies comme suit :

$$\mathbf{M} = \begin{bmatrix} M_1 & 0 \\ 0 & M_2 \end{bmatrix}, \mathbf{K} = \begin{bmatrix} K_1 + K_2 & -K_2 \\ -K_2 & K_2 \end{bmatrix}, \mathbf{C} = \begin{bmatrix} C_1 + C_2 & -C_2 \\ -C_2 & C_2 \end{bmatrix}, \mathbf{A} = \begin{bmatrix} \alpha \\ -\alpha \end{bmatrix}. \tag{4.3}$$

Dans les expressions précédentes, les indices 1 et 2 dénotent respectivement la structure hôte et le microgénérateur. L'expression du courant est similaire à celle utilisée dans les chapitres précédents, excepté que la déflection dépend de la différence des

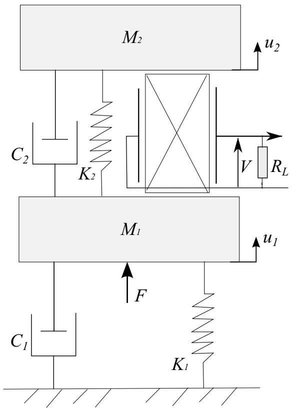

Figure 4.2: Modèle à deux degrés de liberté du système de récupération d'énergie.

déplacements $U_2 - U_1$ plutôt que du déplacement du microgénérateur seul. Ainsi, lorsqu'une charge résistive est connectée, l'expression de la tension dans le domaine fréquentiel est donnée par :

$$\tilde{V}(\omega) = \frac{\alpha R j\omega}{1 + C_0 R j\omega}(\tilde{U_2}(\omega) - \tilde{U_1}(\omega)) = g(\omega)\begin{bmatrix}-1 & 1\end{bmatrix}\begin{Bmatrix}\tilde{U_1}(\omega)\\ \tilde{U_2}(\omega)\end{Bmatrix} \tag{4.4}$$

$$\text{avec } g(\omega) = \frac{\alpha R j\omega}{1 + C_0 R j\omega}, \tag{4.5}$$

En injectant cette expression dans l'équation mécanique, on obtient alors :

$$\begin{Bmatrix}\tilde{U_1}(\omega)\\ \tilde{U_2}(\omega)\end{Bmatrix} = \mathbf{L}(\omega)\begin{Bmatrix}F_M\\ 0\end{Bmatrix}, \tag{4.6}$$

où :

$$\begin{aligned}
&\mathbf{L}(\omega) = \left(\mathbf{I}_2 - \mathbf{G}(\omega)\right)^{-1}\mathbf{T}(\omega)\\
&\mathbf{G}(\omega) = \alpha g(\omega)\mathbf{T}(\omega)\begin{bmatrix}-1 & 1\\ 1 & -1\end{bmatrix}\\
&\mathbf{T}(\omega) = \begin{bmatrix}-M_1\omega^2 + (C_1 + C_2)j\omega + (K_1 + K_2) & -C_2 j\omega - K_2\\ -C_2 j\omega - K_2 & -M_2\omega^2 + C_2 j\omega + K_2\end{bmatrix}^{-1}.
\end{aligned} \quad . \tag{4.7}$$

$\mathbf{I}_2$ étant la matrice identité de taille 2×2. Une fois la matrice de déplacement obtenu, il est alors possible d'exprimer la tension puis la puissance selon la relation :

$$P = \frac{1}{2}\frac{\tilde{V}(\omega)\tilde{V}^*(\omega)}{R_L}, \tag{4.8}$$

4.1.2 Modélisation par éléments finis

Afin de valider le modèle à constantes localisées précédemment établi et de pouvoir analyser plus finement les résultats, un modèle à éléments finis est également proposé. On considèrera pour l'exemple envisagé que la structure hôte et le récupérateur sont de simples poutres encastrées-libres, bien que les principes généraux exposés dans ce chapitre peuvent s'appliquer à tout type de structure. En faisant les hypothèses suivantes :

1. Les structures mécaniques (hôte et récupérateurs) suivent les hypothèses d'Euler-Bernoulli
2. La déformation est dans le plan
3. le champ électrique est constant dans l'élément piézoélectrique
4. L'élément piézoélectrique est isotrope transverse

il est possible d'exprimer la relation entre le vecteur **d** de déplacement et pente et celui **F** de force et moment selon :

$$[\mathbf{M}]\{\ddot{d}(t)\} + [\mathbf{C}]\{\dot{d}(t)\} + [\mathbf{K}]\{d(t)\} - B_1 V(t) = \{\mathbf{F}(t)\}, \tag{4.9}$$

où les matrices **M**, **C** et **K** sont les matrices de masse dynamique, coefficient d'amortissement structurel et raideur en court-circuit obtenues à partir de l'assemblage des matrices de chaque élément, ces dernières étant obtenues en considérant comme fonctions de base la famille des splines cubiques d'Hermite. B_1 est la matrice assemblée traduisant le couplage piézoélectrique, obtenue de manière similaire aux précédentes. Dans le cas de la structure envisagée (Figure 4.3), le noeud en bout de poutre correspondant à la structure hôte est supposé avoir le même déplacement que la base du récupérateur. De même, récupérateur et structure hôte ne partagent pas la même ligne neutre.

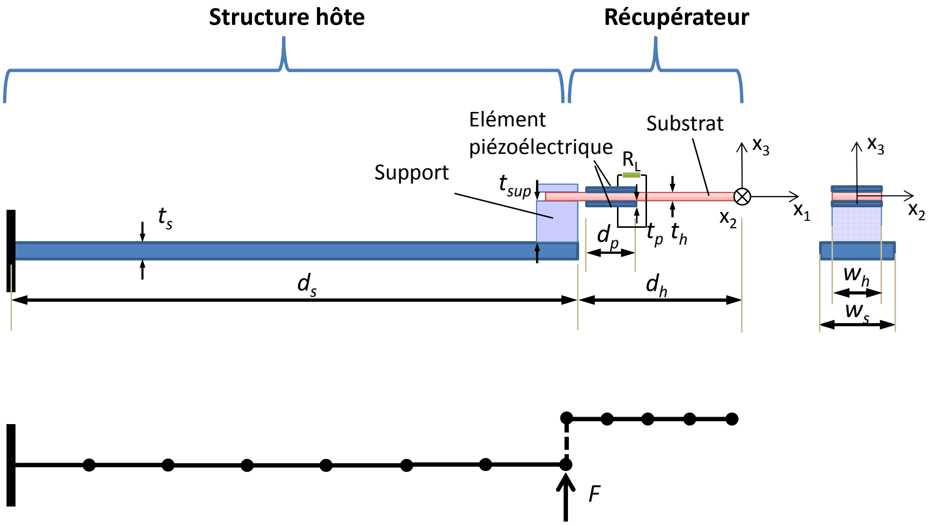

Figure 4.3: Schéma et paramètres géométriques de la structure hôte et du récupérateur.

Par une analyse similaire, la tension peut être exprimée par :

$$\begin{aligned}\dot{V}(t) &= -\frac{d_{31}{t_p}^2}{L_p\left(s_{11}^E + s_{12}^E\right)\varepsilon_{33}^S}\,\dot{\theta}(t)\Big|_{x_0}^{x_0+L_p} - \frac{t_p}{w_p L_p \varepsilon_{33}^S R_L} V(t) \\ &= B_2\,\dot{\theta}(t)\Big|_{x_0}^{x_0+L_p} + B_3 V(t),\end{aligned} \tag{4.10}$$

où θ représente la dérivée spatiale du déplacement et R_L la résistance connectée au système. Les constantes s_{11}^E, S_{12}^E, ϵ_{33}^S et d_{31} sont les compliances élastiques à champ constant, permittivité à déformation constante et constante de charge du matériau piézoélectrique. L_p, w_p et t_p sont la longueur, largeur et épaisseur de l'insert.

Le vecteur déplacement et pente ainsi que la tension sont ensuite donnés par la combinaison des équations mécanique et électrique, qui peuvent ensuite être exprimées dans le domaine fréquentiel afin de s'affranchir du transitoire et faciliter la résolution :

$$\begin{bmatrix} \left([\mathbf{K}] - \omega^2 [\mathbf{M}]\right) + j\,[\mathbf{C}]\,\omega & -B_1 \\ j\omega\mathbf{B}_2 & B_3 - j\omega \end{bmatrix} \begin{bmatrix} \tilde{\mathbf{d}}(\omega) \\ \tilde{V}(\omega) \end{bmatrix} = \begin{bmatrix} \tilde{\mathbf{F}}(\omega) \\ 0 \end{bmatrix} \tag{4.11}$$

$$\tilde{V}(\omega) = \left[B_3 - j\omega\right]^{-1}\left[j\omega\mathbf{B}_2\right] \times \tilde{\mathbf{d}}(\omega). \tag{4.12}$$

Finalement, la puissance récupérée s'obtient à partir de la tension selon :

$$P(\omega) = \frac{\tilde{V}(\omega)\tilde{V}^*(\omega)}{2R_L}. \tag{4.13}$$

4.2 Validation expérimentale

Ce paragraphe propose de vérifier expérimentalement les prédictions théoriques et numériques des modèles précédemment élaborés. Le dispositif expérimental, présenté en Figure 4.4, présente les caractéristiques reportées dans le Tableau 4.1. Une identification préliminaire a également été menée pour déterminer les paramètres du modèle à constantes localisées, qui sont présentés dans le Tableau 4.2.

Les résultats obtenus en termes de déplacement de la structure hôte, de la déflection de la structure du microgénérateur ainsi que de la puissance récupérée sont présentés dans la Figure 4.5, qui inclut le modèle à constantes localisées et l'analyse en éléments finis pour comparaison. Egalement, en termes de déflection du microgénérateur et de

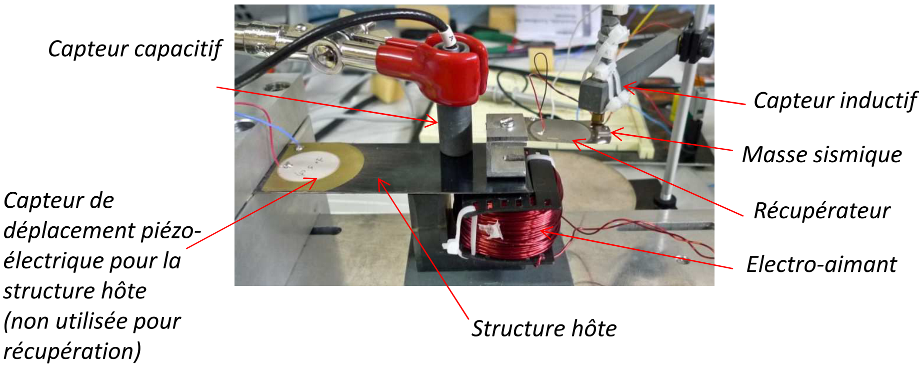

Figure 4.4: Dispositif expérimental.

Tableau 4.1: Caractéristiques des poutres.

Longueur, d_s	0.104 m	**Epaisseur**, t_s	0.52 m
Largeur, w_s	0.04 m	**Module d'Young**, E_s	210 Gpa
Coefficient de Poisson, ν_s	0.3	**Densité**, ρ_s	7450 kg/m^3
Coefficient d'amortissement, ξ_s	0.007		
Longueur, d_h	0.033 m	**Epaisseur**, t_h	49.4 μm
Largeur, w_h	0.02 m	**Module d'Young**, E_h	210 Gpa
Coefficient de Poisson, ν_h	0.3	**Densité**, ρ_h	7480 kg/m^3
Coefficient d'amortissement, ξ_h	0.0658		
Longueur, d_p	0.022 m	**Epaisseur**, t_p	55 μm
Largeur, w_p	0.02 m	**Position**, x_p	0.0033 m
Densité, ρ_p	7900 kg/m^3	**Epaisseur**, t_{sup}	0.00175 m
Constante piézoélectrique, d_{31}	-152.5 $pC.N^{-1}$	**Permittivité**, ε_{33}^S	15.5 $nF.m^{-1}$
Compliances, ${s_{11}}^E$	15.27 $\times 10^{-12}$ Pa^{-1}	${s_{12}}^E$	-5.46 $\times 10^{-12}$ Pa^{-1}

Tableau 4.2: Paramètres expérimentaux.

f_{1s}	26.3 Hz	f_{0s}	26.256 Hz
C_{0s}	40.2 nF	Q_{Ms}	142.23
α_s	2.07×10^{-4}	M_s	0.0115 kg
K_s	314.4 Nm^{-1}	b_s	0.0134 $Nm^{-1}s^{-1}$
f_{1h}	24.05 Hz	f_{0h}	23.45 Hz
C_{0h}	360 nF	Q_{Mh}	36.92
α_h	3.102×10^{-4} N/V	M_h	2.39×10^{-4} kg
K_h	5.467 Nm^{-1}	b_h	9.792×10^{-4} $Nm^{-1}s^{-1}$
F_m	6.2×10^{-4} N	${k_h}^2$	0.0489

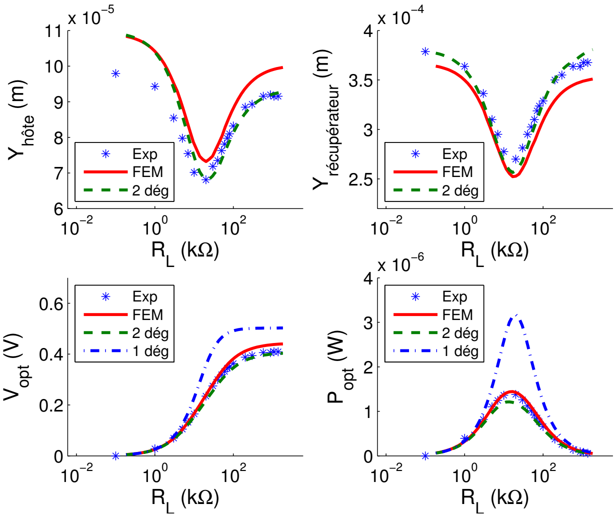

Figure 4.5: Validation expérimentale de la récupération sismique (rapport de masse = 0.0208).

puissance, le modèle à un degré de liberté, qui considère une accélération constante de la base du microgénérateur, est représenté. En plus de l'excellent accord entre théorie, simulation et pratique, on note que, malgré le faible rapport de masse entre le récupérateur et la structure hôte (le premier ayant une masse dynamique 50 fois plus faible que la dernière), le couplage mécanique entre hôte et récupérateur est non négligeable, surtout à la charge optimale où le processus de récupération d'énergie induit une atténuation de plus de 4 dB de la structure hôte (le récupérateur agissant comme un *Tuned Mass Damper* - “Amortisseur à Masse Accordée” - adapté). Ainsi cet amortissement a un impact non négligeable sur la puissance récupérée - cette dernière étant surestimée d'un facteur 2 par l'approximation d'une accélération constante de la base du microgénérateur dans le cas du système à un degré de liberté. Clairement, cette hypothèse n'est pas valide ici, malgré le faible rapport de masse entre le récupérateur et la structure hôte. La Figure 4.6 montre la position du dispositif expérimental par rapport à la puissance maximale récupérée théoriquement. Ainsi, on voit que le rapport de masse optimal est plus faible, ce qui conduirait par ailleurs à un effet d'amortissement de la structure hôte plus important.

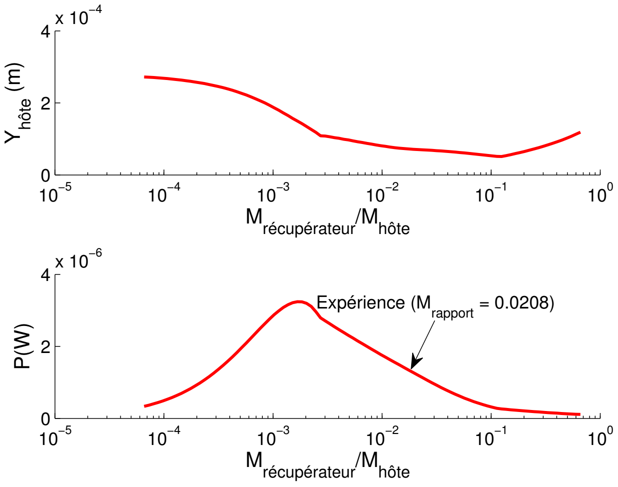

Figure 4.6: Performances optimale du dispositif expérimental prédit par l'approche à constantes localisées.

4.3 Effet du couplage entre récupérateur et structure hôte

Cette partie propose une discussion plus détaillée des différents couplages et couplages inverses qui interviennent dans le cas de microgénérateurs sismiques installés sur une structure hôte. On s'attardera en particulier sur le couplage mécanique entre le récupérateur et la structure hôte. Les paramètres de base étant dérivés du dispositif expérimental exposé dans le paragraphe précédent, il est proposé de faire varier certains de ces paramètres pour quantifier leur effet.

La Figure 4.7 montre l'effet de la variation du rapport de masse entre le récupérateur et l'hôte, en s'assurant que les fréquences des deux systèmes soient bien accordées entre elles. Cette figure démontre clairement qu'une masse optimale existe, relatant le compromis entre transfert énergétique de l'énergie mécanique de la structure hôte vers le récupérateur (toujours sous forme mécanique), et de l'effet d'amortissement du récupérateur qui empêche l'énergie de rentrer dans la structure hôte. On remarque également un glissement de la fréquence de résonance du système global (Figure 4.8), cette dernière pouvant même se dédoubler pour des rapports de masse importants.

L'effet du couplage électromécanique et du facteur de qualité mécanique du microgénérateur est présenté en Figure 4.9. Cette figure montre que l'augmentation des capacités de conversion électromécanique du microgénérateur impacte le rapport de masse optimal, tout comme l'augmentation de son facteur de qualité mécanique (ce

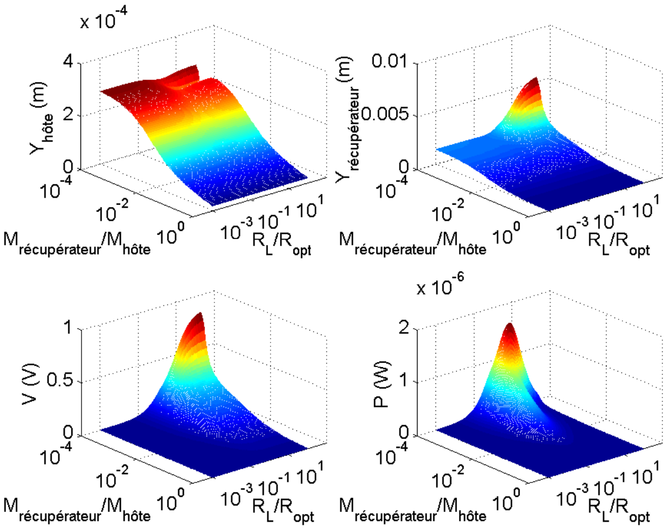

Figure 4.7: Réponses de la structure hôte et du microgénérateur pour différents rapports de masse et charge ; les performances sont optimisées par rapport à la fréquence et la charge résistive est normalisée par rapport à la valeur optimale dans le cas de la technique alternative standard.

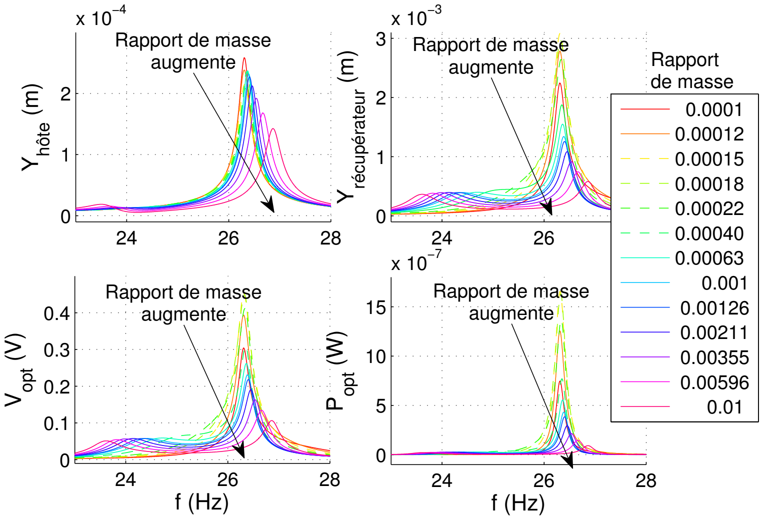

Figure 4.8: Réponses fréquentielles pour plusieurs rapports de masse ; les déplacement, la tension et la puissance récupérée sont calculés pour le rapport de masse et la charge optimaux ($R_L = R_{opt}|_{(M_2/M_1)_{opt}} = 61.8\ \mathrm{k}\Omega$).

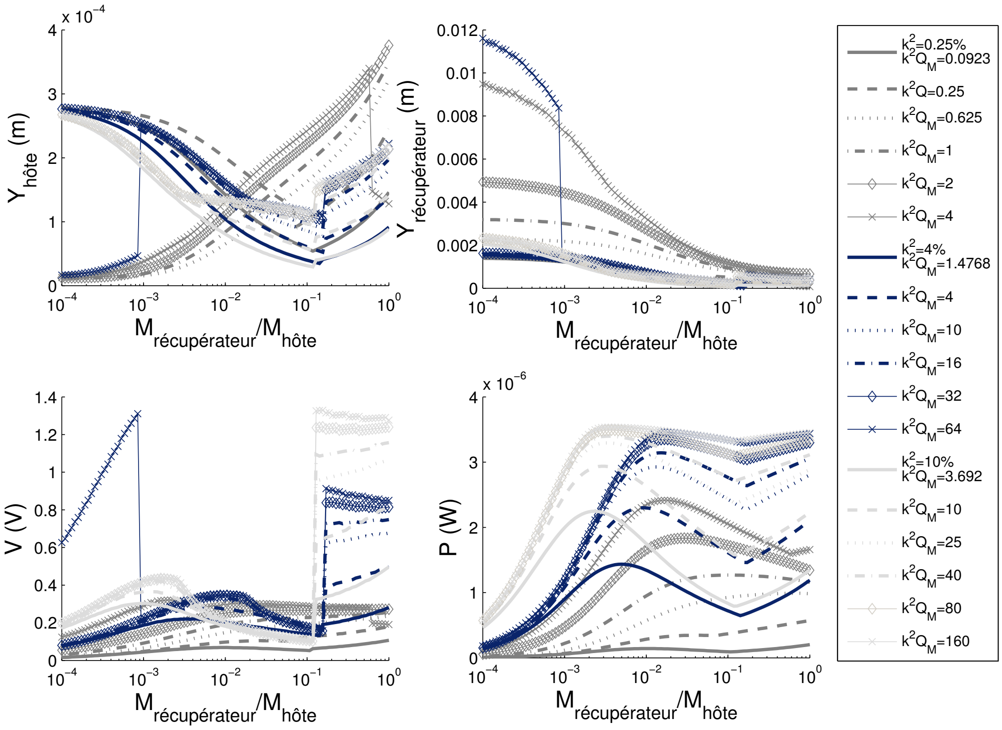

Figure 4.9: Performances optimales en fonction du rapport de masse pour différentes valeurs du facteur de mérite $k^2 Q_M$.

dernier paramètre relatant la facilité de transfert de l'énergie de la structure hôte vers le récupérateur), ce qui s'explique par le double compromis entre l'énergie électrique extraite et l'énergie mécanique du microgénérateur, et entre l'énergie mécanique transférée au microgénérateur et celle toujours présente dans la structure hôte. On remarquera également un phénomène de saut des déplacements et de la tension qui correspondent au cas où la puissance optimal est récupérée pour l'autre pic fréquentiel (du au phénomène de dédoublement de fréquence).

4.4 Cas d'excitations large bande

Les signaux de l'environnement réel sont très rarement monochromatiques. Ainsi, cette partie propose une modélisation stochastique similaire au chapitre précédent pour quantifier les capacités de récupération de systèmes sismiques lorsque l'hôte est soumis à une excitation large bande.

4.4.1 Modélisation

A partir de la modélisation par constantes localisées exposée dans la première partie de ce chapitre, il est possible d'exprimer la densité spectrale de puissance du vecteur des déplacements de la structure hôte et du récupérateur :

$$S_{\mathbf{uu}}(\omega) = |\mathbf{L}(\omega)|^2 S_{\mathbf{FF}}(\omega)\,. \tag{4.14}$$

Conduisant ainsi à l'expression de la puissance récupérée :

$$\begin{aligned} P &= \frac{\langle V^2(t) \rangle}{R_L} = \frac{1}{2\pi}\int_{-\infty}^{\infty} S_{VV}(\omega) d\omega \\ &= \frac{1}{R_L}\frac{1}{2\pi}\int_{-\infty}^{\infty} |\mathbf{gL}(\omega)|^2 S_{\mathbf{FF}}(\omega) d\omega. \end{aligned} \tag{4.15}$$

Dans le cas d'un bruit blanc (densité spectrale d'excitation constante de valeur S_{FF}), cette puissance se simplifie par :

$$P = \frac{1}{R_L}\frac{1}{2\pi} S_{FF}\int_{-\infty}^{\infty} |\mathbf{gL}(\omega)|^2 d\omega. \tag{4.16}$$

alors que dans le cas sinusoïdal où la force est formée de deux Diracs dans le domaine fréquentielle et a une amplitude F_M, la puissance devient :

$$P = \frac{1}{2R_L}|\mathbf{gL}(\omega_0)|^2 {F_M}^2, \tag{4.17}$$

ce qui est similaire à ce qui a été établi dans la littérature.

4.4.2 Discussion

Pour vérification, la Figure 4.10 présente la comparaison entre la modélisation stochastique et celle à constantes localisées dans le cas d'une excitation monochromatique, qui valide la modélisation précédente basée sur l'aspect statistique.

La Figure 4.11 présente la puissance récupérée maximale en fonction du rapport de masse pour plusieurs valeurs du coefficient $k^2 Q_M$ dans le cas d'un bruit blanc. De manière non surprenante, la puissance augmente avec ce paramètre et atteint un plafond pour de fortes valeurs de ce dernier. On remarque également un palier en termes de rapport de masse optimal, qui est expliqué par le fait que le glissement, voire le dédoublement de la fréquence de résonance du système complet (hôte+récupérateur),

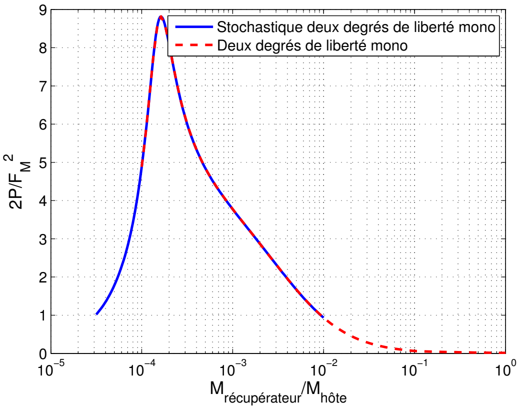

Figure 4.10: Comparaison du modèle stochastique et des résultats obtenus pour une excitation monochromatique.

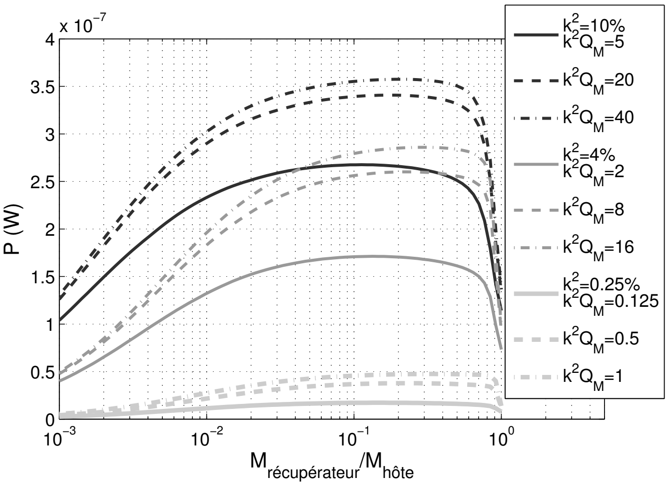

Figure 4.11: Effets du coefficient de couplage et facteur de qualité mécanique sur la puissance récupérée en fonction du rapport de masse pour une excitation en bruit blanc.

est toujours couvert par le spectre de l'excitation, permettant ainsi une plus grande marge de manoeuvre sur la conception du microgénérateur.

Dans le cas d'une excitation plus réduite en bande fréquentielle (profil gaussien d'ouverture variable), présenté en Figure 4.12, ce palier se réduit et la masse optimale diminue alors que la bande fréquentielle devient de plus en plus limitée, passant du cas de bruit blanc au cas monochromatique.

Le cas où la fréquence d'excitation est décalée par rapport à la résonance du système, la Figure 4.13 montre l'effet de ce décalage sur la puissance récupérée en fonction du rapport de masse selon que le facteur de force α ou le coefficient de couplage électromécanique k est considéré constant, avec une excitation en bande étroite. Bien

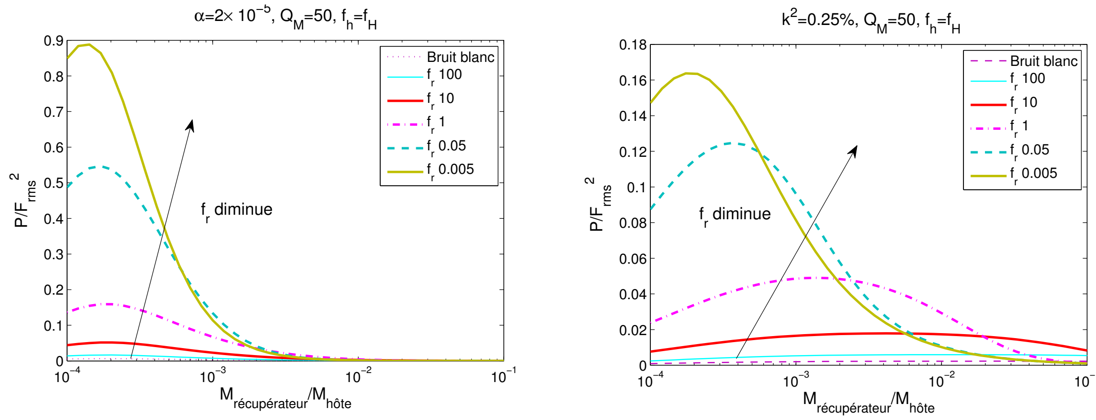

(a) (b)

Figure 4.12: Effet de l'ouverture de bande d'une excitation en cloche sur le sytème {hôte+récupérateur} : (a) à α constant ; (b) à k^2 constant.

que, de manière non surprenante, la puissance décroît avec le décalage, on pourra remarquer que dans le cas d'un facteur de force constant, le rapport de masse optimal et les formes des courbes ne changent pas outre mesure, alors que dans le cas d'un coefficient de couplage constant, ce dernier se décale vers des valeurs plus hautes, toute en ayant une plage plus réduite.

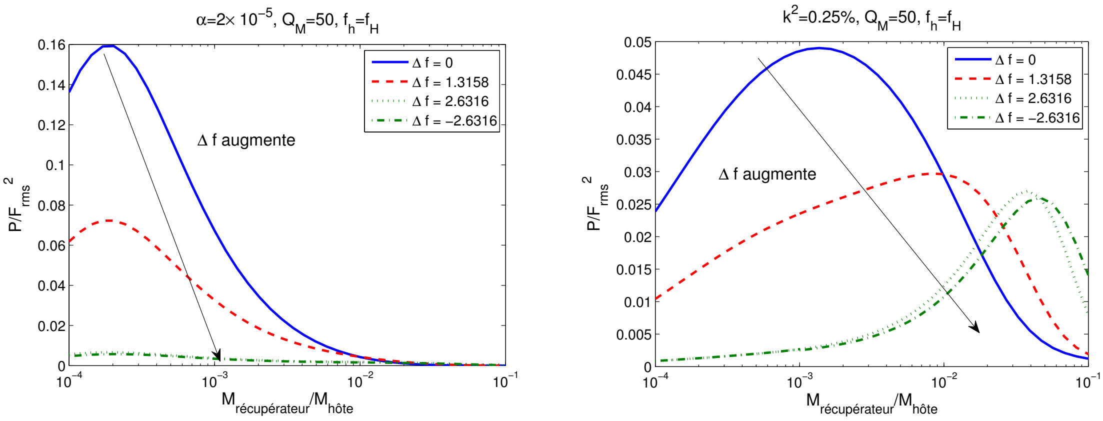

(a) (b)

Figure 4.13: Effet d'un décalage d'une excitation à bande étroite pour un rapport de fréquence unitaire : (a) à α constant ; (b) à k^2 constant.

4.5 Effet du désaccordage entre structure hôte et récupérateur

Cette dernière partie de ce chapitre s'intéresse à l'effet d'un décalage de la fréquence de résonance du microgénérateur par rapport à celle de la structure hôte seule, dans le cas où soit le facteur de force, soit le coefficient de couplage global au carré est considérée constant. En considérant une excitation en bruit blanc, dans le cas d'un facteur de force constant (Figure 4.14 - f_h/f_H étant le rapport de fréquence de résonance entre le microgénérateur et la structure hôte), on remarque des courbes de forme similaires, mais un coefficient de qualité mécanique plus important compense l'effet du décalage uniquement dans le cas d'une excitation monochromatique (en considérant soit la fréquence optimale - global - soit en suivant une seule fréquence, même dans le cas de dédoublage - local).

Pour un coefficient de couplage constant (Figure 4.15(a)), on pourra néanmoins remarquer que l'impact du désaccordage est quasi-nul, ce qui peut être expliqué par la compensation de ce décalage par le contrôle du transfert d'énergie mécanique de la structure hôte vers le récupérateur (le rapport de masse optimal variant énormément et de manière non monotone de ce cas - Figure 4.15(b)).

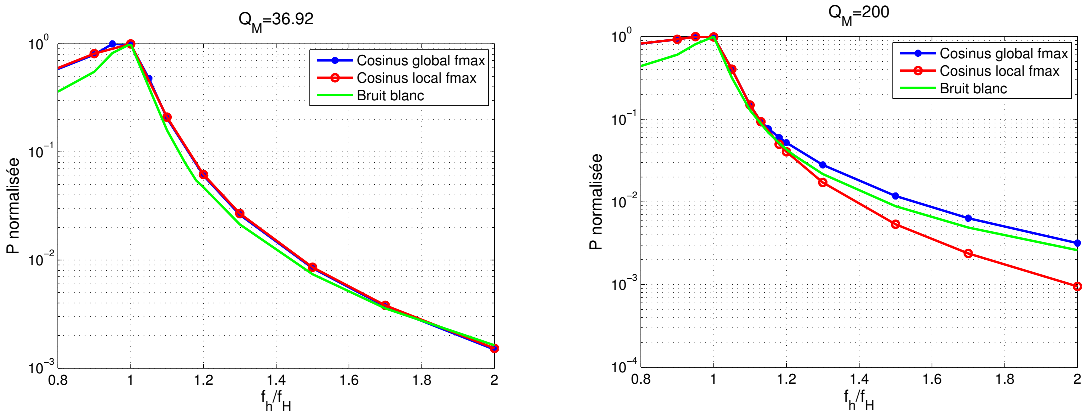

(a) (b)

Figure 4.14: Effet d'un désaccordage sur la puissance récupérée pour α constant et deux valeurs du facteur de qualité mécanique : (a) $Q_M = 36.92$; (b) $Q_M = 36.92$.

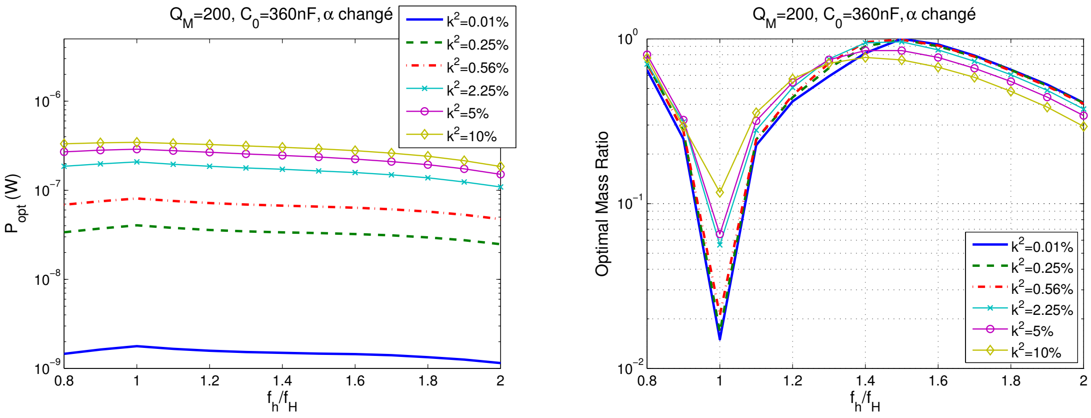

(a) (b)

Figure 4.15: Effet d'un désaccordage sur la puissance récupérée pour k^2 constant : (a) puissance maximale récupérée ; (b) rapport de masse optimal.

4.6 Conclusion

Ce chapitre a apporté une modélisation plus complète des générateurs sismiques, prenant en compte le couplage mécanique inverse induisant une modification du comportement mécanique de la structure hôte. Bien que dans certains cas, la masse dynamique de la structure hôte soit très largement supérieure à celle du récupérateur (infrastructures civiles par exemple), il existe de nombreuses applications visant des dispositifs de taille modeste (comme les machines tournantes). Ceci est d'autant plus vrai que les travaux réalisés dans ce chapitre ont montré un effet non négligeable du au couplage mécano-mécanique entre la structure hôte et le microgénérateur même pour des rapports de masses dynamiques très faibles (différence de trois ordres de grandeurs ou plus). Ainsi, l'hypothèse d'accélération constante couramment utilisée dans la littérature n'est plus valide, et la puissance qui peut être récupérée diminue drastiquement.

Afin de faciliter la conception de microgénérateurs dans le cas d'applications réalistes et étudier les effets de dispersion, les travaux menés dans ce chapitre ont également porté sur l'impact d'une excitation large bande, où les contraintes en termes de rapport de masse optimale sont grandement relâchées par la présence d'un plateau, ainsi que l'effet d'un désaccordage des fréquences de résonance entre l'hôte et le récupérateur, où la puissance peut être maintenue constante dans le cas où le coefficient de couplage électromécanique du microgénérateur est constant. Néanmoins, cette possibilité se fait au prix d'une conception très précise en termes de rapport de masse optimal, mettant une fois de plus en avant la nécessité de prendre en compte toute la chaîne de conversion d'énergie lors de la conception du système de récupération.

5 Conclusions et perspectives

Les travaux de cette thèse se sont attachés à évaluer les performances de microgénérateurs puisant leur énergie dans les vibrations ambiantes par effet piézoélectrique. Cette thématique est présentement très fortement d'actualité du fait de la réduction de la consommation des dispositifs de la microélectronique, de la limitation des batteries et des problèmes environnementaux. Une forte volonté d'utilisation réaliste de tels microgénérateurs a été le fil directeur des études présentées dans ce mémoire.

Dans cette optique, les chapitres 2 et 3 se sont intéressés au cas d'excitation large bande lorsqu'une interface électronique de traitement non-linéaire est utilisée pour augmenter les capacités de conversion; le cas académique qui consiste à considérer une excitation sinusoïdale étant fort peu souvent représentative d'environnements réalistes. Afin de pouvoir utiliser les outils d'analyse de traitement de signal et de processus aléatoire, la technique non-linéaire considérée, nommée PSHI, consiste à inverser rapidement la tension de sortie de l'élément piézoélectrique. Bien que cette technique diffère d'une commutation synchrone avec le déplacement (approche SSHI), ses principes restent relativement similaires. Le chapitre 2 s'est tout d'abord intéressé à modéliser cette technique en utilisant le concept d'"auto-échantillonnage", la technique PSHI pouvant être interprétée comme un échantillonnage de la tension rebouclé sur elle-même. Ainsi, les expressions de déplacement, tension et puissance récupérée ont pu être établies en considérant une excitation quelconque mais de spectre connu (en module et phase). Différents cas de figure, pour valider le concept et l'analyse ou pour quantifier les performances, ont ainsi pu être étudiés. Le chapitre 3 a par la suite étendu cette étude au cas où seule la densité spectrale de puissance de l'excitation est connue ; cette grandeur étant plus communément accessible dans la réalité. Du fait de l'aspect linéaire mais non temporellement invariant de la technique PSHI, une approche stochastique basée sur la cyclostationnarité du signal a été choisie, permettant d'établir la puissance récupérable dans le cas d'une excitation aléatoire. En parallèle, une approche numérique de résolution temporelle a été menée pour valider l'étude, de même qu'une série de mesures expérimentales, confirmant ainsi l'analyse menée. Une étude plus approfondie a montré que, bien que la technique PSHI soit moins performante que le SSHI, cette dernière permet néanmoins de profiter d'un gain non négligeable en termes d'énergie récupérée comparé à l'approche standard, tout en nécessitant une commande beaucoup plus simple. Cette étude s'est néanmoins limitée à une seule fréquence de résonance du microgénérateur (modélisation à un degré de liberté). L'extension des travaux menés ici au cas multimodal serait des plus intéressante à mener. Ceci est d'autant plus vrai que le SSHI voit ses performances dégradées dans ce cas, phénomène qui serait sans doute limité dans le cas du PSHI, la commutation n'étant pas synchronisée au déplacement. De même, le lien entre PSHI et SSHI pourrait être une piste à suivre, par exemple en modélisant le SSHI par le PSHI dans une fenêtre temporelle donnée ; le SSHI global étant alors obtenue par la succession des différentes fenêtres. L'effet de l'introduction d'autres non-linéarités, mécaniques ou électriques (raideur à caractère cubique ou convertisseurs AC/DC par exemple), serait également une voie à explorer.

Enfin, le chapitre 4 s'est attelé à étudier les effets de la récupération par couplage sismique du microgénérateur avec une structure hôte. Il a ainsi été démontré que ce couplage n'est pas négligeable même lorsque les dimensions du récupérateur restent faibles par rapport à celle de la structure hôte, du fait du couplage mécano-mécanique entre microgénérateur et hôte. Ainsi, l'hypothèse classique d'accélération constante sur la base du microgénérateur n'est plus valide et conduit à une surestimation importante de l'énergie récupérable, car seule une partie de la chaîne de conversion est prise en compte. Ceci souligne une fois encore la nécessité de considérer tout les processus de conversion d'énergie, ainsi que les différents couplages bidirectionnels, qui conduisent non seulement au compromis de conversion électromécanique (énergie extraite par rapport à l'énergie mécanique du microgénérateur), mais également au compromis de conversion mécanique entre l'hôte et le récupérateur, c'est-à-dire l'énergie mécanique transférée à ce dernier par rapport à l'énergie mécanique dans la structure hôte ; en d'autre termes, l'énergie mécanique doit toujours pouvoir entrer dans cette dernière. Différentes analyses, en terme de profil d'excitation ou de conception du microgénérateur, ont été menées, montrant les points importants à considérer lors de la conception d'un système de récupération. La combinaison du générateur sismique avec l'interface non-linéaire PSHI ou SSHI et l'analyse de ce système en fonction de plusieurs paramètres (profil excitation par exemple) serait une étude qui pourrait pour-suivre ces travaux. Ainsi cette thèse, se voulant à mi-chemin entre travail académique et considérations réalistes, a dégagé de nouvelles pistes de réflexion, tout en mettant en avant des points importants à considérer lors de l'analyse et/ou de l'implémentation de récupérateurs d'énergie, espérant ainsi apporter une pierre supplémentaire au domaine de la récupération d'énergie, et de manière plus générale au monde passionnant des systèmes multiphysiques.

Bibliography

[1] G. Park, T. Rosing, M. D. Todd, C. R. Farrar, and W. Hodgkiss, "Energy harvesting for structural health monitoring sensor networks," *Journal of Infrastructure Systems*, vol. 14, no. 1, pp. 64–79, 2008. [Online]. Available: http://ascelibrary.org/doi/abs/10.1061/%28ASCE%291076-0342%282008%2914%3A1%2864%29

[2] Y. K. Tan and S. K. Panda, *Sustainable Wireless Sensor Networks*. InTech, 12 2010, ch. Review of Energy Harvesting Technologies for Sustainable Wireless Sensor Network.

[3] S. Roundy, P. K. Wright, and J. Rabaey, "A study of low level vibrations as a power source for wireless sensor nodes," *Computer Communications*, vol. 26, no. 11, pp. 1131 – 1144, 2003, ubiquitous Computing. [Online]. Available: http://www.sciencedirect.com/science/article/B6TYP-47CWTY0-1/2/cf6278ee1732c2c1d225901b19270a10

[4] J. A. Paradiso and T. Starner, "Energy scavenging for mobile and wireless electronics," *IEEE Pervasive Computing*, vol. 4, pp. 18–27, 2005.

[5] S. Priya, "Advances in energy harvesting using low profile piezoelectric transducers," *Journal of Electroceramics*, vol. 19, pp. 167–184, 2007. [Online]. Available: http://dx.doi.org/10.1007/s10832-007-9043-4

[6] F. Yildiz, "Potential ambient energy-harvesting sources and techniques," *Journal of Technology Studies*, vol. 35, pp. 40–48, 2009.

[7] K. Uchida, S. Takahashi, K. Harii, J. Ieda, W. Koshibae, K. Ando, S. Maekawa, and E. Saitoh, "Observation of the spin seebeck effect," *Nature*, vol. 455, pp. 778–781, Oct. 2008.

[8] M. Chen, S.-S. Lu, and B. Liao, “On the figure of merit of thermoelectric generators,” *Journal of Energy Resources Technology*, vol. 127, no. 1, pp. 37–41, 2005. [Online]. Available: http://link.aip.org/link/?JRG/127/37/1

[9] G. Sebald, D. Guyomar, and A. Agbossou, “On thermoelectric and pyroelectric energy harvesting,” *Smart Materials and Structures*, vol. 18, no. 12, p. 125006, 2009. [Online]. Available: http://stacks.iop.org/0964-1726/18/i=12/a=125006

[10] S. A. Omer and D. G. Infield, “Design and thermal analysis of a two stage solar concentrator for combined heat and thermoelectric power generation,” *Energy Conversion and Management*, vol. 41, no. 7, pp. 737 – 756, 2000. [Online]. Available: http://www.sciencedirect.com/science/article/pii/S019689049900134X

[11] R. B. Olsen and D. Evans, “Pyroelectric energy conversion: Hysteresis loss and temperature sensitivity of a ferroelectric material,” *Journal of Applied Physics*, vol. 54, no. 10, pp. 5941–5944, 1983. [Online]. Available: http://link.aip.org/link/?JAP/54/5941/1

[12] R. B. Olsen, D. A. Bruno, J. M. Briscoe, and E. W. Jacobs, “Pyroelectric conversion cycle of vinylidene fluoride-trifluoroethylene copolymer,” *Journal of Applied Physics*, vol. 57, no. 11, pp. 5036–5042, 1985. [Online]. Available: http://link.aip.org/link/?JAP/57/5036/1

[13] H. Zhu, S. Pruvost, D. Guyomar, and A. Khodayari, “Thermal energy harvesting from pb(zn[sub 1/3]nb[sub 2/3])[sub 0.955]ti[sub 0.045]o[sub 3] single crystals phase transitions,” *Journal of Applied Physics*, vol. 106, no. 12, p. 124102, 2009. [Online]. Available: http://link.aip.org/link/?JAP/106/124102/1

[14] V. Gupta, A. Kandhalu, and R. R. Rajkumar, “Energy harvesting from electromagnetic energy radiating from ac power lines,” in *In Proceedings of 2010 ACM Workshop on Hot Topics in Embedded Networked Sensors (HotEMNETS 2010)*. In Proceedings of 2010 ACM Workshop on Hot Topics in Embedded Networked Sensors (HotEMNETS 2010), 2010.

[15] E. M. Yeatman, “Advances in power sources for wireless sensor nodes,” in *Proc. of BSN 2004*, no. 20-21. Proceedings of 1st International Workshop on Body Sensor Networks, 2004.

[16] J.-Y. Park, S.-M. Han, and T. Itoh, “A rectenna design with harmonic-rejecting circular-sector antenna,” *Antennas and Wireless Propagation Letters, IEEE*, vol. 3, no. 1, pp. 52 –54, dec. 2004.

[17] C.-H. Chin, Q. Xue, and C. H. Chan, “Design of a 5.8-ghz rectenna incorporating a new patch antenna,” *Antennas and Wireless Propagation Letters, IEEE*, vol. 4, pp. 175 – 178, 2005.

[18] L. Epp, A. Khan, H. Smith, and R. Smith, “A compact dual-polarized 8.51-ghz rectenna for high-voltage (50 v) actuator applications,” *Microwave Theory and Techniques, IEEE Transactions on*, vol. 48, no. 1, pp. 111 –120, jan 2000.

[19] J. Zbitou, M. Latrach, and S. Toutain, “Hybrid rectenna and monolithic integrated zero-bias microwave rectifier,” *Microwave Theory and Techniques, IEEE Transactions on*, vol. 54, no. 1, pp. 147 –152, jan. 2006.

[20] J. Kim, S. Y. Yang, K. D. Song, S. Jones, and S. H. Choi, “Performance characterization of flexible dipole rectennas for smart actuator use,” *Smart Materials and Structures*, vol. 15, no. 3, p. 809, 2006. [Online]. Available: http://stacks.iop.org/0964-1726/15/i=3/a=017

[21] H. Ostaffe, “Rf energy harvesting enables wireless sensor networks,” Sensors Mag, Tech. Rep., 2009. [Online]. Available: http://www.sensorsmag.com/sensors-mag/rf-energy-harvesting-enables-wireless-sensor-networks-6175

[22] R. L. Bailey, “A proposed new concept for a solar energy converter,” *Journal of Engineering for Power*, p. 73, April 1972.

[23] D. K. Kotter, S. D. Novack, W. D. Slafer, and P. Pinhero, “Solar nantenna electromagnetic collectors,” *ASME Conference Proceedings*, vol. 2008, no. 43208, pp. 409–415, 2008. [Online]. Available: http://link.aip.org/link/abstract/ASMECP/v2008/i43208/p409/s1

[24] J. W. Schwede, I. Bargatin, D. C. Riley, B. E. Hardin, S. J. Rosenthal, Y. Sun, F. Schmitt, P. Pianetta, R. T. Howe, Z.-X. Shen, and N. A. Melosh, “Photon-enhanced thermionic emission for solar concentrator systems,” *Nature Materials*, vol. 9, p. 762âĂŞ767, Sep. 2010. [Online]. Available: http://www.nature.com/nmat/journal/v9/n9/abs/nmat2814.html#supplementary-information

[25] K. A. Cook-Chennault, N. Thambi, and A. M. Sastry, “Powering mems portable devices- review of non-regenerative and regenerative power supply systems with special emphasis on piezoelectric energy harvesting systems,” *Smart Materials and Structures*, vol. 17, no. 4, p. 043001, 2008. [Online]. Available: http://stacks.iop.org/0964-1726/17/i=4/a=043001

[26] W. Li, T. Ho, G. Chan, P. Leong, and H. Y. Wong, “Infrared signal transmission by a laser-micromachined, vibration-induced power generator,” in *Circuits and Systems, 2000. Proceedings of the 43rd IEEE Midwest Symposium on*, vol. 1, 2000, pp. 236 –239 vol.1.

[27] J. Lee, S. Yuen, W. Li, and P. Leong, “Development of an aa size energy transducer with micro resonators,” in *Circuits and Systems, 2003. ISCAS ’03. Proceedings of the 2003 International Symposium on*, vol. 4, may 2003, pp. IV–876 – IV–879 vol.4.

[28] M. El-hami, P. Glynne-Jones, N. M. White, M. Hill, S. Beeby, E. James, A. D. Brown, and J. N. Ross, “Design and fabrication of a new vibration-based electromechanical power generator,” *Sensors and Actuators A: Physical*, vol. 92, no. 1-3, pp. 335 – 342, 2001. [Online]. Available: http://www.sciencedirect.com/science/article/B6THG-43HJVDR-1S/2/f03441700c12e2b4eacead1acbe70b1d

[29] E. P. James, M. J. Tudor, S. P. Beeby, N. R. Harris, P. Glynne-Jones, J. N. Ross, and N. M. White, “An investigation of self-powered systems for condition monitoring applications,” *Sensors and Actuators A: Physical*, vol. 110, no. 1-3, pp. 171 – 176, 2004, selected Papers from Eurosensors XVI Prague, Czech Republic. [Online]. Available: http://www.sciencedirect.com/science/article/B6THG-4BBHC8H-J/2/a537ceddd9f90ab6c3fb65f759402229

[30] R. Amirtharajah and A. P. Chandrakasan, “Self-powered signal processing using vibration-based power generation,” *IEEE Journal of Solid-State Circuits*, vol. 33, pp. 687–695, 1998.

[31] M. E. Staley and A. B. Flatau, “Characterization of energy harvesting potential of terfenol-d and galfenol,” *Proc. SPIE 5746, Smart Structures and Materials 2005: Smart Structures and Integrated Systems*, pp. 630–640, 2005. [Online]. Available: +http://dx.doi.org/10.1117/12.604871

[32] A. Bayrashev, A. Parker, W. Robbins, and B. Ziaie, "Low frequency wireless powering of microsystems using piezoelectric-magnetostrictive laminate composites," in *TRANSDUCERS, Solid-State Sensors, Actuators and Microsystems, 12th International Conference on, 2003*, vol. 2, june 2003, pp. 1707 – 1710 vol.2.

[33] J. Huang, R. C. O'Handley, and D. Bono, "New high-sensitivity hybrid magnetostrictive/electroactive magnetic field sensors," *Proc. SPIE 5050, Smart Structures and Materials 2003: Smart Sensor Technology and Measurement Systems*, pp. 229–237, 2003. [Online]. Available: +http://dx.doi.org/10.1117/12.484257

[34] L. Wang and F. G. Yuan, "Energy harvesting by magnetostrictive material (msm) for powering wireless sensors in shm," *Proc. SPIE 6529, Sensors and Smart Structures Technologies for Civil, Mechanical, and Aerospace Systems 2007*, 2007. [Online]. Available: internal-pdf://Magnetostrictive-0325451278/Magnetostrictive.pdf

[35] S. Meninger, J. Mur-Miranda, R. Amirtharajah, A. Chandrakasan, and J. Lang, "Vibration-to-electric energy conversion," *Very Large Scale Integration (VLSI) Systems, IEEE Transactions on*, vol. 9, no. 1, pp. 64 –76, feb. 2001.

[36] S. Boisseau, G. Despesse, and B. A. Seddik, *Small-Scale Energy Harvesting*. InTech, 2012, ch. Electrostatic Conversion for Vibration Energy Harvesting.

[37] M. Lallart, S. Pruvost, and D. Guyomar, "Electrostatic energy harvesting enhancement using variable equivalent permittivity," *Physics Letters A*, vol. 375, no. 45, pp. 3921 – 3924, 2011. [Online]. Available: http://www.sciencedirect.com/science/article/pii/S0375960111011704

[38] S. Boisseau, G. Despesse, T. Ricart, E. Defay, and A. Sylvestre, "Cantilever-based electret energy harvesters," *Smart Materials and Structures*, vol. 20, no. 10, p. 105013, 2011. [Online]. Available: http://stacks.iop.org/0964-1726/20/i=10/a=105013

[39] E. Halvorsen, E. Westby, S. Husa, A. Vogl, N. Ostbo, V. Leonov, T. Sterken, and T. Kvisteroy, "An electrostatic energy harvester with electret bias," in *Solid-State Sensors, Actuators and Microsystems Conference, 2009. TRANSDUCERS 2009. International*, june 2009, pp. 1381 –1384.

[40] S. Boisseau, G. Despesse, and A. Sylvestre, “Optimization of an electret-based energy harvester,” *Smart Materials and Structures*, vol. 19, no. 7, p. 075015, 2010. [Online]. Available: http://stacks.iop.org/0964-1726/19/i=7/a=075015

[41] Y. Naruse, N. Matsubara, K. Mabuchi, M. Izumi, and S. Suzuki, “Electrostatic micro power generation from low-frequency vibration such as human motion,” *Journal of Micromechanics and Microengineering*, vol. 19, no. 9, p. 094002, 2009. [Online]. Available: http://stacks.iop.org/0960-1317/19/i=9/a=094002

[42] M. Lallart, P.-J. Cottinet, D. Guyomar, and L. Lebrun, “Electrostrictive polymers for mechanical energy harvesting,” *Journal of Polymer Science Part B: Polymer Physics*, vol. 50, pp. 523–535, 2012.

[43] K. Ren, Y. Liu, H. Hofmann, Q. M. Zhang, and J. Blottman, “An active energy harvesting scheme with an electroactive polymer,” *Applied Physics Letters*, vol. 91, no. 13, p. 132910, 2007. [Online]. Available: http://link.aip.org/link/?APL/91/132910/1

[44] P.-J. Cottinet, “Actionnement et récupération d’énergie á l’aide de polyméres électro-actifs,” Ph.D. dissertation, Institut National des Sciences Appliquées de Lyon, 2010.

[45] Y. Liu, K. L. Ren, H. Hofmann, and Q. Zhang, “Investigation of electrostrictive polymers for energy harvesting,” *Ultrasonics, Ferroelectrics and Frequency Control, IEEE Transactions on*, vol. 52, no. 12, pp. 2411 –2417, dec. 2005.

[46] D. Guyomar, L. Lebrun, C. Putson, P.-J. Cottinet, B. Guiffard, and S. Muensit, “Electrostrictive energy conversion in polyurethane nanocomposites,” *Journal of Applied Physics*, vol. 106, no. 1, p. 014910, 2009. [Online]. Available: http://link.aip.org/link/?JAP/106/014910/1

[47] P.-J. Cottinet, D. Guyomar, B. Guiffard, C. Putson, and L. Lebrun, “Modeling and experimentation on an electrostrictive polymer composite for energy harvesting,” *Ultrasonics, Ferroelectrics and Frequency Control, IEEE Transactions on*, vol. 57, no. 4, pp. 774 –784, april 2010.

[48] M. Lallart, P.-J. Cottinet, L. Lebrun, B. Guiffard, and D. Guyomar, “Evaluation of energy harvesting performance of electrostrictive polymer and carbon-filled

terpolymer composites," *Journal of Applied Physics*, vol. 108, no. 3, p. 034901, 2010. [Online]. Available: http://link.aip.org/link/?JAP/108/034901/1

[49] S.-G. Kim, S. Priya, and I. Kanno, "Piezoelectric mems for energy harvesting," *MRS Bulletin*, vol. 37, pp. 1039–1050, 2012. [Online]. Available: http://dx.doi.org/10.1557/mrs.2012.275

[50] J. Baker, S. Roundy, and P. Wright, "Alternative geometries for increasing power density in vibration energy scavenging for wireless sensor networks," in *Proc. 3rd Int. Energy COnversion Engineering Conf. (San Francisco, CA, Aug)*, 2005, pp. 959–70.

[51] T. Starner and J. A. Paradiso, "Human generated power for mobile electronics," in *Low Power Electronics Design*. CRC Press, 2004, pp. 1–35.

[52] A. Badel, "Récupération d'énergie et contrôle vibratoire par éléments piézoélectriques suivant une approche non linéaire," Ph.D. dissertation, Université de Savoie / INSA de Lyon, 2005.

[53] M. E. du Toit, "Modeling and design of a mems piezoelectric vibration energy harvester," Master's thesis, MASSACHUSETTS INSTITUTE OF TECHNOLOGY, 2005.

[54] D. Guyomar, A. Badel, E. Lefeuvre, and C. Richard, "Toward energy harvesting using active materials and conversion improvement by nonlinear processing," *Ultrasonics, Ferroelectrics and Frequency Control, IEEE Transactions on*, vol. 52, no. 4, pp. 584 – 595, april 2005.

[55] Y. C. Shu and I. C. Lien, "Analysis of power output for piezoelectric energy harvesting systems," *Smart Materials and Structures*, vol. 15, no. 6, p. 1499, 2006. [Online]. Available: http://stacks.iop.org/0964-1726/15/i=6/a=001

[56] C. Williams and R. Yates, "Analysis of a micro-electric generator for microsystems," *Sensors and Actuators A: Physical*, vol. 52, no. 1ï£¡ï£¡, pp. 8 – 11, 1996, <ce:title>Proceedings of the 8th International Conference on Solid-State Sensors and Actuators Eurosensors IX</ce:title>. [Online]. Available: http://www.sciencedirect.com/science/article/pii/092442479680118X

[57] H. A. Sodano, G. Park, D. J. Leo, and D. J. Inman, “Model of piezoelectric power harvesting beam,” *ASME Conference Proceedings*, vol. 2003, no. 37076, pp. 345–354, 2003. [Online]. Available: http://link.aip.org/link/abstract/ASMECP/v2003/i37076/p345/s1

[58] G. A. Lesieutre, G. K. Ottman, and H. F. Hofmann, “Damping as a result of piezoelectric energy harvesting,” *Journal of Sound Vibration*, vol. 269, pp. 991–1001, Jan. 2004.

[59] N. Stephen, “On energy harvesting from ambient vibration,” *Journal of Sound and Vibration*, vol. 293, pp. 409 – 425, 2006. [Online]. Available: http://www.sciencedirect.com/science/article/pii/S0022460X05006784

[60] F. Lu, H. P. Lee, and S. P. Lim, “Modeling and analysis of micro piezoelectric power generators for micro-electromechanical-systems applications,” *Smart Material Structures*, vol. 13, pp. 57–63, Feb 2004.

[61] C. D. Richards, M. J. Anderson, D. F. Bahr, and R. F. Richards, “Efficiency of energy conversion for devices containing a piezoelectric component,” *Journal of Micromechanics and Microengineering*, vol. 14, no. 5, p. 717, 2004. [Online]. Available: http://stacks.iop.org/0960-1317/14/i=5/a=009

[62] E. Lefeuvre, D. Audigier, C. Richard, and D. Guyomar, “Buck-boost converter for sensorless power optimization of piezoelectric energy harvester,” *Power Electronics, IEEE Transactions on*, vol. 22, no. 5, pp. 2018 –2025, sept. 2007.

[63] S. Roundy, E. Leland, J. Baker, E. Carleton, E. Reilly, E. Lai, B. Otis, J. Rabaey, P. Wright, and V. Sundararajan, “Improving power output for vibration-based energy scavengers,” *Pervasive Computing, IEEE*, vol. 4, no. 1, pp. 28 – 36, jan.-march 2005.

[64] S. R. Anton and H. A. Sodano, “A review of power harvesting using piezoelectric materials (2003-006),” *Smart Materials and Structures*, vol. 16, no. 3, p. R1, 2007. [Online]. Available: http://stacks.iop.org/0964-1726/16/i=3/a=R01

[65] S. Roundy and Y. Zhang, “Toward self-tuning adaptive vibration-based microgenerators,” in *Proc. SPIE 5649, Smart Structures, Devices, and Systems II, 373*, 2005, pp. 373–384. [Online]. Available: +http://dx.doi.org/10.1117/12.581887

[66] M. Lallart, S. R. Anton, and D. J. Inman, "Frequency self-tuning scheme for broadband vibration energy harvesting," *Journal of Intelligent Material Systems and Structures*, vol. 21, no. 9, pp. 897–906, 2010. [Online]. Available: http://jim.sagepub.com/content/21/9/897.abstract

[67] D. Guyomar, M. Lallart, and T. Monnier, "Stiffness tuning using a low-cost semiactive nonlinear technique," *Mechatronics, IEEE/ASME Transactions on*, vol. 13, no. 5, pp. 604 –607, oct. 2008.

[68] V. R. Challa, M. G. Prasad, Y. Shi, and F. T. Fisher, "A vibration energy harvesting device with bidirectional resonance frequency tunability," *Smart Materials and Structures*, vol. 17, no. 1, p. 015035, 2008. [Online]. Available: http://stacks.iop.org/0964-1726/17/i=1/a=015035

[69] D. Zhu, J. Tudor, and S. Beeby, "Strategies for increasing the operating frequency range of vibration energy harvesters: a review," *Measurement Science and Technology*, vol. 21, no. 2, p. 022001, February 2010. [Online]. Available: http://eprints.soton.ac.uk/268354/

[70] F. Goldschmidtboeing and P. Woias, "Characterization of different beam shapes for piezoelectric energy harvesting," *Journal of Micromechanics and Microengineering*, vol. 18, no. 10, p. 104013, 2008. [Online]. Available: http://stacks.iop.org/0960-1317/18/i=10/a=104013

[71] R. Patel, S. McWilliam, and A. A. Popov, "A geometric parameter study of piezoelectric coverage on a rectangular cantilever energy harvester," *Smart Materials and Structures*, vol. 20, no. 8, p. 085004, 2011. [Online]. Available: http://stacks.iop.org/0964-1726/20/i=8/a=085004

[72] J. Cho, M. Anderson, R. Richards, D. Bahr, and C. Richards, "Optimization of electromechanical coupling for a thin-film pzt membrane: I. modeling," *Journal of Micromechanics and Microengineering*, vol. 15, no. 10, p. 1797, 2005. [Online]. Available: http://stacks.iop.org/0960-1317/15/i=10/a=002

[73] ——, "Optimization of electromechanical coupling for a thin-film pzt membrane: II. experiment," *Journal of Micromechanics and Microengineering*, vol. 15, no. 10, p. 1804, 2005. [Online]. Available: http://stacks.iop.org/0960-1317/15/i=10/a=003

[74] M. Lallart, “Amélioration de la conversion électroactive de matériaux piézoélectriques et pyroélectriques pour le contrôle vibratoire et la récupération d’énergie - application au contrôle de santé structurale auto-alimenté,” Ph.D. dissertation, Institut National des Sciences Appliquées de Lyon, 2008.

[75] G. Ottman, H. Hofmann, A. Bhatt, and G. Lesieutre, “Adaptive piezoelectric energy harvesting circuit for wireless remote power supply,” *Power Electronics, IEEE Transactions on*, vol. 17, no. 5, pp. 669 – 676, sep 2002.

[76] G. Ottman, H. Hofmann, and G. Lesieutre, “Optimized piezoelectric energy harvesting circuit using step-down converter in discontinuous conduction mode,” *Power Electronics, IEEE Transactions on*, vol. 18, no. 2, pp. 696 – 703, Mar. 2003.

[77] E. Lefeuvre, A. Badel, C. Richard, and D. Guyomar, “Piezoelectric energy harvesting device optimization by synchronous electric charge extraction,” *JOURNAL OF INTELLIGENT MATERIAL SYSTEMS AND STRUCTURES*, vol. 16, no. 10, pp. 865–876, OCT 2005.

[78] C. Richard, D. Guyomar, D. Audigier, and G. Ching, “Semi-passive damping using continuous switching of a piezoelectric device,” in *Proc. SPIE 3672, Smart Structures and Materials 1999: Passive Damping and Isolation*, 1999, pp. 104–111. [Online]. Available: +http://dx.doi.org/10.1117/12.349773

[79] C. Richard, D. Guyomar, D. Audigier, and H. Bassaler, “Enhanced semi-passive damping using continuous switching of a piezoelectric device on an inductor,” in *Proc. SPIE 3989, Smart Structures and Materials 2000: Damping and Isolation*, 2000, pp. 288–299. [Online]. Available: +http://dx.doi.org/10.1117/12.384569

[80] Y. Shu, I. Lien, and W. Wu, “An improved analysis of the sshi interface in piezoelectric energy harvesting,” *Smart Material Structures*, vol. 16, pp. 2253–2264, Dec. 2007.

[81] E. Lefeuvre, A. Badel, C. Richard, L. Petit, and D. Guyomar, “A comparison between several vibration-powered piezoelectric generators for standalone systems,” *Sensors and Actuators A: Physical*, vol. 126, no. 2, pp. 405 – 416, 2006. [Online]. Available: http://www.sciencedirect.com/science/article/B6THG-4HTCTHJ-2/2/7cb0b88fafc922d3a2754b50e1429455

[82] M. Lallart, D. Guyomar, Y. Jayet, L. Petit, E. Lefeuvre, T. Monnier, P. Guy, and C. Richard, "Synchronized switch harvesting applied to self-powered smart systems: Piezoactive microgenerators for autonomous wireless receivers," *Sensors and Actuators A: Physical*, vol. 147, no. 1, pp. 263 – 272, 2008. [Online]. Available: http://www.sciencedirect.com/science/article/B6THG-4SBHX0X-1/2/f50eff86a0007f31c07cbe724267d643

[83] D. Guyomar and M. Lallart, "Recent progress in piezoelectric conversion and energy harvesting using nonlinear electronic interfaces and issues in small scale implementation," *Micromachines*, vol. 2, no. 2, pp. 274–294, 2011. [Online]. Available: http://www.mdpi.com/2072-666X/2/2/274

[84] E. Lefeuvre, M. Lallart, C. Richard, and D. Guyomar, *Piezoelectric Ceramics*. InTech, 12 2010, ch. Piezoelectric Material-Based Energy Harvesting Devices: Advance of SSH Optimization Techniques (1999-2009).

[85] D. Guyomar and M. Lallart, *Ferroelectrics*. InTech, 12 2010, ch. Nonlinear Conversion Enhancement for Efficient Piezoelectric Electrical Generators.

[86] D. Guyomar, G. Sebald, S. Pruvost, M. Lallart, A. Khodayari, and C. Richard, "Energy harvesting from ambient vibrations and heat," *Journal of Intelligent Material Systems and Structures*, vol. 20, no. 5, pp. 609–624, 2009. [Online]. Available: http://jim.sagepub.com/content/20/5/609.abstract

[87] I. Lien, Y. Shu, W. Wu, S. Shiu, and H. Lin, "Revisit of series-sshi with comparisons to other interfacing circuits in piezoelectric energy harvesting," *Smart Materials and Structures*, vol. 19, no. 12, pp. 125 009–125 020, 2010. [Online]. Available: http://www.ingentaconnect.com/content/iop/sms/2010/00000019/00000012/art125009

[88] L. Garbuio, M. Lallart, D. Guyomar, C. Richard, and D. Audigier, "Mechanical energy harvester with ultralow threshold rectification based on sshi nonlinear technique," *Industrial Electronics, IEEE Transactions on*, vol. 56, no. 4, pp. 1048 –1056, april 2009.

[89] M. Lallart, L. Garbuio, L. Petit, C. Richard, and D. Guyomar, "Double synchronized switch harvesting (dssh): a new energy harvesting scheme for efficient en-

ergy extraction," *Ultrasonics, Ferroelectrics and Frequency Control, IEEE Transactions on*, vol. 55, no. 10, pp. 2119 –2130, october 2008.

[90] C. Richard, D. Guyomar, and E. Lefeuvre, "Self-powered electronic breaker with automatic switching by detecting maxima or minima of potential difference between its power electrodes," France Patent PCT/FR2005/003 000, 2007.

[91] M. Lallart, E. Lefeuvre, C. Richard, and D. Guyomar, "Self-powered circuit for broadband, multimodal piezoelectric vibration control," *Sensors and Actuators A: Physical*, vol. 143, no. 2, pp. 377 – 382, 2008. [Online]. Available: http://www.sciencedirect.com/science/article/pii/S0924424707008722

[92] L. Tang, Y. Yang, and C. Soh, "Broadband vibration energy harvesting techniques," in *Advances in Energy Harvesting Methods*, N. Elvin and A. Erturk, Eds. Springer New York, 2013, pp. 17–61. [Online]. Available: http://dx.doi.org/10.1007/978-1-4614-5705-3_2

[93] J. Twiefel and H. Westermann, "Survey on broadband techniques for vibration energy harvesting," *Journal of Intelligent Material Systems and Structures*, 2013. [Online]. Available: http://jim.sagepub.com/content/early/2013/02/18/1045389X13476149.abstract

[94] S. Shahruz, "Design of mechanical band-pass filters for energy scavenging," *Journal of Sound and Vibration*, vol. 292, no. 3 - 5, pp. 987 – 998, 2006. [Online]. Available: http://www.sciencedirect.com/science/article/pii/S0022460X05006085

[95] M. Ferrari, V. Ferrari, M. Guizzetti, D. Marioli, and A. Taroni, "Piezoelectric multifrequency energy converter for power harvesting in autonomous microsystems," *Sensors and Actuators A: Physical*, vol. 142, no. 1, pp. 329 – 335, 2008, <ce:title>Special Issue: Eurosensors XX The 20th European conference on Solid-State Transducers</ce:title> <ce:subtitle>Eurosensors 2006</ce:subtitle> <xocs:full-name>Eurosensors 20th Edition</xocs:full-name>. [Online]. Available: http://www.sciencedirect.com/science/article/pii/S0924424707005481

[96] I. C. Lien and Y. C. Shu, "Array of piezoelectric energy harvesting by the equivalent impedance approach," *Smart Materials and Structures*, vol. 21, no. 8,

p. 082001, 2012. [Online]. Available: http://stacks.iop.org/0964-1726/21/i=8/a=082001

[97] L.-C. Blystad, E. Halvorsen, and S. Husa, "Piezoelectric mems energy harvesting systems driven by harmonic and random vibrations," *Ultrasonics, Ferroelectrics and Frequency Control, IEEE Transactions on*, vol. 57, no. 4, pp. 908 –919, april 2010.

[98] L.-C. Blystad and E. Halvorsen, "A piezoelectric energy harvester with a mechanical end stop on one side," in *Design Test Integration and Packaging of MEMS/MOEMS (DTIP), 2010 Symposium on*, may 2010, pp. 259 –262.

[99] H. Liu, C. Lee, T. Kobayashi, C. Tay, and C. Quan, "A mems-based wideband piezoelectric energy harvester system using mechanical stoppers," in *Electron Devices Meeting (IEDM), 2011 IEEE International*, dec. 2011, pp. 29.6.1 –29.6.4.

[100] L.-C. Blystad and E. Halvorsen, "A piezoelectric energy harvester with a mechanical end stop on one side," *Microsystem Technologies*, vol. 17, pp. 505–511, 2011. [Online]. Available: http://dx.doi.org/10.1007/s00542-010-1163-0

[101] L. Tang and Y. Yang, "A multiple-degree-of-freedom piezoelectric energy harvesting model," *Journal of Intelligent Material Systems and Structures*, vol. 23, no. 14, pp. 1631–1647, 2012. [Online]. Available: http://jim.sagepub.com/content/23/14/1631.abstract

[102] X. Tang and L. Zuo, "Enhanced vibration energy harvesting using dual-mass systems," *Journal of Sound and Vibration*, vol. 330, no. 21, pp. 5199 – 5209, 2011. [Online]. Available: http://www.sciencedirect.com/science/article/pii/S0022460X11004044

[103] A. Aladwani, M. Arafa, O. Aldraihem, and A. Baz, "Cantilevered piezoelectric energy harvester with a dynamic magnifier," *Journal of Vibration and Acoustics*, vol. 134, no. 3, p. 031004, 2012. [Online]. Available: http://link.aip.org/link/?VAJ/134/031004/1

[104] W. Zhou, G. R. Penamalli, and L. Zuo, "An efficient vibration energy harvester with a multi-mode dynamic magnifier," *Smart Materials and Structures*, vol. 21, no. 1, p. 015014, 2012. [Online]. Available: http://stacks.iop.org/0964-1726/21/i=1/a=015014

[105] A. Erturk, J. M. Renno, and D. J. Inman, "Piezoelectric energy harvesting from an l-shaped beam-mass structure," *Proc. SPIE 6928, Active and Passive Smart Structures and Integrated Systems 2008*, pp. 69 280I–69 280I–15, 2008. [Online]. Available: +http://dx.doi.org/10.1117/12.776211

[106] R. L. Harne and K. W. Wang, "A review of the recent research on vibration energy harvesting via bistable systems," *Smart Materials and Structures*, vol. 22, no. 2, p. 023001, 2013. [Online]. Available: http://stacks.iop.org/0964-1726/22/i=2/a=023001

[107] D. S. Nguyen and E. Halvorsen, "Analysis of vibration energy harvesters utilizing a variety of nonlinear springs," in *In proceeding of: Power MEMS 2010 Technical Digest Poster Sessions*, 2010.

[108] M. Ferrari, V. Ferrari, M. Guizzetti, B. Andçřů, S. Baglio, and C. Trigona, "Improved energy harvesting from wideband vibrations by nonlinear piezoelectric converters," *Procedia Chemistry*, vol. 1, no. 1, pp. 1203 – 1206, 2009, <ce:title>Proceedings of the Eurosensors XXIII conference</ce:title>. [Online]. Available: http://www.sciencedirect.com/science/article/pii/S1876619609003015

[109] G. Sebald, H. Kuwano, D. Guyomar, and B. Ducharne, "Simulation of a Duffing oscillator for broadband piezoelectric energy harvesting," *Smart Material Structures*, vol. 20, no. 7, p. 075022, Jul. 2011.

[110] ——, "Experimental Duffing oscillator for broadband piezoelectric energy harvesting," *Smart Material Structures*, vol. 20, no. 10, p. 102001, Oct. 2011.

[111] A. M. Wickenheiser and E. Garcia, "Broadband vibration-based energy harvesting improvement through frequency up-conversion by magnetic excitation," *Smart Materials and Structures*, vol. 19, no. 6, p. 065020, 2010. [Online]. Available: http://stacks.iop.org/0964-1726/19/i=6/a=065020

[112] L. Tang, Y. Yang, and C. K. Soh, "Toward broadband vibration-based energy harvesting," *Journal of Intelligent Material Systems and Structures*, vol. 21, no. 18, pp. 1867–1897, 2010. [Online]. Available: http://jim.sagepub.com/content/21/18/1867.abstract

[113] L. M. Miller, E. Halvorsen, T. Dong, and P. K. Wright, “Modeling and experimental verification of low-frequency mems energy harvesting from ambient vibrations,” *Journal of Micromechanics and Microengineering*, vol. 21, no. 4, p. 045029, 2011. [Online]. Available: http://stacks.iop.org/0960-1317/21/i=4/a=045029

[114] L.-C. Blystad and E. Halvorsen, “Simulation of an energy harvesting system with broadband excitation,” in *Systems, Signals and Devices, 2009. SSD ’09. 6th International Multi-Conference on*, march 2009, pp. 1 –5.

[115] E. Halvorsen, L.-C. Blystad, S. Husa, and E. Westby, “Simulation of electromechanical systems driven by large random vibrations,” in *Perspective Technologies and Methods in MEMS Design, 2007. MEMSTECH 2007. International Conference on*, may 2007, pp. 117 –122.

[116] S. Zhao and A. Erturk, “Electroelastic modeling and experimental validations of piezoelectric energy harvesting from broadband random vibrations of cantilevered bimorphs,” *Smart Materials and Structures*, vol. 22, no. 1, p. 015002, 2013. [Online]. Available: http://stacks.iop.org/0964-1726/22/i=1/a=015002

[117] E. Lefeuvre, A. Badel, C. Richard, and D. Guyomar, “Energy harvesting using piezoelectric materials: Case of random vibrations,” *JOURNAL OF ELECTROCERAMICS*, vol. 19, no. 4, pp. 349–355, 2007.

[118] D. Guyomar, C. Richard, and S. Mohammadi, “Semi-passive random vibration control based on statistics,” *Journal of Sound Vibration*, vol. 307, pp. 818–833, Nov. 2007.

[119] D. Guyomar and A. Badel, “Nonlinear semi-passive multimodal vibration damping: An efficient probabilistic approach,” *Journal of Sound Vibration*, vol. 294, pp. 249–268, Jun. 2006.

[120] H. A. Sodano, D. J. Inman, and G. Park, “Generation and storage of electricity from power harvesting devices,” *Journal of Intelligent Material Systems and Structures*, vol. 16, no. 1, pp. 67–75, 2005. [Online]. Available: http://jim.sagepub.com/content/16/1/67.abstract

[121] E. Halvorsen, “Energy harvesters driven by broadband random vibrations,” *Journal of Microelectromechanical Systems*, vol. 17, no. 5, pp. 1061–1071, 2008. [Online]. Available: http://dx.doi.org/10.1109/JMEMS.2008.928709

[122] H. Risken, *The Fokker-Planck Equation: Methods of Solutions and Applications*, 2nd ed. Springer, 1996.

[123] T. K. Caughey, “Derivation and application of the fokker-planck equation to discrete nonlinear dynamic systems subjected to white random excitation,” *The journal of the Acoustical Society of America*, vol. 35, pp. 1683–1692, 1963.

[124] S. Adhikari, M. I. Friswell, and D. J. Inman, “Piezoelectric energy harvesting from broadband random vibrations,” *Smart Materials and Structures*, vol. 18, no. 11, p. 115005, 2009. [Online]. Available: http://stacks.iop.org/0964-1726/18/i=11/a=115005

[125] A. Badel, D. Guyomar, E. Lefeuvre, and C. Richard, “Piezoelectric energy harvesting using a synchronized switch technique,” *Journal of Intelligent Material Systems and Structures*, vol. 17, no. 8-9, pp. 831–839, 2006. [Online]. Available: http://jim.sagepub.com/content/17/8-9/831.abstract

[126] M. Lallart, Y.-C. Wu, and D. Guyomar, “Switching delay effects on nonlinear piezoelectric energy harvesting techniques,” *Industrial Electronics, IEEE Transactions on*, vol. 59, no. 1, pp. 464–472, 2012.

[127] T. von Buren, P. Mitcheson, T. Green, E. Yeatman, A. Holmes, and G. Troster, “Optimization of inertial micropower generators for human walking motion,” *Sensors Journal, IEEE*, vol. 6, no. 1, pp. 28 – 38, feb. 2006.

[128] J. Antoni, “Cyclostationarity by examples,” *Mechanical Systems and Signal Processing*, vol. 23, no. 4, pp. 987 – 1036, 2009. [Online]. Available: http://www.sciencedirect.com/science/article/pii/S0888327008002690

[129] H. Taylor and S. Karlin, *An Introduction to Stochastic Modelling*. Academic Press, Incorporated, 1998. [Online]. Available: http://books.google.fr/books?id=UtPgVrVthF8C

[130] D. Castanon and W. C. Karl. Stochastic processes (class notes). Boston University College of Engineering. [Online]. Available: http://web.mit.edu/hmsallum/www/GradSchool/sc505notes.pdf

[131] C. Gardiner, *Handbook of stochastic methods for physics, chemistry, and the natural sciences*, ser. Springer series in synergetics. Springer, 1994. [Online]. Available: http://books.google.fr/books?id=ZfwaAQAAIAAJ

[132] W. Woyczyński, *A first course in statistics for signal analysis*, 2nd ed. Birkh auser Boston, 2011. [Online]. Available: http://books.google.fr/books?id=XaAmSQbqBc0C

[133] W. A. Gardner, *Cyclostationarity in Communications and Signal Processing*. IEEE, 1993, ch. An Introduction to Cyclostationary Signals.

[134] W. A. Gardner, A. Napolitano, and L. Paura, "Cyclostationarity: Half a century of research," *Signal Processing*, vol. 86, no. 4, pp. 639 – 697, 2006. [Online]. Available: http://www.sciencedirect.com/science/article/pii/S0165168405002409

[135] W. A. Gardner, "The spectral correlation theory of cyclostationary time-series," *Signal Processing*, vol. 11, no. 1, pp. 13 – 36, 1986. [Online]. Available: http://www.sciencedirect.com/science/article/pii/0165168486900927

[136] D. Guyomar and M. Lallart, "Switching loss reduction in nonlinear piezoelectric conversion under pulsed loading," *Ultrasonics, Ferroelectrics and Frequency Control, IEEE Transactions on*, vol. 58, no. 3, pp. 494–502, 2011.

[137] M. Lallart, D. J. Inman, and D. Guyomar, "Transient performance of energy harvesting strategies under constant force magnitude excitation," *Journal of Intelligent Material Systems and Structures*, vol. 21, no. 13, pp. 1279–1291, 2010. [Online]. Available: http://jim.sagepub.com/content/21/13/1279.abstract

[138] J. W. Xu, Y. B. Liu, W. W. Shao, and Z. Feng, "Optimization of a right-angle piezoelectric cantilever using auxiliary beams with different stiffness levels for vibration energy harvesting," *Smart Materials and Structures*, vol. 21, no. 6, p. 065017, 2012. [Online]. Available: http://stacks.iop.org/0964-1726/21/i=6/a=065017

[139] B. Blazejczyk-Okolewska, K. Czolczynski, and T. Kapitaniak, "Dynamics of a two-degree-of-freedom cantilever beam with impacts," *Chaos, Solitons and Fractals*, vol. 40, p. 1991âĂŞ2006, 2009.

[140] A. Badel, G. Sebald, D. Guyomar, M. Lallart, E. Lefeuvre, C. Richard, and J. Qiu, “Piezoelectric vibration control by synchronized switching on adaptive voltage sources: Towards wideband semi-active damping,” *Journal of the Acoustical Society of America*, vol. 119, pp. 2815–2825, 2006.

[141] J. M. Renno, M. F. Daqaq, and D. J. Inman, “On the optimal energy harvesting from a vibration source,” *Journal of Sound and Vibration*, vol. 320, no. 1-2, pp. 386 – 405, 2009. [Online]. Available: http://www.sciencedirect.com/science/article/pii/S0022460X0800669X

[142] R. Elfrink, M. Renaud, T. M. Kamel, C. de Nooijer, M. Jambunathan, M. Goedbloed, D. Hohlfeld, S. Matova, V. Pop, L. Caballero, and R. van Schaijk, “Vacuum-packaged piezoelectric vibration energy harvesters: damping contributions and autonomy for a wireless sensor system,” *Journal of Micromechanics and Microengineering*, vol. 20, no. 10, p. 104001, 2010. [Online]. Available: http://stacks.iop.org/0960-1317/20/i=10/a=104001

[143] Y.-B. Yang, C. Lin, and J. Yau, “Extracting bridge frequencies from the dynamic response of a passing vehicle,” *Journal of Sound and Vibration*, vol. 272, no. 3ÃćâĆňâĂIJ5, pp. 471–493, May 2004. [Online]. Available: http://www.sciencedirect.com/science/article/pii/S0022460X0300378X

[144] S. F. Ali, M. I. Friswell, and S. Adhikari, “Analysis of energy harvesters for highway bridges,” *Journal of Intelligent Material Systems and Structures*, vol. 22, no. 16, pp. 1929–1938, 2011. [Online]. Available: http://jim.sagepub.com/content/22/16/1929.abstract

[145] M. Lallart, Y.-C. Wu, L. Yan, C. Richard, and D. Guyomar, “The effect of seismic energy scavenging on host structure and harvesting performance,” *Smart Materials and Structures*, vol. 22, no. 3, p. 035009, 2013. [Online]. Available: http://stacks.iop.org/0964-1726/22/i=3/a=035009

[146] M. Lallart and D. Guyomar, “An optimized self-powered switching circuit for non-linear energy harvesting with low voltage output,” *Smart Materials and Structures*, vol. 17, no. 3, p. 035030, 2008. [Online]. Available: http://stacks.iop.org/0964-1726/17/i=3/a=035030

List of Tables

List of Figures

Publications

Journal papers

M. Lallart, **Y.-C. Wu** and D. Guyomar, "Switching Delay Effects on Nonlinear Piezoelectric Energy Harvesting Techniques", *IEEE Transactions on Industrial Electronics* **59**(1), 464–472 (2012). doi : 10.1109/TIE.2011.2148675

M. Lallart, **Y.-C. Wu**, C. Richard, D. Guyomar and E. Halvorsen, "Broadband modeling of a nonlinear technique for energy harvesting", *Smart Materials and Structures* **21**(11), 115006 (2012). doi : 10.1088/0964-1726/21/11/115006

M. Lallart, **Y.-C. Wu**, Linjuan Yan, C. Richard and D. Guyomar, "The effect of seismic energy scavenging on host structure and harvesting performance", *Smart Materials and Structures* **22**(3), 035009 (2013). doi : 10.1088/0964-1726/22/3/035009

M. Lallart, L. Yan, **Y.-C. Wu**, and D. Guyomar, "Electromechanical semi-passive nonlinear tuned mass damper for efficient vibration damping", *Journal of Sound and Vibration* **332**(22), 5696–5709 (2013). http://dx.doi.org/10.1016/j.jsv.2013.06.006

Y.-C. Wu, E. Halvorsen, M. Lallart, C. Richard and D. Guyomar, "Stochastic modeling in the frequency domain for energy harvester with switching electronic interface", *IEEE/ASME Transaction on Mechatronics*, **submitted in March, revised in July** (2013).

Y.-C. Wu, M. Lallart, C. Richard and D. Guyomar, "The effect of frequency detuning and seismic energy scavenging on host structure and harvesting performance under a broadband excitation", *Smart Materials and Structures*, **submitted in June, revised in Octorber** (2013).

Conference paper

Y.-C. Wu, M. Lallart, L. Yan, C. Richard and D. Guyomar, "On the self-powering of SHM techniques using seismic energy harvesting," *Proc. SPIE 8695: Health Monitoring of Structural and Biological Systems VII 2013, San Diego, CA* **86951M**, 1679974 (2013). doi : 10.1117/12.2005898

FOLIO ADMINISTRATIF

THESE SOUTENUE DEVANT L'INSTITUT NATIONAL DES SCIENCES APPLIQUEES DE LYON

NOM : **WU** DATE de SOUTENANCE : **17 Septembre 2013**
(avec précision du nom de jeune fille, le cas échéant)

Prénoms : **Yi-Chieh**

TITRE : **Analyse et considérations pratiques de techniques de conversion et récupération d'énergie piézoélectrique linéaires et non-linéaires**

NATURE : **Doctorat** Numéro d'ordre : 2013ISALXXXX

Ecole doctorale : **Mécanique, Energétique, Génie Civil et Acoustique de Lyon**

Spécialité : **Acoustique**

RÉSUMÉ : La décroissance de la consommation électrique des dispositifs électroniques (tels que des réseaux de capteurs autonomes) leur a permis une croissance sans précédent. Néanmoins, les éléments de stockage d'énergie (piles et batteries), bien qu'ayant initialement promus ce développement, sons devenus un frein à la prolifération des microsystèmes électroniques. Cette limitation s'explique par la durée de vie relativement limitée de ces éléments (l'auto-décharge drainant quelquefois plus d'énergie que celle consommée par le système) nécessitant une maintenance non négligeable et prohibitive lorsque les dispositifs sont nombreux et/ou inaccessible, ainsi que par des considérations environnementales ; le processus de recyclage des batteries étant complexe et coûteux. Pour palier à ce problème, la possibilité d'exploiter l'énergie de l'environnement immédiat du dispositif a été proposée et a fait l'objet de nombreuses recherches au cours des dernières années. En particulier, la récupération d'énergie mécanique exploitant l'effet piézoélectrique est l'une des pistes les plus étudiées actuellement pour la conception de microgénérateurs autonomes capables d'alimenter les dispositifs électroniques. Par ailleurs, dans ce domaine, il a été démontré que l'utilisation d'interfaces électroniques effectuant un traitement non-linéaire de la tension de sortie de l'élément actif permet d'améliorer grandement les capacités de conversion (et donc de récupération) de l'énergie vibratoire. L'une de ces approches, nommée «Synchronized Switch Harvesting on Inductor» (récupération par commutation synchronisée sur inductance) s'est montrée particulièrement efficace, pouvant augmenter la quantité d'énergie récupérée par un facteur supérieur à 10. Cette technique consiste à connecter l'élément piézoélectrique sur une inductance pendant un bref instant. L'élément piézoélectrique ayant un comportement diélectrique, ceci forme ainsi un circuit résonant qui conduit à une oscillation de la tension. Si le temps de connexion est choisi comme étant égal à une demi-période du circuit résonant ainsi formé, il se produit une inversion de tension. Cette dernière conduit à un processus cumulatif qui augmente artificiellement la tension de sortie de l'élément piézoélectrique ainsi qu'à une réduction du déphasage entre tension et vitesse de déplacement ; ces deux effets conduisant à l'augmentation importante des capacités de conversion. Néanmoins, l'étude des microgénérateurs d'énergie est quasiment toujours faite en considérant une excitation sinusoïdale, ce qui correspond rarement à la réalité. Peu de travaux expérimentaux, et encore moins théoriques, ont été menés en considérant une excitation large bande (impulsion, bruit…); ceci étant d'autant plus vrai pour les dispositifs incluant un élément non-linéaire. Ainsi l'objectif de cette thèse est d'étudier le comportement des récupérateurs d'énergie piézoélectriques interfacés de manière non-linéaire. Pour ce faire, différentes approches seront prises, en considérant le processus de commutation comme un « auto-échantillonnage » du signal, ou en appliquant des théories d'analyse stochastique pour quantifier les performances du dispositif. Ainsi, plusieurs formes d'excitation appliquée au système pourront être analysées, permettant d'étudier la réponse du système sous des conditions plus réalistes. Toujours dans l'optique d'une implémentation réaliste, un autre objectif de cette thèse consistera à évaluer l'impact de la récupération d'énergie par couplage sismique sur la structure hôte, démontrant la nécessité d'envisager le système dans sa globalité afin de disposer de systèmes performants capables de convertir efficacement l'énergie vibratoire sous forme électrique pour un usage ultérieur.

MOTS-CLES : **Matériaux piézoélectriques, transfert d'énergie, large bande, modélisation stochatique, désaccord de fréquence, effet de couplage, récupérateur sismique**

Laboratoire (s) de recherche : **Laboratoire de Génie Electrique et Ferroélectricité (LGEF) de l'INSA de Lyon**

Directeur de thèse: **Pr. Claude RICHARD**
Co-directeur de thèse: **Dr. Mickaël LALLART**

Président de jury :

Composition du jury : Pr. Bertrand DUBUS
Pr. Emmanuel FOLTETE
Pr. Daniel GUYOMAR
Pr. Einar HALVORSEN
Dr. Mickaël LALLART
Pr. Elie LEFEUVRE
Pr. Claude RICHARD
Pr. Wen-Jong WU